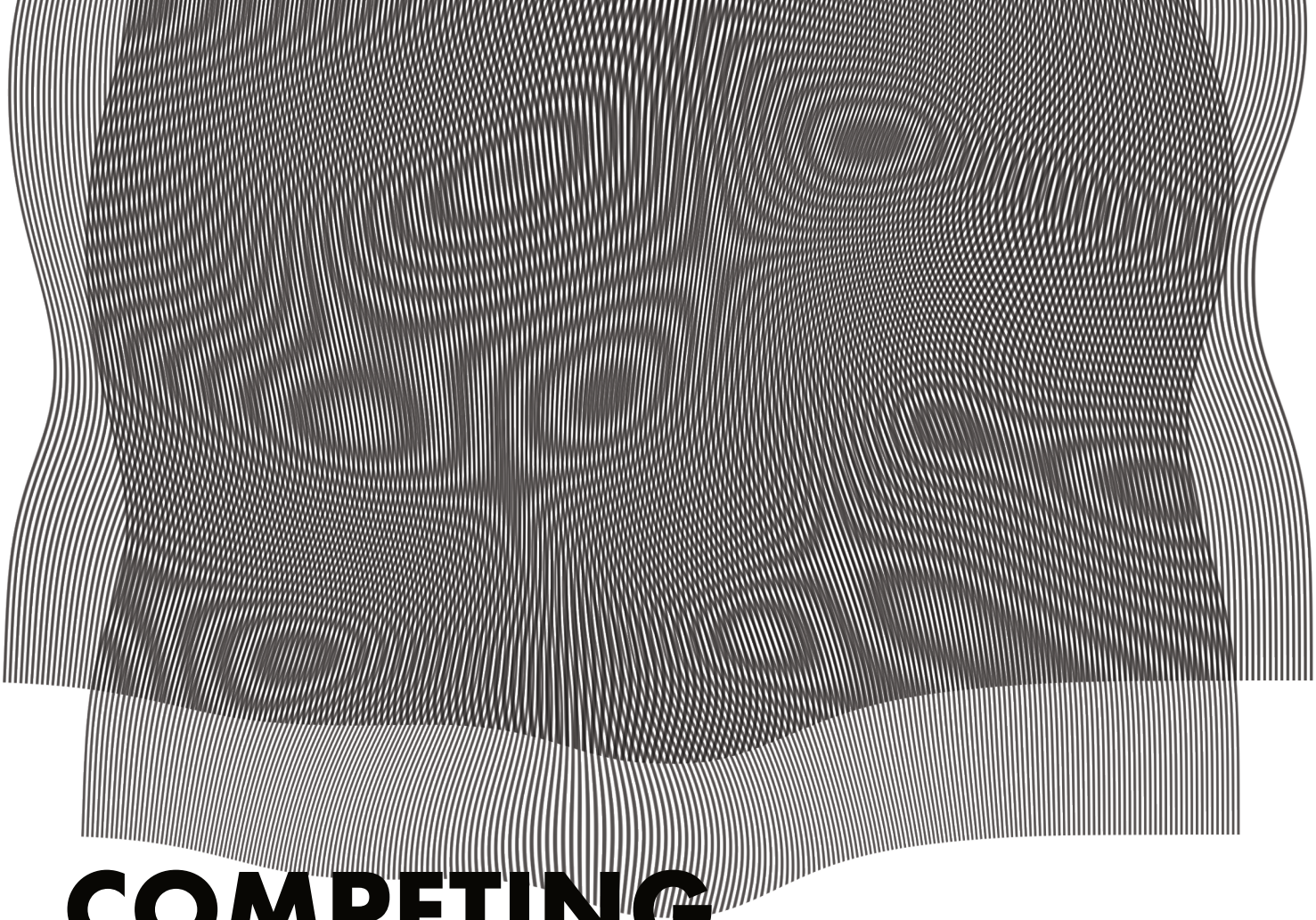

COMPETING ORDERS in the Triangular Lattice Hubbard Model

an Application of the Truncated-Unity Functional Renormalization Group

DISSERTATION

Nico Gneist

2022

Competing Orders in the Triangular Lattice Hubbard Model, an Application of the Truncated-Unity Functional Renormalization Group

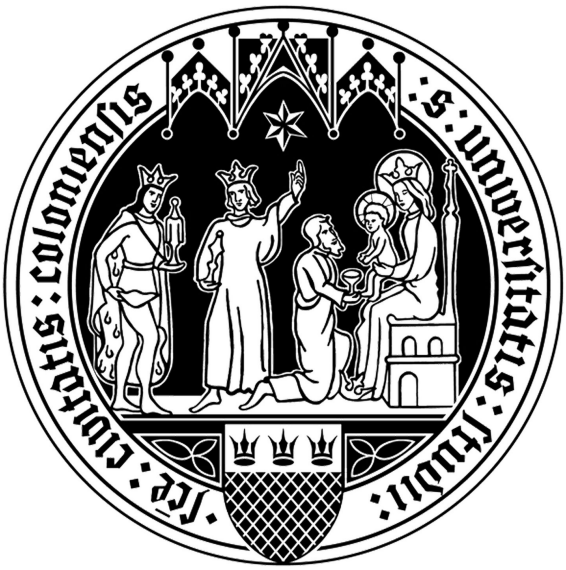

Inaugural-Dissertation
zur
Erlangung des Doktorgrades
der Mathematisch-Naturwissenschaftlichen Fakultät
der Universität zu Köln

vorgelegt von

Nico Gneist
aus Mönchengladbach

August 19th, 2022

Berichterstatter : Prof. Dr. Michael M. Scherer
Prof. Dr. Matteo Rizzi
Tag der mündlichen Prüfung : 19.10.2022

πάντα ῥεῖ - Everything flows

-Heraclitus of Ephesus
(From the Socratic dialogue „Kratylos", c.420 BC)

Just let go
Let it flow, let it flow, let it flow
Everything's gonna work out right
You know?

-Toni Braxton
(From the R&B song „Let It flow", 1995)

Kurzzusammenfassung

In dieser Dissertation präsentieren und implementieren wir die kürzlich entwickelte *truncated-unity functional renormalization group* (TUFRG) für eine Reihe von verschiedenen Hubbard-Modellen auf Dreiecksgittern an Van Hove-Füllung. Diese Arbeit ist in drei Teile gegliedert.

Im ersten Teil präsentieren wir eine kurze Einführung in die allgemeine Natur der entstehenden elektronischen Instabilitäten in korrelierten Fermionensystemen. Zu diesem Zweck führen wir das Hubbard-Modell als paradigmatische Beschreibung korrelierter Elektronen in der Festkörperphysik ein und leiten erste Erkenntnisse über das Auftreten magnetischer und supraleitender Instabilitäten im Sinne der Störungstheorie her. Es wird sich zeigen, dass bereits der kinetische Teil des Hamiltonians entscheidende Informationen über die elektronischen Instabilitäten enthält, welche schließlich durch Wechselwirkungen ausgelöst werden. Dennoch werden wir zeigen, dass die Störungstheorie allein das Auftreten von unkonventioneller Supraleitung nicht erklären kann, sodass direkt die Notwendigkeit begründet ist, im folgenden Kapitel eine Renormierungsgruppenmethode zu entwickeln. Bevor wir damit fortfahren werden wir kurz die BCS-Theorie für unkonventionelle Supraleitung zusammenfassen und leiten folgend die zulässigen Symmetrien für die Funktion der Energielücke für unsere Dreiecksgittersysteme durch einen kurzen Abstecher in die Gruppentheorie her. Diese Einführung wird dann durch einen kurzen Überblick über Moiré-Materialien abgeschlossen, eine neuartige Plattform interessanter stark korrelierter Systeme, welche effektiv durch Hubbard-Modelle beschrieben werden können. Die Existenz dieser effektiven Modelle hebt unsere Untersuchungen ab von der Behandlung paradigmatischer Spielzeugmodelle hin zu tatsächlich relevanten Ergebnissen aktiver Forschung.

Im zweiten Teil wird die TUFRG als eine neue Form der funktionalen Renormierungsgruppe (FRG) eingeführt. Zunächst stellen wir die allgemeinen Grundlagen der FRG dar, um einen Ausgangspunkt für die Herleitung der TUFRG zu erreichten. Die *Flussgleichungen* der FRG werden hier direkt mit allen für unsere Anwendungen notwendigen Symmetrien hergeleitet. Die TUFRG verbessert die Interpretierbarkeit der FRG durch die Einführung einer Kanalzerlegung, sodass bestimmte Diagramme des FRG-Schemas direkt mit dem möglichen Auftreten bestimmter Instabilitäten verknüpft sind. Darüber hinaus verbessert es die numerische Performanz älterer FRG-Schemata durch die Identifizierung unwichtiger Impulsabhängigkeiten, welche anschließend in Formfaktoren entwickelt werden um eine Beschleunigung der Rechenzeit zu erreichen. Wir werden nicht nur den kompletten Kontext der TUFRG von Grund auf herleiten, sondern auch die Details der numerischen Implementierung demonstrieren. Zu diesem Zweck werden mehrere nicht-generische technische Herausforderungen der Anwendungen vorgestellt und die notwendigen numerischen Lösungen bereitgestellt.

Der dritte Teil besteht aus der Anwendung des TUFRG auf drei verschiedene Dreiecksgittermodelle. In der ersten Anwendung werden wir ein SU(2)-invariantes erweitertes Hubbard-Modell auf einem Dreiecksgitter behandeln. Wir werden zunächst eine Spielzeugmodellversion behandeln, welche nur eine Hubbard-Wechselwirkung U und Nächste-Nachbarn-Wechselwirkungen V_1 enthält. Wir werden sehen, dass bereits in diesem einfachen Fall eine Fülle von magnetischen Instabilitäten und Instabilitäten zur unkonventioneller Supraleitung auftauchen, sodass sich ein reichhaltiges Phasendiagramm ergibt. Wir werden die analytischen Erkenntnisse aus dem ersten Kapitel mit den Ergebnissen

hier verknüpfen, sodass überzeugende Argumente für die Fundiertheit unserer numerischen Implementierung gemacht werden können. Anschließend fügen wir dem Modell Wechselwirkungen und Hüpfraten mit längerer Reichweite hinzu, sodass das Modell effektiv ein verdrilltes Übergangsmetall-Dichalcogenid (tTMD)-Heteroschichtensystem beschreibt. Wir werden sehen, dass ein Großteil des qualitativen Verhaltens dieses Modells bereits durch das paradigmatische Spielzeugmodell abgedeckt ist und Veränderungen in der Form der unkonventionellen Supraleitung teilweise durch die Analyse des Kanalflusses verstanden werden können. Der Vollständigkeit halber fügen wir diesem Abschnitt Konvergenzprüfungen hinzu, welche die Korrektheit unserer Ergebnisse demonstrieren.

In der zweiten Anwendung behandeln wir ein spinloses Hubbard-Modell auf einem Dreiecksgitter. Ursprünglich wurde dieses Modell verwendet, um die TUFRG-Ergebnisse mit den Ergebnissen einer anderen FRG-Implementierung zu vergleichen, aber in dieser Dissertation werden wir uns nur auf die TUFRG-Ergebnisse konzentrieren, sodass dieses System als Spielzeugmodell dient. Wir werden hier nur die Nächste-Nachbarn-Wechselwirkung V_1 einbeziehen, aber den Fall einer attraktiven und einer repulsiven Wechselwirkungsstärke untersuchen. Der Vergleich dieser beiden Fälle verdeutlicht den Unterschied des zugrundeliegenden Mechanismus der zur Supraleitung führt, welcher bei einer anziehenden Wechselwirkung trivial und im Falle einer abstoßenden Wechselwirkung weitaus komplexer ist. Wir werden mehrere Phasendiagramme mit unterschiedlichen Wechselwirkungsstärken und Füllungen berechnen und diesen Abschnitt durch zusätzliche Konvergenzprüfungen komplettieren.

In der dritten und letzten Anwendung werden wir erneut ein spinvolles Hubbard-Modell auf einem Dreiecksgitter behandeln, allerdings ohne $\mathrm{SU}(2)$-Symmetrie. Dieses Modell weist zwei nicht entartete Bänder auf sodass die TUFRG muss mit Spin-Freiheitsgraden ausgestattet werden muss um dieser zusätzlichen Quantenzahl Rechnung zu tragen. Dieses Modell ist wesentlich komplexer als seine Gegenstücke in den vorherigen Anwendungen, so dass mehrere Änderungen an unserer numerischen Implementierung vorgenommen werden müssen. Die hier vorgestellten Ergebnisse sind nicht veröffentlicht und dienen dem vorläufigen Verständnis des Modells. Durch den Vergleich numerischer Ergebnisse mit analytischen Erkenntnissen werden wir zeigen, dass die TUFRG eine geeignete und leistungsfähige Methode zur Untersuchung dieses Modells ist. Diese vorläufigen Ergebnisse zeigen bereits eine Fülle exotischer physikalischer Instabilitäten, wie inkommensurate Spindichtewellen und eine ungewöhnliche supraleitende Instabilität namens *Paardichtewelle*. Außerdem weist dieses Modell eine Van-Hove-Singularität höherer Ordnung auf, deren Auswirkungen ebenfalls hier sichtbar werden können.

Abstract

In this PhD thesis, we present and implement the recently developed *truncated-unity functional renormalization group* (TUFRG) for a set of different triangular lattice Hubbard models around Van Hove filling. The thesis is composed into three parts.

In the first part, we will present a brief introduction to the general nature of emerging electronic instabilities in correlated fermion systems. To this purpose, we introduce the Hubbard model as paradigmatic description of correlated electrons in solid state physics and derive first insights about the onset of magnetic and superconductive instabilities in terms of perturbation theory. It will become apparent that already the kinetic part of the Hamiltonian encodes crucial information about these electronic instabilities which are finally triggered by interactions. Nevertheless, we will demonstrate that perturbation theory alone *cannot* explain the occurrence of unconventional superconductivity which directly establishes the necessity to develop renormalization group methods in the following section. Before we proceed there, we will briefly summarise the BCS theory for unconventional superconductivity and derive the allowed symmetries for the gap functions for our triangular lattice systems by are short detour into the realm of group theory. The introduction is then finalized by a short review of Moiré Materials, a novel platform of interesting strongly correlated systems which can be effectively described by Hubbard models. The existence of these effective models elevates our studies from treating paradigmatic toy models to actually delivering relevant results for active research.

In the second part, we will introduce the TUFRG as a novel form of the functional renormalization group (FRG). At first, the general basics of the FRG will be presented as a foundation for deriving the TUFRG method. The *flow equations* of the FRG are directly obtained with all necessary symmetries for our applications. The TUFRG advances the FRG in interpretability by introducing a channel decomposition such that several diagrams of the FRG scheme are directly linked to the possibility of certain instabilities. Moreover, it greatly increases the numerical performance of previous FRG schemes by the identification of unimportant momentum dependencies which are subsequently developed in form factors to generate computational speedup. We will not only derive the complete TUFRG framework from first principles, but also demonstrate the details of the numerical implementation. For this purpose, several non-generic technical challenges of the applications are presented and the necessary numerical solutions are provided.

The third part consists of the application of the TUFRG to three different triangular lattice models.
In the first application, we will treat a SU(2)-invariant extended Hubbard model on a triangular lattice. At first, we will treat a toy model version which only includes a Hubbard interaction U and nearest-neighbour interactions V_1. We will see that already in this simple case a plethora of magnetic instabilities and instabilities towards unconventional superconductivity emerge, such that a rich phase diagram is formed. We will link analytical insights from the first section to these results, allowing us to make convincing arguments for the soundness of our numerical implementation. Subsequently, we will add longer ranged interactions and hoppings to the model such that the model effectively describes a twisted transition metal dichalcogenide (tTMD) heterobilayer system. We will see that a majority of the qualitative behaviour of this model is already covered by the paradigmatic toy model and changes in the form of the unconventional superconductivity can be in parts be understood by the

analysis of the channel flow. For completeness, we add convergence checks to this section, demonstrating the correctness of our results.
In the second application, we will treat a spinless Hubbard model on a triangular lattice. Originally, this model was used to compare TUFRG results with results of another FRG implementation, but in this thesis we will focus on the TUFRG results only such that the system serves as a toy model. We will only include a nearest-neighbour interaction V_1 here, but will investigate the case of an attractive and a repulsive interaction strength. The comparison of these two cases highlights the difference of the underlying mechanism leading to superconductivity which is trivial for an attractive interaction and much more complex in the case of a repulsive interaction. We will deliver several phase diagrams by changing interaction strengths and fillings and will support this section by additional convergence checks.
In the third and last application, we will again treat a spinful Hubbard model on a triangular lattice, but without SU(2)-symmetry. This model will feature two non-degenerate bands and the TUFRG has to be equipped with spin degrees of freedom to account for this additional quantum number. This model is much more complex than its counterparts in the former applications such that several alterations to our numerical implementation have to be made. The results presented here are not published yet and serve as a preliminary understanding of the model. By comparing numerical results with analytical insights, we will demonstrate that the TUFRG is a suitable and powerful method of examining this model. The preliminary results will already feature rich exotic physical instabilities such as incommensurate spin density waves and an unusual superconductive instability called *pair density wave*. Also this model features a *higher order Van Hove singularity*, whose effects also become apparent here.

Contents

Overture

One gram of copper inhabits roughly 10^{23} free electrons moving around in this solid formed by the copper atoms, participating in a plethora of interactions. Those interactions are not only with respect to the ions, but also between the electrons themselves. Moreover, electrons are responsive to the outer temperature and can be influenced by external magnetic and electric fields. Nevertheless, the physical phenomena we experience as humans regarding solid state systems do not showcase any of these multitude of microscopic processes, but are indeed macroscopic. Magnets, insulators, conductors and optical effects appear on ordinary length scales which we can process as humans without technical instruments and just by the bare eye. Without deeper knowledge of physics, we would not directly come up with the idea that these phenomena are rooted in the collective activity of objects which are almost twenty orders of magnitude smaller than we are.

This is the realm of condensed matter physics or - more precise - correlated electron systems. A central philosophical paradigm of this branch of physics was given by Anderson in his famous essay *More is Different* [1]. The effects of correlated electron systems must be understood as *emergent*, meaning that the behaviour of electrons on a larger scale cannot be explained by only examining the single properties of the respective electrons alone. In contrast, this behaviour must be understood as collective phenomenon, with an entirely new set of rules and mechanisms. Therefore, the physical effects on larger scales are accompanied with additional complexity and every reductionist approach, explaining those effects by a decomposition of the constituents of the underlying system, must fail. In some sense, Andersons' essay is a modernized rephrasing of a tenet of ancient Greek philosophy[1]: *the whole is greater than the sum of its parts.*

Leaving philosophy to the old Greeks, we want to be more specific about the physics. The complexity in correlated electron systems stems from electron-electron interactions, mainly the Coulomb interaction which leads to the general repulsive behaviour of two electrons. The complete scene of correlated electrons is set by the movement of the electrons, which is described as hopping in the ion lattice, in combination to thermal excitations and the general repulsive Coulomb interaction. This leads to a complex interplay of different aspects such that a simple treatment of the system to understand the occurring physical effects is not possible.

The physical framework which successfully describes quantum many-body physics is provided by quantum field theory. Originally describing high-energy physics in the context of sub-atomic particles, it moved on being one of the crucial achievements of modern theoretical physics. For condensed matter physics, an intuitive approach of quantum field theory is provided by the path integral formalism:

$$Z = \int D(\bar{\psi}, \psi)\, e^{-S[\bar{\psi},\psi]}.$$

In the spirit of statistical mechanics, all many-body information of a system is encoded in the partition function Z. The path integral accounts for the effects of a system with many or infinite degrees of freedom by the usage of fermionic fields $\psi, \bar{\psi}$, while the action S is the description of this given system

[1] Some sources point to Aristotle for this quote, but apparently the true origin is unclear. Anyway, this is not a thesis in philosophy, so we deem this as good enough for us.

at the microscopical level. Therefore, the path integral formalism mirrors exactly the philosophical presumptions of Anderson. On the right hand side, we have all the microscopic constituents of a solid - given by the continuous fields - and their behaviour is modeled by the action S. The functional integration accounts for all possible configurations of the system weighted with this action. Subsequently, we are reaching an emergent object, the partition function Z, from which we can derive macroscopic effects.

Unfortunately (and not really surprisingly), nature does not reveal itself that easily since the path integral is in general not analytically solvable. This is of course not a problem special to correlated electrons and various analytical and computational methods were developed in the past to treat models accordingly. In this zoo of methods, we will shift our focus on the renormalization group (RG) techniques which emphasise the importance of *scales* explicitly in the formalism of quantum field theory. In a general momentum formulation, the RG was pioneered by Kenneth Wilson [108, 109]. The conceptual core of RG is given by treating fluctuations of the path integral scale by scale, and not in the *unsorted* manner by an ordinary path integral. Starting at high energies (or momenta) the effects of these degrees of freedom are integrated out and the effects are absorbed to the remaining degrees of freedom of the theory. An iterative procedure can then be derived, integrating out energy scale by energy scale. The initial interactions describing the system microscopically are *renormalized*, and the change of these interactions is named *RG flow*.

Metaphorically speaking, the RG acts as the *magnifying glass* or *microscope* of theoretical physics. Starting at high momentum scales (reciprocally corresponding to small length scales), we see a given physical system at a microscopical scale. We look at individual constituents, governed by their microscopical laws and mechanisms. Then, by *zooming out* of the system, i.e. starting the RG procedure, we reach lower momentum scales (larger length scales). The effects of the scale beneath are *coarse grained* and absorbed into the emergent description of the next scale. An iterative application of this procedure leads us to the macroscopic level where all underlying effects are absorbed and we reach at the effective emergent description. It is of course no coincidence that this description matches the proposed epistemological notion favoured by Anderson. The RG procedure is a direct implementation of this idea, providing a description of the emergent behaviour of the vast amount of electrons in a solid.

In this thesis we will work with the *functional renormalization group* (FRG), introduced by Wetterich [107]. The FRG takes the RG idea to an even higher level by re-formulating the path integral itself in the context of scales. For this purpose, the path integral is exchanged for an integro-differential equation: the *flow equation*. The flow equation describes the evolution of the initial interaction S towards the full effective action Γ (which can be understood as an object equivalent to Z) by the trajectory stemming from solving this differential equation. This description is, on a formal level, exact but we will see that also here several approximations and truncations have to be employed to restore a feasible method.

Within this framework, we will treat correlated electron systems and search for *electronic instabilities*, i.e. interaction strengths which diverge under the FRG procedure. These instabilities signal the tendency towards spontaneous symmetry breaking and a corresponding onset of ordering. Our models of choice will be electronic systems near *Van Hove singularities*. These singularities are divergencies in the density of states and will greatly enhance the possibility of aforementioned electronic instabilities. The paradigm of understanding different ordering tendencies was already established before in the discussion of unconventional superconductivity. These competing phases could be successfully explained by the FRG [39] and outgoing from this influential work in 2001 several developments and advancements of the FRG have been made, describing correlated electron systems at various levels of electronic filling and lattice geometries.

One of the most recent versions of the FRG method is the *truncated-unity FRG* (TUFRG)[64, 40, 98]. This scheme advances previous schemes by recognizing that specific diagrams of the FRG description can be directly related to physical phenomena, e.g. superconductivity or magnetism. Consequently, a *channel decomposition*[46] is employed to track the possible onset of an instability of different types (superconductivity, magnetism, charge-density wave) individually. In addition, the diagrammatic structure of these channels allows for an analysis of the dependence of the instabilities to the momenta which are used for the parametrization of the method. Accordingly, the instabilities are mainly mediated by one transfer momentum of the diagrams. In a new formulation of the flow equations, unimportant momenta are expanded into form factors and the TUFRG framework will eventually only depend linearly on the amount of used momenta, allowing for high momentum resolutions. Eventually, the TUFRG improves previous FRG schemes in three aspects: computational speed, interpretability and the possibility to use any kind of Brillouin zone sampling such that incommensurable structures (i.e. structures with pronounced features away from the Fermi surface) can be resolved.

An active and recently established research area governed by correlated electron systems is given by Moiré materials. This research area was ignited by the recent study of twisted bilayer graphene (TBG) [15, 14], illustrating the essence of a Moiré material. Here, two graphene sheets are stacked on each other and a small twist angle is applied to one of these layers. Therefore, a superlattice structure emerges[2]. The length scales of this superlattice is a magnitude larger than the lattices of the single graphene sheets. In this study[15], correlated insulator states and unconventional superconductivity were found, indicating that the observed effects are indeed stemming from strongly correlated electrons. Interestingly, these models feature extremely flat and isolated bands. By these properties, the electron carrier density is easy to tune in these systems since the flatness of the bands leads to a small bandwidth and a large amount of filling situations can be achieved just by an external gate voltage, circumventing problems of chemical doping. Following the stir caused by TBG, a plethora of other Moiré materials were proposed. One of these classes of materials are twisted transition metal dichalcogenides (tTMDs) which are constructed exactly like TBG by just changing the material used for stacking and twisting. Interestingly, these models happen to be effectively capturable by (extended) triangular lattice Hubbard models [112, 79].

This defines the general direction of research followed in this thesis. The following work is divided intro three parts:

1. Introduction. We briefly present the foundations of electronic instabilities and their emergence. For that purpose, we dive into heuristical arguments made in the context of perturbation theory. Eventually, we will see that this perturbative description cannot completely describe the formation of superconductivity in every given model. This indicates to go beyond perturbation theory and develop a RG method to fully resolve the missing components to capture electronic instabilities. In a second section, we give a brief introduction to unconventional superconductivity itself. We describe standard BCS-theory and supplement this discussion by key results of representation theory to classify the gap functions belonging to superconductive instabilities. In a third section, we shortly discuss Moiré materials as possible application cases for triangular lattice Hubbard models.

2. Method. Here we describe and derive the TUFRG scheme used in this thesis. This section starts with a standard introduction of FRG for correlated electron systems which is used as a starting point for the TUFRG method. The application of this method to the triangular lattice Hubbard models is not generic, therefore we will also investigate a selection of conceptual and numerical problems which will arise when treating these models. This is covered in an implementation

[2]The term "Moire" is derived from the so-called Moiré interference pattern which can produced when an opaque ruled pattern with transparent gaps is overlaid on a structure of a similar pattern.

section where the individual parts and purposes of the numerical machinery are discussed.

3. Application. Finally, the TUFRG is applied to three different triangular lattice models near Van Hove filling which are relevant in the context of Moiré materials. We present various instabilities, detected in these studies, and display comprehensive phase diagrams. Furthermore, we will not just exhibit the findings of our studies, but also discuss them in the established context of the first chapter. We derive several sanity checks connected to the basic notions of electronic instabilities to ensure the soundness of the developed numerical methodology.

For now, we spoke about the *content* of this thesis, but there should also be a remark on the *spirit* of this thesis.

As any piece of research, the core aspect of this work is given by developing a tool to collect new data which (hopefully) leads to novel insights into current research areas. Naturally, a large part of this thesis is dedicated to this paradigm. Admittedly, there is a second aspect which we try to cover with care within this work. In lack of a better word, this aspect is *didactics*. It is an explicit goal of this work, to not only add new information and data to the body of research connected to the topics covered here, but also to be a guide for research to come. For that very reason, this thesis is written in a certain *holistic* form which tries to paint a complete picture of how to detect electronic instabilities in Hubbard models and how to specifically capture them by using the novel TUFRG approach. Therefore, the reader may find some passages in this work more didactic than he or she is used to from other theses. This is indeed intended, because we aim to present a work which can be used as a starting point for future practitioners.

CHAPTER 1

Introduction: Competing Order in Triangular Lattice Hubbard Models

This section serves as an introduction to the basic notions of describing fermionic systems and how electronic instabilities towards specific phases can already be concluded from simple channel summations. We will also demonstrate how some cases of superconductivity are rooted in the interplay of different interaction types such that they are not derivable in simple terms. This circumstance justifies the necessity of a renormalization group method which we will establish in chapter 2. We will proceed by briefly summarizing the theory of unconventional superconductivity, whereas we will focus on the relationship of the underlying lattice symmetry of our Hamiltonian and the emerging gap functions. Finally, a short overview of Moiré materials is presented which serve as potential application cases of our method.

1.1 Quantum Many-Body Instabilities in Fermionic Systems

The idea of a metal or a likewise solid state system is - at its core - quite simple. We can think of the system as the composition of two different kinds of entities:

1. The atomic ions which form a periodic geometric structure: the **lattice**.
2. The **electrons** which move through this lattice.

In the context of correlated electron systems, the ions can be assumed to be almost static and their interactions to each other can be reasonably neglected. Therefore, metals are described by the dynamics of the electrons and their interaction effects. These interactions occur between the electrons and the ions, but also among electrons themselves [12]. So, the ions provide the geometrical structure of a system which is eventually described as being purely electronic. But this abridgment should not be confused as being overly simplistic. A plethora of different ground states can be found in these systems when the temperature is lowered, depending on the electronic filling, the geometry of the lattice and the present types of interaction. Some of these tendencies towards specific phases can already be concluded from simple channel summations, but we will show that some materials exhibit behaviour which has to be explained in a more refined manner.

1.1.1 Interacting Fermions and the Hubbard model

The most elementary way to describe $\approx 10^{23}$ electrons in a solid state system is to assume the formation of a **free Fermi gas**. In this concept, the non-interacting electrons possess momentum $\mathbf{k}$, spin σ and charge e^- and move freely in the system. They obey the known Fermi-Dirac statistics and they will fill up all momentum states from the ground state upwards exactly twice (with opposite spins) at $T = 0$ by the Pauli exclusion principle. The highest lying state which is occupied this way signifies the **Fermi energy** E_F.

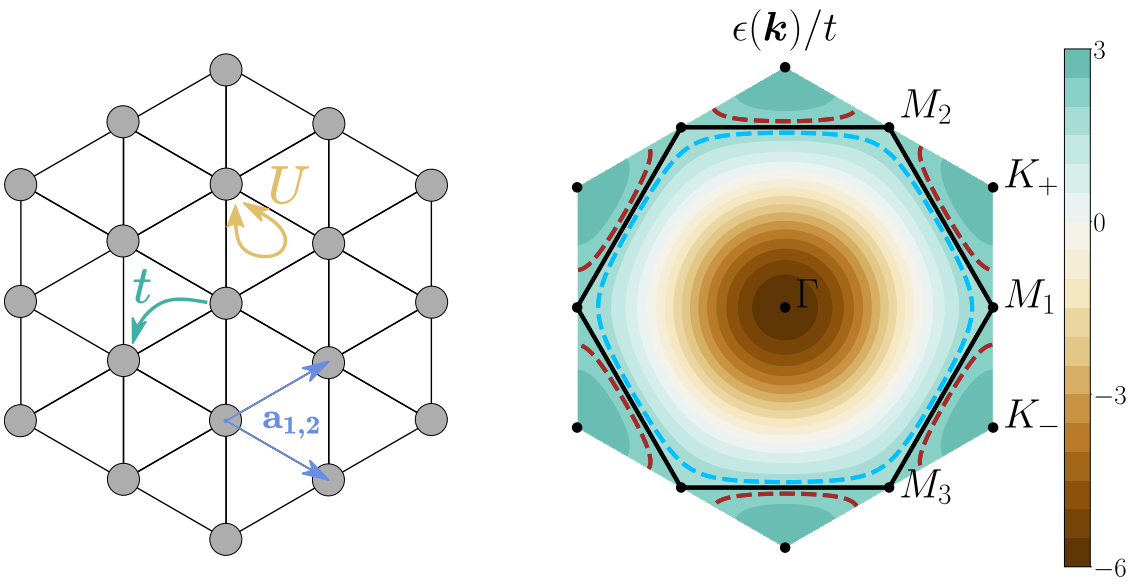

Figure 1.1: **Properties of the triangular lattice Hubbard model:** a) Real space lattice structure of model with hopping t and Coulomb interaction U. b) Dispersion of the model in the first Brillouin zone. The dashed lines correspond to the Fermi surfaces for chemical potentials of $\mu/t = 1.8$ (blue), $\mu/t = 2.0$ (black) and $\mu/t = 2.2$ (brown).

As mentioned before, the phases emerging in correlated electron systems are results of the interactions of electrons such that the Fermi gas cannot be a sufficient description of what we ought to describe. Fortunately, the **Fermi liquid theory** proposed by Landau [103] successfully explains the interaction effects on electrons in metals at low temperatures. In Landau's theory, the interacting Fermi liquid is thought as a state of the system which is adiabatically connected to the non-interacting Fermi gas. Landau showed that the excitations in the Fermi liquid behave mostly similar to the free fermions in the gas: they still keep their fermionic nature and will keep their momentum **k**, spin σ and charge e^- without a change of the Fermi energy. But the adiabatic increase of interactions will lead to a change (or **renormalization**) of dynamic properties like mass m or effective magnetic moment g. These new excitations of the Fermi liquid theory are called **(fermionic) quasiparticles**. Knowing that these quasiparticles are qualitatively now similar to the fermions in the free Fermi gas, we can work safely with Hamiltonians of interacting electrons describing our materials of interest. One of the most paradigmatic Hamiltonian models describing electrons in metals is the **Hubbard model**[45]:

$$H = -t \sum_{\langle i,j\rangle,\sigma} \left(c^\dagger_{i,\sigma} c_{j,\sigma} + h.c. \right) + U \sum_i n_{i\uparrow} n_{i\downarrow} - \mu \sum_{i,\sigma} n_{i\sigma}, \tag{1.1}$$

with electronic annihilation (creation) operators $c^{(\dagger)}_{i,\sigma}$ for lattice site i with spin $\sigma \in \{\uparrow, \downarrow\}$ and density operators $n_{i,\sigma} = c^\dagger_{i,\sigma} c_{i,\sigma}$. Each term resembles one of the aforementioned aspects of electrons moving in an atomic lattice. The first term indicates nearest-neighbour hopping of electrons from lattice site i to j with hopping rate t, i.e. the kinetic part of the electrons. The second term models the Coulomb interaction of the electrons with interaction strength U since the term penalizes situations where two electrons with opposing spins are sitting on the same lattice site. The last term exhibits the chemical potential μ which couples to the density operator. The filling of the system can therefore be changed by tweaking μ. Note that also higher hopping rates t_n and density interactions V_n can be easily added to this model to include effects of n-th nearest-neighbours.

The model Eq. (1.1) does not specify directly the geometry of the underlying lattice. An extensive body of work - in both analytical and numerical terms - cover various geometries of this model (e.g.

see reviews [4],[87]) with a strong focus on the square lattice version of the Hubbard model. In our case, it will be expedient to focus on the triangular lattice Hubbard model, but it should be noted that the arguments of perturbation theory are indeed general and apply to several lattice geometries.

For the triangular lattice we impose the primitive real space vectors $\boldsymbol{a_{1,2}} = a/2\left(\sqrt{3}, \pm 1\right)^T$ with lattice constant a. To extract the dispersion of this model one directly uses a Fourier transform to diagonalize the kinetic part of Eq. (1.1) reaching:

$$\begin{aligned} H_{\text{kin}} &= \sum_{\mathbf{k},\sigma} \xi_{\mathbf{k}} c^\dagger_{\mathbf{k},\sigma} c_{\mathbf{k},\sigma} = \sum_{\mathbf{k},\sigma} \left(\epsilon_{\mathbf{k}} - \mu\right) c^\dagger_{\mathbf{k},\sigma} c_{\mathbf{k},\sigma} \\ \epsilon_{\mathbf{k}} &= -2t \cdot \left(\cos\left(a \cdot \left(\frac{\sqrt{3}}{2} k_x + \frac{1}{2} k_y \right) \right) + \cos\left(a \cdot \left(\frac{\sqrt{3}}{2} k_x - \frac{1}{2} k_y \right) \right) + \cos(a \cdot k_y) \right). \end{aligned} \tag{1.2}$$

The dispersion $\epsilon_{\mathbf{k}}$ (note the spin degeneracy and omitted spin index σ) of this model is displayed in Fig. 1.1, where we show how the Fermi surface changes by including different fillings i.e. varying μ.

1.1.2 The emergence of electronic instabilities

The appearance of instabilities in this paradigmatic model can be better inferred by translating Eq. (1.1) into the formalism of quantum field theory. The object of interest will then be the action:

$$S[\bar{\psi}, \psi] = S_0[\bar{\psi}, \psi] + S_I[\bar{\psi}, \psi], \tag{1.3}$$

$$S_0[\bar{\psi}, \psi] = \int_k \sum_\sigma \left(-i\omega + \xi_{\boldsymbol{k}}\right) \times \bar{\psi}_\sigma(k) \psi_\sigma(k), \tag{1.4}$$

$$S_I[\bar{\psi}, \psi] = \int_{k_1,k_2,k_3,k_4} U \times \bar{\psi}_\uparrow(k_1) \bar{\psi}_\downarrow(k_2) \psi_\downarrow(k_4) \psi_\uparrow(k_3) \times \delta_{1234} \tag{1.5}$$

where $\psi_\sigma(k) = \psi_\sigma(\omega, \boldsymbol{k})$ are Grassmann fields with momentum $\boldsymbol{k}$ in the first Brillouin zone and fermionic Matsubara frequency ω. The integral $\int_k$ is a shorthand notation for $\int_k = T \cdot A_{\text{BZ}}^{-}1 \int_{\text{BZ}} d\boldsymbol{k} \sum_\omega$, integrating over all momenta in the Brillouin zone (normalised to the area of the Brillouin zone A_{BZ}) and summing over the Matsubara frequencies with temperature T. Moreover, we will use the abbreviation $\delta_{1234} = \delta(\boldsymbol{k_1} + \boldsymbol{k_2} - \boldsymbol{k_3} - \boldsymbol{k_4}) \delta(\omega_1 + \omega_2 - \omega_3 - \omega_4)$.

Naturally, for obtaining the full quantum many-body information of a system one is confronted with the task of solving the path integral:

$$Z = \int D(\bar{\psi}, \psi)\, e^{-S[\bar{\psi}, \psi]}$$

which in the majority of the cases is not possible. Nevertheless, the onset of electronic instabilities is already capturable in terms of perturbation theory which is the simplest first method we can apply to this model. For that purpose we rewrite the action Eqs. (1.4) and (1.5) to derive simple Feynman rules to lead through an instructive example of emerging instabilities. For the quadratic part, we will add an explicit second integration to read of the bare propagator:

$$S_0[\bar{\psi}, \psi] = \int_k \int_{k'} \sum_{\sigma,\sigma'} \underbrace{\left(-i\omega + \xi_{\boldsymbol{k}}\right) \times \delta(k - k') \times \delta_{\sigma,\sigma'}}_{\left(G^0_{\sigma,\sigma'}(k,k')\right)^{-1} = (G^0(k))^{-1} \times \delta(k-k') \times \delta_{\sigma,\sigma'}} \times \bar{\psi}_\sigma(k) \psi_{\sigma'}(k'), \tag{1.6}$$

and for the quartic part, we will directly perform one of the momentum integrations to explicitly equip the fields with momentum conservation. In addition, we will shift the momenta such that the parametrization of the interaction inhabits a transfer momentum q which will become practical later:

$$S_I[\bar{\psi}, \psi] = \int_{k,k',q} U \times \bar{\psi}_\uparrow(k+q) \bar{\psi}_\downarrow(k'-q) \psi_\downarrow(k') \psi_\uparrow(k). \tag{1.7}$$

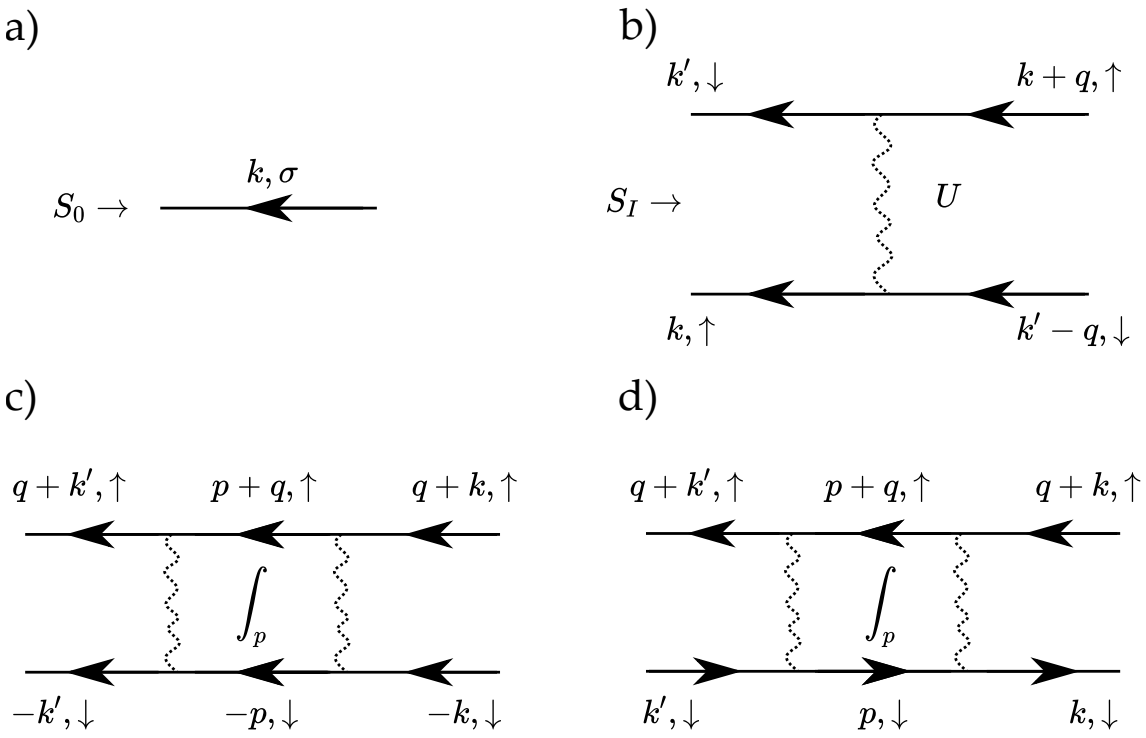

Figure 1.2: **Feynman rules and second order corrections:** a) Feynman rules for bare propagator and interaction vertex derived from the initial action. The propagator is diagonal in both, spin and momentum space and will therefore only connect legs with the same spin and imposes momentum conservation. The spin structure of the interaction vertex is dictated by the initial form of the Hubbard interaction. b),c) A particle-particle and a particle-hole diagram in second order, derived by contracting two vertices with the given propagators. The internal closed loop will result in being the so-called **bubble**.

We aim to investigate if specific correlation functions can gain substantial contributions under corrections of a perturbative expansion. At first, we want to look at a superconducting instabilities. For this purpose, we propose a generalized BCS-like interaction[1]:

$$S_I^{\text{BCS}}[\bar{\psi}, \psi] = \int_{k,k',q} \sum_{\sigma,\sigma'} V^{\text{BCS}}(k,k') \times \bar{\psi}_\sigma(q+k)\bar{\psi}_{\sigma'}(-k)\psi_{\sigma'}(-k')\psi_\sigma(q+k'). \tag{1.8}$$

To probe if an interaction like this will get significant increments, we must treat the connected diagrams of the (time-ordered) two-particle correlation function corresponding to Eq. (1.8). At first, the second order correction will be investigated. For brevity, we want to focus on only one of the contributions regarding of spin indices, namely $\sigma = \uparrow, \sigma' = \downarrow$:

$$G_c^{(4)}(q+k', \uparrow; -k', \downarrow; -k, \downarrow, q+k, \uparrow) = -\langle \psi_\uparrow(q+k')\psi_\downarrow(-k')\bar{\psi}_\downarrow(-k)\bar{\psi}_\uparrow(q+k)\rangle_c \tag{1.9}$$

which is simply done by applying the derived Feynman rules (see Fig. 1.2 a) and contracting two vertices such that the outer indices match those imposed by Eq. (1.9). One of the emerging diagrams at second order is called the **particle-particle diagram** (see Fig. 1.2 b) :

$$\text{PP} - \text{diagram} \rightarrow G^0(q+k')G^0(-k')G^0(q+k)G^0(-k) \times B^{\text{PP}}(q) \tag{1.10}$$

[1] A more detailed perspective for this action is presented in the next section

where the internal closed integration loop will be called the **particle-particle bubble**:

$$B^{\text{pp}}(q) = \int_p G^0(p+q)G^0(-p) = T \times A_{\text{BZ}}^- 1 \int_{\text{BZ}} d\boldsymbol{p} \sum_\omega G^0(\omega_p + \omega_q, \boldsymbol{p}+\boldsymbol{q})G^0(-\omega_p, -\boldsymbol{p})$$
$$= A_{\text{BZ}}^- 1 \int_{\text{BZ}} d\boldsymbol{p} \quad \frac{1 - n_F\left[\xi(-\boldsymbol{p})\right] - n_F\left[\xi(\boldsymbol{p}+\boldsymbol{q})\right]}{i\omega_q + \xi(-\boldsymbol{p}) + \xi(\boldsymbol{p}+\boldsymbol{q})}, \tag{1.11}$$

where we explicitly performed the Matsubara sum[2] to reach the final result featuring the Fermi function $n_F(x)$. We will see later that the explicit evaluation of this particular object is crucial for the onset of an instability. But first, we want to derive a related object by also inspecting a magnetic-like interaction[3]:

$$S_I^M[\bar{\psi}, \psi] = \int_{k,k',q} \sum_{\sigma,\sigma'} V^M(k,k') \times \bar{\psi}_\sigma(q+k)\bar{\psi}_{\sigma'}(k')\psi_{\sigma'}(k)\psi_\sigma(q+k'). \tag{1.12}$$

Repeating the procedure which resulted into the particle-particle diagram, one can derive in second order the **particle-hole diagram** (see Fig. 1.2 c) which inhabits the so called **particle-hole bubble**:

$$B^{\text{ph}}(q) = \int_p G^0(p+q)G^0(p) = T \cdot A_{\text{BZ}}^- 1 \int_{\text{BZ}} d\boldsymbol{p} \sum_\omega G^0(\omega_p + \omega_q, \boldsymbol{p}+\boldsymbol{q})G^0(\omega_p, \boldsymbol{p})$$
$$= A_{\text{BZ}}^- 1 \int_{\text{BZ}} d\boldsymbol{p} \quad \frac{n_F\left[\xi(\boldsymbol{p})\right] - n_F\left[\xi(\boldsymbol{p}+\boldsymbol{q})\right]}{i\omega_q + \xi(\boldsymbol{p}) - \xi(\boldsymbol{p}+\boldsymbol{q})}. \tag{1.13}$$

Naturally, a throughout application of perturbation theory also includes the examination of all emerging diagrams which can appear by applying the Feynman rules of our model, e.g. a proper summation of diagrams for the superconducting correlation function would have the form:

$$\langle \psi_\uparrow(q+k')\psi_\downarrow(-k')\bar{\psi}_\downarrow(-k)\bar{\psi}_\uparrow(q+k)\rangle$$
$$= \frac{\sum_{n=0}^\infty \frac{1}{n!}\langle \left(\psi_\uparrow(q+k')\psi_\downarrow(-k')\bar{\psi}_\downarrow(-k)\bar{\psi}_\uparrow(q+k)\right) \times (-S_I)^n\rangle_0}{\sum_{n=0}^\infty \frac{1}{n!}\langle (-S_I)^n\rangle_0}. \tag{1.14}$$

But we will see that for both physical phenomena described before, already a specific class of diagrams is sufficient to detect a diverging contribution to the correlation function, implying the **possible** onset of an instability.

These specific diagrams are the **particle-particle ladder** and the **particle-hole ladder**. The particle-particle ladder is straightforwardly assembled by repeating the construction which led to the particle-particle diagram also for higher orders of U and **only** including these types of diagrams in the summation Eq. (1.14) (see Fig. 1.3):

$$\langle \psi_\uparrow(q+k')\psi_\downarrow(-k')\bar{\psi}_\downarrow(-k)\bar{\psi}_\uparrow(q+k)\rangle_{\text{PP-Ladder}}$$
$$= G^0(q+k')G^0(-k')G^0(q+k)G^0(-k)\left(-U + U^2 \times B^{\text{pp}}(q) - U^3 \times B^{\text{pp}}(q)^2 + \dots\right)$$
$$= G^0(q+k')G^0(-k')G^0(q+k)G^0(-k)\,\frac{-U}{1 + U \times B^{\text{pp}}(q)}, \tag{1.15}$$

where we evaluated the sum to infinite order in U by using the expression of the geometric series. A similar result can be derived for the magnetic interaction correlator in terms of a particle-hole ladder:

$$\langle \psi_\uparrow(q+k')\psi_\downarrow(k')\bar{\psi}_\downarrow(k)\bar{\psi}_\uparrow(q+k)\rangle_{\text{PH-Ladder}}$$
$$= G^0(q+k')G^0(k')G^0(q+k)G^0(k)\frac{-U}{1 + U \times B^{\text{ph}}(q)}. \tag{1.16}$$

[2] The occurring Matsubara sum is covered in a plethora of standard text books for quantum field theory, see [76] or [122].

[3] In contrast to the BCS interaction, it is often not intuitively visible why this interaction is related to magnetic phenomena. This will become apparent in the discussion of the channel decomposition later in chapter two.

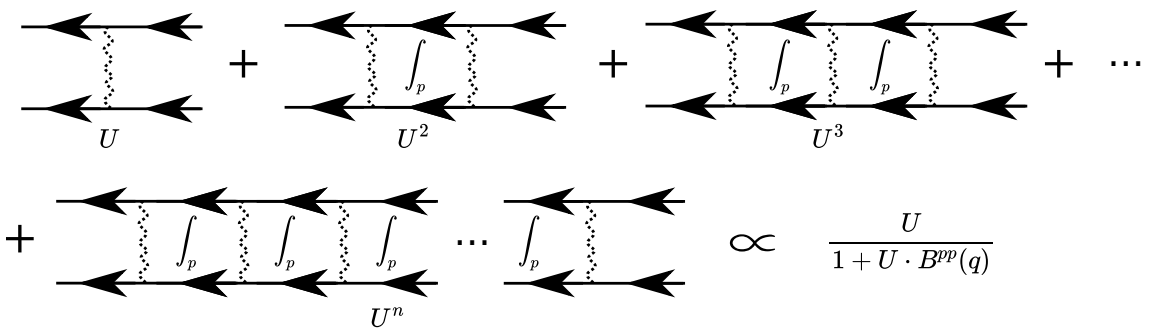

Figure 1.3: **Construction of particle-particle ladder:** Repeated construction of the particle-particle bubble to infinite order eventually builds up to a geometric series which can be evaluated directly.

Before continuing with further analysing the ladders Eqs. (1.15) and (1.16), we want to briefly stop and examine which insights we can now retrieve from this rather simplistic application of perturbation theory.

Confronted with the triangular Hubbard model as a simple and paradigmatic description of electrons in a solid, we were interested in the onset of instabilities i.e. diverging correlation functions which indicate the tendency of the system towards a specific phase. For this purpose, we chose exemplarily the correlator describing a superconductive interaction and another correlator describing magnetic interactions. In terms of a perturbative expansion, we successfully reached at an analytical expression of these correlators by only summing over a selected class of diagrams:

$$\langle \psi_\uparrow(q+k')\psi_\downarrow(-k')\bar{\psi}_\downarrow(-k)\bar{\psi}_\uparrow(q+k)\rangle_{\mathrm{PP-Ladder}} \propto \frac{-U}{1+U\times B^{\mathrm{pp}}(q)},$$
$$\langle \psi_\uparrow(q+k')\psi_\downarrow(k')\bar{\psi}_\downarrow(k)\bar{\psi}_\uparrow(q+k)\rangle_{\mathrm{PH-Ladder}} \propto \frac{-U}{1+U\times B^{\mathrm{ph}}(q)}.$$

The form of these expressions leads us to two important observations:

1. The onset of an instability (diverging correlator) is mainly dependent on the value of the bubbles $B^{\mathrm{ph/pp}}(q)$ as long as the bare propagator is regular.

2. On the other hand, the singular behaviour of these bubbles is mainly influenced by the value of the transfer momentum q.

Therefore, it is now the next logical step to investigate the physical situations which lead to diverging bubbles to understand the emergence of electronic instabilities.

Instabilities towards superconductivity

For finding an instability, we will investigate the case of $q = 0$, i.e. $\boldsymbol{q} = 0, \omega_q = 0$. Using the inversion symmetry of the dispersion Eq. (1.2) one can rewrite the particle-particle bubble Eq. (1.11) and transform it into an energy integral:

$$B^{\mathrm{pp}}(0) = A_{\mathrm{BZ}}^{-1}\int_{\mathrm{BZ}} d\boldsymbol{p}\ \ \frac{1-2n_F\left[\xi(\boldsymbol{p})\right]}{2\xi(\boldsymbol{p})} = \int_{-W}^{+W} d\epsilon\rho(\epsilon)\frac{1-2n_F\left[\epsilon-\mu\right]}{2\left(\epsilon-\mu\right)}. \tag{1.17}$$

Where we introduced the bandwidth W of the dispersion and the density of states $\rho(\epsilon)$. It can be shown that under the assumption that there is no singular behaviour in the density of states $\rho(\epsilon)$, the particle-particle bubble will develop a generic logarithmic dependency[4]:

$$B^{\mathrm{pp}}(0) \propto \rho_F \log\left(W/T\right) \tag{1.18}$$

[4]Precisely, this behaviour is only valid for a dispersion obeying inversion symmetry. For a detailed derivation of this results, see App. A.1.

where we also assumed that the density of states does not differ much from the value obtained at the Fermi surface ρ_F. Therefore, the particle-particle bubble will diverge for $T \to 0$. Considering the denominator of the particle-particle ladder Eq. (1.15) and setting it to zero such that a diverging correlator emerges:

$$1 + U \times B^{\text{pp}}(0) \stackrel{!}{=} 0. \tag{1.19}$$

Considering that the particle-particle bubble is positive, we see that for an initial repulsive interaction ($U > 0$) this condition can not be met, and for $T \to 0$ the correlator will just become small. If indeed the initial interaction would be attractive, i.e. $U = -|U|$ such that:

$$1 - |U| \times B^{\text{pp}}(0) \stackrel{!}{=} 0 \tag{1.20}$$

then there exists a T_c which consequentially leads to a divergence of the particle-particle ladder. This triggers the onset of a superconductive instability with transfer momentum $q = 0$. This behaviour is generic for fermionic systems since the logarithmic divergence of the bubble is only dependend on the inversion symmetry of the dispersion and on a positive density of states at the Fermi surface $\rho_F > 0$.

Indeed, we also want to consider a more special situation, namely a system at **Van Hove filling**. For the triangular lattice model, the Fermi surface for $\mu = 2t$ will have the form of a rotated hexagon (see Fig. 1.1 b) touching the $\boldsymbol{M}$ points. These points are special, because they will lead to a logarithmic divergence of the density of states. In vicinity of these points, the density of states can be described as:

$$\rho(\epsilon) \propto \log\left(\frac{W}{|\epsilon - \epsilon_{VH}|}\right) \tag{1.21}$$

where ϵ_{VH} is the energy at these points, called **Van Hove singularities**. This additional divergence will lead to a double-logarithmic divergence of the particle-particle bubble:

$$B^{\text{pp}}(0) \propto \log^2(W/T)\,. \tag{1.22}$$

The effect of this divergence will be the same: for an attractive U there will be an emerging instability towards superconductivity for $q = 0$ at low T. The nature of the double-logarithmic divergence will become important later when we discuss competing orders.

Instabilities towards magnetism

We will now repeat the analysis for the particle-hole bubble. At first, it should be noted that the particle-hole bubble is strictly i) real and ii) negative (as long as the dispersion inhabits inversion symmetry). Also, we will set the external Matsubara frequency to zero, $\omega_q = 0$. The criterion of a divergence regarding the denominator of the particle-hole ladder Eq. (1.16) is then given by:

$$1 - U \times |B^{\text{ph}}(0, \boldsymbol{q})| \stackrel{!}{=} 0. \tag{1.23}$$

Differently to the particle-particle case, the singularity of the particle-hole bubble does not generally appear for the transfer momentum $\boldsymbol{q} = 0$. Instead, the transfer momentum which leads to a divergence of the particle-hole bubble is connected to the so-called **nesting vector**. We describe **perfect nesting** as a situation where every point of the Fermi surface can be mapped to another point of the Fermi surface by a vector $\boldsymbol{q}_{\text{Nesting}}$, such that:

$$\epsilon(\boldsymbol{k}) = -\epsilon(\boldsymbol{k} + \boldsymbol{q}_{\text{Nesting}}). \tag{1.24}$$

This situation is realized in the Van Hove filling case, see Fig. (1.1). Moreover, the presence of the Van Hove singularity itself will add a logarithmic dependence to the bubble. In total, at Van Hove filling the form of the particle-hole bubble is given by[5]:

$$B^{\text{ph}}(0, \boldsymbol{q}_{\text{Nesting}}) \propto -\log^2(W/T)\,. \tag{1.25}$$

[5] For a detailed derivation, see App. A.2

So, for a repulsive U, we can directly expect an instability towards magnetism at low temperatures with transfer momentum $\boldsymbol{q} = \boldsymbol{q}_{\text{Nesting}}$. From the construction of the magnetic interaction Eq. (1.12), it can be derived that the emerging instability indeed is a spin density wave with modulation vector $\boldsymbol{q}_{\text{Nesting}}$. A special case is given if this transfer momentum happens to be zero: then the emerging instability will be a ferromagnet (since the spins are not modulating at all).

Roundup

This brief presentation of electronic instabilities in the Hubbard model serves this work in two ways. First, the general mechanism of emerging instabilities has been established. We will understand and discuss instabilities as the divergence of specific interaction types. These instabilities indicate that cases of symmetry breaking are **possible**, such that the system transfers to a respective phase. The instabilities are mainly driven by the behaviour of the particle-particle and particle-hole bubble, whose singular features are dictated by the underlying kinetic electronic behaviour. We derived that a particle-particle bubble divergence is generic and can only be realized if the initial interaction of the model is attractive. For the magnetic interaction, we saw that instabilities are directly driven by the existence of nesting vectors. Both tendencies towards these instabilities are also amplified by the presence of a Van Hove singularity.
Second, the usage of ladder summations as a perturbative framework also limits our perspective and cannot explain all possible phases of a system. The ladder summations can only signal the onset of superconductivity when the initial interaction is attractive. This does of course not imply that superconductivity with a repulsive interaction is in general out-ruled. To provide an understanding for these situations, we have to expand our theoretical approach such that additional crucial effects beyond ladder summations are accounted for.

1.1.3 The peculiar absence of attractive interaction or: competing instabilities

To answer the proposed question of the previous section, we want to shift the focus on materials which are actually capturable by the Hubbard model: cuprate superconductors [92, 86]. Cuprates are 3D materials where layers of copper oxides (CuO_2) are alternating with layers of metal oxides (XO with X a metal). The metals in the metal oxide layers can be replaced with other metals such that an experimentalist can decide to add electrons or holes into the system, a procedure called **chemical doping**. Therefore, these layers effectively act as charge reservoirs for the copper oxide planes. The copper oxide planes can then be treated as 2D models, where the filling is affected by the doping. Several angle-resolved photoemission (ARPES) studies have been conducted for cuprates, finding an antiferromagnetic phase which can be superseded by phases of superconductivity by variation of the filling [23, 3, 83] (see Fig. 1.4 for more details). In theoretical works, several ab-initio calculations successfully derived (square lattice) Hubbard models as an effective description for the cuprate band structures [120, 47, 69, 38, 37]. In perspective of our previous analysis this begs the question:

- How is superconductivity possible from an initial repulsive interaction?

To this end, we follow the lead suggested by the body of theoretical work and investigate the square lattice Hubbard model including also next-to nearest neighbours (indicated with a sum over $\langle\langle i,j\rangle\rangle$) with coupling t':

$$H = -t\sum_{\langle i,j\rangle,\sigma}\left(c^\dagger_{i,\sigma}c_{j,\sigma} + h.c.\right) - t'\sum_{\langle\langle i,j\rangle\rangle,\sigma}\left(c^\dagger_{i,\sigma}c_{j,\sigma} + h.c.\right) + U\sum_i n_{i\uparrow}n_{i\downarrow} - \mu\sum_{i,\sigma} n_{i\sigma}. \quad (1.26)$$

The dispersion is given by:

$$\xi_{\mathbf{k}} = -2t\left(\cos(a\cdot k_x) + \cos(a\cdot k_y)\right) - 4t'\cos(a\cdot k_x)\cos(a\cdot k_y) - \mu, \quad (1.27)$$

where the $\boldsymbol{X}$-points at $(0,\pm\pi)$, $(\pm\pi,0)$ will be Van Hove singularities. The Fermi surface can be tuned to those points by imposing $\mu_{\text{VH}} = 4t'$. The value of t' is mostly estimated to be ranging from

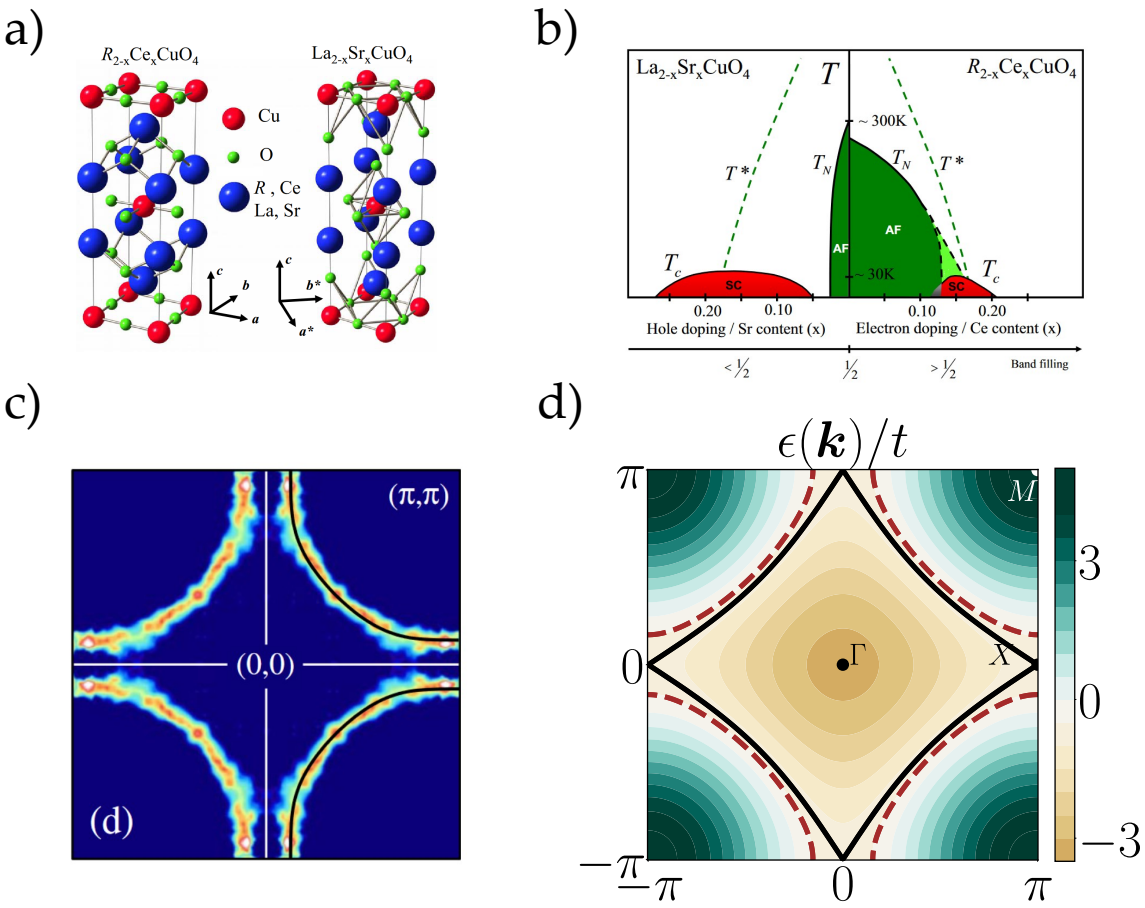

Figure 1.4: **Superconductivity in cuprates:** a) Crystal structure of the cuprates $R_{2-x}Ce_xCuO_4$ and $La_{2-x}Sr_xCuO_4$ taken from [3]. b) Phase diagram of the cuprates in a), displaying a transition from magnetism to superconductivity for under- or overdoping also taken from [3] c) ARPES measurment of cuprate $Tl_2Ba_2CuO_{6+\delta}$ showing the Fermi surface, taken from [83]. d) Dispersion of the square lattice Hubbard model with $t = 1$, $t' = -0.2t$. The black line corresponds to Van Hove filling $\mu = 4t'$, the dashed brown line to underdoping with $\mu = 2.4t'$.

$-0.1t$ to $-0.5t$ and will effectively add a small curvature to the Fermi surfaces (see Fig. 1.4 d). We focus on the findings derived by perturbation theory and establish the following scenarion:

- The Fermi surface can be tuned to a Van Hove singularity at the $\boldsymbol{X}$-points by selecting $\mu_{\text{VH}} = 4t'$
- At Van Hove filling, the Fermi surface is perfectly nested for $t' = 0$ and will have remnants of this effect if t' is still small.
- Therefore, the particle-particle bubble will have a double-logarithmic divergence for $q = 0$ and the particle-hole bubble will also feature a double-logarithmic divergence for $\boldsymbol{q} = \boldsymbol{q}_{\text{Nesting}}$.

From this, two questions arise:

1. To which of these two instabilities will the ground state finally tend, if both bubbles have the same degree of divergence?
2. How can a superconductive instability emerge in the first place if the interaction U is not attractive?

To answer these questions we must acknowledge that our perturbative approach negligently dismissed diagrams of mixed quality i.e. where the divergent particle-particle and particle-hole bubble are both part of. We can understand these missing diagrams as **feedback** of the two phenomena: the possible onset of superconductivity or magnetism may have far reaching consequences on other correlators. Since we only analysed the ladder summations, these effects were immediately neglected (similar to neglecting certain fluctuations when choosing a specific channel in mean field theory).

Consequently, convincing theoretical explanations for the superconducting phases in the square lattice Hubbard model have been made in the scope of the **renormalization group** (RG). We want to discuss and introduce the (functional) RG in detail later, but still want to highlight that the immense advantage of RG techniques lies in accounting for all interacting channels and their respective feedback on each other on the same footing, overcoming the problem which comes with using perturbation theory. Using parquet RG [67] or functional RG [93], the emergent phases of d-wave superconductivity could be identified in the square lattice Hubbard model which was also anticipated by other works [104, 96]. The intuitive essence of the mechanism can be understood as follows: near the Van Hove filling with perfect nesting, the system will develop a strong tendency towards antiferromagnetism (as already anticipated by the particle-hole ladder since our initial interaction U is repulsive). While this tendency grows, the feedback of the magnetic channel on the superconductive channel may eventually induce an attractive component, enabling the option of Cooper-pairing. The result of which instability will prevail eventually depends strongly on the model parameters. As a rule of thumb, situations at perfect nesting will in the majority of the cases induce an instability towards antiferromagnetism and will only make space for superconductivity if the Fermi surface is tuned lightly away from the Van Hove point or by systematically reducing the amount of nesting (which can be done by tuning t').

The situation of superconductivity in cuprates serves therefore as a paradigmatic example of **competing instabilities**. We will see that the models which we will eventually investigate in this thesis obey the same principles and can be understood under a similar perspective.

1.2 A brief summary of unconventional superconductivity

While it was presumed that the reader already knows about some fundamental aspects of superconductivity in the previous part, we will briefly review the basic notions of this phase of matter in this section. The benefit of this summary is twofold: on one hand, a discussion about the elementary theory of superconductivity - namely the (generalized) BCS theory - should be included to ensure a specific degree of completeness of this work. But moreover, the results derived in this section which will become indeed practical in the application of our method later. To be precise, the treatment of the generalized BCS theory provides the form of the superconductive gap equation and the possible symmetries of its solutions, the gap functions $\Delta_{\boldsymbol{k}}$.

Until today, superconductivity prevails of being one of the most interesting and fascinating phenomena of modern physics. Historically, the story of superconducitivity starts in 1911 with Heike Kamerlingh Onnes who discovered at first that the resistance of mercury spontaneously drops when cooled below a critical temperature of $T_c = 4.2K$. Initially only described as a perfect **conductor**, this perspective changed when in 1933 Meissner and Ochsenfeld discovered that metals entering a superconducting phase also fully expel all external magnetic fields entering the superconductor [71]. Therefore these materials are in fact not perfect conductors, but perfect **diamagnets**. The first major breakthrough from the side of the theory was proposed by Leon Cooper in 1956, making a profound argument that an ordinary Fermi gas cannot be a stable ground state of an electronic system if an electron-electron attraction of arbitrarily weak strength is included [22]. Indeed, the derived consequence is the formation of a ground state inhabiting so-called **Cooper pairs**, two electrons with opposing momentum which are created simultaneously above the Fermi energy which lead to

a destabilization of the Fermi surface. In 1957, Bardeen, Cooper and Schrieffer (BCS) published the BCS-theory as the groundbreaking contribution to the theoretical explanation of superconductivity [7]. The aformentioned pairing of electrons could be captured with a model Hamiltonian:

$$H_{\text{BCS}} = \sum_{\boldsymbol{k},\sigma} \xi_{\boldsymbol{k},\sigma} c^\dagger_{\boldsymbol{k},\sigma} c_{\boldsymbol{k},\sigma} + \sum_{\boldsymbol{k},\boldsymbol{k'}} V_{\boldsymbol{k},\boldsymbol{k'}} c^\dagger_{\boldsymbol{k},\uparrow} c^\dagger_{-\boldsymbol{k},\downarrow} c_{-\boldsymbol{k'},\downarrow} c_{\boldsymbol{k'},\uparrow}. \tag{1.28}$$

Notably, the attractive interaction leading to the Cooper pairing was found to be mediated by the coupling of the phonons to the electrons. In a simplistic manner, this mechanism can be imagined like this: the (negatively charged) electrons moving through the solid can attract the (positively charged) ions of the lattice. Since the timescales on which the ions move are much slower than the scales of the electron, the ions (which are now moved away from their resting position) form a positive charge in space, leading to the attraction of another electron, effectively describing an attractive electron-electron interaction. This mechanism was already discovered before the formulation of the BCS-theory by Fröhlich [27] who also showed that this interaction is effectively only strong in the vicinity of the Fermi surface. The interaction $V_{\boldsymbol{k},\boldsymbol{k'}}$ in Eq. (1.28) can then be replaced by:

$$V_{\boldsymbol{k},\boldsymbol{k'}} = \begin{cases} -|V_0| & \text{if } \epsilon_{\boldsymbol{k},\sigma} \approx \epsilon_{\boldsymbol{k}_F,\sigma} \\ 0 & \text{otherwise} \end{cases} \tag{1.29}$$

Proceeding in the history of superconductivity, several different origins for the pairing potential have been found. Of major influence were the studies of ^{3}He, showing mechanisms induced by Van-der-Waals interactions [63], but of course also the aforementioned cuprates feature an unconventional mechanism mediated by magnetic fluctuations [96]. To account also for these possible mechanisms, the model Hamiltonian Eq. (1.28) should be extended to a generalized form which we will present in the first subsection. The majority of the reproduction of the generalized BCS-theory here relies on the review by Sigrist [100].

1.2.1 Generalized BCS-Theory

We start with the generalized BCS Hamiltonian[6]

$$H = \sum_{\boldsymbol{k},\sigma} \xi_k c^\dagger_{\boldsymbol{k},\sigma} c_{\boldsymbol{k},\sigma} + \frac{1}{2} \sum_{\boldsymbol{k},\boldsymbol{k'}} \sum_{\sigma_1,\sigma_2,\sigma_3,\sigma_4} V_{\boldsymbol{k},\boldsymbol{k'};\sigma_1,\sigma_2,\sigma_3,\sigma_4} \times c^\dagger_{\boldsymbol{k},\sigma_1} c^\dagger_{-\boldsymbol{k},\sigma_2} c_{-\boldsymbol{k'},\sigma_4} c_{\boldsymbol{k'},\sigma_3}, \tag{1.30}$$

where in perspective to our Hubbard model we assume a spin-degeneracy in terms of the bands $\xi_{k,\sigma} = \xi_k$. This Hamiltonian is treated in terms of a mean field decoupling. For this purpose we impose the expectation values of the cooper pairs as follows:

$$c^\dagger_{\boldsymbol{k},\sigma_1} c^\dagger_{-\boldsymbol{k},\sigma_2} = \langle c^\dagger_{\boldsymbol{k},\sigma_1} c^\dagger_{-\boldsymbol{k},\sigma_2} \rangle + \left[c^\dagger_{\boldsymbol{k},\sigma_1} c^\dagger_{-\boldsymbol{k},\sigma_2} - \langle c^\dagger_{\boldsymbol{k},\sigma_1} c^\dagger_{-\boldsymbol{k},\sigma_2} \rangle \right], \tag{1.31}$$

$$c_{-\boldsymbol{k'},\sigma_4} c_{\boldsymbol{k'},\sigma_3} = \langle c_{-\boldsymbol{k'},\sigma_4} c_{\boldsymbol{k'},\sigma_3} \rangle + \left[c_{-\boldsymbol{k'},\sigma_4} c_{\boldsymbol{k'},\sigma_3} - \langle c_{-\boldsymbol{k'},\sigma_4} c_{\boldsymbol{k'},\sigma_3} \rangle \right], \tag{1.32}$$

where the content of the brackets $[\dots]$ can be understood as the fluctuations around the mean field expectation value. By plugging Eqs. (1.31),(1.32) into the Hamiltonian Eq. (1.30), we reach the de-

[6] Notice that we used this structure in the previous section to probe a superconducting correlator in Eq. (1.8). Although we used a simplified spin structure there, namely imposing SU(2) invariance and also enabling the possibility of a nonzero transfer momentum q.

coupled Hamiltonian:

$$\begin{aligned} H =& H_0 + H_{\text{Int}} + H_{\text{Int}'} \\ H_0 =& \sum_{\boldsymbol{k},\sigma} \xi_{\boldsymbol{k}} c^\dagger_{\boldsymbol{k},\sigma} c_{\boldsymbol{k},\sigma} \end{aligned} \tag{1.33}$$

$$H_{\text{Int}} = +\frac{1}{2} \sum_{\boldsymbol{k},\boldsymbol{k'}} \sum_{\sigma_1,\sigma_2,\sigma_3,\sigma_4} V_{\boldsymbol{k},\boldsymbol{k'};\sigma_1,\sigma_2,\sigma_3,\sigma_4} \times \left[\langle c^\dagger_{\boldsymbol{k},\sigma_1} c^\dagger_{-\boldsymbol{k},\sigma_2} \rangle c_{-\boldsymbol{k'},\sigma_4} c_{\boldsymbol{k'},\sigma_3} + c^\dagger_{\boldsymbol{k},\sigma_1} c^\dagger_{-\boldsymbol{k},\sigma_2} \langle c_{-\boldsymbol{k'},\sigma_4} c_{\boldsymbol{k'},\sigma_3} \rangle \right] \tag{1.34}$$

$$H_{\text{Int}'} = -\frac{1}{2} \sum_{\boldsymbol{k},\boldsymbol{k'}} \sum_{\sigma_1,\sigma_2,\sigma_3,\sigma_4} V_{\boldsymbol{k},\boldsymbol{k'};\sigma_1,\sigma_2,\sigma_3,\sigma_4} \times \langle c^\dagger_{\boldsymbol{k},\sigma_1} c^\dagger_{-\boldsymbol{k},\sigma_2} \rangle \langle c_{-\boldsymbol{k'},\sigma_4} c_{\boldsymbol{k'},\sigma_3} \rangle \tag{1.35}$$

where we want to focus on H_{Int} for now. We define the gap functions as:

$$\Delta_{\boldsymbol{k},\sigma\sigma'} = -\sum_{\tilde{\boldsymbol{k}},\tilde{\sigma},\tilde{\sigma}'} V_{\boldsymbol{k},\tilde{\boldsymbol{k}};\sigma,\sigma',\tilde{\sigma},\tilde{\sigma}'} \langle c_{-\tilde{\boldsymbol{k}},\tilde{\sigma}'} c_{\tilde{\boldsymbol{k}},\tilde{\sigma}} \rangle \tag{1.36}$$

$$\Delta^*_{-\boldsymbol{k},\sigma'\sigma} = -\sum_{\tilde{\boldsymbol{k}},\tilde{\sigma},\tilde{\sigma}'} V_{\boldsymbol{k},\tilde{\boldsymbol{k}};\tilde{\sigma},\tilde{\sigma}',\sigma,\sigma'} \langle c^\dagger_{\tilde{\boldsymbol{k}},\tilde{\sigma}} c^\dagger_{-\tilde{\boldsymbol{k}},\tilde{\sigma}'} \rangle \tag{1.37}$$

to recast H_{Int} into:

$$H_{\text{Int}} = -\frac{1}{2} \sum_{\boldsymbol{k},\sigma,\sigma'} \left[\Delta^*_{\boldsymbol{k},\sigma,\sigma'} c_{\boldsymbol{k},\sigma} c_{-\boldsymbol{k},\sigma'} + \Delta_{\boldsymbol{k},\sigma,\sigma'} c^\dagger_{\boldsymbol{k},\sigma} c^\dagger_{-\boldsymbol{k},\sigma'} \right]. \tag{1.38}$$

Dismissing $H_{\text{Int}'}$ now, the rest of the Hamiltonian can be cast into the following form:

$$H = \sum_{\boldsymbol{k}} \boldsymbol{C}^\dagger_{\boldsymbol{k}} \boldsymbol{H}_{\boldsymbol{k}} \boldsymbol{C}_{\boldsymbol{k}} \tag{1.39}$$

where the matrix $\boldsymbol{H}$ is defined as:

$$\boldsymbol{H}_{\boldsymbol{k}} = \frac{1}{2} \begin{pmatrix} \mathbb{1}\xi_{\boldsymbol{k}} & \bar{\Delta}_{\boldsymbol{k}} \\ \bar{\Delta}^\dagger_{\boldsymbol{k}} & \mathbb{1} - \xi_{-\boldsymbol{k}} \end{pmatrix} \quad , \bar{\Delta}_{\boldsymbol{k}} = \frac{1}{2} \begin{pmatrix} \Delta_{\boldsymbol{k},\uparrow\uparrow} & \Delta_{\boldsymbol{k},\uparrow\downarrow} \\ \Delta_{\boldsymbol{k},\downarrow\uparrow} & \Delta_{\boldsymbol{k},\downarrow\downarrow} \end{pmatrix} \tag{1.40}$$

and spinor $\boldsymbol{C}_{\boldsymbol{k}}$ are defined as:

$$\boldsymbol{C}_{\boldsymbol{k}} = \begin{pmatrix} c_{\boldsymbol{k},\uparrow} & c_{\boldsymbol{k},\downarrow} & c^\dagger_{-\boldsymbol{k},\uparrow} & c^\dagger_{-\boldsymbol{k},\downarrow} \end{pmatrix}^T. \tag{1.41}$$

Ultimate goal is to diagonalize the Hamiltonian. This can be achieved by a Bogolyubov transformation, meaning we need an unitary transformation $\boldsymbol{U}_{\boldsymbol{k}}$ such that:

$$\boldsymbol{E}_{\boldsymbol{k}} = \boldsymbol{U}^\dagger_{\boldsymbol{k}} \boldsymbol{H}_{\boldsymbol{k}} \boldsymbol{U}_{\boldsymbol{k}} = \begin{pmatrix} E_{\boldsymbol{k},+} & 0 & 0 & 0 \\ 0 & E_{\boldsymbol{k},-} & 0 & 0 \\ 0 & 0 & -E_{-\boldsymbol{k},+} & 0 \\ 0 & 0 & 0 & -E_{-\boldsymbol{k},-} \end{pmatrix}. \tag{1.42}$$

This Bogolyubov transformation is given by:

$$\boldsymbol{U}_{\boldsymbol{k}} = \begin{pmatrix} \bar{u}_{\boldsymbol{k}} & \bar{v}_{\boldsymbol{k}} \\ \bar{v}^*_{-\boldsymbol{k}} & \bar{u}^*_{-\boldsymbol{k}} \end{pmatrix} \quad , \bar{u}_{\boldsymbol{k}} = \mathbb{1} \times \frac{E_{\boldsymbol{k}} + \xi_{\boldsymbol{k}}}{\sqrt{2E_{\boldsymbol{k}} \left(E_{\boldsymbol{k}} + \xi_{\boldsymbol{k}} \right)}} \quad , \bar{v}_{\boldsymbol{k}} = \bar{\Delta}_{\boldsymbol{k}} \times \frac{-1}{\sqrt{2E_{\boldsymbol{k}} \left(E_{\boldsymbol{k}} + \xi_{\boldsymbol{k}} \right)}} \tag{1.43}$$

Here, the usage of unity pariring i.e. $\Delta\Delta^\dagger \propto \mathbb{1}$ will guarantee that $E_{\boldsymbol{k},+} = E_{\boldsymbol{k},-} = E_{\boldsymbol{k}}$. The final Hamiltonian is cast into:

$$H = \sum_{\boldsymbol{k}} \boldsymbol{A}^\dagger_{\boldsymbol{k}} E_{\boldsymbol{k}} \boldsymbol{A}_{\boldsymbol{k}}, \quad \boldsymbol{C}_{\boldsymbol{k}} = \boldsymbol{U}_{\boldsymbol{k}} \boldsymbol{A}_{\boldsymbol{k}}, \quad \boldsymbol{A}_{\boldsymbol{k}} = \begin{pmatrix} a_{\boldsymbol{k},+} & a_{\boldsymbol{k},-} & a^\dagger_{-\boldsymbol{k},+} & a^\dagger_{-\boldsymbol{k},-} \end{pmatrix}^T \tag{1.44}$$

where a Bogolyubov transformation is constructed in such a way that the emerging quasiparticles $a^{(\dagger)}_{\boldsymbol{k},\pm}$ still satisfy fermionic commutation relations. The energy and gap are finally given by:

$$E_{\boldsymbol{k}} = \sqrt{\xi_{\boldsymbol{k}}^2 + |\Delta_{\boldsymbol{k}}|^2}, \quad |\Delta_{\boldsymbol{k}}|^2 = \frac{1}{2}\mathrm{tr}\left(\bar{\Delta}_{\boldsymbol{k}}\bar{\Delta}^\dagger_{\boldsymbol{k}}\right). \tag{1.45}$$

To reach at the gap function, we replace the fermionic operators of the mean field defined before Eq. (1.36) by those defined by the Bogolyubov transformation Eq. (1.44) eventually leading to:

$$\Delta_{\boldsymbol{k},\sigma\sigma'} = -\sum_{\boldsymbol{k}',\sigma_3,\sigma_4} V_{\boldsymbol{k},\boldsymbol{k}';\sigma,\sigma',\sigma_3\sigma_4} \frac{\Delta_{\boldsymbol{k}',\sigma_3\sigma_4}}{2E_{\boldsymbol{k}'}} \tanh\left(\frac{E_{\boldsymbol{k}'}}{2T}\right). \tag{1.46}$$

For the actual use for the applications later, we can further simplify this. In the application B, the fermions will carry no spin entirely, such that the whole 2×2 spin structure shrinks to a scalar. In the application A, we will treat a SU(2) invariant system. In the framework of the FRG, this will lead to an interaction like:

$$V_{\boldsymbol{k},\boldsymbol{k}';\sigma_1,\sigma_2,\sigma_3\sigma_4} = V_{\boldsymbol{k},\boldsymbol{k}'}\delta_{\sigma_1,\sigma_3}\delta_{\sigma_2,\sigma_4} + \tilde{V}_{\boldsymbol{k},\boldsymbol{k}'}\delta_{\sigma_1,\sigma_4}\delta_{\sigma_2,\sigma_3}, \tag{1.47}$$

where it will be sufficient to solve the equations for the first part only. Including the constraint $\delta_{\sigma_1,\sigma_3}\delta_{\sigma_2,\sigma_4}$ in Eq. 1.46 will lead to $\Delta_{\boldsymbol{k},\sigma\sigma'} = \Delta_{\boldsymbol{k}}$ for all combinations of σ,σ'. Therefore the gap equation fo application A and B is given by:

$$\Delta_{\boldsymbol{k}} = -\sum_{\boldsymbol{k}'} V_{\boldsymbol{k},\boldsymbol{k}'} \frac{\Delta_{\boldsymbol{k}'}}{2E_{\boldsymbol{k}'}} \tanh\left(\frac{E_{\boldsymbol{k}'}}{2T}\right). \tag{1.48}$$

For the practical use of this equation, we want to derive an eigenvalue equation from it. For that purpose, we state that the system is near the critical temperature T_c such that the gap $\Delta_{\boldsymbol{k}}$ is right about to open up to a finite value, but still such that $E_{\boldsymbol{k}} \approx \xi_{\boldsymbol{k}}$ holds. Therefore Eq. (1.48) is rewritten:

$$\Delta_{\boldsymbol{k}} = -\sum_{\boldsymbol{k}'} V_{\boldsymbol{k},\boldsymbol{k}'} \frac{\Delta_{\boldsymbol{k}'}}{2\xi_{\boldsymbol{k}'}} \tanh\left(\frac{\xi_{\boldsymbol{k}'}}{2T_c}\right). \tag{1.49}$$

Which can then be treated as an eigenvalue problem if $V_{\boldsymbol{k},\boldsymbol{k}'}$ is given for the range of momenta we desire. In the end, the interaction $V_{\boldsymbol{k},\boldsymbol{k}'}$ will be delivered effectively by the FRG calculations. To interpret the eigenvalues of this equation we can revisit Eq. (1.49) in a further approximation. For that purpose, we note that the function $\tanh(x/2T_c)/x$ will have its maximal value at $x = 0$ and will decay quickly if deviating from this value, especially if T_c is small. This observation transfers to the fact that the major contributions are coming from the Fermi surface, i.e. $\xi_{\boldsymbol{k}} = 0$. Therefore, the highest increments to the right hand side of the equation are stemming from an energy range in a tiny shell around the Fermi surface $[-\epsilon_c, \epsilon_c]$ i.e. we introduce a cutoff energy ϵ_c. Approximating that the interaction $V_{\boldsymbol{k},\boldsymbol{k}'}$ and the density of states in this shell are not changing much when moved along a direction which is not the direction of the Fermi surface, we can approximate the gap equation with the following energy integral:

$$-\sum_{\boldsymbol{k}'} V_{\boldsymbol{k},\boldsymbol{k}'} \frac{\Delta_{\boldsymbol{k}'}}{2\xi_{\boldsymbol{k}'}} \tanh\left(\frac{\xi_{\boldsymbol{k}'}}{2T_c}\right) \approx -\left[V_{\boldsymbol{k},\boldsymbol{k}'}\Delta_{\boldsymbol{k}'}\right]_{\boldsymbol{k},\boldsymbol{k}'\text{near FS}} \underbrace{\int_{-\epsilon_c}^{+\epsilon_c} \rho(0)\frac{1}{2\epsilon}\tanh\left(\frac{\epsilon}{2T_c}\right) d\epsilon}_{\approx\rho(0)\log(1.13\epsilon_c/T_c)=\nu^{-1}}. \tag{1.50}$$

So, when focusing on the contributions near the Fermi surface only, the gap equation will finally simplify to:

$$\nu\Delta_{\boldsymbol{k}} = -\left[V_{\boldsymbol{k},\boldsymbol{k}'}\Delta_{\boldsymbol{k}'}\right]_{\boldsymbol{k},\boldsymbol{k}'\text{near FS}} \tag{1.51}$$

and the eigenvalues λ of this problem (namely diagonalizing $V_{\boldsymbol{k},\boldsymbol{k}'}\Delta_{\boldsymbol{k}'}$) can now be related to the constant ν finally delivering the context:

$$\begin{aligned} &\lambda = \nu \\ &\lambda = \left(\rho(0)\log(1.13\epsilon_c/T_c)\right)^{-1} \\ \iff\ &T_c = 1.13\epsilon_c \exp(-1/\lambda\rho(0)) \end{aligned} \tag{1.52}$$

such that the eigenvector $\Delta^i_{\boldsymbol{k}}$ with the highest eigenvalue λ^i will result into the highest critical temperature T_c and will therefore be the first superconducting state which will be realized. Throughout this thesis we will call this eigenvector the **leading gap**.

This small detour gained us insight about a suitable physical interpretation of the eigenvalues of the gap equation. For all practical applications, we are not restricted to values of $\boldsymbol{k}$ on the Fermi surface only and will indeed use Eq. (1.49) for the calculation of the leading gap.

1.2.2 Symmetry of Gap functions

It is of no surprise that the symmetry of the underlying Hamiltonian will have consequences on the form of the emergent superconductive gap function $\Delta_{\boldsymbol{k}}$. In practice, the gaps can be classified in the context of the point group on which the kinetic Hamiltonian is defined on. In this section, we will derive the possible gap functions for a system on a triangular lattice. For this purpose, the necessary elements of group theory and representation theory are introduced directly in the context of the triangular lattice. We will refrain from proving the needed mathematical theorems but will instead use the necessary foundations of the theory to derive the classification scheme of the gap functions in a pragmatic and practical way. For an in-depth discussion of the mathematical background, the reader is referred to the standard literature (highly recommending: [117]) or the thesis by Platt [85], from which this section is compiled from.

The triangular lattice and the point group C_{6v}

Choosing one lattice site in the triangular lattice as the origin, we can find a set of operations which leave the lattice invariant i.e. the state of the lattice after the application is identical to the state before applying the operation. Naturally for lattices, these operations are rotations and reflections and are collected in so-called **point groups**. The point group which leaves the triangular lattice invariant is C_{6v}, including rotations around the z-axis with angles $\phi = \pm\frac{2\pi}{6}, \pm\frac{2\pi}{3}, \frac{2\pi}{2}$ and in addition six reflections (see Fig. 1.5). The elements of the point group form a group (hence the name) which is formally defined as:

Definition 1 (Group)**.** *A group $G = \{G, \circ\}$ is a set G equipped with a multiplication law "$\circ$" such that the following axioms hold:*

- *The multiplication is associative:* $(g_1 \circ g_2) \circ g_3 = g_1 \circ (g_2 \circ g_3)$.
- *It exists a neutral element* E *such that for every* $g_i \in G$: $g_i \circ \mathrm{E} = \mathrm{E} \circ g_i = g_i$.
- *For each element* g_i *in the group exists an inverse element* $g_i^{-1} \in G$ *such that:* $g_i \circ g_i^{-1} = g_i^{-1} \circ g_i = \mathrm{E}$.

Where it is implied that the multiplication law always maps on the group again, i.e. $g_i \circ g_j \in G$ *for all* $g_i, g_j \in G$.

A straightforward way to fully describe a group is implemented by employing a **multiplication table**. Since the multiplication of two group elements always results again in a group element, we can sufficiently and completely define a group by the results of these multiplications (see Fig. 1.5).

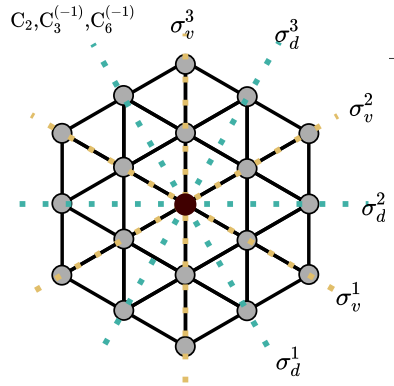

	E	C_6	C_6^{-1}	C_3	C_3^{-1}	C_2	σ_v^1	σ_v^2	σ_v^3	σ_d^1	σ_d^2	σ_d^3
E	E	C_6	C_6^{-1}	C_3	C_3^{-1}	C_2	σ_v^1	σ_v^2	σ_v^3	σ_d^1	σ_d^2	σ_d^3
C_6	C_6	C_3	E	C_2	C_6^{-1}	C_3^{-1}	σ_d^2	σ_d^3	σ_d^1	σ_v^1	σ_v^2	σ_v^3
C_6^{-1}	C_6^{-1}	E	C_3^{-1}	C_6	C_2	C_3	σ_d^1	σ_d^2	σ_d^3	σ_v^3	σ_v^1	σ_v^2
C_3	C_3	C_2	C_6	C_3^{-1}	E	C_6^{-1}	σ_v^2	σ_v^3	σ_v^1	σ_d^2	σ_d^3	σ_d^1
C_3^{-1}	C_3^{-1}	C_6^{-1}	C_2	E	C_3	C_6	σ_v^3	σ_v^1	σ_v^2	σ_d^3	σ_d^1	σ_d^2
C_2	C_2	C_3^{-1}	C_3	C_6^{-1}	C_6	E	σ_d^3	σ_d^1	σ_d^2	σ_v^2	σ_v^3	σ_v^1
σ_v^1	σ_v^1	σ_d^1	σ_d^2	σ_v^3	σ_v^2	σ_d^3	E	C_3^{-1}	C_3	C_6	C_6^{-1}	C_2
σ_v^2	σ_v^2	σ_d^2	σ_d^3	σ_v^1	σ_v^3	σ_d^1	C_3	E	C_3^{-1}	C_2	C_6	C_6^{-1}
σ_v^3	σ_v^3	σ_d^3	σ_d^1	σ_v^2	σ_v^1	σ_d^2	C_3^{-1}	C_3	E	C_6^{-1}	C_2	C_6
σ_d^1	σ_d^1	σ_v^3	σ_v^1	σ_d^3	σ_d^2	σ_v^2	C_6^{-1}	C_2	C_6	E	C_3^{-1}	C_3
σ_d^2	σ_d^2	σ_v^1	σ_v^2	σ_d^1	σ_d^3	σ_v^3	C_6	C_6^{-1}	C_2	C_3	E	C_3^{-1}
σ_d^3	σ_d^3	σ_v^2	σ_v^3	σ_d^2	σ_d^1	σ_v^1	C_2	C_6	C_6^{-1}	C_3^{-1}	C_3	E

Figure 1.5: **Properties of the C_{6v} point group.** Display of the respective symmetry operations leaving the triangular lattice invariant, differentiating between the reflections σ_x^i and the rotations C_n around $2\pi/N$ also accounting for possible rotation directions. The multiplication table of the point group C_{6v} indicates the operations which are equal to the multiplication of two operations of the group.

Representation, conjugacy class and character

If the reader forms the opinion that the characterization of the symmetry group of a lattice by a multiplication table *feels* in some sort clunky and awkward, then he or she is certainly right. In practice, physicist tend to think about symmetry operations in terms of *matrices* instead of elaborate multiplication tables. Labeling the lattice sites - outgoing from the origin - with a real space vector (x, y), we can *represent* the group elements as matrices. What is done in physics intuitively, is actually the usage of a **representation** of a group which is formally defined as follows:

Definition 2 (Representation)**.** *A group $\{F, \cdot\}$ is called a representation of a group $\{G, \circ\}$, if there exists a mapping $\Gamma : F \longmapsto G$, such that for every element $g_i, g_j \in G$ holds: $\Gamma(g_i) \cdot \Gamma(g_j) = \Gamma(g_i \circ g_j)$.*

In our practical applications, Γ will be matrices and " $\cdot$ " the ordinary matrix multiplication. The nature of a representation is very literal. On one hand, there exists the abstract *group* which is completely defined by a multiplication table and is not cast in a specific form which would make an application feasible. It is the *representation* which lends the abstract group a tangible form. The necessary condition that a representation actually faithfully resembles the underlying structure of the group operations is exactly implemented by the property $\Gamma(g_i) \cdot \Gamma(g_j) = \Gamma(g_i \circ g_j)$ which ensures that the rules of the multiplication table are inherited by the representation. The following collection displays one example representation of C_{6v}, consisting of the matrices a physicist would intuitively write down for the appearing rotations and reflections.

$$\Gamma(E) = \begin{pmatrix} 1 & 0 \\ 0 & 1 \end{pmatrix}, \quad \Gamma(C_6) = \begin{pmatrix} \frac{1}{2} & \frac{\sqrt{3}}{2} \\ -\frac{\sqrt{3}}{2} & \frac{1}{2} \end{pmatrix}, \quad \Gamma(C_6^{-1}) = \begin{pmatrix} \frac{1}{2} & -\frac{\sqrt{3}}{2} \\ \frac{\sqrt{3}}{2} & \frac{1}{2} \end{pmatrix},$$

$$\Gamma(C_3) = \begin{pmatrix} -\frac{1}{2} & -\frac{\sqrt{3}}{2} \\ \frac{\sqrt{3}}{2} & -\frac{1}{2} \end{pmatrix}, \quad \Gamma(C_3^{-1}) = \begin{pmatrix} -\frac{1}{2} & \frac{\sqrt{3}}{2} \\ -\frac{\sqrt{3}}{2} & -\frac{1}{2} \end{pmatrix}, \quad \Gamma(C_2) = \begin{pmatrix} -1 & 0 \\ 0 & -1 \end{pmatrix},$$

$$\Gamma(\sigma_v^1) = \begin{pmatrix} \frac{1}{2} & -\frac{\sqrt{3}}{2} \\ -\frac{\sqrt{3}}{2} & -\frac{1}{2} \end{pmatrix}, \quad \Gamma(\sigma_v^2) = \begin{pmatrix} \frac{1}{2} & \frac{\sqrt{3}}{2} \\ \frac{\sqrt{3}}{2} & -\frac{1}{2} \end{pmatrix}, \quad \Gamma(\sigma_v^3) = \begin{pmatrix} -1 & 0 \\ 0 & 1 \end{pmatrix},$$

$$\Gamma(\sigma_d^1) = \begin{pmatrix} -\frac{1}{2} & -\frac{\sqrt{3}}{2} \\ -\frac{\sqrt{3}}{2} & \frac{1}{2} \end{pmatrix}, \quad \Gamma(\sigma_d^2) = \begin{pmatrix} 1 & 0 \\ 0 & -1 \end{pmatrix}, \quad \Gamma(\sigma_d^3) = \begin{pmatrix} -\frac{1}{2} & \frac{\sqrt{3}}{2} \\ \frac{\sqrt{3}}{2} & \frac{1}{2} \end{pmatrix}$$

In addition, there is another structure one would intuitively think of for which a formally defined object exists. When looking at Fig. 1.5 again, we directly group the different symmetry operations into different sub-classes. There are obviously the different rotations, there are the reflections for which

the reflection axes are going straight through the nearest neighbour lattice sites ($\sigma_v^{1,2,3}$) and the reflections where the reflection axes go through the bonds ($\sigma_d^{1,2,3}$). Also, there is the identify itself doing nothing to the lattice. In representation theory, this is formally defined as **conjugacy** and **conjugacy classes**:

- Two elements $g_i, g_j \in G$ are **conjugate**, if there exists another element in the group $A \in G$ such that $g_i = A \circ g_j \circ A^{-1}$. By transitivity, if an element g_i is conjugate to g_j and g_j otherwise to g_k, then also g_i and g_k are conjugate.
- All elements which are conjugate to each other are forming a so-called **conjugacy class**.

The different conjugacy classes can be calculated straightforwardly by the definition. It is no coincidence that these classes will match the intuitive grouping which we can already think of before explicitly calculating these classes:

$$\begin{array}{llll} \mathrm{E} = \{E\}, & 2\mathrm{C}_6 = \{\mathrm{C}_6, \mathrm{C}_6^{-1}\}, & 2\mathrm{C}_3 = \{\mathrm{C}_3, \mathrm{C}_3^{-1}\}, & \mathrm{C}_2 = \{\mathrm{C}_2\}, \\ & 3\sigma_d = \{\sigma_d^1, \sigma_d^2, \sigma_d^3\}, & 3\sigma_v = \{\sigma_v^1, \sigma_v^2, \sigma_v^3\}. & \end{array}$$

Central to the nature of representations is the question: is a given representation **irreducible**? To define this property, we also define the notion of **equivalent** representations:

- Two representations Γ_μ,Γ_ν of the same group are equivalent if there exists a matrix U such that $\Gamma_\mu(g_i) = U \cdot \Gamma_\nu(g_i) \cdot U^{-1}$ for all $g_i \in G$.
- If a representation Γ is equivalent to a representation where all matrices have a common block structure, i.e. $\Gamma(g_i) = \begin{pmatrix} \Gamma^{11}(g_i) & 0 \\ 0 & \Gamma^{22}(g_i) \end{pmatrix}$ then the representation is called reducible. Otherwise the representation is irreducible (an irreducible representation is abbreviated by the name **irrep**).

If one desires now to check if a representation (e.g. the intuitive representation above) is irreducible, one must now complete the tedious task to work out a matrix U which transforms the matrices of the representation into a common block structure if possible. Fortunately, there are other ways to determine the irreducibility of a representation, but for this purpose an additional property has to be founded, namely the **character**. This is defined as follows:

Definition 3 (Character)**.** *The **character** $\chi_\Gamma(g_i)$ of an group element $g_i \in G$ in a representation Γ is the trace of the corresponding matrix: $\chi_\Gamma(g_i) = \mathrm{Tr}(\Gamma(g_i))$.*

We note two important insights:

- The trace is cyclic, therefore all elements of a conjugacy class have the same character.
- The character is therefore in fact a property of the conjugacy class, not of the objects themselves. We will denote the application of the character in an irrep Γ_μ on a class c_i as: $\chi_{\Gamma_\mu}(c_i) = \chi_\mu(c_i)$.

Now that all the groundwork is defined, we can actually proceed to the character table which condenses the essential information of the irreps of a point group.

Character table

In terms of mathematical rigor, we will allow us the freedom to take some leaps here now and state the important results about characters and irreps without proving or developing them. In the end, we will give some intuitive rationalizations about the correctness of these results.

At first, it is stated that the amount of conjugacy classes of a point group N_c are equivalent to the

C_{6v}	E	$2C_6$	$2C_3$	C_2	$3\sigma_d$	$3\sigma_v$
A_1	$+1$	$+1$	$+1$	$+1$	$+1$	$+1$
A_2	$+1$	$+1$	$+1$	$+1$	-1	-1
B_1	$+1$	-1	$+1$	-1	$+1$	-1
B_2	$+1$	-1	$+1$	-1	-1	$+1$
E_1	$+2$	$+1$	-1	-2	0	0
E_2	$+2$	-1	-1	$+2$	0	0

Table 1.1: Character table of the point group C_{6v}.

amount of different irreps for the group N_i. Furthermore, the conjugacy classes and irreps are connected by two orthogonality theorems:

$$\sum_i |c_i| \chi_\mu^*(c_i)\chi_\nu(c_i) = \delta_{\mu\nu} N_G, \tag{1.53}$$

$$\sum_\mu \chi_\mu^*(c_i)\chi_\mu(c_j) = \delta_{ij} \frac{N_G}{|c_i|}, \tag{1.54}$$

where N_G is the amount of elements in the group (i.e. for C_{6v} we have 12 elements) and $|c_i|$ is the amount of elements in a conjugacy class c_i. With these orthogonality relations and the insight that we will have exactly 6 irreps for 6 conjugacy classes, we can construct the so-called **character table** (Table 1.1). In this table, the characters of the different conjugacy classes are presented for all six irreps (named A_1, A_2, B_1, B_2, E_1 and E_2). By using this character table, we can now answer the question if our formerly proposed representation (the "intuitive" matrices) is an irrep or not. This can be done by selecting one matrix for every conjugacy class and calculate its trace. Consequently it becomes apparent that the representation is equivalent to the E_1 irrep since all characters match. The character table therefore encodes all relevant information about the irreps of a given point group and provides a simple criterion to check for reducibility of a given representation.

It should be noted that some of the irreps in the character table are qualitatively different from the rest, namely $E_{1,2}$. From the definition of the representation it directly follows that the matrix representing the unity group element always also has to be an unity itself. Investigating the first column of the character table, we can read off the character of the unity in each irrep. For $A_{1,2}$, $B_{1,2}$ this character is $+1$, implying that the unity is just the scalar 1. Therefore, these irreps are one-dimensional and the characters of the conjugacy classes are also directly the elements of the irrep itself. It is easy to see that the multiplication of the different characters in those four irreps faithfully represent the initial multiplication table of the C_{6v} point group.

For $E_{1,2}$, the character of the unity is $+2$, revealing that these irreps are two-dimensional (i.e. 2×2 matrices). In this case, the character of the conjugacy classes obviously cannot be equated to the an element of the irrep itself since the trace does not provide any information about the off-diagonal elements of the matrices.

Projection and basis functions

The practical use of the character table will become apparent when we go back to the eigenvalue problem of the gap function Eq. (1.49):

$$\Delta_{\boldsymbol{k}} = -\sum_{\boldsymbol{k}'} \tilde{V}_{\boldsymbol{k},\boldsymbol{k}'} \Delta_{\boldsymbol{k}'} \tag{1.55}$$

where we absorbed the factor consisting of the dispersion and the $\tanh(\dots)$ into the new interaction $\tilde{V}_{\boldsymbol{k}}$. $\tilde{V}_{\boldsymbol{k}}$ will inherit the symmetries from the initial BCS Hamiltonian, where it should be highlighted

that also the symmetries of the point group C_{6v} are leaving the interaction invariant. Under the assumption that these symmetries still hold, we can now apply the framework of representation theory to the eigenvalue problem to derive the following key results[7]:

- The diagonalization of $\tilde{V}_{\boldsymbol{k},\boldsymbol{k}'}$ leads to a diagonal matrix $D_{\boldsymbol{k},\boldsymbol{k}'}$ with eigenvalues λ^i. The corresponding eigenspaces are ordered with respect to the derived irreps of C_{6v}.
- Since the irreps are either 1- or 2-dimensional, the corresponding eigenspaces belonging to the eigenvalues λ^i are also either 1- or 2-dimensional. In the latter case, this means that there exists a 2×2 block inside $D_{\boldsymbol{k},\boldsymbol{k}'}$ with degenerated eigenvalues $\lambda^{i_1} = \lambda^{i_2}$.
- The eigenvectors of our problem are the eigenfunctions $\Delta^i_{\boldsymbol{k}}$ corresponding to eigenvalue λ^i. We remind ourselves that the eigenfunction belonging to the highest eigenvalue was the leading gap function of the superconductor.
- In standard linear algebra, vectors in the span of an eigenspace can be expressed as linear combinations of these eigenvectors. Since the eigenspaces are either 1- or 2-dimensional, the corresponding functions $f^i_{\boldsymbol{k}}$ in a subspace belonging to eigenfunction $\Delta^i_{\boldsymbol{k}}$ can be expressed as:

$$\begin{aligned} f^i_{\boldsymbol{k}} &= \alpha \Delta^i_{\boldsymbol{k}} \\ f^i_{\boldsymbol{k}} &= \alpha \Delta^{i,(1)}_{\boldsymbol{k}} + \beta \Delta^{i,(2)}_{\boldsymbol{k}} \end{aligned}$$

  with some coefficients α, β depending if λ^i belongs to 1-dimensional or 2-dimensional subspace.
- The eigenfunctions $\Delta^i_{\boldsymbol{k}}$ extracted from the diagonalization will be equivalent to the basis functions of the irrep Γ which can be derived by applying a projection operator to a suitable basis function of momentum space:

$$P^{(\mu)} = \sum_{i=1}^{N_G} \frac{d^\mu}{N_G} \chi^*(g_i)_\mu \Gamma(g_i), \tag{1.56}$$

  where d^μ is the dimension of the irrep Γ which are indexed with μ where the numbers $\mu = 1, 2, 3, 4, 5, 6$ correspond to the listing in the character table. The aforementioned basis function can be derived in momentum space by using plane wave basis functions.

In [85], it was nicely shown how this procedure can be executed. It was shown that one useful procedure uses basis functions on the lattice as basis functions of the real space on which the projector Eq. (1.56) is applied to. In contrast to [85], we will derive the lattice harmonics directly in momentum space by using plane waves as basis functions of momentum space:

$$b_i(\boldsymbol{k}) = e^{i \boldsymbol{R}_i \boldsymbol{k}} \tag{1.57}$$

where $\boldsymbol{R}_i$ are real space lattice vectors of the triangular lattice as numerated in Fig. 1.6. We apply the projection operator Eq. (1.56):

$$P^\mu b_i(\boldsymbol{k}) = \sum_{j=1}^{N_G} \frac{d^\mu}{N_g} \chi_\mu(g_j) e^{i(\Gamma^\mu(g_j)\boldsymbol{R}_i)\boldsymbol{k}} \tag{1.58}$$

The application of the symmetry operators $(\Gamma^\mu(g_i)\boldsymbol{R}_i)$ in the projection operator Eq. (1.58) will map $\boldsymbol{R}_i$ to one of the other real space vectors $\boldsymbol{R}_j$ with the same distance. We will proceed and offer a recipe to construct a lattice harmonic of nth order for a desired irrep.

[7] Again, we will just state this result without proving them since this would be immensely out of the scope of this introductory chapter. For a more detailed look for these results we advise [50].

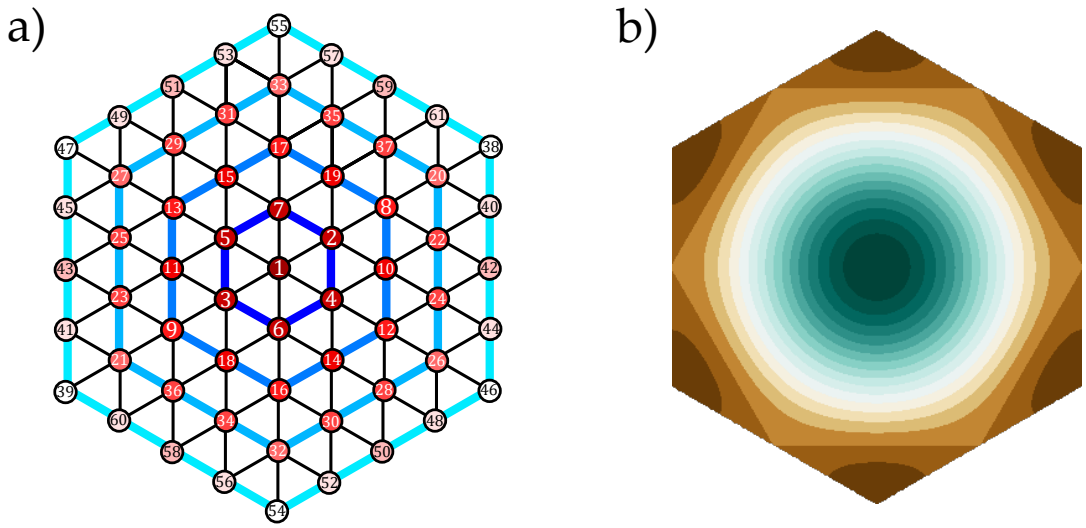

Figure 1.6: a) Numeration of first 61 lattice sites, including 0th to 8th nearest neighbours. b) momentum basis function of the irrep A_1 in first order.

For the one-dimensional irreps (i.e. A_1, A_2, B_1, B_2) we choose a lattice vector $\boldsymbol{R}_i$ displayed in Fig. 1.6 a. The distance to the origin corresponds to the order of the lattice harmonic. Therefore, for a first order lattice harmonic, we have to choose a nearest-neighbour lattice vector, e.g. $\boldsymbol{R}_2$. For higher orders, we have to select a lattice vector with larger distance. Two suitable sets for the different orders of vectors are given by:

Order	Set 1	Set 2
1st	$\boldsymbol{R}_2$	$\boldsymbol{R}_4$
2nd	$\boldsymbol{R}_{10}$	$\boldsymbol{R}_{14}$
3rd	$\boldsymbol{R}_8$	$\boldsymbol{R}_{12}$
4th	$\boldsymbol{R}_{22}$	$\boldsymbol{R}_{28}$
5th	$\boldsymbol{R}_{20}$	$\boldsymbol{R}_{26}$
6th	$\boldsymbol{R}_{42}$	$\boldsymbol{R}_{50}$
7th	$\boldsymbol{R}_{40}$	$\boldsymbol{R}_{48}$
8th	$\boldsymbol{R}_{38}$	$\boldsymbol{R}_{46}$

where the signification of the second set will become apparent when we move over to the two-dimensional irreps E_1, E_2. For a practical example we will now construct the first order lattice harmonic for the irrep A_1. The character table indicates that all characters are given by $+1$ for this irrep. The expansion of Eq. (1.58) is then given by:

$$\begin{aligned} P^1 b_2(\boldsymbol{k}) = \frac{1}{12}\big((+1)\times e^{i\boldsymbol{R}_2\boldsymbol{k}} + (+1)\times e^{i\boldsymbol{R}_7\boldsymbol{k}} + (+1)\times e^{i\boldsymbol{R}_4\boldsymbol{k}} \\ (+1)\times e^{i\boldsymbol{R}_3\boldsymbol{k}} + (+1)\times e^{i\boldsymbol{R}_5\boldsymbol{k}} + (+1)\times e^{i\boldsymbol{R}_6\boldsymbol{k}} \\ (+1)\times e^{i\boldsymbol{R}_2\boldsymbol{k}} + (+1)\times e^{i\boldsymbol{R}_6\boldsymbol{k}} + (+1)\times e^{i\boldsymbol{R}_5\boldsymbol{k}} \\ (+1)\times e^{i\boldsymbol{R}_4\boldsymbol{k}} + (+1)\times e^{i\boldsymbol{R}_7\boldsymbol{k}} + (+1)\times e^{i\boldsymbol{R}_3\boldsymbol{k}}\big) \\ = \frac{1}{3}\left(\cos\left(\boldsymbol{k}\cdot\boldsymbol{R}_2\right) + \cos\left(\boldsymbol{k}\cdot\boldsymbol{R}_4\right) + \cos\left(\boldsymbol{k}\cdot\boldsymbol{R}_6\right)\right) \\ = 2\cos\left(k_x\sqrt{3}/2\right)\cos\left(k_y/2\right)\cos\left(k_y\right). \end{aligned} \tag{1.59}$$

This lattice harmonic is depicted in Fig. 1.6 b. For the other one-dimensional irreps the procedure is done analogously, where only the values of the characters change and therefore some of the signs in front of the plane waves.

For the construction of the lattice harmonics of the two-dimensional irreps we have to compose a superposition of two lattice harmonics built from non-parallel vectors $\boldsymbol{R}_i$. Now the second set of the of the table becomes handy: we will construct for a given order two lattice harmonics. One with the vector of set 1 and another with the vector of set 2. Then we will calculate two superpositions by adding/subtracting these lattice harmonics. For example for the E_2 ($\mu = 6$) irrep of first order, we would select vector $\boldsymbol{R}_2$ and $\boldsymbol{R}_4$ such that:

$$\begin{aligned} P^6 b_2(\boldsymbol{k}) + P^6 b_4(\boldsymbol{k}) = \\ \frac{2}{3}\left(\cos\left(\frac{3k_x}{2}\right)\cos\left(\frac{\sqrt{3}k_y}{2}\right) - \cos\left(\sqrt{3}k_y\right)\right), \\ P^6 b_2(\boldsymbol{k}) - P^6 b_4(\boldsymbol{k}) = \\ -\left(\sin\left(\frac{3k_x}{2}\right)\sin\left(\frac{\sqrt{3}k_y}{2}\right)\right). \end{aligned}$$

The basis functions for all irreps are depicted from order 1 to 8 in Fig. 1.7.

Gap function and Fermi surface: a word on nomenclature

In a last consideration, we want to investigate the behaviour of the mean field energy regarding the presence of a superconductor and its gap function. For simplicity, we will refrain ourselves to the simple, ungeneralized BCS Hamiltonian Eq. (1.28) for this discussion, but the arguments made here generalize also to other systems. In this case, The matrix structure of the gap function becomes a scalar function $\bar{\Delta}_{\boldsymbol{k}} \to \Delta_{\boldsymbol{k}}$, and the Hamiltonian before application of the Bogolyubov transformation is a 2×2 matrix:

$$\boldsymbol{H}_{\boldsymbol{k}} = \begin{pmatrix} \xi_{\boldsymbol{k}} & \Delta_{\boldsymbol{k}} \\ \Delta^*_{\boldsymbol{k}} & -\xi_{-\boldsymbol{k}} \end{pmatrix}. \tag{1.60}$$

Where after the application of the Bogolyubov transformation the energies are given as:

$$E_{\boldsymbol{k}} = \pm\sqrt{\xi^2_{\boldsymbol{k}} + |\Delta_{\boldsymbol{k}}|^2}. \tag{1.61}$$

The Fermi surface is given by the values of $\boldsymbol{k}$ which lead to $\xi_{\boldsymbol{k}} = 0$ since we measure the dispersion in distance to the Fermi surface energy. By the expression Eq. (1.61), it is possible to have momenta $\boldsymbol{k}$ for which is $E_{\boldsymbol{k}}$ is zero due to the fact that $\xi_{\boldsymbol{k}}$ and $|\Delta_{\boldsymbol{k}}|^2$ can vanish simultaneously. Geometrically, these points can be understood as *nodes* since the Fermi surface crosses the zeros of the given gap function $\Delta_{\boldsymbol{k}}$. These nodes represent locations in the Brillouin zone where gapless excitations are possible (by the touching of the quasi-particle energies Eq. (1.61)) and are therefore energetically unfavourable [10]. This heuristic construction delivers therefore the argument that the leading gap function $\Delta_{\boldsymbol{k}}$ should have as few nodes as possible[8].

An interesting way to fulfill this condition is given by the two-dimensional irreps of the point group. As we showed before, the leading gap lies in the subspace of the leading eigenvalue λ^i corresponding to one of the irreps. While the one-dimensional irreps will therefore deliver only one lattice harmonic of those displayed in Fig. 1.7, the two-dimensional irreps represent a two-dimensional space and the

[8] It is important to acknowledge that this argument is indeed *heuristic*. While delivering a good rule of thumb, we will see later in the result chapter that it is not universally applicable.

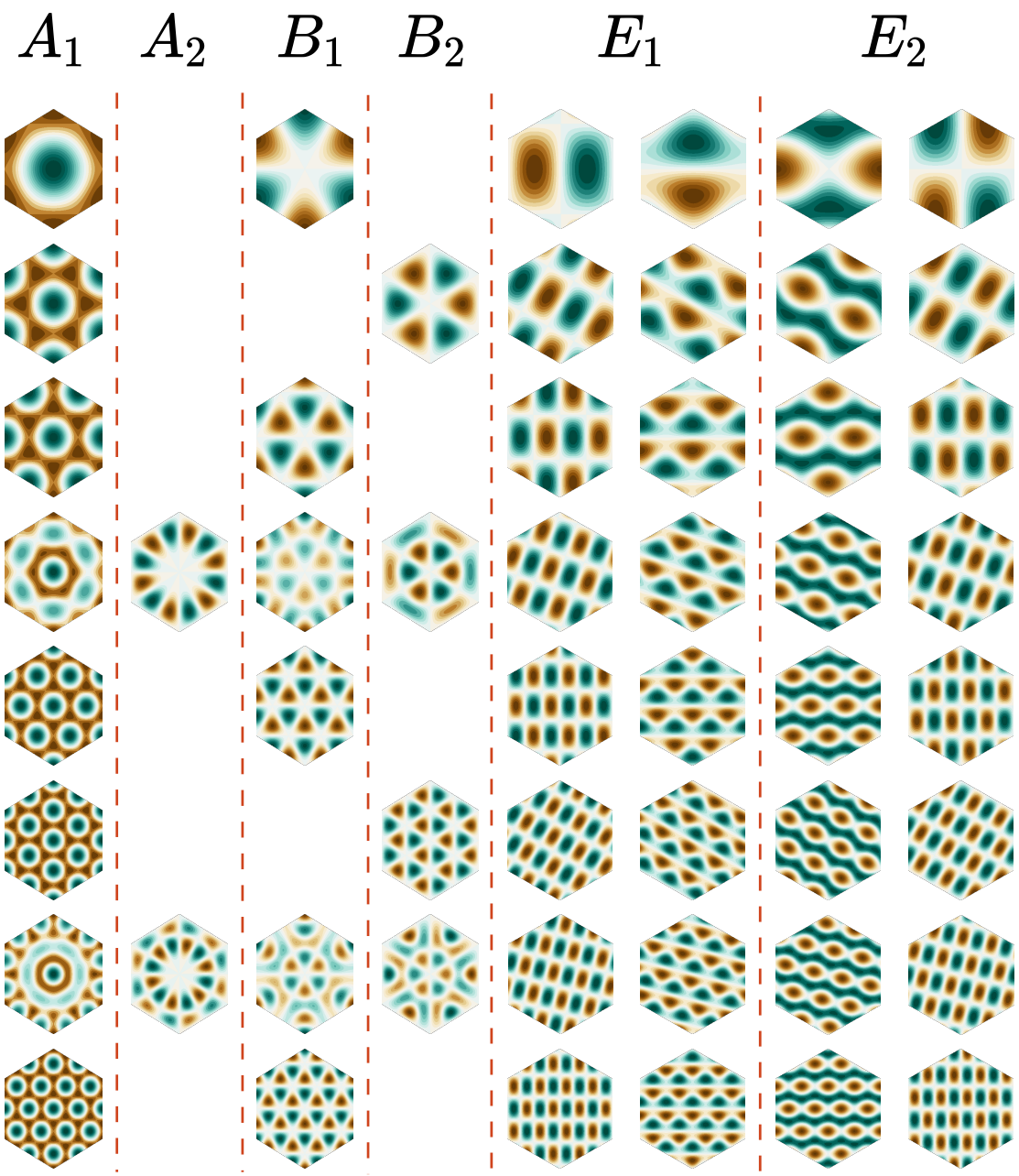

Figure 1.7: All possible basis functions for the irreps of point group C_{6v} up to order 8.

emerging total gap function $\Delta_{\boldsymbol{k}}$ can be a superposition of two lattice harmonics if the leading eigenvalue λ^i is degenerated:

$$\Delta_{\boldsymbol{k}} = \alpha \Delta_{\boldsymbol{k}}^{i,(1)} + \beta \Delta_{\boldsymbol{k}}^{i,(2)}, \tag{1.62}$$

where α and β can be complex numbers. So, while the isolated lattice harmonics of the two-dimensional irreps E_1 and E_2 may have nodes with a given Fermi surface, the complex superposition of two lattice harmonics of a given order may lead to a fully gapped state since their contribution to the quasiparticle energy is given by $|\Delta_{\boldsymbol{k}}|^2$. By the heuristic argument that nodeless states are favoured, the actual occurrence of these gaps is in general to be expected. Indeed, we will detect candidates for such gap functions later in chapter 3.

In the most simple combination, we set $\alpha = 1$ and $\beta = \pm i$. Therefore, the system has to *chose* one of the signs regarding the complex component, indicating the presence of time-reversal breaking [89, 106]. For that reason, these superconductors are called *chiral*. In terms of nomenclature, super-

conductors featuring a lattice harmonic of the E_1 irrep is called *d-wave* superconductors. For making the nomenclature more precise, the chiral variant of these superconductors are then called *d+id* superconductors.

Interestingly, the chiral superconductors are distinct from their non-chiral counterparts in terms of *topology*. A Chern number can be constructed as follows [106, 10]:

$$\mathcal{C} = \frac{1}{4\pi} \int_{\boldsymbol{k}} \boldsymbol{m}_{\boldsymbol{k}} \cdot \left(\frac{\partial \boldsymbol{m}_{\boldsymbol{k}}}{\partial k_x} \times \frac{\partial \boldsymbol{m}_{\boldsymbol{k}}}{\partial k_y} \right), \tag{1.63}$$

with a pseudospin vector:

$$\boldsymbol{m}_{\boldsymbol{k}} = \frac{1}{\sqrt{\xi_{\boldsymbol{k}}^2 + |\Delta_{\boldsymbol{k}}|^2}} \begin{pmatrix} \mathrm{Re}(\Delta_{\boldsymbol{k}}) \\ \mathrm{Im}(\Delta_{\boldsymbol{k}}) \\ \xi_{\boldsymbol{k}} \end{pmatrix}. \tag{1.64}$$

For a gap function of the form of Eq. (1.62), this construction delivers a touchstone to determine its chirality. From Eq. (1.63) it is obvious that any gap function which is purely real or imaginary will lead to $\mathcal{C} = 0$. Chiral gap functions subsequently are able to return non-zero values, $\mathcal{C} \neq 0$. This property delivers not only a measure to differentiate between chiral and non-chiral gaps in a purely theoretical manner, but it is also linked to experiments. It has been demonstrated that the Chern number of the gap function directly enhances the quantum spin and thermal Hall conductance measured in experiments[99, 44]. Therefore, we reach at an experimental verifiable quantity which reveals hints about the nature of a present superconducting gap function.

Précis

In the end, the essential content of this section is embodied by three important key results.

1. By the means of the BCS theory, it is possible to reduce the problem of finding a superconducting gap function to an eigenvalue problem which only includes the pairing interaction $V_{\boldsymbol{k},\boldsymbol{k}'}$. Effectively, this pairing interaction will be the result of our calculations after applying the functional renormalization group, stated in the next section.

2. The symmetry of the gap function, which is obtained by diagonalization, is dictated by the point group of the triangular lattice. The main result of the application of representation theory in this context leads to the insight that the leading gap $\Delta_{\boldsymbol{k}}$ will be of the form of an irrep basis function or -more directly- in the form of one of the functions depicted in Fig. 1.7.

3. For the occurrence of a gap function belonging to a two-dimensional irrep, the system inhabits the possibility of featuring a chiral superconductor which is characterized by a complex superposition of two lattice harmonics of the irrep. These chiral gap functions can be differentiated from the non-chiral gap functions by the calculation of a Chern number $\mathcal{C}$ which for the non-chiral cases is trivially zero. This construction has direct consequences to experiments since a non-zero Chern number enhances quantum spin and thermal Hall responses. Therefore the detour in group and representation theory is connected again to the real world eventually, delivering a criterion for differentiating between the topological property of a given superconductor.

This finalizes our discussion about unconventional superconductivity. In the next section we will proceed with describing our models of interest.

1.3 Moiré materials

In this last section of the introductory chapter, we will discuss a specific class of materials, namely Moiré materials which sparked numerous research interests in the last years. Starting with twisted bilayer graphene which historically started the recent history of Moiré materials, we will then proceed to twisted bilayer transition metal dichalcogenides which serve as an ideal plattform of triangular lattice systems exhibiting unconventional superconductivity.

1.3.1 Twisted bilayer graphene (TBG)

Before discussing the nature of Moiré materials we want to shift the focus to single layer graphene since the distinct structures of Moiré materials are actually rooted in structures which emerge already in single layer graphene. Since the groundbreaking work in 2004 by Geim et al.[28] there has been a tremendous body of research work committed to this material as plattform for a plethora of quantum many-body effects like magnetism, superconductivity or the occurrence of the anomalous integer quantum hall effect (for a compiled review see [16]). The fundamentals of graphene which are reproduced here are presented as usual in the canonical literature (e.g. see [52]).

A single layer of graphene consists of carbon atoms which are arranged in a honeycomb lattice structure. The spinful electrons in this system can be described by a tight-binding Hamiltonian:

$$H = -t \sum_{\langle i,j \rangle} \sum_{\sigma} \left(a^{\dagger}_{i,\sigma} b_{j,\sigma} + \text{h.c} \right), \tag{1.65}$$

where in this simple model we only take nearest-neighbour hopping into account. The operators $a^{(\dagger)}_{i,\sigma}, b^{(\dagger)}_{i,\sigma}$ create(annihilate) an electron on lattice site i with spin σ for sublattice a or b. This sublattice structure is needed since the honeycomb lattice is *not* a Bravais lattice. Instead the fundamental Bravais lattice of graphene is a triangular lattice with lattice vectors (see Fig. 1.8 a):

$$\boldsymbol{a}_1 = \frac{a}{2}\left(3, \sqrt{3}\right)^T, \quad \boldsymbol{a}_2 = \frac{a}{2}\left(3, -\sqrt{3}\right)^T, \quad a \approx 1.42\text{Å}$$

with a two-atomic basis with distance $\boldsymbol{\delta} = (-a, 0)^T$ to incorporate the two sublattices. This Hamiltonian can be diagonalized by going into Fourier space, resulting eventually into:

$$H = \sum_{\boldsymbol{k},\sigma} \left(\epsilon_{\boldsymbol{k},+} a^{\dagger}_{\boldsymbol{k},\sigma} a_{\boldsymbol{k},\sigma} + \epsilon_{\boldsymbol{k},-} b^{\dagger}_{\boldsymbol{k},\sigma} b_{\boldsymbol{k},\sigma} \right) \tag{1.66}$$

with two bands indexed as $b = \pm 1$ and the (spin-degenerated) dispersions:

$$\epsilon_{\boldsymbol{k},b} = b \times t\sqrt{3 + f(\boldsymbol{k})}, \tag{1.67}$$

$$f(\boldsymbol{k}) = 2\cos\left(\sqrt{3}k_y a\right) + 4\cos\left(\frac{\sqrt{3}}{2}k_y a\right)\cos\left(\frac{3}{2}k_x a\right). \tag{1.68}$$

At half-filling (i.e. no chemical potential), the Fermi surface is at the Dirac points $\boldsymbol{K}, \boldsymbol{K'}$ (see Fig. 1.8 b), where both bands exactly touch each other. The structures which emerge here are called **Dirac cones**, where in close vicinity of the $\boldsymbol{K}, \boldsymbol{K'}$ points the dispersion features a linear slope. We can derive a low energy theory which is valid as long as the electrons stay in the vicinity of the Fermi energy by Taylor expanding the dispersion Eq. (1.67) around the Dirac points:

$$H_{\boldsymbol{K}(\boldsymbol{K'})} = \frac{3at}{2} \sum_{\boldsymbol{q},\sigma} \psi^{\dagger}_{\boldsymbol{q},\sigma} \begin{pmatrix} 0 & q_x \mp i q_y \\ q_x \pm i q_y & 0 \end{pmatrix} \psi_{\boldsymbol{q},\sigma} = v_F \sum_{\boldsymbol{q},\sigma} \psi^{\dagger}_{\boldsymbol{q},\sigma} \left[\boldsymbol{\sigma} \cdot \boldsymbol{q}\right]^{(*)} \psi_{\boldsymbol{q},\sigma} \tag{1.69}$$

where we collect the former operators in $\psi_{\boldsymbol{q},\sigma} = (a_{\boldsymbol{k},\sigma}, b_{\boldsymbol{k},\sigma})^T$. The vector $\boldsymbol{q}$ must be understood as momentum close to the $\boldsymbol{K}(\boldsymbol{K'})$ point, $\boldsymbol{q} = \boldsymbol{k} - \boldsymbol{K}(\boldsymbol{K'})$ such that $\boldsymbol{q} = 0$ is the momentum directly

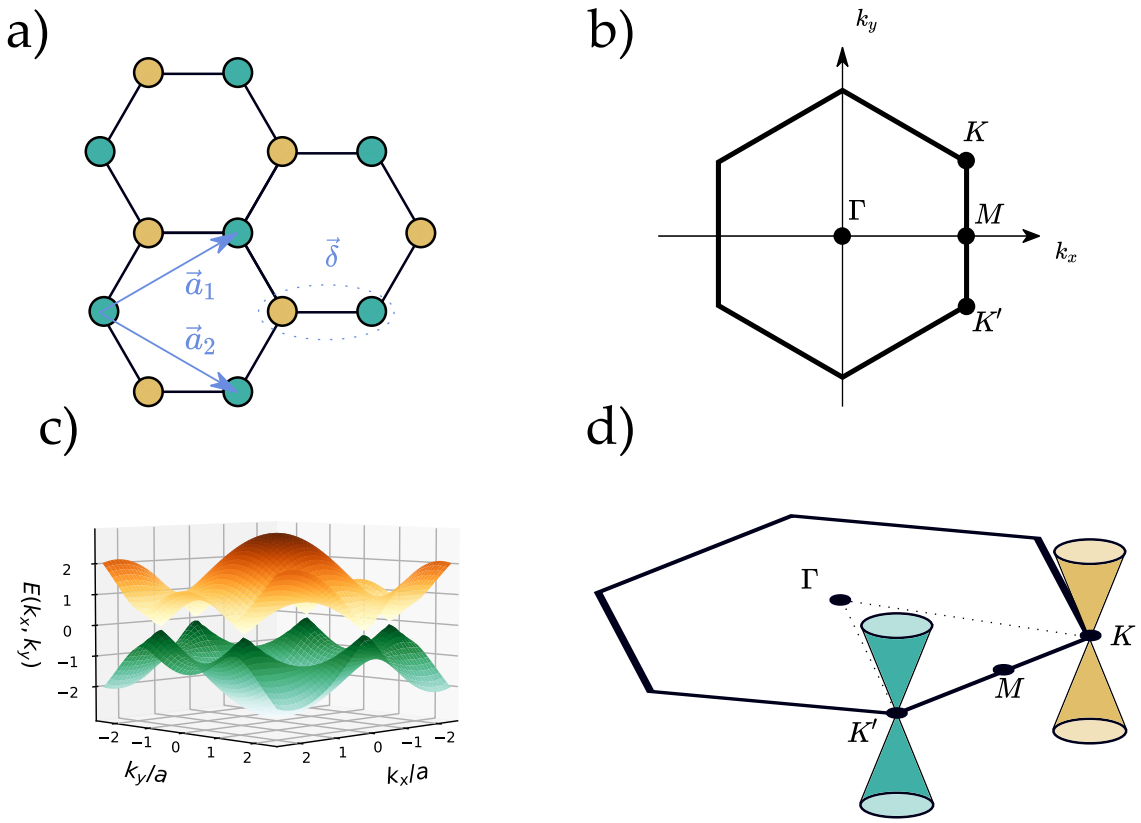

Figure 1.8: **Properties of single layer graphene:** a) Real space lattice structure of graphene tight-binding model with sublattice A (brown) and B (green) forming the basis (blue ellipsis). b) Brillouin zone of graphene with symmetry points $\boldsymbol{\Gamma}$, $\boldsymbol{M}$, $\boldsymbol{K}$ and $\boldsymbol{K'}$. c) Band structure of graphene plotted for one spin in first Brillouin zone. d) Sketch of the two in-equivalent Dirac cones in the Brillouin zone at $\boldsymbol{K}$ and $\boldsymbol{K'}$, depicting that an electron in one cone is in momentum space well separated from the other cone.

at a respective Dirac point. We collect two Pauli matrices in the vector $\boldsymbol{\sigma} = (\sigma_x, \sigma_y)^T$ and define the Fermi velocity $v_F = 3at/2$. Since these two Dirac cones are in-equivalent and well separated in terms of momentum, an electron in one of these cones will stay at this cone as long as no strong scattering events take place. To build a complete low energy effective model of graphene which accounts for both Dirac cones, we will introduce now the new spinor $\Psi_{\boldsymbol{q},\sigma} = (a_{\boldsymbol{q},\sigma}, b_{\boldsymbol{q},\sigma}, a_{\boldsymbol{q'},\sigma}, b_{\boldsymbol{q'},\sigma})^T$ and expand the Hamiltonian to a 4×4 structure:

$$H = \sum_{\boldsymbol{q},\sigma} \Psi^\dagger_{\boldsymbol{q},\sigma} \begin{pmatrix} H_{\boldsymbol{K}} & 0 \\ 0 & H_{\boldsymbol{K'}} \end{pmatrix} \Psi_{\boldsymbol{q},\sigma}, \tag{1.70}$$

where two block Hamiltonians include the two seperate Dirac cones. Since the emergent low energy Hamiltonian Eq. (1.70) decomposes in a diagonal of two blocks, we can therefore interpret the two Dirac cones as new quantum numbers, namely the **valley degree of freedom**. In the low energy Hamiltonian an electron is therefore completely described by its momentum $\boldsymbol{q} = \boldsymbol{k} - \boldsymbol{K}(\boldsymbol{K'})$, its spin σ and its location in momentum space i.e. if it sits near $\boldsymbol{K}$ or $\boldsymbol{K'}$. We will see later that the interplay of different valleys is essential for constructing effective Hubbard models for Moiré Materials.

The recent enthusiasm for Moiré materials can be traced back to the works of Cao et al. in 2017 [15] although there are works in 2011 which preceded these studies by Bistrizer and MacDonald [9]. The (obviously) underlying effect of Moiré materials is the **Moiré effect** which describes the interference

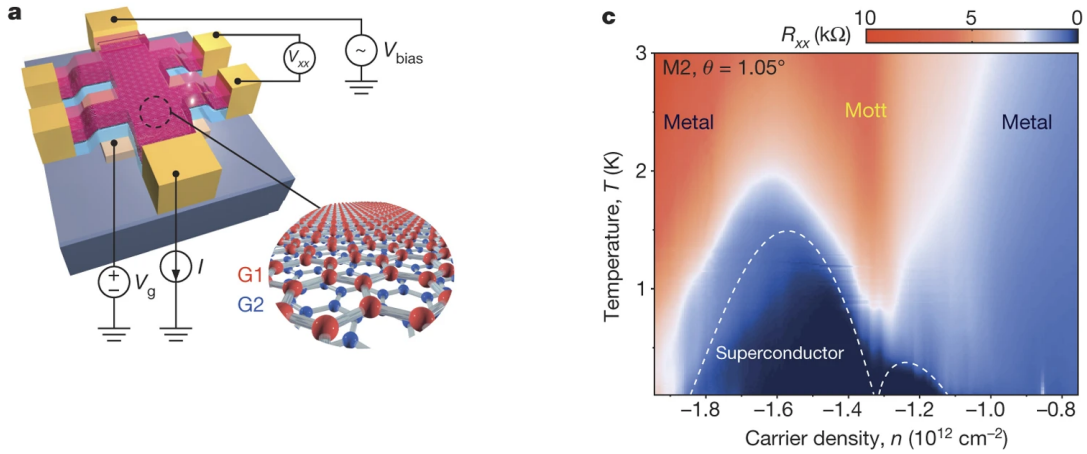

Figure 1.9: **Original graphics taken from** [15]: a) Schematic representation of a TBG measurement device. The four-probe measurement measures the resistance $R_{xx} = V_{xx}/I$. The graphene sheets G1,G2 are *sandwiched* by two hexagonal boron nitride layers where the bottom layer is connected to the gate voltage V_g to control the carrier density n. b) Phase diagram of TBG at an angle of $\theta = 1.05$deg. Two superconducting domes are formed around half filling, with a Mott insulator state in between. The highest critical temperature for the onset of superconductivity is $T_c \approx 1.7K$.

pattern which is produced if two patterns with transparent gaps are laid on each other. In condensed matter physics, this emergent Moiré pattern was first produced by stacking two single layer Graphene sheets on each other and twist them with certain angle θ.

Experimental results

As shown in [15], there exist specific so called *magic angles* for the bilayer of twisted graphene sheets where the emergent band structure will feature low-lying bands with a pronounced flatness. In the specific case of the (smallest) magic angle of $\theta \approx 1.1$ deg, the total bandwidth of these bands is in the order of magnitude of 10 meV and they are also well separated from the rest of the system. The tremendous advantage of this small bandwidth is the tunability in terms of a gate voltage. The amount of electron carriers can be easily controlled with the application of an external voltage, allowing for an extraordinary controllable system in terms of the electronic filling. The compiled phase diagrams from those experiments is displayed in Fig. 1.9 and show the existence of a correlated insulator and two superconducting domes with $T \approx 1.7K$ as highest transition temperature around half filling. In [15] it is also argued that a phonon-mediated mechanism for the superconductivity is unlikely. Therefore TBG is indeed a platform exhibiting unconventional superconductivity with an extraordinary level of control over the filling. Most interestingly, if we compare the phase diagram in Fig. 1.9 with the phase diagram of a cuprate in Fig. 1.4 b in the previous section, a striking resemblance becomes apparent. This sparks the idea that the phase diagram of TBG may also be explainable by the paradigm of competing instabilities of a Hubbard model.

Theoretical description

We will give a brief overview how TBG can be described from the theoretical side. The methodology to do so translates also to Moiré systems other than TBG. Actually, this description comes in two steps. At first we will show how the continuum models are build for TBG, based on the aspects we already described for single layer Graphene. Outgoing from these continuum models, one can actually in a second step derive an effective Hubbard model for the lowest lying flat bands.

A theoretical description of twisted bilayer graphene was actually already published in 2011 by Bistrizer

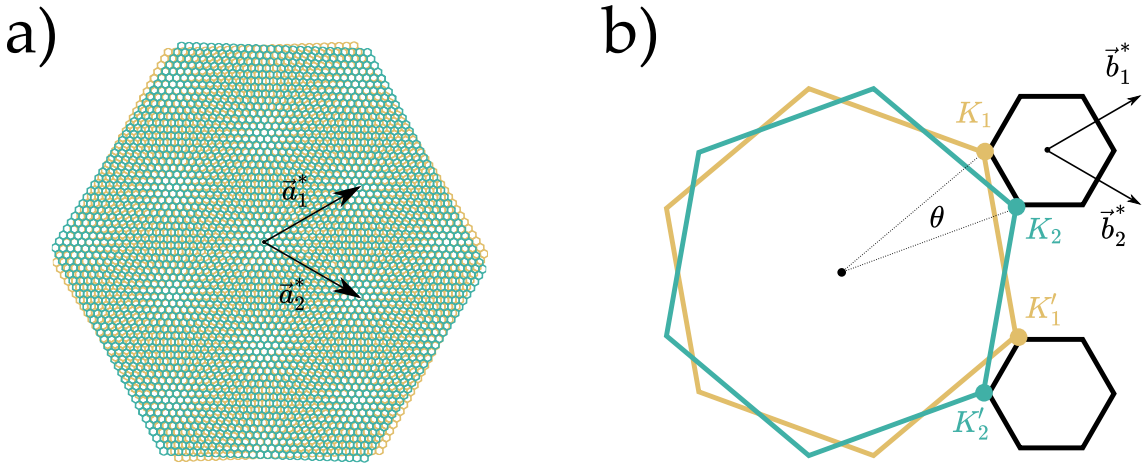

Figure 1.10: **Geometry of TBG in real space and momentum space**: a) An example of TBG with real space Moiré vectors $\boldsymbol{a}_{1,2}^*$ connecting different regions of AA-stacking. b) The Brillouin zone of the single graphene sheets and the emerging tiny Brillouin zones of the Moiré superlattice for each valley. Since the momentum space is reciprocal to real space, the larger Moiré unit cell will lead to a smaller Brillouin zone. Since the two valleys at $\boldsymbol{K}$, $\boldsymbol{K'}$ are still well separated for small angles in momentum space, one can derive a continuum model for each valley, for example for $\boldsymbol{K}$ by including both Dirac cones at $\boldsymbol{K}_1$, $\boldsymbol{K}_2$ from each sheet and adding an interlayer coupling U.

and MacDonald [9]. For the construction of this low energy effective model it is appropriate to investigate the geometry of a Moiré pattern constructed by TBG. For brevity we will consider AA-stacked TBG, meaning that one sheet is put onto another sheet such that the respective A-sublattices are directly below each other. The rotational axis is therefore going though two A sublattice points, one from each layer. If the twisting angle θ is a commensurate magic angle, then there will be an emergent superlattice (i.e. the Moiré structure) for which we can define new basis vectors $\boldsymbol{a}_{1,2}^*$ (see Fig. 1.10 a). The Brillouin zones of the twisted graphene sheets will evidently also be twisted. The Brillouin zone of the Moiré superlattice will be much smaller than of its corresponding single layer counter parts, caused by the larger real space structure of the superlattice. As discussed before, in a low energy effective model we only have to describe a single graphene sheet in the vicinity of the respective Dirac cones. The idea of the construction for TBG is now to couple the Dirac cones of two graphene sheets in terms of an **interlayer coupling** U or sometimes also called a **Moiré potential**. This is valid for small angles, causing that the Dirac cones of each layer will be in short distance to each other in momentum space (see Fig. 1.10 b). Conclusively, two valleys $\xi = \pm$ at $\boldsymbol{K}$ and $\boldsymbol{K'}$ emerge and each of those can be described independently as:

$$H_{\boldsymbol{K}}^{\text{TBG}} = \begin{pmatrix} H_{\boldsymbol{K}_1} & U \\ U^\dagger & H_{\boldsymbol{K}_2} \end{pmatrix}, \tag{1.71}$$

where $H_{\boldsymbol{K}_{1,2}}$ are the low energy Hamiltonians at the Dirac cones at the $\boldsymbol{K}$ point of layer 1 and 2 respectively. The main challenge which remains in this approach is the modelling of the interlayer hopping U, for which various methods exist in terms of tight-binding approaches [73, 59, 101]. This sets out the general idea of the TBG continuum model, such that the band structure can be derived by diagonalization of the Hamiltonian[9].

In a second step, it is possible to only describe the lowest lying flat bands of the model by deriving an effective Hubbard model from the continuum model. A successful implementation of this procedure was demonstrated by Koshino et al. [60]. The general procedure demands that one introduces Bloch states for the derived continuum model which will then serve as a starting point to derive Wannier

[9] For a general review of the method to derive the continuum model of TBG there exists the recent review by Andrei and MacDonald [2].

states which are localized at the AA-points of the TBG. Outgoing from this construction, it is possible to derive an effective honeycomb tight-binding model which is defined on the Moiré sublattice:

$$H = \sum_{\xi=\pm} \sum_{ij} t(\boldsymbol{r}_{ij}) e^{i\xi\phi(\boldsymbol{r}_i j)} c^\dagger_{i\xi} c_{j\xi}, \tag{1.72}$$

where the hopping $t(\boldsymbol{r}_{ij})$ between lattice site i and j is also multiplied with a phase factor $\phi(\boldsymbol{r}_i j)$. One conclusion by Koshino et al. is that a sufficiently large amount of these hoppings have to be included to faithfully reproduce the low-lying band structure whose numerical values can be derived by the Wannier-based approach. Notably, the spin degree of freedom will not translate into the effective description, but the valley degree ξ will inherit a $\mathrm{SU}(2)$ structure. The possibility of deriving a tight binding model of the TBG enables the possibility to view occurring phases through the lens of competing instabilities when interactions are included which highlights the importance of this methodology.

Obviously, the construction of Moiré superlattices is not only restricted to TBG. Several other materials haven been proposed to engineer Moiré structures. It is a disadvantage of TBG that the emerging tight binding model is also defined on a honeycomb lattice which in terms of the sublattice structures directly poses a greater challenge than for example triangular lattices. Fortunately, there exists also a class of models which results into triangular effective models which we will present next.

1.3.2 Twisted bilayer transition metal dichalcogenides

The procedure to stack graphene sheets onto each other and twist them can also be implemented for transition metal dichalcogenides (TMDs). A TMD consists of three layers MX_2:

- Two layers of chalcogen atoms X_2, like Sulfur (S), Selenium (Se) or Tellurium (Te),
- One layer of transition metal atoms M, like Molybden (Mo) or Tungsten (W),

where the chalcogen layers are building the top and bottom layer with the transition metal layer in-between. While these materials have therefore an actual lattice structure in 3D, its extraordinary thinness allows for a 2D description. A top view on a TMD will reveal a hexagonal lattice structure, where the sublattices A and B are now made of different atoms, namely chalcogen or transition metal atoms. The body of work considering the experimental properties and physical applications of TMDs largely exceed the scope of this section, for which we advise to the literature [68, 58]. In terms of this work, we will directly consider the properties of the electronic band structure of TMDs.

A special feature of TMDs is the breaking of inversion symmetry and the strong spin-orbit coupling. In the example of WSe_2 this will lead to a valence band with a large spin-splitting with a considerable gap to the conduction bands with a weak spin-splitting [65, 91]. This results into a non-degenerate valence band, with maxima located at the $\boldsymbol{K}, \boldsymbol{K'}$ points. Instead of Dirac cones, we can approximate in a continuum model these maxima as parabolic $\epsilon_{\boldsymbol{k}} \propto -(\boldsymbol{k} - \boldsymbol{K})^2$ [112]. Importantly, the inversion symmetry breaking will lead to the fact that the spins and valleys are *locked* i.e. at the $\boldsymbol{K}$ points the high lying valence band is of $\sigma = \uparrow$ and at the in-equivalent $\boldsymbol{K'}$ point it is of $\sigma = \downarrow$.

These materials can now be used to construct Moiré materials called twisted TMDs (or tTMDs) by reproducing the approach used in TBG. Naturally one has two choices for these constructions. First, one can take two different TMDs to build a tTMD which is called a tTMD heterobilayer. Second, one can take two sheets made from the same TMD resulting into a tTMD homobilayer. Both materials can effectively be described by a tight-binding model on a triangular lattice as follows.

tTMD heterobilayers

Recent works developed a continuum model for tTMD heterobilayers by the theoretical description of twisted WX_2/MoX_2 ($X = S, Se$) systems [112]. In the example of WSe_2/MoS_2, experiments in-

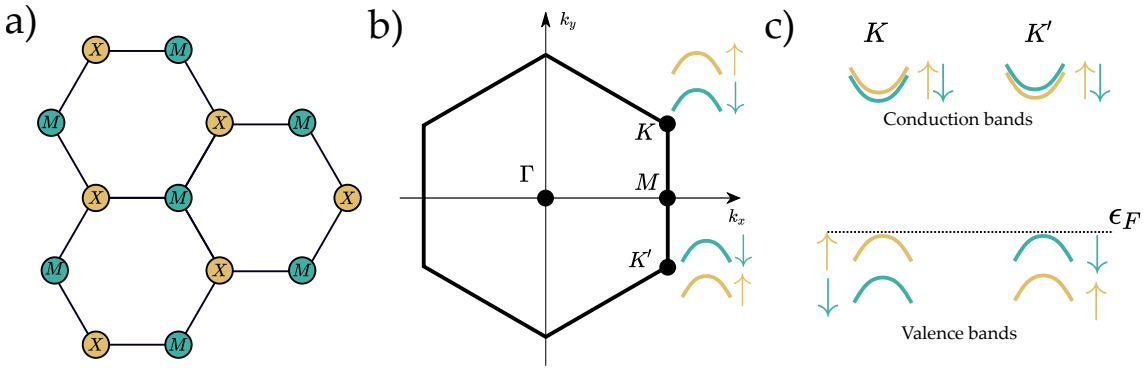

Figure 1.11: **Geometry of a TMD in real space and momentum space**: a) Monolayer TMDs are effectively 2D materials with a honeycomb structure. As a noticeable difference to graphene, the different sublattices are actually made out of different atoms, namely a transition metal M and a chalcogenide X whereas in graphene both sublattices are made of carbon atoms. b) The spin-valley locking in TMD will lead to two non-degenerate valence bands for the spins with maximums at the $\boldsymbol{K}, \boldsymbol{K'}$ points. The inversion symmetry breaking imposes that both valleys will have a different highest lying valence band with regard to the spin. c) Detailed view at the $\boldsymbol{K}, \boldsymbol{K'}$ points regarding valence and conduction bands. The conduction bands do only exhibit a small spin-splitting, while the valence bands are separated by a strong spin-splitting. Eventually, the Fermi energy of the Moiré material ϵ_F will be close to the high lying valence bands, such that an isolated treatment of these bands for a continuum model is possible.

dicate that the valence band of the WSe_2 layer lies inside a gap of MoS_2 bands [119, 80]. Therefore, a continuum model can be built from the high lying valence band (see Fig. 1.11 c) of the WSe_2, and the Moiré structure stemming from the coupling to the MoS_2 layer with applied magic angle adds an periodic Moiré potential to the continuum model description[10]. The whole band structure can then by derived by the diagonalization of the continuum Hamiltonian. The inversion symmetry of the TMD monolayer enforces that the dispersion has the same form at the $\boldsymbol{K}$ and $\boldsymbol{K'}$ point, although these maxima come from different spin bands. Consequently, by using only one band per symmetry point for the construction of the continuum model, the spin and valley degree of freedom will become equivalent due to the spin-valley-locking of the dispersion. After diagonalization, this model will feature separated flat bands at highest energy. For these bands only, a fit can be employed by an effective tight-binding model on the triangular Moiré superlattice. Another study finds that this model should include hoppings t_n and interactions V_n up to third nearest-neighbour in addition to an onsite interaction U for a realistic description [121]:

$$H_{\text{Heterobilayer}} = -\sum_n \sum_{\langle ij\rangle_n} \sum_\sigma t_n \left(c^\dagger_{i\sigma} c_{j\sigma} + \text{h.c.}\right) - \mu \sum_{i\sigma} n_{i\sigma} + U \sum_i n_{i\uparrow} n_{i\downarrow} + \sum_n \sum_{\langle ij\rangle_n} \sum_{\sigma\sigma'} V_n n_{i\sigma} n_{j\sigma'} \,. \tag{1.73}$$

Therefore, the effective description of this tTMD heterobilayer material is indeed given by an extended triangular lattice Hubbard model. We note that the spin-degree of freedom can be used equivalently to the valley ξ due to the spin-valley locking. The spin/valley is a $\mathrm{SU}(2)$ quantum number now, with two spin/valley-degenerated bands.

tTMD homobilayers

A continuum model and an effective description of a tTMD homobilayer system was alredy investigated for system composed of two WSe_2 layers [79]. The crucial difference in these models is given

[10] For a detailed derivation of this potential, the reader is advised to [49].

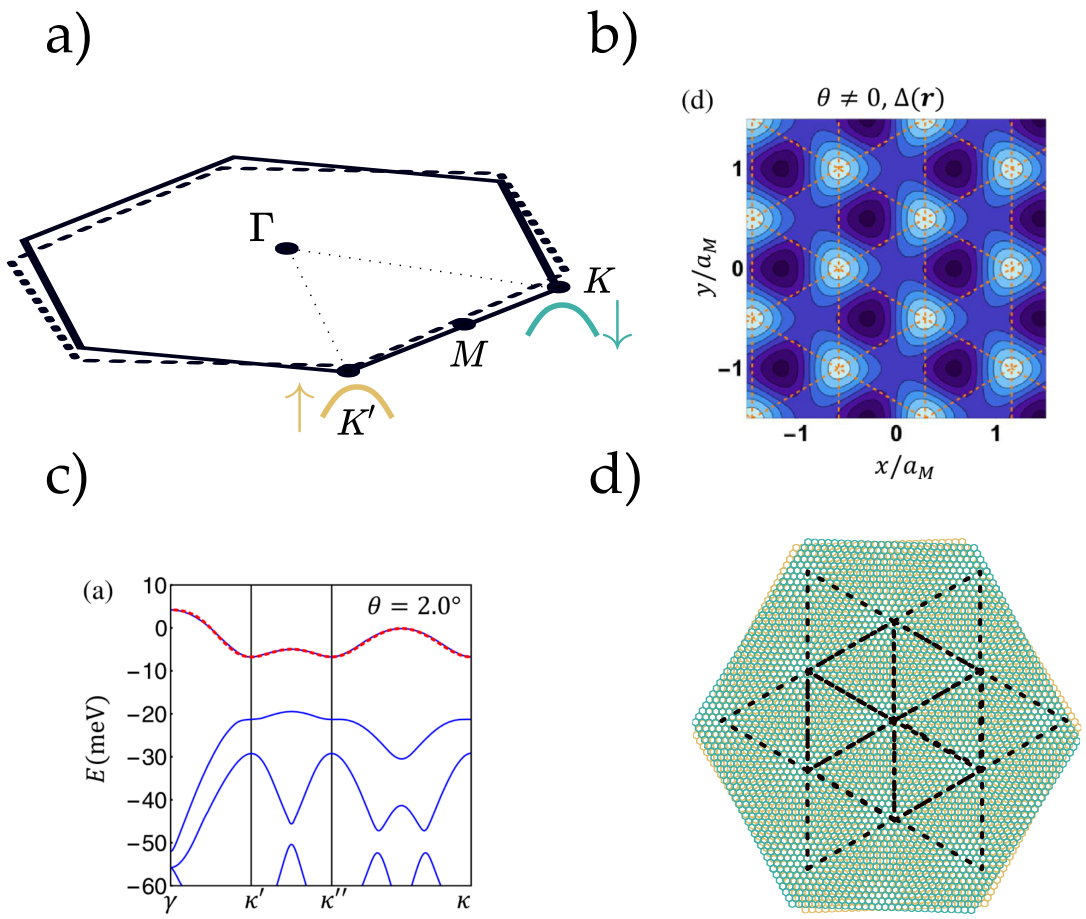

Figure 1.12: **Sketch for effective description of tTMD heterobilayers**: a) Twisted Brillouin zones of two different twisted TMD layers. The WSe_2 (solid) contributes valence bands (green/yellow) of different spin/valleys to the continuum model. The coupling to the MoS_2 layer (dashed) leads to the formation of flat bands. b) Original figure taken from [112]. The Moiré potential in real space $\Delta(\boldsymbol{r})$ stems from the coupling of both twisted layers. c) Original figure taken from [112]. The emergent band structure after diagonalizing the continuum Hamiltonian. The red flat band on top is isolated from the other bands. d) The red band in c) can be fitted by a tight-binding model defined on the triangular Moiré superlattice (dashed).

by the fact that both monolayer systems contribute bands to the effective description since the valence bands of both systems are identical. Effectively, the method to produce an effective triangular lattice Hamiltonian is analogue to the heterobilayer system. Since we are confronted with a degeneracy of the bands at the $\boldsymbol{K}$ and $\boldsymbol{K'}$ point of the single layers, the effective Hubbard model will also inhabit this degeneracy. Interestingly, this degeneracy can be lifted by the inclusion of an out-of-plane electric field, called the *displacement field*. This field splits the bands at the respective points, leading to two non-degenerate bands in the effective model. The Hamiltonian of this system is given by[79, 116]:

$$H_{\text{Homobilayer}} = -2|t| \sum_{\boldsymbol{k},\boldsymbol{\delta}} \sum_{\sigma} \cos\left(\boldsymbol{k}\cdot\boldsymbol{\delta} + \sigma\cdot\phi\right) c^{\dagger}_{\boldsymbol{k},\sigma} c_{\boldsymbol{k},\sigma} + U \sum_{i} c^{\dagger}_{i,\uparrow} c_{i,\downarrow} \tag{1.74}$$

where $\phi \in [0, \pi/2]$ represents the strength of the displacement field. $\boldsymbol{\delta}$ are the vectors to three selected nearest-neighbour lattice sites in a triangular lattice. This model will *not* inhabit a SU(2)-invariance for $\phi \neq 0$. In addition to this model, also longer-ranged hoppings and interactions can be included to fit the minimal model to realistic materials [79].

Both of the proposed Hubbard models inhabit nesting effects and Van Hove singularities similar to

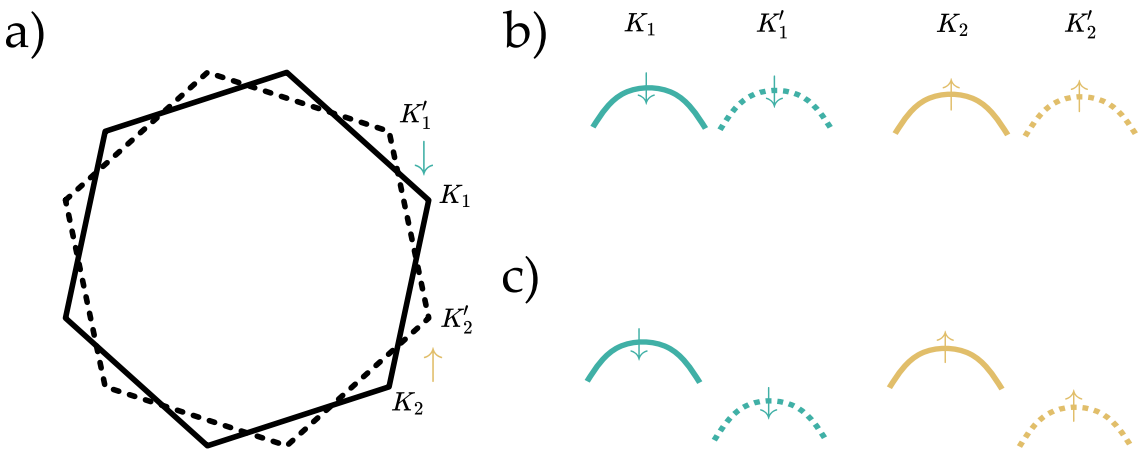

Figure 1.13: **Sketch for effective description of tTMD homobilayer**: a) Twisted Brillouin zones of two TMDs of the same material. The spin-down maxima of the separate bands are located at $\boldsymbol{K}_1^{(\prime)}$, while the spin-up maxima are located at $\boldsymbol{K}_2^{(\prime)}$. The strategey of deriving an effective description is similar to the case of heterobilayers, but now both monolayers contribute bands to the formation of the Moiré band structure in addition of forming a Moiré potential b) Without a displacement field, the four depicted maxima are equal in form, such that the effective model will consist of two degenerated bands . c) Applying the displacement field, the band degeneracy can be lifted, also leading to non-degenerate bands in the effective model.

our paradigmatic triangular lattice Hubbard model as described in the previous sections. So, they are suitable models from the perspective of competing instabilities and will therefore be treated later as such.

1.4 The scope of this thesis

In this last section, we will give a brief précis of this introductory chapter. Afterwards, we will establish the further direction of this thesis.

- At first we gave a heuristic overview of the origin of electronic instabilities. We showed that instabilities towards magnetism or superconductivity may be induced by electron-electron interactions in a triangular lattice Hubbard model. Furthermore, we argued that the main impact for the formation of these instabilities stems from the singular behaviour of particle-particle and particle-hole bubbles. The underlying conditions for the divergence of these objects is rooted in the geometry of the Fermi surface, where the occurrence of perfect nesting and the presence of a Van Hove singularity leads to logarithmic divergencies in the respective channels.

- The limitations of perturbation theory become visible, if multiple divergencies appear to happen at the same time. Moreover, perturbation theory fails to explain how the onset of superconductivity may happen if the model does not possess an attractive interaction to begin with. These problems were present in the description of cuprates which calls for a method beyond perturbation theory is necessary for the description of competing orders. Indeed, renormalization group methods were able to explain the superconductivity mechanism in absence of an attractive bare interaction which establishes the justification to work in this framework.

- Of the various possible instabilities, we took a special look at unconventional superconductivity. We presented how to deduce the superconducting gap function $\Delta_{\boldsymbol{k}}$ by the usage of an eigenvalue equation which incorporates the interaction responsible for Cooper pairing. In a short excursion into the realm of representation theory we showed that the possible forms of $\Delta_{\boldsymbol{k}}$ are dictated by the point group describing the lattice on which the Hamiltonian is defined on. In our example, this is the triangular lattice and the C_{6v} point group.

- In the last section, we gave a quick overview over Moiré materials, especially tTMDs. We presented that already established research derived effective triangular lattice Hubbard models for tTMDs, where the models for heterobilayers and homobilayers differ qualitatively from each other by the presence of $\mathrm{SU}(2)$-invariance.

The conclusion of these points renders the triangular lattice Hubbard model to be extraordinary useful for describing possible unconventional superconductors in tTMDs. While there exists a large amount of FRG studies about the square and honeycomb lattice Hubbard model [42, 39, 115, 32, 55, 54], we notice that the work on the triangular lattice does not match this quantity, although substantial work for competing orders also exist here [41, 20].

The goal of this work is now to develop and implement a renormalization group method to investigate triangular lattice Hubbard models beyond perturbation theory. This specific method will be the truncated-unity functional renormalization group. This thesis will therefore proceed as follows:

1. Chapter 2 introduces and establishes the truncated-unity functional renormalization group as one of the most recent variations of the functional renormalization methods. In this chapter, we will briefly lay out the idea and basics of functional renormalization group in general and then move over to the truncated-unity ansatz. Following the formal description and derivation, we will also describe the concrete numerical implementation, where we will outline the computational challenges and the respective solutions.

2. In chapter 3, we will apply the developed method to triangular lattice Hubbard models in three distinct cases:

   (a) At first, we will tackle spinful fermions on a triangular lattice with $\mathrm{SU}(2)$-invariance. Here, we will investitagte two cases: at first a rather simplistic model with only nearest-neighbour hopping and interaction and then a more realistic model with longer ranged

hoppings and interactions which models a tTMD heterobilayer system. We will demonstrate that a domain of unconventional superconductivity exists in the tTMD heterobilayer which is in general already strongly present in the paradigmatic description.

(b) In a second application, a model of spinless fermions on a triangular lattice is treated. This model serves more as toy model than a realization of a physical material. This work was initiated to compare the truncated-unity scheme to the so-called patching scheme, a previous variant of functional renormalization. Again, we will find phaes of unconventional superconductivity.

(c) In a third and last application, we will deal with spinful fermions on a triangular lattice *without* $\mathrm{SU}(2)$. Here we will use the effective tight-binding model describing a tTMD homobilayer system. Here, we want to especially study the effects of the displacement field.

CHAPTER 2

Method:
The Truncated-Unity Functional Renormalization Group

In this chapter we will derive and develop the method of our choice to treat triangular lattice Hubbard models: **the truncated-unity functional renormalization group**. First, we will give an introduction to the general framework of the functional renormalization group for correlated fermion systems. Then, we will proceed to the truncated-unity ansatz. After the formal derivation of this method, we will turn to its numerical implementation, where a number of computational challenges arise. We will discuss, how these challenges can be solved to ensure that our developed numerical tool is equipped with the necessary stability and performance speed to be a viable approach to investigate the competing orders in triangular lattice systems.

2.1 The Functional Renormalization Group

In the first chapter we already made the case that the behaviour of a condensed matter system with $\approx 10^{23}$ electrons and its emergent qualities is ultimately encoded in the path integral:

$$Z = \int D(\bar{\psi}, \psi)\, e^{-S[\bar{\psi},\psi]}.$$

Here, we are confronted with the enormous challenge of solving this integral which is in a closed analytical form almost never possible to treat since every kind of interaction will alter the Gaussian quality of the integrand to something more complex, leading to all the difficulties preventing the existence of an exact solution. On a philosophical note, the author wants to share the opinion that it is really baffling that exactly that part which renders nature so complex -namely the interaction between particles- has its corresponding complex counterpart in the realm of mathematics in the form of non-Gaussian structures in the path integral. In an overly simplified point of view, the plethora of different methods developed in the area of quantum field theory are a consequence of our inability to solve its central object analytically without approximation.

One of these methods is the renormalization group (RG), one of the great achievements of theoretical physics in the last 100 years. The important cornerstone of RG is the emphasis of including *scales* when thinking about physical systems. The famous example of block spins by Kadanoff [51] accentuates this notion for condensed matter physics where the coupling of microscopic spins J is *renormalized* by grouping spins to a new, emergent spin at a higher length scale. The repetition of this construction allows for a function describing the coupling J for larger and larger length scales, delivering a prescription for the emerging macroscopic system by developing J to the desired scale.

This idea was formalized by Wilson [108, 109], who translated this idea into momentum space. Here, the central notion is to integrate out high momentum degrees of freedom in the path integral in a small *momentum shell* between $\Lambda/b < k < \Lambda$ and absorb the effects into the remaining integrand

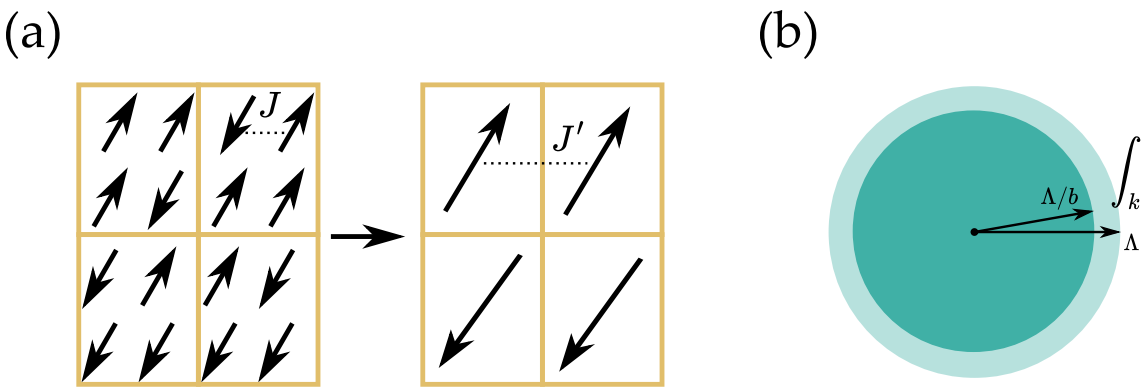

Figure 2.1: **Basic RG schemes:** a) Kadanoff block spin renormalization. The couplings between the macroscopic spins is given by J. By grouping and averaging four spins to are new, larger spin, a new coupling J' is introduced which describes the effective interaction between the new spins. By iterating this procedure, a renormalization group application in real space formed. b) Wilsonian momentum space renormalization. By describing a theory in theory space, a small shell between Λ/b and Λ is integrated. The effects of this integral are absorbed in the theory. Repeating these steps leads to a renormalization group application in momentum space.

with an scaling factor b. After rescaling the momenta $b \cdot k \rightarrow k$, this procedure can be repeated to derive the RG flow for the coupling parameters of a given action.

A modern RG approach is the functional renormalization group (FRG), pioneered by Wetterich [107]. The FRG method focuses on the *effective action* Γ instead on the partition sum Z[1]. The effective action Γ generates all *one-particle-irreducible* (1PI) diagrams of a given theory and is therefore suitable to treat all the occurring contributions to the integrand of the path integral in a constructive manner. Compared to Wilsonian RG, the FRG is based on exchanging the integration of the path integral by solving an integro-differential equation for a scale dependent effective action Γ_Λ. By design, this object is equal to the initial action $\Gamma_{\Lambda^{UV}} = S$ at a given ultraviolet cutoff and equal to the effective action at the infrared cutoff $\Gamma_{\Lambda \rightarrow 0} = \Gamma$. The evolution from one of these extreme cases to another is governed by a *flow equation* $\frac{d}{d\Lambda}\Gamma_\Lambda$ where the initial condition reflects an unperformed path integral and a solved differential equation to the infrared regime corresponds to a full integration of the path integral, including all quantum effects.

In this first subsection, we will derive the general framework of FRG, starting from deriving the general flow equation and moving on to deriving a set of flow equations for our proposed electronic systems by the usage of symmetries. Noticeably, we will see that also the FRG approach cannot solve the path integral in the end in closed form; we will have to impose certain truncations to arrive at a form which is feasible for numerical calculations.

The presentation and compilation of this subsection relies on the standard review articles by Metzner et. al [72], Platt et. al [84] and the work by Honerkamp and Salmhofer [94].

2.1.1 Flows and functionals

At first we will derive the flow equations for the **Schwinger functional** (the generating functional of all connected diagrams) and for the **effective action** (the generating functional for all 1PI diagrams). Eventually, we will exclusively use the flow of the effective action and the flow of the Schwinger functional is a means to an end, namely deriving the flow of the effective action in the first place. We will start by defining some nomenclature and will then guide through the general steps of the derivations.

[1] While also other FRG schemes exist, we will limit ourselves to the effective action approach.

Finally, we will adopt the notion of the **vertex expansion** to derive the characteristical **hierachy of differential equations** used in condensed matter applications.

Adopting notation

We will start by leaning on the general expression of the action of an electronic system as presented in section 1, Eqs. (1.4) and (1.5). For this purpose, the action was decomposed in a kinetic part S_0 and an interacting part S_I. Starting with the kinetic part and assuming that by diagonalization the dispersion $\xi_\sigma(\boldsymbol{k})$ of the system was already obtained:

$$\begin{aligned}
S_0\left[\bar{\psi},\psi\right] =& -\int_k \sum_\sigma \left(i\omega - \xi_\sigma(\boldsymbol{k})\right) \bar{\psi}_\sigma(\boldsymbol{k})\psi_\sigma(\boldsymbol{k}) \\
=& -\int_{k,k'} \sum_{\sigma,\sigma'} \left(i\omega - \xi_\sigma(\boldsymbol{k})\right) \delta\left(k-k'\right)\delta_{\sigma,\sigma'} \times \bar{\psi}_\sigma(\boldsymbol{k})\psi_{\sigma'}(\boldsymbol{k}') \\
=& -\int_{k,k'} \sum_{\sigma,\sigma'} \left(i\omega - \xi_\sigma(\boldsymbol{k})\right) \delta\left(k-k'\right)\delta_{\sigma,\sigma'} \times \bar{\psi}_\sigma(\boldsymbol{k})\psi_{\sigma'}(\boldsymbol{k}') \\
=& -\int_{k,k'} \sum_{\sigma,\sigma'} \left(G^0_\sigma(\boldsymbol{k})\right)^{(-1)} \delta\left(k-k'\right)\delta_{\sigma,\sigma'} \times \bar{\psi}_\sigma(\boldsymbol{k})\psi_{\sigma'}(\boldsymbol{k}') \\
=& -\sum\!\!\!\!\!\!\int_{K,K'} \left(G^0(K,K')\right)^{(-1)} \times \bar{\psi}(K)\psi(K') \\
=& -\left(\bar{\psi}, (G^0)^{(-1)}\psi\right),
\end{aligned} \tag{2.1}$$

where we introduced a superindex $K = (\boldsymbol{k},\omega,\sigma)$ with the respective integration/summation $\sum\!\!\!\!\!\!\int_K = \int_k \sum_\sigma = A_{\mathrm{BZ}}^{-1} T \int d\boldsymbol{k} \sum_\omega \sum_\sigma$. Furthermore we defined the bare propagator:

$$G^0(K,K') = \frac{1}{i\omega - \xi_\sigma(\boldsymbol{k})}\delta(k-k')\times\delta_{\sigma,\sigma'} =: G^0(K)\times\delta(K-K') \tag{2.2}$$

and adopted the notation $\left(\bar{\psi},\dots\psi\right)$ for the general matrix multiplication and integration/summation over all indices. Starting form the establishment of this notation, we define the interaction part of the action S_I:

$$S\left[\bar{\psi},\psi\right] = -\left(\bar{\psi},(G^0)^{(-1)}\psi\right) + S_I\left[\bar{\psi},\psi\right], \tag{2.3}$$

$$S_I\left[\bar{\psi},\psi\right] = \sum\!\!\!\!\!\!\int_{K_1',K_2',K_1,K_2} V(K_1',K_2',K_1,K_2)\times\bar{\psi}(K_1')\bar{\psi}(K_2')\psi(K_2)\psi(K_1), \tag{2.4}$$

where $V(K_1',K_2',K_1,K_2)$ is an arbitrary interaction strength. Notice that the order of indices in the fields ψ are not in the same order as in the interaction strength which is indeed intended. This choice was made such that the diagrams emerging in this section have a clearer structure later.

Flow equation for the Schwinger functional

At first, we want to treat the Schwinger functional [76] with new fermionic source fields $\eta,\bar{\eta}$:

$$\mathcal{G}[\bar{\eta},\eta] = -\log\int D(\bar{\psi},\psi)\, e^{-S[\bar{\psi},\psi]+(\bar{\eta},\psi)+\left(\bar{\psi},\eta\right)}. \tag{2.5}$$

All connected diagrams can be obtained from this functional by taking the derivative as follows:

$$\begin{aligned}
&G^{(2m)}\left(K_1',\dots K_m';K_m'\dots K_1\right) \\
&\qquad = -\langle\bar{\psi}_1,\dots\bar{\psi}_m;\psi_m\dots\psi_1\rangle_c \\
&\qquad = (-1)^m \frac{\delta^{2m}\mathcal{G}[\bar{\eta},\eta]}{\delta\bar{\eta}(K_1)\dots\delta\bar{\eta}(K_m)\delta\eta(K_m')\dots\delta\eta(K_1')}\Big|_{\eta,\bar{\eta}=0}.
\end{aligned} \tag{2.6}$$

At this point, we want to introduce the **scale parameter** Λ to the functional, i.e. $\mathcal{G} \to \mathcal{G}^\Lambda$. The effect of the scale on the Schwinger functional should be defined as follows:

$$\mathcal{G}^\Lambda = \begin{cases} \mathcal{G} & \Lambda \to 0 \\ 0 & \Lambda \to \infty \end{cases}$$

i.e. restoring the original functional for vanishing scale parameter and going to zero for the infinite large scales to employ a well behaved boundary condition for the emerging differential equation. This is implemented by equipping the bare propagator with the scale as follows:

$$\left(G^{0,\Lambda}\right)^{(-1)} = \begin{cases} \left(G^0\right)^{(-1)} & \Lambda \to 0 \\ \infty & \Lambda \to \infty \end{cases}.$$

The correct behaviour of this implementation is obvious for $\Lambda \to 0$, while for $\Lambda \to \infty$ one is referenced to the path integral and acknowledging that $\left(G^{0,\Lambda}\right)^{(-1)}$ behaves as an infinite mass term for $\Lambda \to \infty$. The introduction of this scale is often implemented by the multiplication of the bare propagator with a suitable cutoff function. One example is given by a Heavyside function regarding the momenta $\boldsymbol{k}$:

$$G^{0,\Lambda}(K) = \Theta(|\xi_\sigma(\boldsymbol{k})| - \Lambda)\frac{1}{i\omega - \xi_\sigma(\boldsymbol{k})}. \tag{2.7}$$

Here it also becomes apparent that the cutoff function also regularizes infrared divergencies occuring for $\omega, \xi(\boldsymbol{k}) \to 0$. The cutoff function can be implemented in various forms (momentum, Matsubara, temperature) and shapes (smooth or sharp) which will be discussed in more detail in section 2.2.4. The exact choice of the regulator scheme is not important for the general discussion of this section.

We will now derive a differential equation for the Schwinger functional. Starting from the ultraviolet regime $\Lambda \to \infty$, this differential equation establishes a smooth interpolation to the infrared regime $\Lambda \to 0$. The derivation is done by taking the scale derivative of the Schwinger functional and calculating in a straight-foward manner:

$$\begin{aligned}
\frac{d}{d\Lambda}\mathcal{G}^\Lambda &= -e^{\mathcal{G}^\Lambda}\left(\frac{d}{d\Lambda}e^{-\mathcal{G}^\Lambda}\right) \\
&= -e^{\mathcal{G}^\Lambda}\frac{d}{d\Lambda}\int D(\bar\psi,\psi)e^{-S^\Lambda+(\bar\eta,\psi)+\left(\bar\psi,\eta\right)} \\
&= -e^{\mathcal{G}^\Lambda}\int D(\bar\psi,\psi)\left(-\frac{d}{d\Lambda}S_0^\Lambda\right)e^{-S^\Lambda+(\bar\eta,\psi)+\left(\bar\psi,\eta\right)} \\
&= e^{\mathcal{G}^\Lambda}\int D(\bar\psi,\psi)\left(\sum\!\!\!\!\!\!\int_{K,K'}\left(\dot G^{0,\Lambda}(K,K')\right)^{(-1)}\bar\psi(K)\psi(K')\right)e^{-S^\Lambda+(\bar\eta,\psi)+\left(\bar\psi,\eta\right)} \\
&= e^{\mathcal{G}^\Lambda}\int D(\bar\psi,\psi)\left(\sum\!\!\!\!\!\!\int_{K,K'}\left(\dot G^{0,\Lambda}(K,K')\right)^{(-1)}\frac{\delta}{\delta\eta(K)}\frac{\delta}{\delta\bar\eta(K')}\right)e^{-S^\Lambda+(\bar\eta,\psi)+\left(\bar\psi,\eta\right)} \\
&= e^{\mathcal{G}^\Lambda}\left(\sum\!\!\!\!\!\!\int_{K,K'}\left(\dot G^{0,\Lambda}(K,K')\right)^{(-1)}\frac{\delta}{\delta\eta(K)}\frac{\delta}{\delta\bar\eta(K')}\right)\int D(\bar\psi,\psi)e^{-S^\Lambda+(\bar\eta,\psi)+\left(\bar\psi,\eta\right)} \\
&= e^{\mathcal{G}^\Lambda}\left(\sum\!\!\!\!\!\!\int_{K,K'}\left(\dot G^{0,\Lambda}(K,K')\right)^{(-1)}\frac{\delta}{\delta\eta(K)}\frac{\delta}{\delta\bar\eta(K')}\right)e^{-\mathcal{G}^\Lambda}.
\end{aligned} \tag{2.8}$$

Where we denoted for brevity the scale derivative acting on the inverse bare propagator as:

$$\left(\dot{G}^{0,\Lambda}(K,K')\right)^{(-1)} = \frac{d}{d\Lambda}\left(G^0(K,K')\right)^{(-1)}$$

Proceeding from this, the flow equation is derived by performing the two remnant derivatives respective to the fields $\eta, \bar{\eta}$:

$$\frac{\delta}{\delta\eta(K)}\frac{\delta}{\delta\bar{\eta}(K')}e^{-\mathcal{G}^\Lambda} = \left(\frac{-\delta^2\mathcal{G}}{\delta\eta(K)\delta\bar{\eta}(K')} + \frac{-\delta\mathcal{G}^\Lambda}{\delta\eta(K)}\frac{-\delta\mathcal{G}^\Lambda}{\delta\bar{\eta}(K')}\right)e^{-\mathcal{G}^\Lambda}, \tag{2.9}$$

such that by plugging Eq. (2.9) into Eq. (2.8) we finally reach:

$$\begin{aligned}\frac{d}{d\Lambda}\mathcal{G}^\Lambda &= \sum\!\!\!\!\!\!\int_{K,K'}\left(\left(\dot{G}^{0,\Lambda}(K,K')\right)^{(-1)}\frac{-\delta^2\mathcal{G}}{\delta\eta(K)\delta\bar{\eta}(K')} + \left(\dot{G}^{0,\Lambda}(K,K')\right)^{(-1)}\frac{-\delta\mathcal{G}^\Lambda}{\delta\eta(K)}\frac{-\delta\mathcal{G}^\Lambda}{\delta\bar{\eta}(K')}\right)\\ &= \left(\sum\!\!\!\!\!\!\int_{K,K'}\left(\dot{G}^{0,\Lambda}(K,K')\right)^{(-1)}\frac{-\delta^2\mathcal{G}}{\delta\eta(K)\delta\bar{\eta}(K')}\right) + \left(\frac{\delta\mathcal{G}^\Lambda}{\delta\eta}, \left(\dot{G}^{0,\Lambda}\right)^{(-1)}\frac{\delta\mathcal{G}^\Lambda}{\delta\bar{\eta}}\right).\end{aligned} \tag{2.10}$$

Which is the final form of the flow equation for the Schwinger functional. As mentioned before, we will just use Eq. (2.10) as an identity for the derivation of the flow for the effective action.[2]

Flow equation for the effective action

Now, we are moving over to the flow equation of the effective action which will be much more practical and interpretable for our purposes.

While the Schwinger functional generates all connected Green's functions, the effective action will generate all 1PI diagrams. The effective action is obtained by the Schwinger functional via a Legendre transformation. Since we already equipped the Schwinger functional with a scale, the effective action will also inherit a scale dependence:

$$\Gamma^\Lambda\left[\bar{\psi},\psi\right] = \mathcal{G}[\bar{\eta}^\Lambda,\eta^\Lambda] + \left(\bar{\eta}^\Lambda,\psi\right) + \left(\bar{\psi},\eta^\Lambda\right), \tag{2.11}$$

where the scale originates from the Legendre transformation, since η^Λ and $\bar{\eta}^\Lambda$ are functions of $\bar{\psi},\psi$ as:

$$\psi(K) = -\frac{\delta\mathcal{G}[\bar{\eta}^\Lambda,\eta^\Lambda]}{\delta\bar{\eta}^\Lambda(K')}, \qquad \bar{\psi}(K') = \frac{\delta\mathcal{G}[\bar{\eta}^\Lambda,\eta^\Lambda]}{\delta\eta^\Lambda(K)}. \tag{2.12}$$

The 1PI diagrams $\Gamma^{(2m)}$ with $2m$ legs are finally generated by the effective action by also taking the derivative with respect to the fields:

$$\Gamma^{\Lambda,(2m)}\left(K'_1\dots K'_m, K_m\dots K_1\right) = \frac{\delta^{(2m)}\Gamma^\Lambda\left[\bar{\psi},\psi\right]}{\delta\bar{\psi}(K'_1)\dots\delta\bar{\psi}(K'_m)\delta\psi(K_m)\dots\delta\psi(K_1)}. \tag{2.13}$$

From the definition of the effective action Eq. (2.12) it holds:

$$\boldsymbol{\Gamma}^{\Lambda,(2)} = \begin{pmatrix}\frac{\delta^2\Gamma^\Lambda}{\delta\bar{\psi}(K')\delta\psi(K')} & -\frac{\delta^2\Gamma^\Lambda}{\delta\bar{\psi}(K')\delta\bar{\psi}(K)}\\ -\frac{\delta^2\Gamma^\Lambda}{\delta\psi(K')\delta\psi(K)} & \frac{\delta^2\Gamma^\Lambda}{\delta\psi(K')\delta\bar{\psi}(K)}\end{pmatrix} = -\begin{pmatrix}\frac{\delta^2\mathcal{G}^\Lambda}{\delta\bar{\eta}(K)\delta\eta(K')} & -\frac{\delta^2\mathcal{G}^\Lambda}{\delta\bar{\eta}(K)\delta\bar{\eta}(K')}\\ -\frac{\delta^2\mathcal{G}^\Lambda}{\delta\eta(K)\delta\eta(K')} & \frac{\delta^2\mathcal{G}^\Lambda}{\delta\eta(K)\delta\bar{\eta}(K')}\end{pmatrix}^{-1} = \left(\boldsymbol{\mathcal{G}}^{\Lambda,(2)}\right)^{-1}. \tag{2.14}$$

[2] If one still desires to investigate FRG methods based on the Schwinger functional, we point to the reviews [6, 24], where this flavour of FRG is known under the name *Polchinski RG* or *Exact RG*.

Stating from the definition, we begin deriving the flow equation for the effective action again by taking the scale derivative:

$$\frac{d}{d\Lambda}\Gamma^{\Lambda}\left[\bar{\psi},\psi\right] = \frac{d}{d\Lambda}\left(\mathcal{G}[\bar{\eta}^{\Lambda},\eta^{\Lambda}] + \left(\bar{\eta}^{\Lambda},\psi\right) + \left(\bar{\psi},\eta^{\Lambda}\right)\right), \tag{2.15}$$

where after application of the chain rule to the Schwinger functional, the additional terms cancel such that:

$$\frac{d}{d\Lambda}\Gamma^{\Lambda}\left[\bar{\psi},\psi\right] = \frac{\partial}{\partial\Lambda}\mathcal{G}[\bar{\eta}^{\Lambda},\eta^{\Lambda}]\mid_{\bar{\eta}^{\Lambda},\eta^{\Lambda}\text{ fixed}}. \tag{2.16}$$

For the right hand side we derived Eq. (2.10) before. Inserting this expression and further manipulations yields:

$$\begin{aligned}\frac{d}{d\Lambda}\Gamma^{\Lambda} &= \left(\sum\!\!\!\!\!\!\int_{K,K'}\left(\dot{G}^{0,\Lambda}(K,K')\right)^{(-1)}\frac{-\delta^2\dot{\mathcal{G}}}{\delta\eta(K)\delta\bar{\eta}(K')}\right) + \left(\frac{\delta\mathcal{G}^{\Lambda}}{\delta\eta},\left(\dot{G}^{0,\Lambda}\right)^{(-1)}\frac{\delta\mathcal{G}^{\Lambda}}{\delta\bar{\eta}}\right)\\ &= -\frac{1}{2}\mathrm{Tr}\left(\left(\dot{\boldsymbol{G}}^{0,\Lambda}\right)^{(-1)}\left(\boldsymbol{\Gamma}^{\Lambda,(2)}\right)^{-1}\right) - \left(\bar{\psi},\left(\dot{G}^{0,\Lambda}\right)^{(-1)}\psi\right)\end{aligned} \tag{2.17}$$

For the second line we used the definitions of the Legendre transformation Eq. (2.12) and the identity Eq. (2.14). Furthermore we introduced:

$$\left(\dot{\boldsymbol{G}}^{0,\Lambda}\right)^{(-1)} = \mathrm{diag}\left(\left(\dot{G}^{0,\Lambda}\right)^{(-1)}, -\left(\dot{G}^{0,\Lambda}\right)^{(-1),T}\right). \tag{2.18}$$

By reframing the equation Eq. (2.17) by deriving the flow for the difference between scale dependent and original inverse bare propagator: $R^{\Lambda} = \left(G^{0,\Lambda}\right)^{(-1)} - \left(G^{0}\right)^{(-1)}$ (see Ellwanger and Wetterich [26] for details), one can derive the interpretable boundary conditions:

$$\Gamma^{\Lambda} = \begin{cases}\Gamma & :\Lambda\to 0\\ S & :\Lambda\to\Lambda_{\mathrm{UV}}\end{cases}.$$

Now, the flow equation Eq. (2.17) interpolates smoothly between two systems. Starting at the ultraviolet cutoff as an initial scale where the action S is defined on, the flow equation describes an evolution in the space of the functionals which eventually leads to the effective action Γ. This implements the idea of the FRG as a differential equation analogon for the path integral. The initial condition S corresponds to a path integral which has not been calculated yet: no quantum fluctuations are included to the action, since the integration is not performed. The final result of the differential equation is the effective action Γ, resembling the full execution of the path integral calculation (although technically Z still has to be converted to Γ). The intriguing mechanism of the FRG consists of what happens *in between* these two extreme cases: instead of actually calculating the path integral, the different quantum fluctuations - which would be included by the path integral - are accounted for scale by scale, by solving the flow equation Eq. (2.17).

The form of the derived flow equation is still exact at this point and can be thought of as a *reformulation* of the basis object of quantum field theory. Nevertheless, the complex form of this equation does not allow for a straightforward solution right away. To derive a feasible scheme allowing for solving the flow equation, we will now introduce the expansion of the effective action in terms of vertices.

Vertex expansion

For the vertex expansion, the effective action is expanded with respect to the fields as:

$$\Gamma^{\Lambda}\left[\bar{\psi},\psi\right]=\sum_{m=0}^{\infty}\mathcal{A}^{(2m)}\left[\bar{\psi},\psi\right], \tag{2.19}$$

$$\mathcal{A}^{(2m)}\left[\bar{\psi},\psi\right]=\frac{(-1)^m}{(m!)^2}\sum_{\substack{K_1,\dots K_m\\K_1',\dots K_m'}}\Gamma^{(2m),\Lambda}(K_1,\dots K_m,K_1',\dots K_m')\times \psi(\bar{K}_1')\dots\psi(\bar{K}_m')\psi(K_m)\dots\psi(K_1), \tag{2.20}$$

such that the effective action is decomposed in terms of 1PI diagrams of different orders. The awkward expression in Eq. (2.17) is the inverse of the second variation of the effective action. Consequently, it is useful to isolate the field-independent part of this object. For that purpose, we construct the object $\boldsymbol{\Sigma}^{\Lambda}$ containing contributions of quadratic order in fields or higher:

$$\boldsymbol{\Sigma}^{\Lambda}=-\boldsymbol{\Gamma}^{\Lambda,(2)}+\left(\boldsymbol{G}^{\Lambda}\right)^{-1} \tag{2.21}$$

where $\boldsymbol{G}^{\Lambda}=\mathrm{diag}\left(G^{\Lambda},-\left(G^{\Lambda}\right)^{T}\right)$. By a rearrangement of the terms we arrive at:

$$\left(\boldsymbol{\Gamma}^{\Lambda,(2)}\right)^{(-1)}=\left((\boldsymbol{G}^{\Lambda})^{(-1)}-\boldsymbol{\Sigma}^{\Lambda}\right)^{-1}=\left(\mathbb{1}-\boldsymbol{G}^{\Lambda}\boldsymbol{\Sigma}^{\Lambda}\right)^{-1}\boldsymbol{G}^{\Lambda}, \tag{2.22}$$

Ultimately, we want to exchange the problematic object in the flow equation (2.17) by an expansion. This expansion is done in the manner of a geometric series:

$$\begin{aligned}\left(\boldsymbol{\Gamma}^{\Lambda,(2)}\right)^{(-1)}&=\left(\mathbb{1}-\boldsymbol{G}^{\Lambda}\boldsymbol{\Sigma}^{\Lambda}\right)^{-1}\boldsymbol{G}^{\Lambda}\\&=\sum_{i=0}^{\infty}\left(\boldsymbol{G}^{\Lambda}\boldsymbol{\Sigma}^{\Lambda}\right)^{i}\boldsymbol{G}^{\Lambda}\\&=\left(\mathbb{1}+\boldsymbol{G}^{\Lambda}\boldsymbol{\Sigma}^{\Lambda}+\boldsymbol{G}^{\Lambda}\boldsymbol{\Sigma}^{\Lambda}\boldsymbol{G}^{\Lambda}\boldsymbol{\Sigma}^{\Lambda}+\dots\right)\boldsymbol{G}^{\Lambda}\\&=\boldsymbol{G}^{\Lambda}\left(\mathbb{1}+\boldsymbol{\Sigma}^{\Lambda}\boldsymbol{G}^{\Lambda}+\boldsymbol{\Sigma}^{\Lambda}\boldsymbol{G}^{\Lambda}\boldsymbol{\Sigma}^{\Lambda}\boldsymbol{G}^{\Lambda}+\dots\right)\end{aligned} \tag{2.23}$$

By obtaining this expansion, the flow equation (Eq. (2.17)) can now be cast into the following form:

$$\begin{aligned}\frac{d}{d\Lambda}\Gamma^{\Lambda}&=-\frac{1}{2}\mathrm{Tr}\left(\dot{\boldsymbol{G}}^{0,\Lambda}\left(\boldsymbol{\Gamma}^{\Lambda,(2)}\right)^{-1}\right)-\left(\bar{\psi},\left(\dot{G}^{0,\Lambda}\right)^{(-1)}\psi\right)\\&=-\frac{1}{2}\mathrm{Tr}\left(\dot{\boldsymbol{G}}^{0,\Lambda}\boldsymbol{G}^{\Lambda}\left(\mathbb{1}+\boldsymbol{\Sigma}^{\Lambda}\boldsymbol{G}^{\Lambda}+\boldsymbol{\Sigma}^{\Lambda}\boldsymbol{G}^{\Lambda}\boldsymbol{\Sigma}^{\Lambda}\boldsymbol{G}^{\Lambda}+\dots\right)\right)-\left(\bar{\psi},\left(\dot{G}^{0,\Lambda}\right)^{(-1)}\psi\right)\\&=-\frac{1}{2}\mathrm{Tr}\left(\dot{\boldsymbol{G}}^{0,\Lambda}\boldsymbol{G}^{\Lambda}\right)-\left(\bar{\psi},\left(\dot{G}^{0,\Lambda}\right)^{(-1)}\psi\right)\\&+\frac{1}{2}\mathrm{Tr}\left(\boldsymbol{S}^{\Lambda}\left(\boldsymbol{\Sigma}^{\Lambda}+\boldsymbol{\Sigma}^{\Lambda}\boldsymbol{G}^{\Lambda}\boldsymbol{\Sigma}^{\Lambda}+\boldsymbol{\Sigma}^{\Lambda}\boldsymbol{G}^{\Lambda}\boldsymbol{\Sigma}^{\Lambda}\boldsymbol{G}^{\Lambda}\boldsymbol{\Sigma}^{\Lambda}+\dots\right)\right).\end{aligned} \tag{2.24}$$

Where we defined the single-scale propagator:

$$\boldsymbol{S}^{\Lambda}=-\boldsymbol{G}^{\Lambda}\left(\dot{\boldsymbol{G}}^{0,\Lambda}\right)^{(-1)}\boldsymbol{G}^{\Lambda} \tag{2.25}$$

$$S^{\Lambda}=-G^{\Lambda}\left(\dot{G}^{0,\Lambda}\right)^{-1}G^{\Lambda}=\frac{d}{d\Lambda}G^{\Lambda}\Big|_{\Sigma^{\Lambda}\text{fixed}} \tag{2.26}$$

$$\left(G^{\Lambda}\right)^{-1}=\left(G^{0,\Lambda}\right)^{-1}-\Sigma^{\Lambda}. \tag{2.27}$$

In the last line we related the self-energy Σ^{Λ} to the full propagator via the Dyson equation. Now, Eq. (2.24) serves as new form of the flow equation.

Hierarch of flow equations

The final step is now done by expressing the effective action Eq. (2.24) by the vertex expansion Eq. (2.19) and compare coefficients of the expressions on both sides. Eventually, for every 1PI diagram with $2m$ legs in Eq. (2.22) we can derive a single flow equation. Explicitly for $m = 1$ and $m = 2$ this will result into:

$$\frac{d}{d\Lambda}\Sigma^{\Lambda}(K', K) = \sum\!\!\!\!\!\!\int_{P,P'} S^{\Lambda}(P, P')\Gamma^{(4),\Lambda}(K', P', K, P) \tag{2.28}$$

$$\begin{aligned}\frac{d}{d\Lambda}\Gamma^{(4),\Lambda}(K_1', K_2', K_1, K_2) = &\sum\!\!\!\!\!\!\int_{P_1,P_1'} \sum\!\!\!\!\!\!\int_{P_2,P_2'} G^{\Lambda}(P_1, P_1')S^{\Lambda}(P_2, P_2') \\ &+ \left[\Gamma^{(4),\Lambda}(K_1', K_2', P_1, P_2) \times \Gamma^{(4),\Lambda}(P_1', P_2', K_1, K_2)\right] \\ &- \left[\Gamma^{(4),\Lambda}(K_1', P_2', K_1, P_1) \times \Gamma^{(4),\Lambda}(P_1', K_2', P_2, K_2) + (P_1 \leftrightarrow P_2, P_1' \leftrightarrow P_2')\right] \\ &+ \left[\Gamma^{(4),\Lambda}(K_2', P_2', K_1, P_1) \times \Gamma^{(4),\Lambda}(P_1', K_1', P_2, K_2) + (P_1 \leftrightarrow P_2, P_1' \leftrightarrow P_2')\right] \\ &- \sum\!\!\!\!\!\!\int_{P,P'} S^{\Lambda}(P, P')\Gamma^{(6),\Lambda}(K_1', K_2', P', K_1, K_2, P).\end{aligned} \tag{2.29}$$

At this point we want to give a brief précis of the presented derivation.

- We exchanged performing the path integral by solving a differential equation for the scale dependent effective action Γ^{Λ}. This objects interpolates between the microscopic action $S = \Gamma^{\Lambda=\Lambda_{\text{UV}}}$ and the full effective action $\Gamma = \Gamma^{\Lambda=0}$. Therefore, the FRG flow can be understood as a trajectory in an abstract *theory space* which indicates the value of the components of the evolving functional, where the starting point is S and the end point is Γ, (see Fig. 2.2 a). We can understand the derived flow equation Eq. (2.24) as a reformulation of the path integral and the expression is up to this point still exact.

- By the means of the vertex expansion, we were able to derive for every 1PI diagram of arbitrary order a dedicated flow equation. While we only presented two of them explicitly (it will become apparent in the next section that we do not need more diagrams for our description), a simple set of rules directly stems from the form of the general flow equation Eq. (2.24). The trace leads to a one-loop structure on the right hand side of a flow equation. Therefore, the flow equation of a 1PI diagram $\Gamma^{(2m),\Lambda}$ is given by all constructed diagrams which have $2m$ external legs and only include one closed loop. In addition, one of the propagators connecting these diagrams has to be the single-scale propagator S^{Λ}. A selection of flow diagrams is displayed in Fig. 2.2 b.

- By these rules, it is obvious that the flow equation for $\Gamma^{(2m),\Lambda}$ will always also depend on the diagram $\Gamma^{(2m+2),\Lambda}$ by directly forming a tadpole diagram on the right hand side. Therefore, we are confronted with a hierarchy for a tower of coupled differential equations which is not closed. Eventually we will have to employ a suitable truncation to frame the flow equations solvable.

2.1.2 Truncation

We will now abolish the exactness of the derived flow equations by the implementation of a truncation scheme which eventually leads to a numerically solvable system of differential equations. The used truncation scheme includes three aspects:

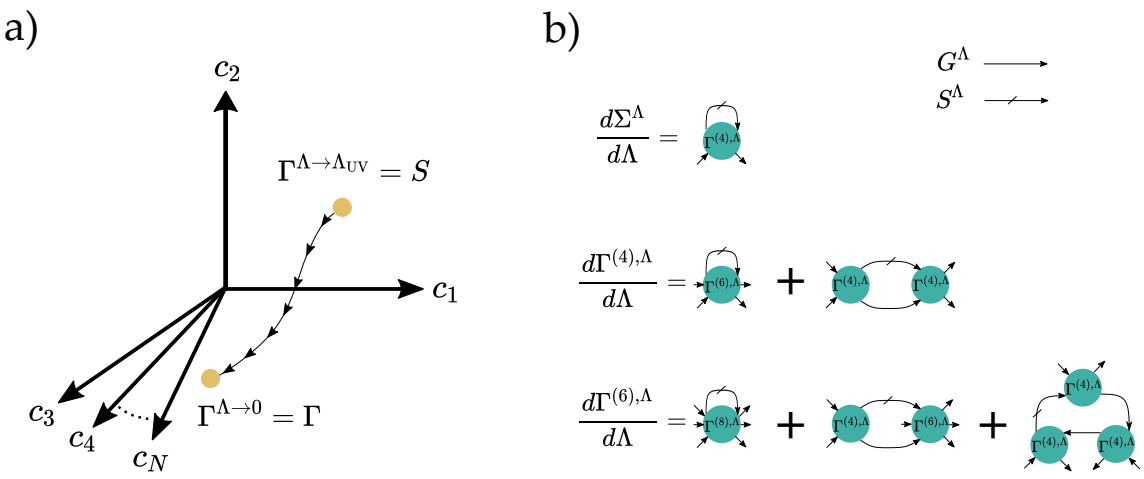

Figure 2.2: **FRG flow and diagram hierachy:** a) Depiction of the FRG flow, connecting the microscopical action S and ending in the full effective action Γ. The trajectory in theory space indicates how the couplings of the general functional Γ^Λ change while solving the flow equation. b) Diagrammatic representation of the flow equations after employing the vertex expansion for the first three diagrams. The right hand side of the diagrams match the external legs of the left hand side and always includes exactly one closed loop and one single-scale propagator S^Λ. Each diagram of order $2m$ will depend on the diagram of the next order $2m+2$, indicated by the tadpole diagrams shown at first on the respective right hand side.

- We will neglect all vertices with $m > 2$ such that the only class of diagrams, which will survive in the truncation scheme, is the class of four-legged diagrams. The pragmatical reasoning to implement this approximation is given by the fact that the aforementioned tower of differential equations becomes capped such that only a finite set of differential equations have to be solved. A justification of this approximation for weak and intermediate coupling regimes was given by Salmhofer and Honerkamp [94] at the example of the $m = 3$ diagram. At initial scales, diagrams of order $m = 3$ will be zero since no bare initial interaction is of this type. Diagrams with $m = 2$ will grow slowly and and are still relatively small. The flow equation for $m = 3$ diagrams depends in the order of three on $m = 2$ diagrams, leading to small increments of these diagrams. The problematic regime is reached when diagrams of order $m = 2$ start to diverge (i.e. are flowing to a strong coupling regime), causing also $m = 3$ contributions to become large. Since we are going to stop the flow calculation later anyway when a divergency sets on, we can therefore use this approximation scheme.

- We will neglect self-energy corrections and consequentially drop the flow equation $\frac{d}{d\Lambda}\Sigma^\Lambda$. Naturally, all occurring propagators which connect diagrams in the flow equations will then be bare propagators. This approximation is applicable, as it has also be shown that the self-energy is contributing to third order to the $m = 2$ diagram [72]. Note that the truncation of higher order diagrams and self-energy corrections may be valid in weak coupling applications, but becomes much more delicate in terms of strong coupling applications [90, 53, 5]

- Finally, we will drop the external frequency dependence of the vertices, i.e. only the internal Matsubara dependence of the bare propagators is included which becomes a continuum for low temperatures and will be the limit we are working in. It has been shown that the most singular part of the vertex sits at zero Matsubara frequency [72] which was already foreshadowed by the analysis of the bubbles in section 1 which also inhabited this feature. Since we are interested in many-body instabilities, i.e. divergencies of the vertex, this approximation is expedient for our application.

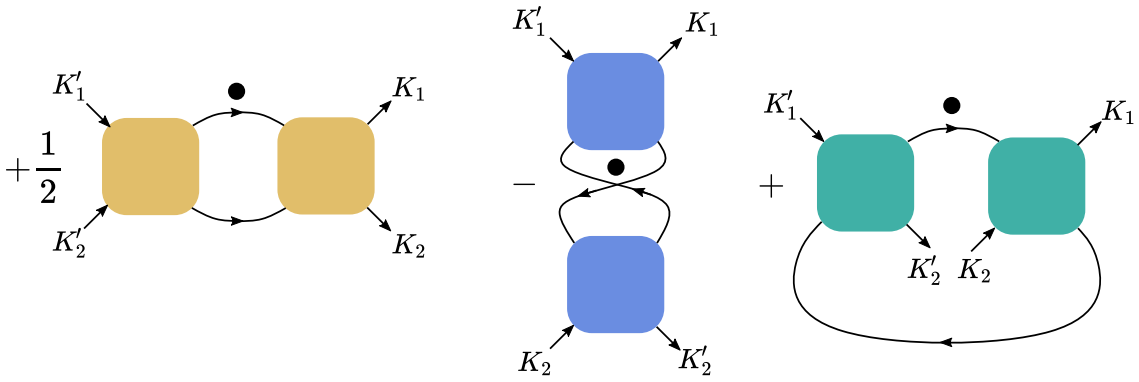

Figure 2.3: **Remaining diagrams after application of truncation:** All of the three diagram classes in Eq.(2.31) consist of two vertices with four legs connected by the term $\dot{B}^{\Lambda}(P_1, P_1', P_2, P_2')$ inhabiting the single-scale propagator and the full propagator. The dot indicates the scale derivative $\frac{d}{d\Lambda}$. The four-point vertex is for all three diagrams still the same object, the colours do only mark the different diagram classes.

While this truncation (which we will call level-2 truncation) appears to be invasive, it has been successfully demonstrated that competing orders in the context of the Hubbard model could be treated in this approximation scheme [39, 115, 32]. Competition between unconventional superconductivity and magnetism at van Hove filling could be captured for Hubbard models on the square [42], honeycomb [55] and triangular lattice [41]. While the exactness is therefore lost at this point, it should be highlighted that the substantial aspect of the flow equations (even in this truncated form) is given by taking different types of diagrams into account on equal footing.

For further simplification, we slightly rewrite the remaining diagrams in Eq. (2.29). With the definition of the single-scale propagator Eq. (2.26), we employ[3]:

$$\begin{aligned}\dot{B}^{\Lambda}(P_1, P_1', P_2, P_2') =& \frac{d}{d\Lambda}(G^{\Lambda}(P_1, P_1')G^{\Lambda}(P_2, P_2')) \\ =& G^{\Lambda}(P_1, P_1')S^{\Lambda}(P_2, P_2') + S^{\Lambda}(P_1, P_1')G^{\Lambda}(P_2, P_2')\end{aligned} \tag{2.30}$$

Now, the flow Eq. (2.29) is cast into the following form:

$$\begin{aligned}\frac{d}{d\Lambda}\Gamma^{(4),\Lambda}(K_1', K_2', K_1, K_2) = & \sum\!\!\!\!\!\!\int_{P_1, P_1'} \sum\!\!\!\!\!\!\int_{P_2, P_2'} \dot{B}^{\Lambda}(P_1, P_1', P_2, P_2') \\ \times \Bigg(& + \frac{1}{2}\left[\Gamma^{(4),\Lambda}(K_1', K_2', P_1, P_2) \times \Gamma^{(4),\Lambda}(P_1', P_2', K_1, K_2)\right] \\ & - \left[\Gamma^{(4),\Lambda}(K_1', P_2', K_1, P_1) \times \Gamma^{(4),\Lambda}(P_1', K_2', P_2, K_2)\right] \\ & + \left[\Gamma^{(4),\Lambda}(K_1', P_1', P_2, K_2) \times \Gamma^{(4),\Lambda}(P_2', K_2', K_1, P_1)\right] \Bigg)\end{aligned} \tag{2.31}$$

where for the first and third line we have to use the remnant of the Grassmann anti-symmetry. Precisely, this is the opportunity to switch the first two or last two arguments with the expense of an

[3] We still write this identity with the full propagator. We will install the reduction to the bare propagator due to the absence of self-energy later.

additional minus sign:

$$\Gamma^{(4),\Lambda}(K_1', K_2', K_1, K_2) = -\Gamma^{(4),\Lambda}(K_1', K_2', K_2, K_1)$$
$$= -\Gamma^{(4),\Lambda}(K_2', K_1', K_1, K_2) = +\Gamma^{(4),\Lambda}(K_2', K_1', K_2, K_1).$$

In the first line we also doubled the term $G^\Lambda S^\Lambda$ to cast this line into the desired form. We will see later that each of these three diagrams will result into the description of a specific interaction type, namely pairing/superconductivity, charge density and magnetism/spin density. For further simplifications of Eq. (2.31) we will now take the symmetries of the system into account.

2.1.3 Symmetries

We will exploit the symmetries of the system to reduce the complexity of the flow equations. The origin of these symmetries is delivered by the bare model. Since the symmetries should hold for the complete FRG flow[4], we can impose the following symmetry considerations for the flow equations. Furthermore, there is of course the symmetry of the underlying triangular lattice. Indeed, we will not use the lattice symmetries at this point. Instead these symmetries are exploited later when we derive the truncated-unity approach. For brevity, we will state the consequences of the symmetries without presenting the corresponding calculations, for a detailed look into this procedure we refer to [84].

Translation invariance

The translational invariance of the system with respect to imaginary time and real space results in the conservation of Matsubara frequency and momentum respectively:

$$\begin{aligned}\Gamma^{(4),\Lambda}(K_1', K_2', K_1, K_2) =& \Gamma^{(4),\Lambda}(K_1', K_2', K_1, K_2) \times \delta(K_1' + K_2' - K_1 - K_2) \\ =& \Gamma^{(4),\Lambda}(K_1', K_2', K_1, K_1' + K_2' - K_1) \\ =& \Gamma^{(4),\Lambda}(K_1', K_2', K_1),\end{aligned} \tag{2.32}$$

where in the last line we dropped the last argument of the vertex which is meant as an implication of the conservation.

SU(2)-invariance

In the presence of SU(2)-invariance for the spins we follow the construction presented in [94]. For that purpose, the vertex is rewritten with explicit spin degrees of freedom:

$$\Gamma^{(4),\Lambda}(K_1', K_2', K_1, K_2) = \Gamma^{(4),\Lambda}_{\sigma_1'\sigma_2'\sigma_1\sigma_1}(k_1', k_2', k_1, k_2). \tag{2.33}$$

Then the decomposition for a SU(2)-invariant vertex is given by:

$$\Gamma^{(4),\Lambda}_{\sigma_1'\sigma_2'\sigma_1\sigma_2}(k_1', k_2', k_1, k_2) = V^{(4),\Lambda}(k_1', k_2', k_1, k_2) \times \delta_{\sigma_1'\sigma_2}\delta_{\sigma_2'\sigma_1} - \tilde{V}^{(4),\Lambda}(k_1', k_2', k_1, k_2) \times \delta_{\sigma_1'\sigma_1}\delta_{\sigma_2'\sigma_2}. \tag{2.34}$$

Indeed, it is sufficient to treat only one of the two emerging vertices $V^{(4),\Lambda}, \tilde{V}^{(4),\Lambda}$ since it holds by employing Grassmann anti-symmetry:

$$\begin{aligned}\Gamma^{(4),\Lambda}_{\sigma_1'\sigma_2'\sigma_1\sigma_2}(k_1', k_2', k_1, k_2) &= -\Gamma^{(4),\Lambda}_{\sigma_1'\sigma_2'\sigma_2\sigma_1}(k_1', k_2', k_2, k_1) \\ &= -V^{(4),\Lambda}(k_1', k_2', k_2, k_1) \times \delta_{\sigma_1'\sigma_1}\delta_{\sigma_2'\sigma_2} \\ &\quad + \tilde{V}^{(4),\Lambda}(k_1', k_2', k_2, k_1) \times \delta_{\sigma_1'\sigma_2}\delta_{\sigma_2'\sigma_1}.\end{aligned} \tag{2.35}$$

[4] Indeed, our scheme is not able to allow flows into regimes where symmetries are broken such that this statement is valid. However, methods to employ also the possibility of flowing into phases with broken symmetries exist[95], but we will refrain from these in this thesis.

And concluding by comparison of coefficients regarding the spin Kronecker-δ:

$$V^{(4),\Lambda}(k_1', k_2', k_1, k_2) = \tilde{V}^{(4),\Lambda}(k_1', k_2', k_2, k_1). \tag{2.36}$$

For a spin-invariant system we will therefore only explicitly solve the flow for the vertex $V^{(4),\Lambda}$. This vertex itself has no explicit spin-dependency anymore, but the symmetry expresses itself in the terms of δ-functions which allows only for a specific set of contractions of two diagrams. Diagrammatically, we will indicate this feature by implying that the spin degree of freedom is conserved along the edges of the diagram, see Fig. 2.4 b.

2.1.4 Explicit flow equations

We will now derive the explicit flow equations for the three applications of this thesis by using the presented symmetries. The flow equations for the spinless model and for the model with no SU(2)-invariance will have the same structure regarding the emerging diagrams. The only aspect differentiating these flow equations is the spin degree of freedom σ which is excluded in the superindex K for the spinless application. We will now explicitly drop the external frequency dependence as already mentioned in the truncation scheme. From the definition of the bare propagator Eq. (2.2) follows:

$$\dot{B}(P_1, P_1', P_2, P_2') = \frac{d}{d\Lambda}\left(G^{0,\Lambda}(P_1)G^{0,\Lambda}(P_2)\right) \times \delta(P_1 - P_1')\delta(P_2 - P_2'), \tag{2.37}$$

where we now also followed our truncation and replaced the full propagators by bare propagators.

Equations without SU(2)-invariance (Application B and C)

We will use the translational invariance Eq. (2.32) with the aforementioned notation for momentum conservation. We already directly employ the approximation of dropping all external Matsubara frequency dependencies:

$$\Gamma^{(4),\Lambda}_{\sigma_1',\sigma_2',\sigma_1,\sigma_2}(\boldsymbol{k_1'}, \boldsymbol{k_2'}, \boldsymbol{k_1}, \boldsymbol{k_2}) \to V^{\Lambda}_{\sigma_1',\sigma_2',\sigma_1,\sigma_2}(\boldsymbol{k_1'}, \boldsymbol{k_2'}, \boldsymbol{k_1}). \tag{2.38}$$

Finally, by application of these expressions to Eq. (2.31) and using the momentum conservation to shift around momentum indices, we arrive at:

$$\begin{aligned}\frac{d}{d\Lambda}V^{\Lambda}_{\sigma_1',\sigma_2',\sigma_1,\sigma_2}(\boldsymbol{k_1'}, \boldsymbol{k_2'}, \boldsymbol{k_1}, \boldsymbol{k_2}) = \tau^{\mathrm{pp}}_{\sigma_1',\sigma_2',\sigma_1,\sigma_2}(\boldsymbol{k_1'}, \boldsymbol{k_2'}, \boldsymbol{k_1}, \boldsymbol{k_2}) + \tau^{\mathrm{ph,d}}_{\sigma_1',\sigma_2',\sigma_1,\sigma_2}(\boldsymbol{k_1'}, \boldsymbol{k_2'}, \boldsymbol{k_1}, \boldsymbol{k_2}) \\ + \tau^{\mathrm{ph,cr}}_{\sigma_1',\sigma_2',\sigma_1,\sigma_2}(\boldsymbol{k_1'}, \boldsymbol{k_2'}, \boldsymbol{k_1}, \boldsymbol{k_2})\end{aligned} \tag{2.39}$$

$$\begin{aligned}\tau^{\mathrm{pp}}_{\sigma_1',\sigma_2',\sigma_1,\sigma_2}(\boldsymbol{k_1'}, \boldsymbol{k_2'}, \boldsymbol{k_1}, \boldsymbol{k_2}) = \frac{1}{2}\int_p \sum_{\nu_1',\nu_2',\nu_1,\nu_2} \frac{d}{d\Lambda}[G^{0,\Lambda}_{\nu_1',\nu_1}(i\omega_p, \boldsymbol{p} + \boldsymbol{k_1'} + \boldsymbol{k_2'})G^{0,\Lambda}_{\nu_2',\nu_2}(-i\omega_p, -\boldsymbol{p})] \\ \times V^{\Lambda}_{\sigma_1',\sigma_2',\nu_1',\nu_2'}(\boldsymbol{k_1'}, \boldsymbol{k_2'}, \boldsymbol{p} + \boldsymbol{k_1'} + \boldsymbol{k_2'}) \times V^{\Lambda}_{\nu_1,\nu_2,\sigma_1,\sigma_2}(\boldsymbol{p} + \boldsymbol{k_1'} + \boldsymbol{k_2'}, -\boldsymbol{p}, \boldsymbol{k_1})\end{aligned} \tag{2.40}$$

$$\begin{aligned}\tau^{\mathrm{ph,d}}_{\sigma_1',\sigma_2',\sigma_1,\sigma_2}(\boldsymbol{k_1'}, \boldsymbol{k_2'}, \boldsymbol{k_1}, \boldsymbol{k_2}) = -\int_p \sum_{\nu_1',\nu_2',\nu_1,\nu_2} \frac{d}{d\Lambda}[G^{0,\Lambda}_{\nu_1',\nu_1}(i\omega_p, \boldsymbol{p} + \boldsymbol{k_1'} - \boldsymbol{k_1})G^{0,\Lambda}_{\nu_2,\nu_2'}(i\omega_p, \boldsymbol{p})] \\ \times V^{\Lambda}_{\sigma_1',\nu_2',\sigma_1,\nu_1'}(\boldsymbol{k_1'}, \boldsymbol{p}, \boldsymbol{k_1}) \times V^{\Lambda}_{\nu_1,\sigma_2',\nu_2,\sigma_2}(\boldsymbol{p} + \boldsymbol{k_1'} - \boldsymbol{k_1}, \boldsymbol{k_2'}, \boldsymbol{p})\end{aligned} \tag{2.41}$$

$$\begin{aligned}\tau^{\mathrm{ph,cr}}_{\sigma_1',\sigma_2',\sigma_1,\sigma_2}(\boldsymbol{k_1'}, \boldsymbol{k_2'}, \boldsymbol{k_1}, \boldsymbol{k_2}) = +\int_p \sum_{\nu_1',\nu_2',\nu_1,\nu_2} \frac{d}{d\Lambda}[G^{0,\Lambda}_{\nu_1',\nu_1}(i\omega_p, \boldsymbol{p} + \boldsymbol{k_1'} - \boldsymbol{k_2})G^{0,\Lambda}_{\nu_2,\nu_2'}(i\omega_p, \boldsymbol{p})] \\ \times V^{\Lambda}_{\sigma_1',\nu_2',\nu_1',\sigma_2}(\boldsymbol{k_1'}, \boldsymbol{p}, \boldsymbol{p} + \boldsymbol{k_1'} - \boldsymbol{k_2}) \times V^{\Lambda}_{\nu_1,\sigma_2',\sigma_1,\nu_2}(\boldsymbol{p} + \boldsymbol{k_1'} - \boldsymbol{k_2}, \boldsymbol{k_2'}, \boldsymbol{k_1})\end{aligned} \tag{2.42}$$

where (as stated before) for a spinless system one only has to omit all spin indices σ, ν and the respective sums. We remind the reader that the integral $\int_p$ describes the integration over momenta in the Brillouin zone $\boldsymbol{p}$ and the Matsubara sum over frequencies ω_p: $\int_p = \mathrm{A}_{BZ}^{-1} T \int d\boldsymbol{p} \sum_{\omega_p}$.

Equations with SU(2)-invariance (Application A)

For the derivation of the SU(2)-invariant flow equation, we have invest an extra step. At first, we apply the translational invariance Eq. (2.32) and spin invariance Eq. (2.34) to the vertex:

$$\Gamma^{(4),\Lambda}_{\sigma_1',\sigma_2',\sigma_1,\sigma_1}(\boldsymbol{k}_1',\boldsymbol{k}_2',\boldsymbol{k}_1,\boldsymbol{k}_2) \to V^\Lambda(\boldsymbol{k}_1',\boldsymbol{k}_2',\boldsymbol{k}_1)\delta_{\sigma_1'\sigma_2}\delta_{\sigma_2'\sigma_1} - \bar{V}^\Lambda(\boldsymbol{k}_1',\boldsymbol{k}_2',\boldsymbol{k}_1)\delta_{\sigma_1'\sigma_1}\delta_{\sigma_2'\sigma_2}, \quad (2.43)$$

where (as stated before) it is sufficient to derive a flow equation for V^Λ only. To proceed, we express the vertex on *both sides* of Eq. (2.31) by the new vertices after the application of the symmetries Eq. (2.43). To derive the correct flow equation for V^Λ, we have to sort the right hand side of the Eq. (2.31) in terms of the spin Kronecker deltas $\delta_{\sigma_1'\sigma_2}\delta_{\sigma_2'\sigma_1}$ to project all necessary terms to the flow equation. The consequences of the SU(2)-invariance are twofold. At first, we will get different prefactors in contrast to the former derived flow equations. More substantively, the amount of possible diagram contractions shrinks such that only specific classes of diagrams remain.

$$\begin{aligned}\frac{d}{d\Lambda}V^\Lambda(\boldsymbol{k}_1',\boldsymbol{k}_2',\boldsymbol{k}_1,\boldsymbol{k}_2) = \tau^{\mathrm{pp}}(\boldsymbol{k}_1',\boldsymbol{k}_2',\boldsymbol{k}_1,\boldsymbol{k}_2) &+ \tau^{\mathrm{ph,d}}(\boldsymbol{k}_1',\boldsymbol{k}_2',\boldsymbol{k}_1,\boldsymbol{k}_2) \\ &+ \tau^{\mathrm{ph,cr}}(\boldsymbol{k}_1',\boldsymbol{k}_2',\boldsymbol{k}_1,\boldsymbol{k}_2) \end{aligned} \quad (2.44)$$

$$\begin{aligned}\tau^{\mathrm{pp}}(\boldsymbol{k}_1',\boldsymbol{k}_2',\boldsymbol{k}_1,\boldsymbol{k}_2) = \int_p \frac{d}{d\Lambda}[G^{0,\Lambda}(i\omega_p,\boldsymbol{p}+\boldsymbol{k}_1'+\boldsymbol{k}_2')G^{0,\Lambda}(-i\omega_p,-\boldsymbol{p})] \\ \times V^\Lambda(\boldsymbol{k}_1',\boldsymbol{k}_2',\boldsymbol{p}+\boldsymbol{k}_1'+\boldsymbol{k}_2')\times V^\Lambda(\boldsymbol{p}+\boldsymbol{k}_1'+\boldsymbol{k}_2',-\boldsymbol{p},\boldsymbol{k}_1),\end{aligned} \quad (2.45)$$

$$\begin{aligned}\tau^{\mathrm{ph,d}}(\boldsymbol{k}_1',\boldsymbol{k}_2',\boldsymbol{k}_1,\boldsymbol{k}_2) = \int_p \frac{d}{d\Lambda}[G^{0,\Lambda}(i\omega_p,\boldsymbol{p}+\boldsymbol{k}_1'-\boldsymbol{k}_1)G^{0,\Lambda}(i\omega_p,\boldsymbol{p})] \\ [V^\Lambda(\boldsymbol{k}_1',\boldsymbol{p},\boldsymbol{p}+\boldsymbol{k}_1'-\boldsymbol{k}_1)\times V^\Lambda(\boldsymbol{p}+\boldsymbol{k}_1'-\boldsymbol{k}_1,\boldsymbol{k}_2',\boldsymbol{p}) \\ +V^\Lambda(\boldsymbol{k}_1',\boldsymbol{p},\boldsymbol{k}_1)\times V^\Lambda(\boldsymbol{p}+\boldsymbol{k}_1'-\boldsymbol{k}_1,\boldsymbol{k}_2',\boldsymbol{k}_2) \\ -2V^\Lambda(\boldsymbol{k}_1',\boldsymbol{p},\boldsymbol{k}_1)\times V^\Lambda(\boldsymbol{p}+\boldsymbol{k}_1'-\boldsymbol{k}_1,\boldsymbol{k}_2',\boldsymbol{p})],\end{aligned} \quad (2.46)$$

$$\begin{aligned}\tau^{\mathrm{ph,cr}}(\boldsymbol{k}_1',\boldsymbol{k}_2',\boldsymbol{k}_1,\boldsymbol{k}_2) = \int_p \frac{d}{d\Lambda}[G^{0,\Lambda}(i\omega_p,\boldsymbol{p}+\boldsymbol{k}_1'-\boldsymbol{k}_2)G^{0,\Lambda}(i\omega_p,\boldsymbol{p})] \\ \times V^\Lambda(\boldsymbol{k}_1',\boldsymbol{p},\boldsymbol{p}+\boldsymbol{k}_1'-\boldsymbol{k}_2)\times V^\Lambda(\boldsymbol{p}+\boldsymbol{k}_1'-\boldsymbol{k}_2,\boldsymbol{k}_2',\boldsymbol{k}_1).\end{aligned} \quad (2.47)$$

Précis of section 2.1

- In this section, we defined the basic notions of the FRG method which exchanges the path integral of a quantum many-body system with a differential equation for the scale-dependent effective action Γ^Λ, namely Eq. (2.17).
- By expanding the effective action into orders of 1PI diagrams, we were able to derive a hierarchy of flow equations Eq. (2.29). This tower of equations is not closed and therefore not feasible for a numerical implementation.
- We chose a truncation scheme, namely only keeping vertices of fourth order, neglecting self-energy corrections and dropping the external frequency dependence. This procedure leads to an actual solvable set of diagrams Eq. (2.31).

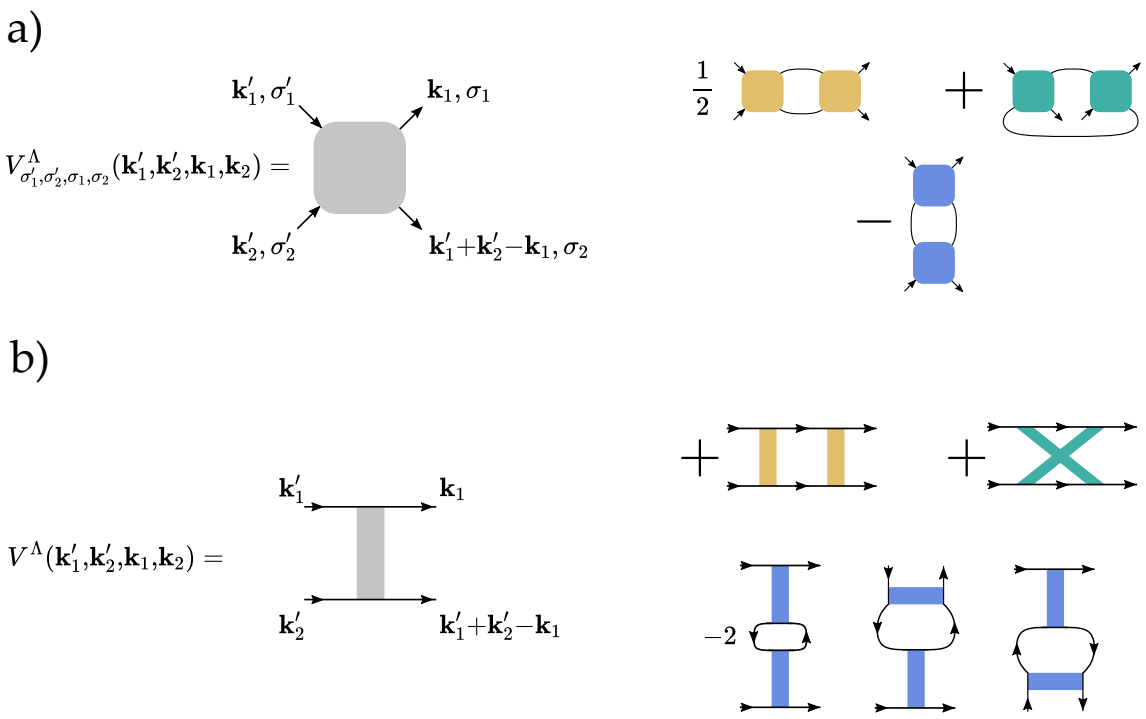

Figure 2.4: **Diagrammatic depiction of the flow equation for the four-legged vertex:** a) Without SU(2)-invariance, the outer indices are the momentum in the Brillouin zone $\boldsymbol{k}$ and the spin σ if the model happens to be spinful. The diagrams of the flow equation on the right hand side will look still similar to those in Fig. 2.2 where we omitted the dot for the derivative for brevity. b) Including SU(2)-invariance, it is implied that the spin σ is conserved along the upper and lower edge of the vertex, leaving only the momentum in the Brillouin zone $\boldsymbol{k}$ as an outer index. Therefore, only a subset of diagrams will remain in contrast to a).

- Eventually by the inclusion of symmetries, we derived the final version of the flow equations of the four-legged vertex. For a system without SU(2)-invariance, these equations are given by Eqs. (2.40)-(2.42). For a system including SU(2)-invariance, the proper flow equations are Eqs. (2.45)-(2.47). For a diagrammatic representation of these equations, we refer to Fig. 2.4.
- The three types of diagrams are now labeled as τ^{pp},$\tau^{\mathrm{ph,cr}}$ and $\tau^{\mathrm{ph,d}}$ abbreviating **particle-particle**, **particle-hole crossed** and **particle-hole direct**. These names refer to the fact that for the first type of diagram (yellow) the vertices are connected by a particle-particle bubble, while the other diagrams (blue/green) are connected by a particle-hole bubble (and a scale-derivative $d/d\Lambda$). We encountered this feature already in section 1.1 while discussing the possible formation of instabilities. The *crossed* and *direct* names for the particle-hole diagrams stem from the SU(2)-invariant flow equation and refer to the depiction of the two vertices.
- In both sets of equations we shifted the momenta around with the usage of momentum conservation such that a specific combination of momenta is carried by the propagators. This will make the diagrams interpretable in a simpler way which we will see in the next section.

This derivation ends section 2.1. The key elements of this section are the flow equations Eqs. (2.40)-(2.42) and Eqs. (2.45)-(2.47) from which we can now start doing numerical investigations. Effectively, this approach can be boiled down to implementing a solver for the differential equation for $V^{\Lambda}_{\sigma_1',\sigma_2',\sigma_1,\sigma_1}(\boldsymbol{k}_1', \boldsymbol{k}_2', \boldsymbol{k}_1)$ or $V^{\Lambda}(\boldsymbol{k}_1', \boldsymbol{k}_2', \boldsymbol{k}_1)$ respectively. In both cases, the amount of equations to solve per step scales with N_k^3, where N_k is the amount of chosen momenta $\boldsymbol{k}$ in the Brillouin zone. This poses a numerical challenge, since even for a relatively small amount of momenta $N_{\boldsymbol{k}} \approx 100$ this will result to $1,000,000$ equations to solve for each step. Indeed, an established scheme which

was implemented for this flow equation is the so-called *patching scheme* [39, 115, 32] where the actual sampling points in the Brillouin zone are chosen to be on the Fermi surface which should account for the most important contributions to the flow equations. In the next section, we will derive a more recent scheme for solving the flow equations, called the *truncated-unity* approach which will eventually lead to a linear scaling in momentum instead of cubic scaling like in the patching scheme. This allows for a higher momentum resolution where the discretization points are not restricted to be placed on the Fermi surface.

Sidenote: The derived flow equations differ from these used in the publications [29, 30] by a global sign. This global sign stems from the convention of how to write down the differential equation solver for the derivative $\frac{d}{d\Lambda}$. We decided to do the derivation in this section as presented such that it is in congruence with the standard literature. In section 2.3.4 we will treat this peculiar feature again in more detail.

2.2 The Truncated-Unity approach

In this section we will present and derive the Truncated-Unity Functional Renormalization Group (TUFRG) [64, 40, 98] as an advanced scheme to treat the emerging FRG flow equations. The key property of this approach is exchanging the three momentum arguments of the vertex by one very specific momentum argument and two form factors, an idea which was initially proposed by Husemann and Salmhofer [46]. The choice of the specific momentum for the parametrization is motivated by the physical insights presented in the context of section 1.1, namely that the transfer momentum of the particle-particle and particle-hole bubble is mainly responsible for the onset of an instability. Since the other two momenta are then deemed as playing no crucial role for this formation, they will consequently be expanded into form factors which can be reasonably truncated at a finite order. Therefore, we will reach at a superior scaling for the flow equations in terms of momenta which is only linear. This improvement opens up the possibility of including additional quantum numbers (like spin,orbital or sublattice indices) in the FRG flow. The inclusion of these quantum numbers would frame the application in previous schemes extraordinary challenging, since the additional numerical cost of dealing with these quantum numbers in addition to the already poor cubic scaling in momenta results into an unfavourable high-dimensional object.

We will derive and discuss the TUFRG in context of the SU(2)-invariant flow equations here, although the majority of the discussion also applies to the other flow equations presented in section 2.1. The respective TUFRG equations for each case are presented in the application sections later as a summary.

2.2.1 Channel decomposition

As a first step, we want to motivate the decomposition of the FRG flow into specific physical channels [46]. This is a crucial step for developing the TUFRG method, although it should be mentioned that this decomposition is not exclusive for the TUFRG, but can also be applied in other schemes [25, 11]. Previously, we derived the flow equations for a SU(2)-invariant interaction where we also imposed translation invariance. Since we truncated all interaction vertices with six legs or more, the vertex expansion Eq. (2.19) for interactions does only consist of the terms:

$$\Gamma_V^\Lambda = \frac{1}{2} \int_{k_1,k_2,k_3,k_4} V^\Lambda(k_1,k_2,k_3,k_4)\delta(k_1+k_2-k_3-k_4)\sum_{\sigma,\sigma'}\bar{\psi}_\sigma(k_1)\bar{\psi}_{\sigma'}(k_2)\psi_{\sigma'}(k_4)\psi_\sigma(k_3), \tag{2.48}$$

where we also directly applied mentioned symmetries. Note that we changed the notation here to be consistent with the publications/applications later. The four momenta are therefore relabeled:

$$(k_1', k_2', k_1, k_2) \to (k_1, k_2, k_3, k_4)$$

We will inspect the flow equations Eqs. (2.45)-(2.47) in perspective of this interaction to receive a physical interpretation of the diagrams.

Analysis of the particle-particle diagram

We will start with the particle-particle contribution:

$$\begin{aligned}\tau^{\mathrm{pp}}(\boldsymbol{k}_1,\boldsymbol{k}_2,\boldsymbol{k}_3,\boldsymbol{k}_4) = \int_p \frac{d}{d\Lambda}[G^{0,\Lambda}(i\omega_p,\boldsymbol{p}+\boldsymbol{k}_1+\boldsymbol{k}_2)G^{0,\Lambda}(-i\omega_p,-\boldsymbol{p})] \\ \times V^\Lambda(\boldsymbol{k}_1,\boldsymbol{k}_2,\boldsymbol{p}+\boldsymbol{k}_1+\boldsymbol{k}_2)\times V^\Lambda(\boldsymbol{p}+\boldsymbol{k}_1+\boldsymbol{k}_2,-\boldsymbol{p},\boldsymbol{k}_3).\end{aligned}$$

For a first hint of a physical interpretation for this diagram class we notice that the combination of bare propagators equals the definition of the particle-particle bubble as described in section 1, Eq. (1.11), with transfer momentum $\boldsymbol{q} = \boldsymbol{k_1}+\boldsymbol{k_2}$. In this section we showed that the occurrence of an instability

towards superconductivity is linked to the divergence of this exact bubble which in turn is sensitive to the value of the transfer momentum $\boldsymbol{q}$. A divergence of this bubble will therefore also manifest in a divergence of the diagram τ^{pp} due to the singular contributions such that we suspect that this diagram effectively describes the contributions towards pairing interactions which are generated in the FRG flow.

For a more detailed investigation we will now treat at a typical pairing interaction and try to relate it to Eq. (2.48). Starting with:

$$S^P[\bar{\psi},\psi] = \int\limits_{q,k,k'} \Phi^P(q;k,k') \sum_{\sigma,\sigma'} \bar{\psi}_\sigma(q+k)\bar{\psi}_{\sigma'}(-k)\psi_{\sigma'}(-k')\psi_\sigma(q+k') \tag{2.49}$$

where this pairing interaction was constructed after the BCS-like interactions described in section 1.2. We also include the symmetries used for Eq. (2.48). In addition, we allow for a general transfer momentum q. This particular momentum is notated at first position in the pairing interaction strength $\Phi^P(q;k,k')$ to highlight its importance. We will relate this pairing interaction to Eq. (2.48) by explicitly shifting and renaming the momenta:

$$\begin{aligned} q+k &= k_1 \\ -k &= k_2 \\ q+k' &= k_3 \\ -k' = k_4 &= k_1+k_2-k_3 \end{aligned}$$

which in reciprocal relation indicates:

$$\begin{aligned} q &= k_1+k_2 \\ k &= -k_2 \\ k' &= -k_4 \end{aligned}$$

Then the proposed interaction vertex has the new form:

$$S^P[\bar{\psi},\psi] = \int\limits_{k_1,k_2,k_3,k_4} \Phi^P(k_1+k_2;-k_2,-k_4) \sum_{\sigma,\sigma'} \bar{\psi}_\sigma(k_1)\bar{\psi}_{\sigma'}(k_2)\psi_{\sigma'}(k_4)\psi_\sigma(k_1+k_2-k_4). \tag{2.50}$$

This expression possesses the same structure like the general effective action in our approach Eq. (2.48) in terms of Grassmann fields. Also, the transfer momentum of this interaction term happens to be k_1+k_2 (the first argument of Φ^P) which also aligns with the transfer momentum in the particle-particle diagram τ^{pp}. Therefore, it is indeed reasonable to interpret this diagram as the contributions to the pairing vertex where $q = k_1+k_2$ is the crucial transfer momentum which determines the singular behaviour of the particle-particle bubble.

We will repeat this analysis for the other diagrams.

Analysis of the direct particle-hole diagram

The two remaining diagram classes $\tau^{\text{ph,d}}$ and $\tau^{\text{ph,cr}}$ do both include the definition of the particle-hole bubble, but with two distinct transfer momenta. To gain insight about the physical interpretation of both diagrams, we will propose two different interaction types and relate each to one diagram. We will start with the $\tau^{\text{ph,d}}$ diagram class and propose a charge density wave (CDW). A CDW describes a state of order where charge modulates through a lattice with modulation vector $\boldsymbol{q}$. Similar to the analysis in section 1.1, where the transfer momentum of the spin density wave (SDW) (i.e. the nesting vector)

corresponded to the modulation vector of the wave, we assume a similar structure for the CDW. To construct a general CDW interaction, we start with the Hamiltonian:

$$H = \sum_{\boldsymbol{k},\boldsymbol{k'}} n^{\dagger}_{\boldsymbol{k},\boldsymbol{q}} n_{\boldsymbol{k'},\boldsymbol{q}} \tag{2.51}$$

$$n_{\boldsymbol{k},\boldsymbol{q}} = \sum_{\boldsymbol{k},\sigma} c^{\dagger}_{\boldsymbol{k}+\boldsymbol{q},\sigma} c_{\boldsymbol{k},\sigma}. \tag{2.52}$$

In field theory, this can then be translated to the action:

$$S^D[\bar{\psi},\psi] = \int\limits_{q,k,k'} \Phi^D(q;k,k') \sum_{\sigma,\sigma'} \bar{\psi}_{\sigma}(q+k)\bar{\psi}_{\sigma'}(k')\psi_{\sigma'}(q+k')\psi_{\sigma}(k), \tag{2.53}$$

where we included $\Phi^D(q;k,k')$ as interaction strength. Again, we impose the notation to keep track of the transfer momentum q as first argument. We will shift the momenta:

$$\begin{aligned} q+k &= k_1 \\ k' &= k_2 \\ k &= k_3 \\ q+k' = k_4 &= k_1+k_2-k_3 \end{aligned}$$

and in reciprocal relation:

$$\begin{aligned} q &= k_1 - k_3 \\ k &= k_3 \\ k' &= k_2 \end{aligned}$$

such that:

$$S^D[\bar{\psi},\psi] = \int\limits_{k_1,k_2,k_3,k_4} \delta(k_1+k_2-k_3-k_4)\Phi^D(k_1-k_3;k_3,k_2) \sum_{\sigma,\sigma'} \bar{\psi}_{\sigma}(k_1)\bar{\psi}_{\sigma'}(k_2)\psi_{\sigma'}(k_4)\psi_{\sigma}(k_3). \tag{2.54}$$

Therefore, the transfer momentum of the CDW interaction given by $q = k_1 - k_3$ does indeed match the transfer momentum of the particle-hole bubble in the direct particle-hole diagram $\tau^{\mathrm{ph,d}}$ and we will interpret this diagram class the contributions towards a density-density interaction which favours the onset of a CDW instability.

Analysis of the crossed particle-hole diagram

The last diagram does also include a particle-hole bubble, but with another transfer momentum. We will a propose a SDW as possible interpretation for this diagram. Starting with the Hamiltonian of a SDW with transfer momentum $\boldsymbol{q}$:

$$H = \sum_{\boldsymbol{p},\boldsymbol{k}} \vec{S}^{\dagger}_{\boldsymbol{p},\boldsymbol{q}} \cdot \vec{S}_{\boldsymbol{k},\boldsymbol{q}}, \tag{2.55}$$

$$\vec{S}_{\boldsymbol{k},\boldsymbol{q}} = \frac{1}{2} \sum_{\alpha,\beta} c^{\dagger}_{\boldsymbol{k}+\boldsymbol{q},\alpha} \cdot \vec{\sigma}_{\alpha\beta} \cdot c_{\boldsymbol{k},\beta}, \tag{2.56}$$

where $\vec{\sigma}$ is the vector of Pauli matrices. Using the identity:

$$\vec{\sigma}^{\dagger}_{\alpha\beta} \cdot \vec{\sigma}_{\alpha'\beta'} = 2\delta_{\alpha,\beta'}\delta_{\alpha',\beta} - \delta_{\alpha,\beta}\delta_{\alpha',\beta'}, \tag{2.57}$$

we can cast the Hamiltonian into the form:

$$H = \frac{1}{2}\sum_{\boldsymbol{p},\boldsymbol{k}}\sum_{\alpha,\beta} c^\dagger_{\boldsymbol{p},\alpha} c_{\boldsymbol{p}+\boldsymbol{q},\beta} c^\dagger_{\boldsymbol{k}+\boldsymbol{q},\alpha} c_{\boldsymbol{k},\beta} - \frac{1}{4}\sum_{\boldsymbol{p},\boldsymbol{k}}\sum_{\alpha,\beta} c^\dagger_{\boldsymbol{p},\alpha} c_{\boldsymbol{p}+\boldsymbol{q},\alpha} c^\dagger_{\boldsymbol{k}+\boldsymbol{q},\beta} c_{\boldsymbol{k},\beta}. \tag{2.58}$$

The second term will again result into a density-density term which was already captured by the direct particle-particle diagram. So, we focus on the first term describing the magnetic interaction only. Using the field theoretical description and translating the Hamiltonian to an action:

$$S^C[\bar{\psi},\psi] = \int_{q,k,k'} \Phi^C(q;k,k') \sum_{\sigma,\sigma'} \bar{\psi}_\sigma(q+k)\bar{\psi}_{\sigma'}(k')\psi_{\sigma'}(k)\psi_\sigma(q+k') \tag{2.59}$$

with interaction strength $\Phi^C(q;k,k')$. We employ again a shift to the momenta and reach:

$$\begin{aligned} q+k &= k_1 \\ k' &= k_2 \\ q+k' &= k_3 \\ k &= k_4 \end{aligned}$$

and in reciprocal relation:

$$\begin{aligned} k &= k_1 - k_4 \\ k &= k_4 \\ k' &= k_2. \end{aligned}$$

Such that the rewritten action reads:

$$S^C[\bar{\psi},\psi] = \int_{k_1,k_2,k_3,k_4} \delta(k_1+k_2-k_3-k_4)\Phi^C(k_1-k_4;k_4,k_2) \sum_{\sigma,\sigma'} \bar{\psi}_\sigma(k_1)\bar{\psi}_{\sigma'}(k_2)\psi_{\sigma'}(k_4)\psi_\sigma(k_3). \tag{2.60}$$

Since the crossed particle-hole diagram class $\tau^{\text{ph,cr}}$ includes a particle-hole bubble with transfer momentum $q = k_1 - k_4$, we will relate it to the possibility of a magnetic instability. Interestingly, it directly shows that a substantial amount of growth in a magnetic interaction also leads to contributions to the density-density channel as expected for SDWs.

The analysis of three different diagrams of the flow equations for the systems leads us to the implementation of the **channel decomposition**, meaning that from the general flow equation:

$$\frac{d}{d\Lambda} V^\Lambda = \tau^{\text{pp}} + \tau^{\text{d}} + \tau^{\text{ph,cr}}, \tag{2.61}$$

we are motivated to decompose V^Λ into channels such that the three discussed interactions are visible in each channel. For that purpose, we use the parametrization scheme already derived in the analysis of the three diagram classes and impose for our flow equations (where we directly omitted the frequency dependence):

$$\begin{aligned} V^\Lambda(\boldsymbol{k}_1,\boldsymbol{k}_2,\boldsymbol{k}_3,\boldsymbol{k}_4) = V^0(&\boldsymbol{k}_1,\boldsymbol{k}_2,\boldsymbol{k}_3,\boldsymbol{k}_4) \\ &+ \Phi^{P,\Lambda}(\boldsymbol{k}_1+\boldsymbol{k}_2;-\boldsymbol{k}_2,-\boldsymbol{k}_4) \\ &+ \Phi^{D,\Lambda}(\boldsymbol{k}_1-\boldsymbol{k}_3;\boldsymbol{k}_3,\boldsymbol{k}_2) \\ &+ \Phi^{C,\Lambda}(\boldsymbol{k}_1-\boldsymbol{k}_4;\boldsymbol{k}_4,\boldsymbol{k}_2) \end{aligned} \tag{2.62}$$

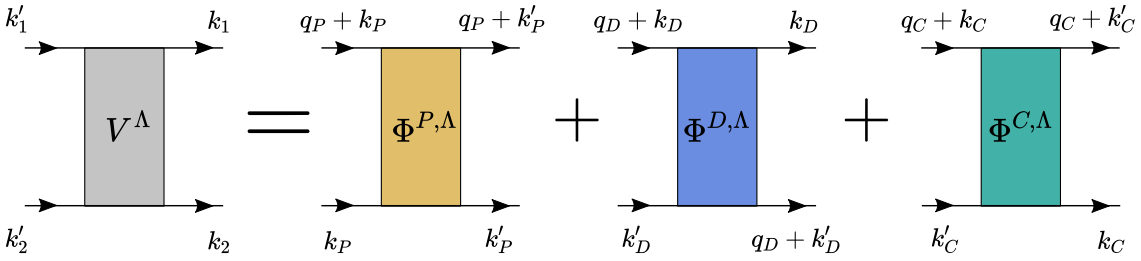

Figure 2.5: **Channel decomposition of V^Λ:** By the analysis of the diagrams, the vertex V^Λ is decomposed into three channels $\Phi^{X,\Lambda}$ with $X = P, D, C$. The transfer momentum q_X and the other two momenta k_X, k_X' are given in a summary table in the text.

where $V^{0,\Lambda}$ accounts for initial conditions as seen later. All three interaction channels $\Phi^{X,\Lambda}$, $X = P, D, C$ are now also scale dependent. One can check the correctness of this decomposition by plugging Eq. (2.62) into Eq. (2.48) where it becomes apparent that the three aforementioned interaction types are reproduced. By taking the derivative of Eq. (2.62), we distribute the scale derivative on the three channels and impose that these objects only depend on their specific diagram class:

$$\frac{d}{d\Lambda}\Phi^{P,\Lambda}(\boldsymbol{k}_1 + \boldsymbol{k}_2; -\boldsymbol{k}_2, -\boldsymbol{k}_4) = \tau^{\mathrm{pp}}(\boldsymbol{k}_1, \boldsymbol{k}_2, \boldsymbol{k}_3, \boldsymbol{k}_4) \tag{2.63}$$

$$\frac{d}{d\Lambda}\Phi^{D,\Lambda}(\boldsymbol{k}_1 - \boldsymbol{k}_3; \boldsymbol{k}_3, \boldsymbol{k}_2) = \tau^{\mathrm{ph,d}}(\boldsymbol{k}_1, \boldsymbol{k}_2, \boldsymbol{k}_3, \boldsymbol{k}_4) \tag{2.64}$$

$$\frac{d}{d\Lambda}\Phi^{C,\Lambda}(\boldsymbol{k}_1 - \boldsymbol{k}_4; \boldsymbol{k}_4, \boldsymbol{k}_2) = \tau^{\mathrm{ph,cr}}(\boldsymbol{k}_1, \boldsymbol{k}_2, \boldsymbol{k}_3, \boldsymbol{k}_4) \tag{2.65}$$

The channel decomposition can be summarized as:

Channel X	P	D	C
Interaction type	Pairing	Density	Magnetic
Transfer momentum q_X	$\boldsymbol{k}_1 + \boldsymbol{k}_2$	$\boldsymbol{k}_1 - \boldsymbol{k}_3$	$\boldsymbol{k}_1 - \boldsymbol{k}_4$
Momentum k_X	$-\boldsymbol{k}_2$	$\boldsymbol{k}_3$	$\boldsymbol{k}_4$
Momentum k_X'	$-\boldsymbol{k}_4$	$\boldsymbol{k}_2$	$\boldsymbol{k}_2$
Flow contribution	τ^{pp}	$\tau^{\mathrm{ph,d}}$	$\tau^{\mathrm{ph,cr}}$

2.2.2 Derivation

We will now derive the TUFRG flow equations. As laid out before, the transfer momentum $\boldsymbol{q}$ is of higher relevance, since its value determines the possible onset of an instability. Therefore, we want to keep track of this momentum and expand the other two momenta $\boldsymbol{k}, \boldsymbol{k'}$ into form factors:

$$\Phi^{X,\Lambda}(\boldsymbol{q}; \boldsymbol{k}, \boldsymbol{k'}) = \sum_{l,l'} X^{l,l'}(\boldsymbol{q}) \times f_l^*(\boldsymbol{k}) f_{l'}(\boldsymbol{k'}) \tag{2.66}$$

$$X^{l,l'}(\boldsymbol{q}) = \int_{\boldsymbol{k},\boldsymbol{k'}} \Phi^{X,\Lambda}(\boldsymbol{q}, \boldsymbol{k}, \boldsymbol{k'}) \times f_l(\boldsymbol{k}) f_{l'}^*(\boldsymbol{k'}) \tag{2.67}$$

where the momentum integral includes the normalization with respect to the Brillouin zone, $\int_{\boldsymbol{k}} = A_{\mathrm{BZ}}^{-1} \int d\boldsymbol{k}$. There are several choices for selecting a set of form factors $f_l(\boldsymbol{k})$ which only have to fulfill a unity condition:

$$\delta(\boldsymbol{p} - \boldsymbol{k}) = \sum_l f_l^*(\boldsymbol{p}) f_l(\boldsymbol{k}) \tag{2.68}$$

$$\delta_{l,l'} = \int_{\boldsymbol{k}} f_l(\boldsymbol{k}) f_{l'}^*(\boldsymbol{k}). \tag{2.69}$$

Declaring our specific choice of form factors later, the derivation is kept general for now. We will guide through the derivation of the TUFRG equation only for the particle-particle channel now, since the derivation for the other two channels work analogously. The general strategy is as follows: we will derive a flow equation for the form factor dependent channels $X^{l,l'}(\boldsymbol{q})$ by using the channel decomposition Eq. (2.63). For that purpose, we will use the insertion of unities expressed by form factors Eq. (2.68). For the particle-particle diagram, we start therefore by taking the derivative of Eq. (2.67) with respect to the flow parameter Λ:

$$\frac{d}{d\Lambda}P^{l,l'}(\boldsymbol{q}) = \int\limits_{\boldsymbol{k},\boldsymbol{k'}} \frac{d}{d\Lambda}\Phi^{P,\Lambda}(\boldsymbol{q};\boldsymbol{k},\boldsymbol{k'}) \times f_l(\boldsymbol{k}) f^*_{l'}(\boldsymbol{k'}). \tag{2.70}$$

By the channel decomposition Eq. (2.63) , the derivative of the $\Phi^{P,\Lambda}$ channel can be exchanged with the particle-particle diagram τ^{pp}. Adjusting the respective arguments eventually leads to:

$$\begin{aligned}\frac{d}{d\Lambda}\Phi^{P,\Lambda}(\boldsymbol{q},\boldsymbol{k},\boldsymbol{k'}) &= \tau^{\text{pp}}(\boldsymbol{q}+\boldsymbol{k},-\boldsymbol{k},\boldsymbol{q}+\boldsymbol{k'},-\boldsymbol{k'}) \\ &= \int_p \frac{d}{d\Lambda}\left[G^{0,\Lambda}(i\omega_p,\boldsymbol{p}+\boldsymbol{q})G^{0,\Lambda}(-i\omega_p,-\boldsymbol{p})\right] \\ &\times V^{\Lambda}(\boldsymbol{q}+\boldsymbol{k},-\boldsymbol{k},\boldsymbol{q}+\boldsymbol{p}) \\ &\times V^{\Lambda}(\boldsymbol{q}+\boldsymbol{p},-\boldsymbol{p},\boldsymbol{q}+\boldsymbol{k'}).\end{aligned} \tag{2.71}$$

At this point, we are going to decouple the vertices momentum-wise from the bubble by including a δ-function for the connecting momentum $\boldsymbol{p}$:

$$\begin{aligned}\frac{d}{d\Lambda}\Phi^{P,\Lambda}(\boldsymbol{q};\boldsymbol{k},\boldsymbol{k'}) &= \tau^{\text{pp}}(\boldsymbol{q}+\boldsymbol{k},-\boldsymbol{k},\boldsymbol{q}+\boldsymbol{k'},-\boldsymbol{k'}) \\ &= \int_p \frac{d}{d\Lambda}\left[G^{0,\Lambda}(i\omega_p,\boldsymbol{p}+\boldsymbol{q})G^{0,\Lambda}(-i\omega_p,-\boldsymbol{p})\right] \\ &\times \int_{\tilde{\boldsymbol{k}}} V^{\Lambda}(\boldsymbol{q}+\boldsymbol{k},-\boldsymbol{k},\boldsymbol{q}+\tilde{\boldsymbol{k}}) \times \delta(\tilde{\boldsymbol{k}}-\boldsymbol{p}) \\ &\times \int_{\tilde{\boldsymbol{k}'}} V^{\Lambda}(\boldsymbol{q}+\boldsymbol{p},-\tilde{\boldsymbol{k}'},\boldsymbol{q}+\boldsymbol{k'}) \times \delta(\boldsymbol{p}-\tilde{\boldsymbol{k}'}).\end{aligned} \tag{2.72}$$

Now the two δ-functions are expressed via form factors Eq. (2.68):

$$\begin{aligned}\frac{d}{d\Lambda}\Phi^{P,\Lambda}(\boldsymbol{q},\boldsymbol{k},\boldsymbol{k'}) &= \tau^{\text{pp}}(\boldsymbol{q}+\boldsymbol{k},-\boldsymbol{k},\boldsymbol{q}+\boldsymbol{k'},-\boldsymbol{k'}) \\ &= \int_p \frac{d}{d\Lambda}\left[G^{0,\Lambda}(i\omega_p,\boldsymbol{p}+\boldsymbol{q})G^{0,\Lambda}(-i\omega_p,-\boldsymbol{p})\right] \\ &\times \int_{\tilde{\boldsymbol{k}}} V^{\Lambda}(\boldsymbol{q}+\boldsymbol{k},-\boldsymbol{k},\boldsymbol{q}+\tilde{\boldsymbol{k}}) \times \sum_{l_1} f^*_{l_1}(\tilde{\boldsymbol{k}}) f_{l_1}(\boldsymbol{p}) \\ &\times \int_{\tilde{\boldsymbol{k}'}} V^{\Lambda}(\boldsymbol{q}+\boldsymbol{p},-\tilde{\boldsymbol{k}'},\boldsymbol{q}+\boldsymbol{k'}) \times \sum_{l_2} f^*_{l_2}(\boldsymbol{p}) f_{l_2}(\tilde{\boldsymbol{k}'}).\end{aligned} \tag{2.73}$$

A last rearrangement yields:

$$\begin{aligned}\frac{d}{d\Lambda}\Phi^{P,\Lambda}(\boldsymbol{q},\boldsymbol{k},\boldsymbol{k'}) &= \tau^{\text{pp}}(\boldsymbol{q}+\boldsymbol{k},-\boldsymbol{k},\boldsymbol{q}+\boldsymbol{k'},-\boldsymbol{k'}) \\ &= \sum_{l_1,l_2}\int_p \frac{d}{d\Lambda}\left[G^{0,\Lambda}(i\omega_p,\boldsymbol{p}+\boldsymbol{q})G^{0,\Lambda}(-i\omega_p,-\boldsymbol{p})\right] f_{l_1}(\boldsymbol{p}) f^*_{l_2}(\boldsymbol{p}) \\ &\times \int_{\tilde{\boldsymbol{k}}} V^{\Lambda}(\boldsymbol{q}+\boldsymbol{k},-\boldsymbol{k},\boldsymbol{q}+\tilde{\boldsymbol{k}}) \times f^*_{l_1}(\tilde{\boldsymbol{k}}) \\ &\times \int_{\tilde{\boldsymbol{k}'}} V^{\Lambda}(\boldsymbol{q}+\boldsymbol{p},-\tilde{\boldsymbol{k}'},\boldsymbol{q}+\boldsymbol{k'}) \times f_{l_2}(\tilde{\boldsymbol{k}'}).\end{aligned} \tag{2.74}$$

The final step for the derivation consists of plugging expression Eq. (2.74) back into Eq. (2.70) which (after a shifting around the expressions) results into:

$$\begin{aligned}\frac{d}{d\Lambda}P^{l,l'}(\boldsymbol{q}) = \\ &= \sum_{l_1,l_2}\Bigg\{ \\ &\int_p \frac{d}{d\Lambda}\left[G^{0,\Lambda}(i\omega_p,\boldsymbol{p}+\boldsymbol{q})G^{0,\Lambda}(-i\omega_p,-\boldsymbol{p})\right] f_{l_1}(\boldsymbol{p})f^*_{l_2}(\boldsymbol{p}) \\ &\times \int_{\boldsymbol{k},\tilde{\boldsymbol{k}}} V^{\Lambda}(\boldsymbol{q}+\boldsymbol{k},-\boldsymbol{k},\boldsymbol{q}+\tilde{\boldsymbol{k}})\times f_l(\boldsymbol{k})f^*_{l_1}(\tilde{\boldsymbol{k}}) \\ &\times \int_{\tilde{\boldsymbol{k}}',\boldsymbol{k}'} V^{\Lambda}(\boldsymbol{q}+\boldsymbol{p},-\tilde{\boldsymbol{k}}',\boldsymbol{q}+\boldsymbol{k}')\times f_{l_2}(\tilde{\boldsymbol{k}}')f^*_{l'}(\boldsymbol{k}')\Bigg\}. \end{aligned} \tag{2.75}$$

Since the length of this equation is a bit unwieldy, we will cast it into a more concise form:

$$\frac{d}{d\Lambda}P^{l,l'}(\boldsymbol{q}) = \sum_{l_1,l_2} V^P_{l,l_1}(\boldsymbol{q})\dot{B}^-_{l_1,l_2}(\boldsymbol{q})V^P_{l',l_2}(\boldsymbol{q}) \tag{2.76}$$

where we defined:

$$\dot{B}^-_{l,l'}(\boldsymbol{q}) = \int_p \frac{d}{d\Lambda}\left[G^{0,\Lambda}(i\omega_p,\boldsymbol{p}+\boldsymbol{q})G^{0,\Lambda}(-i\omega_p,-\boldsymbol{p})\right] f_l(\boldsymbol{p})f^*_{l'}(\boldsymbol{p}), \tag{2.77}$$

$$V^P_{l,l'}(\boldsymbol{q}) = \int_{\boldsymbol{k},\boldsymbol{k}'} V^{\Lambda}(\boldsymbol{q}+\boldsymbol{k},-\boldsymbol{k},\boldsymbol{q}+\boldsymbol{k}')\times f_l(\boldsymbol{k})f^*_{l'}(\boldsymbol{k}'). \tag{2.78}$$

In a complete analogous way, we can repeat this procedure for the particle-hole diagrams, resulting into:

$$\begin{aligned}\frac{d}{d\Lambda}D^{l,l'}(\boldsymbol{q}) = &\sum_{l_1,l_2}\Big[V^C_{l,l_1}(\boldsymbol{q})\dot{B}^+_{l_1,l_2}(\boldsymbol{q})V^D_{l',l_2}(\boldsymbol{q}) + V^D_{l,l_1}(\boldsymbol{q})\dot{B}^+_{l_1,l_2}(\boldsymbol{q})V^C_{l',l_2}(\boldsymbol{q}) \\ &- 2V^D_{l,l_1}(\boldsymbol{q})\dot{B}^+_{l_1,l_2}(\boldsymbol{q})V^D_{l',l_2}(\boldsymbol{q})\Big], \end{aligned} \tag{2.79}$$

$$\frac{d}{d\Lambda}C^{l,l'}(\boldsymbol{q}) = \sum_{l_1,l_2} V^C_{l,l_1}(\boldsymbol{q})\dot{B}^+_{l_1,l_2}(\boldsymbol{q})V^C_{l',l_2}(\boldsymbol{q}), \tag{2.80}$$

where we respectively defined:

$$\dot{B}^+_{l,l'}(\boldsymbol{q}) = \int_p \frac{d}{d\Lambda}\left[G^{0,\Lambda}(i\omega_p,\boldsymbol{p}+\boldsymbol{q})G^{0,\Lambda}(i\omega_p,\boldsymbol{p})\right] f_l(\boldsymbol{p})f^*_{l'}(\boldsymbol{p}), \tag{2.81}$$

$$V^D_{l,l'}(\boldsymbol{q}) = \int_{\boldsymbol{k},\boldsymbol{k}'} V^{\Lambda}(\boldsymbol{q}+\boldsymbol{k},\boldsymbol{k}',\boldsymbol{k})\times f_l(\boldsymbol{k})f^*_{l'}(\boldsymbol{k}'), \tag{2.82}$$

$$V^C_{l,l'}(\boldsymbol{q}) = \int_{\boldsymbol{k},\boldsymbol{k}'} V^{\Lambda}(\boldsymbol{q}+\boldsymbol{k},\boldsymbol{k}',\boldsymbol{q}+\boldsymbol{k}')\times f_l(\boldsymbol{k})f^*_{l'}(\boldsymbol{k}'). \tag{2.83}$$

We will call $V^X_{l,l'}(\boldsymbol{q})$ the **cross-channel projections** of the respective channels and $\dot{B}^{\pm}_{l,l'}(\boldsymbol{q})$ the form factor dependent particle-particle (-) and particle-hole (+) **bubble integration**. At this point we should employ a brief recapitulation:

- We analyzed the diagrams of the "ordinary" flow Eqs. (2.45)-(2.47) and were able to interpret those physically by identifying the particle-particle and particle-hole bubble in the diagrams. A comparison with some paradigmatic interaction Hamiltonians led us to the conclusion that the three terms can be understood as contributions to a superconducting (τ^{pp}), CDW ($\tau^{\mathrm{ph,d}}$) and SDW ($\tau^{\mathrm{ph,cr}}$) interaction. Therefore, an instability in a given system towards one of these phases should manifest itself in of the three respective channels, since the divergence of the bubble plays a crucial role in this emergence (as discussed in section 1.1).

- Motivated by these interpretations, we employed the channel decomposition Eq. (2.62) such that the vertex V^{Λ} is decomposed into the three interaction types discussed before. The parametrization of these channels is chosen a way that exactly these interaction types can be reconstructed by insertion in Eq. (2.48). We then proceeded and imposed three differential equations, relating each channel to its corresponding diagram Eq. (2.63).

- Keeping track of the transfer momentum $\boldsymbol{q}$, we expanded the other momenta into form factors since they only play a minor role in the onset of an instability. The form factors can be chosen arbitrarily as long as they form a unity in momentum and form factor space Eqs.(2.68), (2.69). Using these definitions, we were able to derive the TUFRG flow equations for the form factor dependent channels $X^{l,l'}(\boldsymbol{q})$.

- Notice that this decomposition does not violate the feature of FRG in omitting feedback of different diagrams to each other. The cross-channel projections $V^{X}_{l,l'}(\boldsymbol{q})$ still depend on the original interaction V^{Λ} and therefore the feedback of the channels onto each other is still fully present.

Now we may ask the question: **Which advantage was achieved by this reformulation?** The new flow equations (Eqs. (2.76),(2.79) and (2.80)) do not have any numerical advantage on a formal level. The former flow equations were defined by three momenta, therefore for N_k chosen momenta to sample a Brillouin zone the amount of equations to solve would scale with N_k^3. The new flow equations depend on one momentum $\boldsymbol{q}$ and two form factor arguments l, l', therefore scaling with $N_{\boldsymbol{q}} \times N_l^2$. The numerical advantage of this method is now achieved by **truncating the unity**, i.e. the sums $\sum_l$ will eventually only cover a small set of form factors such that N_l^2 becomes relatively small, allowing for a high scaling of momenta $N_{\boldsymbol{q}}$. Naturally, this constitutes an approximation, since the unity conditions Eqs. (2.68) and (2.69) are only correct by including an infinite amount of form factors.

We will see in the next section how a specific choice of form factors delivers a substantial physical picture to understand the effect of the inclusion of form factors in the flow equations. This will grant us an interpretable rational for employing the truncation of the form factors.

2.2.3 Form factors

As previously shown, any well behaved set of functions $f_l(\boldsymbol{k})$ can be selected as form factors, as long as this set confirms the unity conditions Eqs. (2.68),(2.69). In the most pragmatic way, the simplest choice of these form factors are therefore **plane waves**:

$$f_l(\boldsymbol{k}) = e^{i\boldsymbol{k}\boldsymbol{R}_l} \tag{2.84}$$

where $\boldsymbol{R}_l$ is an real space lattice vector of the lattice, i.e. in our case of the triangular lattice. This choice has three major advantages.

- We will show that the idea of truncating the form factor sum can be understood as truncating long-distance effects which should have only weak impact on the emerging short-range physics.

- The cross-channel projections can be rewritten in a form which is numerically much easier to handle.

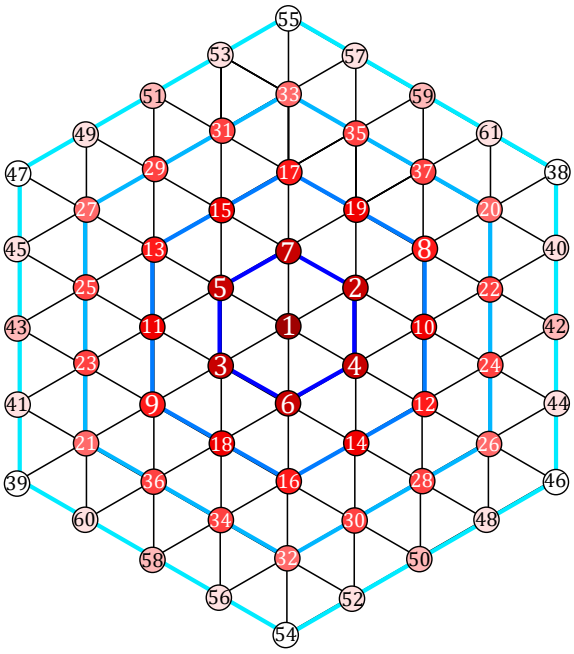

Figure 2.6: **Numeration of real space vectors in the triangular lattice:** The red shades indicate the distance to the origin. Throughout this thesis, $N_l = 61$ is the highest amount of form factors which is included.

- In contrast to form factors which are designed after specific symmetries (for example used in studies for the square lattice in [36, 35]), the plane waves will act as an unbiased choice with respect to the emergent symmetry of the gap function as long as form factors of sufficient range are included.

At first, we will elaborate on the physical interpretation of the form factors. For the numeration of the form factors, we will name the lattice sites as already chosen in in section 1.2 where the lattice harmonics of the gap equations were derived. The two basis vectors of the triangular lattice in this numeration coincide with $l = 2$ and $l = 4$:

$$\boldsymbol{R}_{2,4} = \boldsymbol{a}_{1,2} = a/2\left(\sqrt{3}, \pm 1\right)^T. \tag{2.85}$$

To study the effect of the form factors, we consider again the pairing interaction Eq. (2.49) as an example and express the channel $\Phi^{P,\Lambda}$ by its form factor counterpart:

$$\begin{aligned}
S^P[\bar{\psi},\psi] &= \int_{\boldsymbol{q},\boldsymbol{k},\boldsymbol{k'}} \Phi^P(\boldsymbol{q};\boldsymbol{k},\boldsymbol{k'}) \sum_{\sigma,\sigma'} \bar{\psi}_\sigma(\boldsymbol{q}+\boldsymbol{k})\bar{\psi}_{\sigma'}(-\boldsymbol{k})\psi_{\sigma'}(-\boldsymbol{k'})\psi_\sigma(\boldsymbol{q}+\boldsymbol{k'}) \\
&\overset{(2.66)}{=} \int_{\boldsymbol{q},\boldsymbol{k},\boldsymbol{k'}} \left(\sum_{l,l'} P^{l,l'}(\boldsymbol{q}) \times f_l^*(\boldsymbol{k}) f_{l'}(\boldsymbol{k'})\right) \sum_{\sigma,\sigma'} \bar{\psi}_\sigma(\boldsymbol{q}+\boldsymbol{k})\bar{\psi}_{\sigma'}(-\boldsymbol{k})\psi_{\sigma'}(-\boldsymbol{k'})\psi_\sigma(\boldsymbol{q}+\boldsymbol{k'}) \\
&= \int_{\boldsymbol{q}} \sum_{\sigma,\sigma'} \sum_{l,l'} P^{l,l'}(\boldsymbol{q}) \times \underbrace{\left(\int_{\boldsymbol{k}} \bar{\psi}_\sigma(\boldsymbol{q}+\boldsymbol{k})\bar{\psi}_{\sigma'}(-\boldsymbol{k}) f_l^*(\boldsymbol{k})\right)}_{=:\left(F^l_{\sigma'\sigma}(\boldsymbol{q})\right)^\dagger} \\
&\qquad \times \underbrace{\left(\int_{\boldsymbol{k'}} \psi_{\sigma'}(-\boldsymbol{k'})\psi_\sigma(\boldsymbol{q}+\boldsymbol{k'}) f_{l'}(\boldsymbol{k'})\right)}_{=:F^{l'}_{\sigma'\sigma}(\boldsymbol{q})}
\end{aligned} \tag{2.86}$$

Now, the pairing interaction decomposes into two fermion bilinears $(F^{l'}_{\sigma'\sigma}(\boldsymbol{q}))^{(\dagger)}$ which are decoupled in momentum space regarding $\boldsymbol{k}$ and $\boldsymbol{k'}$. The effect of the form factors become apparent by transforming these bilinears into real space:

$$\begin{aligned} F^{l'}_{\sigma'\sigma}(\boldsymbol{q}) &= \int_{\boldsymbol{k'}} \psi_{\sigma'}(-\boldsymbol{k'})\psi_{\sigma}(\boldsymbol{q}+\boldsymbol{k'})f_{l'}(\boldsymbol{k'}) \\ &\overset{\text{Fourier}}{=} \sum_{\boldsymbol{R}} \psi_{\sigma'}(\boldsymbol{R}+\boldsymbol{R}'_l)\psi_{\sigma}(\boldsymbol{R}) \times e^{i\boldsymbol{q}\boldsymbol{R}}. \end{aligned} \tag{2.87}$$

This reveals that $F^{l'}_{\sigma'\sigma}(\boldsymbol{q})$ sums over all fermion bilinears which are connected by the lattice vector $\boldsymbol{R}_{l'}$. Therefore, by the sum $\sum_l$ in Eq. (2.86), all effects of fermion bilinears with distance vectors $\boldsymbol{R}_l$ are included. So, a truncation of this very sum excludes effects of fermions of this distance. This serves an opportunity to develop a specific rational in truncating this sum. We will assume that the emergent physics is mainly dependent on the short-range effects of the fermions. In consequence, we will truncate form factors describing effects of larger distances, meaning that we will include form factors up to specific distance shells. In Fig. 2.6 these shells are indicated by the blue hexagons. The 0th shell does only include one form factor $\boldsymbol{R}_1 = (0,0)^T$ which we will call the **on-site form factor**. The next shell includes all form factors up to $l = 7$, which are the nearest-neighbour form factors. The second shell includes in total all form factors from $l = 1$ to $l = 19$ which includes on-site, nearest-neighbour, second nearest-neighbour and third nearest-neighbour form factors. We want to stress here that we always select the form factors in terms of the **hexagonal shell** and not the total distance e.g. second- or third-nearest neighbour. The reason for this choice will become apparent when we discuss the symmetries of the bubble integrations in section 2.3.2. We will call these hexagon shells N_s with N_l form factors. The following table specifies the details of those shells. As a second

N_s	N_l	Corresponding nearest-neighbor shells
0	1	on-site only
1	7	0th - 1st nearest-neighbors
2	19	0th - 3rd nearest-neighbors
3	37	0th - 5th nearest-neighbors
4	61	0th - 8th nearest-neighbors

aspect, we want to present how the plane-wave form factors simplify the cross-channel projections Eqs. (2.78),(2.82) and (2.83). As before, we will show this for the P channel only since it applies to the other channels in an analogue way. Starting with Eq. (2.78), we will use the channel decomposition Eq. (2.62) to break the cross-channel projection into four parts:

$$\begin{aligned} V^P_{l,l'}(\boldsymbol{q}) &= \int_{\boldsymbol{k},\boldsymbol{k'}} V^{\Lambda}(\boldsymbol{q}+\boldsymbol{k},-\boldsymbol{k},\boldsymbol{q}+\boldsymbol{k'}) \times f_l(\boldsymbol{k}) f^*_{l'}(\boldsymbol{k'}) \\ &\overset{(2.62)}{=} \int_{\boldsymbol{k},\boldsymbol{k'}} V^{0}(\boldsymbol{q}+\boldsymbol{k},-\boldsymbol{k},\boldsymbol{q}+\boldsymbol{k'}) \times f_l(\boldsymbol{k}) f^*_{l'}(\boldsymbol{k'}) \\ &\quad + \int_{\boldsymbol{k},\boldsymbol{k'}} \Phi^{P,\Lambda}(\boldsymbol{q},\boldsymbol{k},\boldsymbol{k'}) \times f_l(\boldsymbol{k}) f^*_{l'}(\boldsymbol{k'}) \\ &\quad + \int_{\boldsymbol{k},\boldsymbol{k'}} \Phi^{D,\Lambda}(\boldsymbol{k}-\boldsymbol{k'},\boldsymbol{q}+\boldsymbol{k'},-\boldsymbol{k}) \times f_l(\boldsymbol{k}) f^*_{l'}(\boldsymbol{k'}) \\ &\quad + \int_{\boldsymbol{k},\boldsymbol{k'}} \Phi^{C,\Lambda}(\boldsymbol{q}+\boldsymbol{k}+\boldsymbol{k'},-\boldsymbol{k'},-\boldsymbol{k}) \times f_l(\boldsymbol{k}) f^*_{l'}(\boldsymbol{k'}) \\ &= V^{0,P}_{l,l'}(\boldsymbol{q}) + P^{l,l'}(\boldsymbol{q}) + V^{D\to P}_{l,l'}(\boldsymbol{q}) + V^{C\to P}_{l,l'}(\boldsymbol{q}). \end{aligned} \tag{2.88}$$

Each of the four terms includes the projection of the components of the channel decomposition onto the P channel. $V_{l,l'}^{0,P}(\boldsymbol{q})$ contains the projection of the initial conditions onto the P channel. It is no surprise that the projection of $\Phi^{P,\Lambda}$ onto itself will just result again in the P channel again: $P^{l,l'}(\boldsymbol{q})$. The other two terms are the projection of the D and C channel onto the P channel and the double integration over the Brillouin zone can be simplified by using the plane wave form factors. We will guide through $V_{l,l'}^{D\to P}(\boldsymbol{q})$ to demonstrate this. By taking the derived expression and expanding $\Phi^{D,\Lambda}$ again in its form factor depending shape:

$$\begin{aligned} V_{l,l'}^{D\to P}(\boldsymbol{q}) &= \int\limits_{\boldsymbol{k},\boldsymbol{k'}} \Phi^{D,\Lambda}(\boldsymbol{k}-\boldsymbol{k'},\boldsymbol{q}+\boldsymbol{k'},-\boldsymbol{k}) \times f_l(\boldsymbol{k}) f_{l'}^*(\boldsymbol{k'}) \\ &= \int\limits_{\boldsymbol{k},\boldsymbol{k'}} \left(\sum_{\tilde{l},\tilde{l'}} D^{\tilde{l},\tilde{l'}}(\boldsymbol{k}-\boldsymbol{k'}) f_{\tilde{l}}^*(\boldsymbol{q}+\boldsymbol{k'}) f_{\tilde{l'}}(-\boldsymbol{k}) \right) \times f_l(\boldsymbol{k}) f_{l'}^*(\boldsymbol{k'}). \end{aligned} \tag{2.89}$$

At this point, we define the Fourier transform of the channels as:

$$\tilde{X}^{l,l}(\boldsymbol{R}_l) = \int_{\boldsymbol{p}} X^{l,l'}(\boldsymbol{p}) \times e^{-i\boldsymbol{p}\boldsymbol{R}_l}, \quad X = P, C, D. \tag{2.90}$$

We apply the Fourier transform, express the form factors explicitly in their plane wave form and order the exponentials with respect to the momenta:

$$V_{l,l'}^{D\to P}(\boldsymbol{q}) = \int\limits_{\boldsymbol{k},\boldsymbol{k'}} \sum_{\tilde{l},\tilde{l'}} \sum_{L} \tilde{D}^{\tilde{l},\tilde{l'}}(\boldsymbol{R}_l) \times e^{i\boldsymbol{k}(\boldsymbol{R}_L - \boldsymbol{R}_{\tilde{l'}} + \boldsymbol{R}_l)} \times e^{i\boldsymbol{k'}(-\boldsymbol{R}_L - \boldsymbol{R}_{\tilde{l}} + \boldsymbol{R}_{l'})} \times e^{-i\boldsymbol{q}\boldsymbol{R}_{\tilde{l'}}}, \tag{2.91}$$

performing the integrals will reveal δ-functions such that the equation eventually yields:

$$V_{l,l'}^{D\to P}(\boldsymbol{q}) = \sum_{L} \tilde{D}^{L,-L+l-l'}(-\boldsymbol{R}_{l'} - \boldsymbol{R}_L) \times e^{-i\boldsymbol{q}\boldsymbol{R}_L}. \tag{2.92}$$

The additions and subtractions of the form factor indices imply the sum of the lattice vectors belonging to these form factors, e.g. $l - l' - L \to \boldsymbol{R}_l - \boldsymbol{R}_{l'} - \boldsymbol{R}_L = \boldsymbol{R}_M \to M$. Therefore, Eq. (2.92) highlights the computational advantage of the plane wave form factors. Initially, we had to perform a double integral over the Brillouin zone. Now, for a fixed pair of l, l', we only have to perform a single summation over form factors $\sum_L$. Considering that we will truncate this sum by only taking at maximum 61 form factors into account, this procedure vastly simplifies the calculation of the cross-channel projections. We have to repeat this derivation for all three channels by including the channel decomposition such that in total we will end up with:

$$V_{l,l'}^{P}(\boldsymbol{q}) = V_{l,l'}^{0,P}(\boldsymbol{q}) + P^{l,l}(\boldsymbol{q}) + V_{l,l'}^{D\to P}(\boldsymbol{q}) + V_{l,l'}^{C\to P}(\boldsymbol{q}), \tag{2.93}$$

$$V_{l,l'}^{D\to P}(\boldsymbol{q}) = \sum_{L} \tilde{D}^{L,-L+l-l'}(-\boldsymbol{R}_{l'} - \boldsymbol{R}_L) \times e^{-i\boldsymbol{q}\boldsymbol{R}_L}, \tag{2.94}$$

$$V_{l,l'}^{C\to P}(\boldsymbol{q}) = \sum_{L} \tilde{C}^{L,-L+l+l'}(-\boldsymbol{R}_L + \boldsymbol{R}_{l'}) \times e^{-i\boldsymbol{q}(\boldsymbol{R}_L - \boldsymbol{R}_{l'})}. \tag{2.95}$$

For the D channel:

$$V_{l,l'}^{D}(\boldsymbol{q}) = V_{l,l'}^{0,D}(\boldsymbol{q}) + D^{l,l}(\boldsymbol{q}) + V_{l,l'}^{P\to D}(\boldsymbol{q}) + V_{l,l'}^{C\to D}(\boldsymbol{q}), \tag{2.96}$$

$$V_{l,l'}^{P\to D}(\boldsymbol{q}) = \sum_{L} \tilde{P}^{L,L-l-l'}(-\boldsymbol{R}_l) \times e^{-i\boldsymbol{q}(\boldsymbol{R}_L - \boldsymbol{R}_{l'})}, \tag{2.97}$$

$$V_{l,l'}^{C\to D}(\boldsymbol{q}) = \sum_{L} \tilde{C}^{L,L-l+l'}(-\boldsymbol{R}_l) \times e^{-i\boldsymbol{q}\boldsymbol{R}_L}, \tag{2.98}$$

and for the C channel:

$$V^{C}_{l,l'}(\boldsymbol{q}) = V^{0,C}_{l,l'}(\boldsymbol{q}) + C^{l,l}(\boldsymbol{q}) + V^{P\to C}_{l,l'}(\boldsymbol{q}) + V^{D\to C}_{l,l'}(\boldsymbol{q}), \tag{2.99}$$

$$V^{P\to C}_{l,l'}(\boldsymbol{q}) = \sum_{L} \tilde{P}^{L,-L+l+l'}(-\boldsymbol{R}_L + \boldsymbol{R}_{l'}) \times e^{-i\boldsymbol{q}(\boldsymbol{R}_L - \boldsymbol{R}'_l)}, \tag{2.100}$$

$$V^{D\to C}_{l,l'}(\boldsymbol{q}) = \sum_{L} \tilde{D}^{L,L-l+l'}(-\boldsymbol{R}_l) \times e^{-i\boldsymbol{q}\boldsymbol{R}_L}. \tag{2.101}$$

2.2.4 Regulator

Until now we kept the exact nature of the scale parameter Λ abstract. The derivative of the form factor dependent bubble integrations can be concluded as:

$$\dot{B}^{\pm}_{l,l'}(\boldsymbol{q}) = \int_p \frac{d}{d\Lambda}\left[G^{0,\Lambda}(i\omega_p, \boldsymbol{p}+\boldsymbol{q})G^{0,\Lambda}(\pm i\omega_p, \pm\boldsymbol{p})\right] f_l(\boldsymbol{p}) f^*_{l'}(\boldsymbol{p}) \tag{2.102}$$

In fact, there are many different shapes and forms to introduce the necessary regularization scheme for the propagator $G^{0,\Lambda}$ which we introduced in section 2.1:

$$G^{0,\Lambda} = \begin{cases} G^0 & \Lambda \to 0 \\ 0 & \Lambda \to \Lambda_{\mathrm{UV}} \end{cases}$$

An intuitive way of introducing the correct behaviour in these limits is employed by using a step function in momentum space:

$$G^{0,\Lambda}(i\omega_p, \boldsymbol{p}) = \Theta(\xi(\boldsymbol{p}) - \Lambda)\frac{1}{i\omega - \xi(\boldsymbol{p})}, \tag{2.103}$$

where the Heavy-side function can also be exchanged by a smooth cutoff as long as the correct behavior in the limits is secured. The derivative $\frac{d}{d\Lambda}$ acting on the bare propagator (equipped with this cutoff function) will implement a scheme resembling the Wilsonian momentum shell integration since performing this derivative explicitly yields:

$$\frac{d}{d\Lambda}G^{0,\Lambda}(i\omega_p, \boldsymbol{p}) = \frac{d\Theta(|\xi(\boldsymbol{p})| - \Lambda)}{d\Lambda}\frac{1}{i\omega_p - \xi(\boldsymbol{p})} \propto \delta(|\xi(\boldsymbol{p})| - \Lambda)G^0(i\omega_p, \boldsymbol{p}), \tag{2.104}$$

such that the bare propagator does only „survive" if the energy corresponding to the momentum $\xi(\boldsymbol{p})$ equals the scale Λ. Therefore, by solving the flow equation starting from the bandwidth $W = \Lambda_{\mathrm{UV}}$ (since all energies larger than W will never satisfy the argument of the δ-function and are therefore irrelevant), downwards to $\Lambda \to 0$, the effects of each scale Λ are included, momentum shell for momentum shell. Although this implementation is intuitively pleasing, it is flawed in a way that fluctuations towards ferromagnetism are artificially suppressed [43].

Fortunately, there are other cutoff schemes which circumvent this problem. We want to discuss briefly two of those. One of these choices is given by implementing the regularization with respect to the Matsubara frequencies instead of the momenta which is called the **Ω-scheme** [46]:

$$G^{0,\Omega}(i\omega_p, \boldsymbol{p}) = \frac{\omega_p^2}{\omega_p^2 + \Omega^2}\frac{1}{i\omega_p - \xi(\boldsymbol{p})}, \tag{2.105}$$

where the scale is relabeled to $\Lambda \to \Omega$. While this scheme is not prone to the artificial suppression of fluctuations, it comes with the technical disadvantage that the Matsubara summation in Eq. (2.102) cannot be calculated in a simple manner anymore, since the two propagators will develop non-trivial poles in the complex plane due to the structure of the regularization function.

A third possibility is given by choosing the temperature as flow parameter, called the T-flow scheme [43]. Let us consider a typical action with translational symmetry where we now explicitly write down the temperature scaling of the terms stemming, from the Matsubara summations:

$$\begin{aligned} S =& A_{\mathrm{BZ}}^{-1} \int_{\boldsymbol{k}} T \sum_{\omega} \sum_{\sigma} \left(i\omega - \xi_\sigma(\boldsymbol{k})\right) \bar{\psi}_\sigma(k)\psi_\sigma(k) \\ &+ A_{\mathrm{BZ}}^{-3} \int_{\boldsymbol{k}_1,\boldsymbol{k}_2,\boldsymbol{k}_3} T^3 \sum_{\omega_1,\omega_2,\omega_3} V(k_1,k_2,k_3) \times \sum_{\sigma,\sigma'} \bar{\psi}_\sigma(k_1)\bar{\psi}_{\sigma'}(k_2)\psi_{\sigma'}(k_1+k_2-k_3)\psi_\sigma(k_3). \end{aligned} \tag{2.106}$$

For a proper usage of the temperature T as a flow parameter, the interaction term should not directly depend on T. This can be achieved by the rescaling of the fields:

$$\psi_\sigma(k) = \eta_\sigma(k) \times T^{-3/4}, \tag{2.107}$$

such that the interaction becomes temperature independent and the bare propagator scales with $T^{-1/2}$:

$$\begin{aligned} S =& A_{\mathrm{BZ}}^{-1} \int_{\boldsymbol{k}} T^{-1/2} \sum_{\omega} \sum_{\sigma} \left(i\omega - \xi_\sigma(\boldsymbol{k})\right) \bar{\eta}_\sigma(k)\eta_\sigma(k) \\ &+ A_{\mathrm{BZ}}^{-3} \int_{\boldsymbol{k}_1,\boldsymbol{k}_2,\boldsymbol{k}_3} \sum_{\omega_1,\omega_2,\omega_3} V(k_1,k_2,k_3) \times \sum_{\sigma,\sigma'} \bar{\eta}_\sigma(k_1)\bar{\eta}_{\sigma'}(k_2)\eta_{\sigma'}(k_1+k_2-k_3)\eta_\sigma(k_3). \end{aligned} \tag{2.108}$$

Honerkamp and Salmhofer showed [43] that by replacing the scale-derivative accordingly, this scheme indeed fulfills the regularization scheme needed for the FRG implementation. In practice, this scheme is formulated as:

$$\begin{aligned} \frac{d}{d\Lambda} \rightarrow& \quad \frac{d}{dT}, \\ G^{0,\Lambda}(i\omega_p,\boldsymbol{p}) \rightarrow& \quad G^{0,T}(i\omega_p,\boldsymbol{p}) = \frac{T^{1/2}}{i\omega_p - \xi(\boldsymbol{p})}, \end{aligned} \tag{2.109}$$

$$\begin{aligned} S^{0,\Lambda}(i\omega_p,\boldsymbol{p}) \rightarrow& \quad S^{0,T}(i\omega_p,\boldsymbol{p}) = -G^{0,T}(i\omega_p,\boldsymbol{p}) \left(\frac{d}{dT}\left(G^{0,T}(i\omega_p,\boldsymbol{p})\right)^{-1}\right) G^{0,T}(i\omega_p,\boldsymbol{p}) \\ &= -T^{-1/2} \frac{i\omega_p - \xi(\boldsymbol{p})}{(i\omega_p + \xi(\boldsymbol{p}))^2}. \end{aligned} \tag{2.110}$$

Here it should be noted that for the result of the single-scale propagator one also has to take care of the temperature dependence of the Matsubara frequency. By repeating the derivation for the general FRG flow equations, we will eventually arrive at the same flow equations naturally where the bubble integrations read:

$$\begin{aligned} \dot{B}^{\pm}_{l,l'}(\boldsymbol{q}) = A_{\mathrm{BZ}}^{-1} \int_{\boldsymbol{p}} \sum_{\omega_p} [&G^{0,T}(i\omega_p,\boldsymbol{p}+\boldsymbol{q}) S^T(\pm i\omega_p,\pm\boldsymbol{p}) \\ &+ S^T(i\omega_p,\boldsymbol{p}+\boldsymbol{q}) G^{0,T}(\pm i\omega_p,\pm\boldsymbol{p})] f_l(\boldsymbol{p}) f^*_{l'}(\boldsymbol{p}) \end{aligned} \tag{2.111}$$

where it should be noted that the normalization of Matsubara summation with T is not appearing here since the initial prefactor was absorbed by the bare propagator in the derivation of the T-flow equations. By computing the integrand with definitions Eqs. (2.109),(2.110) one gets:

$$\begin{aligned} &G^{0,T}(i\omega_p,\boldsymbol{p}+\boldsymbol{q}) S^T(\pm i\omega_p,\pm\boldsymbol{p}) + S^T(i\omega_p,\boldsymbol{p}+\boldsymbol{q}) G^{0,T}(\pm i\omega_p,\pm\boldsymbol{p}) \\ &\qquad = \frac{d}{dT}\left[T \times G^{0,T}(i\omega_p,\boldsymbol{p}+\boldsymbol{q}) G^{0,T}(\mp i\omega_p,\mp\boldsymbol{p})\right] \end{aligned} \tag{2.112}$$

such that the whole bubble integral during the flow is determined as:

$$\dot{B}(\boldsymbol{q})^{\pm}_{l,l'} = A_{\mathrm{BZ}}^{-1} \int d\boldsymbol{p} \sum_{\omega_p} \frac{d}{dT} \left[T \times G^{0,T}(i\omega_p, \boldsymbol{p}+\boldsymbol{q}) G^{0,T}(\pm i\omega_p, \pm\boldsymbol{p}) \right] f_l(\boldsymbol{p}) f^*_{l'}(\boldsymbol{p}).$$

By passing the Matsubara summation past the internal expression, we can finally just execute the particle-particle $(-)$ and particle-hole $(+)$ diagram term as usual (as already done in section 1.1):

$$\dot{B}(\boldsymbol{q})^{+}_{l,l'} = -\int_{\boldsymbol{p}} \frac{n'_F(\xi(\boldsymbol{q}+\boldsymbol{p})) - n'_F(\xi(\boldsymbol{p}))}{\xi(\boldsymbol{q}+\boldsymbol{p}) - \xi(\boldsymbol{p})} f_l(\boldsymbol{p}) f^*_{l'}(\boldsymbol{p}), \tag{2.113}$$

$$\dot{B}(\boldsymbol{q})^{-}_{l,l'} = +\int_{\boldsymbol{p}} \frac{n'_F(\xi(\boldsymbol{q}+\boldsymbol{p})) + n'_F(\xi(-\boldsymbol{p}))}{\xi(\boldsymbol{q}+\boldsymbol{p}) + \xi(-\boldsymbol{p})} f_l(\boldsymbol{p}) f^*_{l'}(\boldsymbol{p}). \tag{2.114}$$

n'_F is the temperature-derivative of the Fermi function. It is an obvious disadvantage that we cannot calculate the FRG flow for finite temperatures in this scheme such that the results of emerging instabilities are only valid at the critical temperature. Since this is actually everything we want to achieve in the first place, we will accept this disadvantage and prefer the temperature scheme in our calculations since the form of the bubbles Eqs.(2.113),(2.114) are cast into a feasible form for a numerical implementation.

This ends the section about the theoretical foundations of the TUFRG. By illuminating the relationship of the three diagrams in the „ordinary" FRG scheme to possible physical instabilities, we were able to derive this new formalism which does only depend on one momentum $\boldsymbol{q}$ (namely the important transfer momentum) and two form factors l, l'. While many possibilities exist for the choice of these form factors, we showed that the plane wave form factors $f_l(\boldsymbol{k}) = e^{i\boldsymbol{k}\boldsymbol{R}_l}$ equip the TUFRG with two advantages. At first, the truncation of form factors can be rationalized by connecting a form factor $f_l(\boldsymbol{k})$ to the real space vector $\boldsymbol{R}_l$ and therefore the truncation is justified by arguing that the emerging instabilities in the final TUFRG application will be mainly deviated by short-range physics. Second, we showed that this choice of form factors also greatly reduces the numerical effort for calculating the cross-channel projections. Eventually, we established the usefulness of the temperature flow as a regularization scheme, since this scheme does not artificially suppress magnetic fluctuations and gains a numerical advantages for the bubble integrations. Since all separated objects of the TUFRG are now developed, we will proceed to the actual numerical implementation of the method for triangular lattice systems.

2.3 Implementation

The general method of the TUFRG and the choice of specific technical aspects, namely the form factors and the regulator scheme, are now specified. Now we will present the implementation of TUFRG and again use the SU(2)-invariant model as an example. For the spinless system (application B) the vast majority of this discussion does also apply. For the spinful model without SU(2)-invariance (application C), some substantial alterations have to be made which we will discuss at the given time later in the respective section.

The most general form of the SU(2)-invariant Hamiltonian treated in application A is given by:

$$\begin{aligned} H = & \underbrace{-\sum_{n}\sum_{\langle ij\rangle_n}\sum_{\sigma} t_n \left(c^\dagger_{i\sigma}c_{j\sigma} + \text{h.c.}\right) - \mu\sum_{i\sigma} n_{i\sigma}}_{=:H_{\text{Kin}}} \\ & \underbrace{+ U\sum_i n_{i\uparrow}n_{i\downarrow} + \sum_n\sum_{\langle ij\rangle_n}\sum_{\sigma\sigma'} V_n n_{i\sigma}n_{j\sigma'}}_{=:H_{\text{Int}}} . \end{aligned} \tag{2.115}$$

Where we allow for the largest distance of the hopping parameters and the density-density interactions to be third-neighbour distance, i.e. $n = 1, 2, 3$. In this section we will not only show how the TUFRG is applied in general, but we will also go into the details of technical difficulties which happen to occur when solving the TUFRG flow equations numerically. Therefore, we will treat these aspects of the method in the order they are appearing in the code. This covers the following steps:

1. We will show how the interaction parameters in Eq. (2.115) are projected into the channels to instate the correct initial conditions.
2. The bubble integrations $\dot{B}(\boldsymbol{q})^{\pm}_{l,l'}$ are non-trivial and have to be carried out with great care. Moreover, we will present how the symmetries of the form factors can be used to improve the computational performance of these integrations.
3. Until now, we did not exploit the symmetry of the lattice for the TUFRG flow equations. We will present how this can be done on the level of the vertices $X^{l,l'}(\boldsymbol{q})$ such that the numerical cost can be substantively reduced.
4. After the increment of the flow equation is calculated, we will show how the differential equations are solved. We will also comment on the sign-convention here which can lead to a global minus sign of the flow equations.
5. Finally, we will briefly recap how to use the eigenvalue equation from section 1.2 to calculate the leading gap(s)by using the renormalized vertex $P^{l,l'}(\boldsymbol{q})$.

2.3.1 Initial conditions

We already encountered the projections of the initial conditions onto the channels when we derived the simplification of the cross-channel projections by the plane wave form factors:

$$V^{0,P}_{l,l'}(\boldsymbol{q}) = \int_{\boldsymbol{k},\boldsymbol{k}'} V^0(\boldsymbol{q}+\boldsymbol{k}, -\boldsymbol{k}, \boldsymbol{q}+\boldsymbol{k}') \times f_l(\boldsymbol{k}) f^*_{l'}(\boldsymbol{k}'), \tag{2.116}$$

$$V^{0,D}_{l,l'}(\boldsymbol{q}) = \int_{\boldsymbol{k},\boldsymbol{k}'} V^0(\boldsymbol{q}+\boldsymbol{k}, \boldsymbol{k}', \boldsymbol{k}) \times f_l(\boldsymbol{k}) f^*_{l'}(\boldsymbol{k}'), \tag{2.117}$$

$$V^{0,C}_{l,l'}(\boldsymbol{q}) = \int_{\boldsymbol{k},\boldsymbol{k}'} V^0(\boldsymbol{q}+\boldsymbol{k}, \boldsymbol{k}', \boldsymbol{q}+\boldsymbol{k}') \times f_l(\boldsymbol{k}) f^*_{l'}(\boldsymbol{k}'). \tag{2.118}$$

Therefore, the only object which has to be derived is the initial interaction V^0. This expression is defined by taking the interacting part of Eq. (2.115) and cast it into a form resembling Eq. (2.48) by the means of a Fourier transformation:

$$H_{\text{Int}} \to \frac{1}{2} \int_{\boldsymbol{k}_1,\boldsymbol{k}_2,\boldsymbol{k}_3,\boldsymbol{k}_4} V^0(\boldsymbol{k}_1,\boldsymbol{k}_2,\boldsymbol{k}_3,\boldsymbol{k}_4)\delta(\boldsymbol{k}_1+\boldsymbol{k}_2-\boldsymbol{k}_3-\boldsymbol{k}_4)\sum_{\sigma,\sigma'} c^\dagger_\sigma(\boldsymbol{k}_1)c^\dagger_{\sigma'}(\boldsymbol{k}_2)c_{\sigma'}(\boldsymbol{k}_4)c_\sigma(\boldsymbol{k}_3). \tag{2.119}$$

We will show this procedure explicitly for the Hubbard interaction and the density-density interactions V_n for the SU(2)-invariant model.

Projection of U

We rewrite the Hubbard interaction term at first and transform it consequently into momentum space:

$$\begin{aligned} U\sum_i n_{i\uparrow}n_{i\downarrow} = U\sum_i c^\dagger_{i\uparrow}c_{i\uparrow}c^\dagger_{i\downarrow}c_{i\downarrow} = \frac{U}{2}\sum_i\sum_{\sigma,\sigma'} c^\dagger_{i,\sigma}c^\dagger_{i,\sigma'}c_{i,\sigma'}c_{i,\sigma} \\ \overset{\text{Fourier}}{=} \frac{1}{2}\int_{\boldsymbol{k}_1,\boldsymbol{k}_2,\boldsymbol{k}_3,\boldsymbol{k}_4} U\times\delta(\boldsymbol{k}_1+\boldsymbol{k}_2-\boldsymbol{k}_3-\boldsymbol{k}_4)\sum_{\sigma,\sigma'} c^\dagger_\sigma(\boldsymbol{k}_1)c^\dagger_{\sigma'}(\boldsymbol{k}_2)c_{\sigma'}(\boldsymbol{k}_4)c_\sigma(\boldsymbol{k}_3). \end{aligned} \tag{2.120}$$

Comparing with Eq. (2.119) yields for the Hubbard interaction:

$$V^0(\boldsymbol{k}_1,\boldsymbol{k}_2,\boldsymbol{k}_3,\boldsymbol{k}_4) = U.$$

Since for this interaction there is no additional momentum structure, the projection is identical for the three different channels Eqs. (2.116),(2.117),(2.118):

$$V^{0,P(C,D)}_{l,l'}(\boldsymbol{q}) = \int_{\boldsymbol{k},\boldsymbol{k}'} U\times f_l(\boldsymbol{k})f^*_{l'}(\boldsymbol{k}') = \int_{\boldsymbol{k},\boldsymbol{k}'} U\times e^{i\boldsymbol{R}_l\boldsymbol{k}}\,e^{-i\boldsymbol{R}_{l'}\boldsymbol{k}'} = U\delta(\boldsymbol{R}_l)\delta(\boldsymbol{R}_{l'}). \tag{2.121}$$

Projection of V_n

For the density-density interactions of nth nearest neighbors, the projection onto the three channels will have different forms. But the structure for different values of n will be identical and only differ in the set of lattice vectors to sum over. Again starting by rewriting the interaction term in real space:

$$\begin{aligned} V_n\sum_{\langle ij\rangle_n}\sum_{\sigma\sigma'} n_{i\sigma}n_{j\sigma'} = V_n\sum_{\langle ij\rangle_n}\sum_{\sigma\sigma'} c^\dagger_{i,\sigma}c_{i,\sigma}c^\dagger_{j,\sigma'}c_{j,\sigma'} = \frac{V_n}{2}\sum_i\sum_{\boldsymbol{\delta}_n}\sum_{\sigma,\sigma'} c^\dagger_{i,\sigma}c^\dagger_{i+\boldsymbol{\delta}_n,\sigma'}c_{i+\boldsymbol{\delta}_n,\sigma'}c_{i,\sigma} \\ \overset{\text{Fourier}}{=} \frac{1}{2}\int_{\boldsymbol{k}_1,\boldsymbol{k}_2,\boldsymbol{k}_3,\boldsymbol{k}_4}\sum_{\boldsymbol{\delta}_n} V_n\times e^{i\boldsymbol{\delta}_n(\boldsymbol{k}_2-\boldsymbol{k}_4)}\delta(\boldsymbol{k}_1+\boldsymbol{k}_2-\boldsymbol{k}_3-\boldsymbol{k}_4)\sum_{\sigma,\sigma'} c^\dagger_\sigma(\boldsymbol{k}_1)c^\dagger_{\sigma'}(\boldsymbol{k}_2)c_{\sigma'}(\boldsymbol{k}_4)c_\sigma(\boldsymbol{k}_3). \end{aligned} \tag{2.122}$$

Where $\boldsymbol{\delta}_n$ indicates the lattice vectors connecting the n-th nearest neighbours. Again, by comparing the derived expression with Eq. (2.48) we conclude:

$$V^0(\boldsymbol{k}_1,\boldsymbol{k}_2,\boldsymbol{k}_3,\boldsymbol{k}_4) = \sum_{\boldsymbol{\delta}_n} V_n\times e^{i\boldsymbol{\delta}_n(\boldsymbol{k}_2-\boldsymbol{k}_4)}.$$

Explicitly for the projection onto the P channel Eq.(2.116) this results into:

$$\begin{aligned} V^{0,P}_{l,l'}(\boldsymbol{q}) &= \int_{\boldsymbol{k},\boldsymbol{k}'} V_n\sum_{\boldsymbol{\delta}_n} e^{i\boldsymbol{\delta}_n(-\boldsymbol{k}+\boldsymbol{k}')}\times f_l(\boldsymbol{k})f^*_{l'}(\boldsymbol{k}') = \int_{\boldsymbol{k},\boldsymbol{k}'} V_n\sum_{\boldsymbol{\delta}_n} e^{i\boldsymbol{\delta}_n(-\boldsymbol{k}-\boldsymbol{k}')}\times e^{i\boldsymbol{R}_l\boldsymbol{k}}e^{-i\boldsymbol{R}_{l'}\boldsymbol{k}'} \\ &= V_n\int_{\boldsymbol{k},\boldsymbol{k}'}\sum_{\boldsymbol{\delta}_n} e^{i\boldsymbol{k}(\boldsymbol{R}_l-\boldsymbol{\delta}_n)}\times e^{i\boldsymbol{k}'(\boldsymbol{\delta}_n-\boldsymbol{R}_{l'})} = V_n\sum_{\boldsymbol{\delta}_n}\delta(\boldsymbol{R}_l-\boldsymbol{\delta}_n)\times\delta(\boldsymbol{\delta}_n-\boldsymbol{R}_{l'}) \\ &= V_n\times\delta(\boldsymbol{R}_l-\boldsymbol{R}_{l'}) \qquad \text{for}: \boldsymbol{R}_l,\boldsymbol{R}_{l'}\in\{\boldsymbol{\delta}_n\}. \end{aligned} \tag{2.123}$$

In a similar fashion, one can derive the projections into the other channels for these interaction terms.

Complete set of initial conditions

Compactly, all initial conditions for the interactions U and $V_{1,2,3}$ are given by:

$$V_{1,1}^{0,P}(\boldsymbol{q}) = V_{1,1}^{0,C}(\boldsymbol{q}) = U \tag{2.124}$$

$$V_{l,l}^{0,P}(\boldsymbol{q}) = V_{l,l}^{0,C}(\boldsymbol{q}) = V_1, \qquad \text{for} : l \in \{2,3,4,5,6,7\} \tag{2.125}$$

$$V_{l',l'}^{0,P}(\boldsymbol{q}) = V_{l',l'}^{0,C}(\boldsymbol{q}) = V_2, \qquad \text{for} : l' \in \{10,11,14,15,18,19\} \tag{2.126}$$

$$V_{l'',l''}^{0,P}(\boldsymbol{q}) = V_{l'',l''}^{0,C}(\boldsymbol{q}) = V_3, \qquad \text{for} : l'' \in \{8,9,12,13,16,17\} \tag{2.127}$$

$$V_{1,1}^{0,D}(\boldsymbol{q}) = U + V_1 \sum_l e^{i\boldsymbol{R}_l \boldsymbol{q}} + V_2 \sum_{l'} e^{i\boldsymbol{R}_{l'} \boldsymbol{q}} + V_3 \sum_{l''} e^{i\boldsymbol{R}_{l''} \boldsymbol{q}}. \tag{2.128}$$

For the model without spins and the model with spins but without SU(2)-symmetry, we have to be careful about keeping the anti-symmetry of the initial conditions intact. Also, we have to be careful about the order of the spin indices in the later case. For a the complete set of these initial conditions, see Appendices A.3 and A.5 respectively.

2.3.2 Symmetries of bubble integrations

The bubble integrations connect the vertices of the flow equations (2.76),(2.79) and it will turn out that these objects are by far the most challenging part of the numerical implementation with the given truncations. The difficulties are stemming mainly from two aspects:

1. The integrations will feature sharp peaks at lower scales such that the integrand becomes harder and harder to integrate properly while continuing the flow. This does not only lead to problems regarding the numerical cost, but also calls for the implementation of a sophisticated integration scheme, carefully ensuring the correctness of the results.

2. We have to perform $N_{\boldsymbol{q}} \times N_l^2$ of these challenging integrals when no symmetries are used. So, the computational run-time is increased to an unusable amount such that we have to exploit the present symmetries to frame this feasible.

We will present how these problems can be successfully solved. For the first aspect, we will construct an adaptive integration routine which is specifically tailored to our present FRG implementation. For the second aspect, we will demonstrate how the symmetries of the plane wave form factors can be employed such that necessary computational effort for the full calculation of the bubble integrations is vastly reduced.

Adaptive integration routine

We want to explicitly describe the goal of this section for clarity. We are going to develop a routine such that the bubble integrations are correctly and quickly executed. These objects depend only on the dispersion of the underlying model and the given scale. Since we decided on the temperature flow, this scale is naturally the temperature and our objects of interest are:

$$\dot{B}(\boldsymbol{q})^{+}_{l,l'} = -\int_{\boldsymbol{p}} \frac{n_F'(\xi(\boldsymbol{q}+\boldsymbol{p})) - n_F'(\xi(\boldsymbol{p}))}{\xi(\boldsymbol{q}+\boldsymbol{p}) - \xi(\boldsymbol{p})} f_l(\boldsymbol{p}) f_{l'}^*(\boldsymbol{p}),$$

$$\dot{B}(\boldsymbol{q})^{-}_{l,l'} = +\int_{\boldsymbol{p}} \frac{n_F'(\xi(\boldsymbol{q}+\boldsymbol{p})) + n_F'(\xi(-\boldsymbol{p}))}{\xi(\boldsymbol{q}+\boldsymbol{p}) + \xi(-\boldsymbol{p})} f_l(\boldsymbol{p}) f_{l'}^*(\boldsymbol{p}),$$

$$\begin{aligned}\xi(\boldsymbol{k}) = &-2t_1[\cos(k_y) + 2\cos(k_y/2)\cos(\sqrt{3}k_x/2)] \\ &-2t_2[2\cos(3k_y/2)\cos(\sqrt{3}k_x/2) + \cos(\sqrt{3}k_x)] \\ &-2t_3[\cos(2k_y) + 2\cos(k_y)\cos(\sqrt{3}k_x)] - \mu,\end{aligned}$$

$$n_F'(x) = \frac{d}{dT}\frac{1}{e^{x/T}+1} = \frac{x}{2T^2}\frac{1}{\cosh\left(\frac{x}{T}\right)+1}.$$

Here, we extracted the dispersion $\xi(\boldsymbol{k})$ just by diagonalization of the kinetic part in Eq. (2.115) by using a Fourier transformation and setting the lattice constant $a = 1$ for brevity. With all three hoppings $t_{1,2,3}$ present, the tuning of the Fermi surface to the Van Hove singularity at the **M** points is given by:

$$\mu_{\mathrm{VH}} = 2(t_1 + t_2 - 3t_3).$$

In the following, we will call a system with $\mu < \mu_{\mathrm{VH}}$ as being **underdoped** and a system with $\mu > \mu_{VH}$ **overdoped**. A system with $\mu = \mu_{VH}$ will obviously be called to be at **Van Hove filling**. Examples for these three scenarios are shown in Fig. 2.7 a. As a first step, we want to introduce how we will perform a 2D integration in the Brillouin zone. We will employ a polar coordinate integration by using the $\boldsymbol{\Gamma}$ point as the origin for some function $f(\boldsymbol{k})$. The hexagonal shape of the Brillouin zone dictates that for every angle ϕ the maximal length of the ρ integration is different, namely the edge of the Brillouin zone $\rho_{\mathrm{max}}(\phi)$, unlike for the integration of circular shaped forms where the maximal length is constant. Therefore the polar integration is given by:

$$A_{\mathrm{BZ}}^{-1} \int d\boldsymbol{k} f(\boldsymbol{k}) = A_{\mathrm{BZ}}^{-1} \int_0^{2\pi} d\phi \int_0^{\rho_{\mathrm{max}}(\phi)} f(\boldsymbol{k}(\rho, \phi)) \times \rho \, d\rho. \tag{2.129}$$

Employing a suitable numerical implementation, we will choose an angular resolution N_A which places N_A „beams" in the Brillouin zone where the radial integrations will be evaluated (see Fig. 2.7 b). Then, angular distance of these beams is $\Delta\phi = 2\pi/N_A$. The discretized version of Eq. (2.129) with N_A selected angles ϕ_i, $i = 0, \ldots, N_A - 1$ is given by:

$$A_{\mathrm{BZ}}^{-1} \int d\boldsymbol{k} f(\boldsymbol{k}) \approx A_{\mathrm{BZ}}^{-1} \sum_{i=0}^{N_A - 1} \Delta\phi \left[\int_0^{\rho_{\mathrm{max}}(\phi_i)} f(\boldsymbol{k}(\rho, \phi_i)) \times \rho \, d\rho \right]. \tag{2.130}$$

Following this approach, we are now confronted with solving N_A 1D integrals in radial direction ρ for all chosen angles ϕ_i. In practice, the function $f(\boldsymbol{k})$ will be the bubble integrals $\dot{B}(\boldsymbol{q})^{\pm}_{l,l'}$. These objects distinctly feature the temperature-derivative of the Fermi function $n'_F(x)$ which will lead to complications in carrying out the computation. In general, $n'_F(x)$ will develop sharp features around $x = 0$ if the temperature becomes small. This includes especially the Fermi surface for our bubble integrals. Therefore we will employ a routine for the radial integrations Eq. (2.130) such that two aspects are covered:

1. We avoid to miss the sharp peak of the integrand at the Fermi surface by splitting the radial integral into two integrations: one defined between 0 to ρ_F (the position of the Fermi surface) and a second one defined between ρ_F to ρ_{rmax}.

2. In both of these intervals, the function will be integrated adaptively such that additional features are approached with a reasonable amount of numerical effort.

The adaptive integration scheme will work as follows: given a radial resolution N_R for the integration of the beams, the intervals are split into $N_R - 1$ sub-intervals. These are calculated by a trapezoidal rule. After this procedure, each interval is split again in $N_R - 1$ sub-intervals and these are again integrated by a trapezoidal rule. If this finer integration scheme does not change the value of the former integration by a significant amount (for which we will determine a criterion by using a *relative tolerance* and an *absolute tolerance*), then the integration is deemed as converged. We will repeat this procedure until all initial sub-intervals are converged (see Fig. 2.8). While this procedure works well for the case of underdoping, it has to be slightly changed for overdoped Fermi surfaces. In this case, the Fermi surface will develop *pockets* around the K, K′ points and there are some areas where a beam from the origin to the edge of the Brillouin zone will not cut the Fermi surface at all. In this case, we will implement beams with a kink such that all beams contribute a substantial value to the integration. The first section of these beams is constructed as before, going from the Γ point radially towards the edges of the Brillouin zone, although this time the beam goes only to the *nesting line*, i.e.

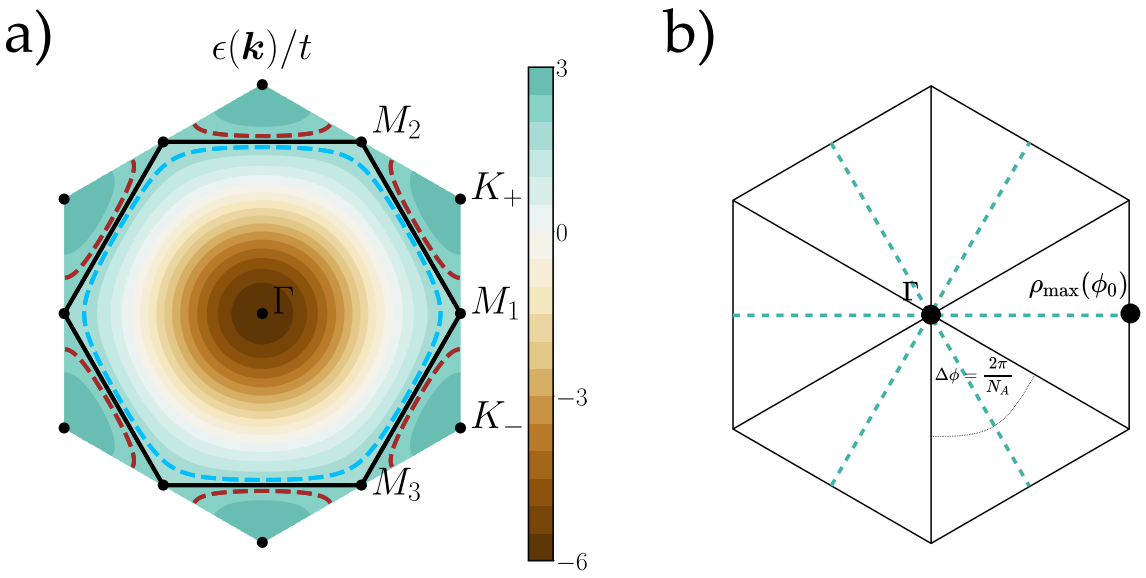

Figure 2.7: **Filling situations and discretization:** a) Fermi surfaces for the triangular lattice tight-binding model for $t_1 = 1.0$, $t_2 = t_3 = 0.0$. The Van Hove filling is given by $\mu_{VH} = 2t_1$ here. Furthermore, we show the underdoped case (blue) at $\mu = 1.9t_1$ and the overdoped case (red) at $\mu = 2.1t_1$. b) Example discretization of the polar integration of the Brillouin zone for $N_A = 6$. The six green beams are 1D integrations regarding the radial coordinate ρ where the integration range goes from $\rho = 0$ (Γ point) to $\rho = \rho_{\max}(\phi_i)$ which is the edge of the Brillouin zone for a respective angle ϕ_i. Two beams are separated by the angular distance $2\pi/N_A$ which is also the width of the angular sector each integration beam represents (black triangle).

the Fermi surface at Van Hove filling. The complement part of this beam will then go from the K, K′ points radially to the point where the other beam ended (see Fig. 2.9). The intervals themselves are then treated exactly as in the underdoped case with the adaptive trapezoidal routine.

Since the function becomes sharper at lower temperatures and the *hard* part of the integral will concentrate on smaller regions on the ρ-axis, we will scale N_R with the temperature. Then, the important small regions will not have unnecessary large initial sizes leading to a high amount of iterations until the sharp peaks are properly integrated. This scaling is done with respect to the orders of magnitude of the temperature:

$$N_R = 3 \times 2^{\lceil \log_{10}(|t|/T) \rceil},$$

i.e. we will start with $N_R = 3$ and double this number for each lower order of magnitude reached. For the angular resolution N_A, it has been sufficient to choose numbers between 120 and 360. The tolerance values are selected as:

$$\text{relative tolerance} = 10^{-3}, \qquad \text{absolute tolerance} = 10^{-10}.$$

This concludes the construction of the integration routine. We will present in the applications later that this routine faithfully reproduces expected behaviour of the bubbles.

Symmetry properties of form factors

While the adaptive routine is now developed, we are still confronted with the problem that this integral has to be performed for each RG step for $N_{\boldsymbol{q}} \times N_l^2$ components in slight variations depending on the form factor indices. We will show now that the scaling stemming from the form factors l, l' can actually be drastically reduced.

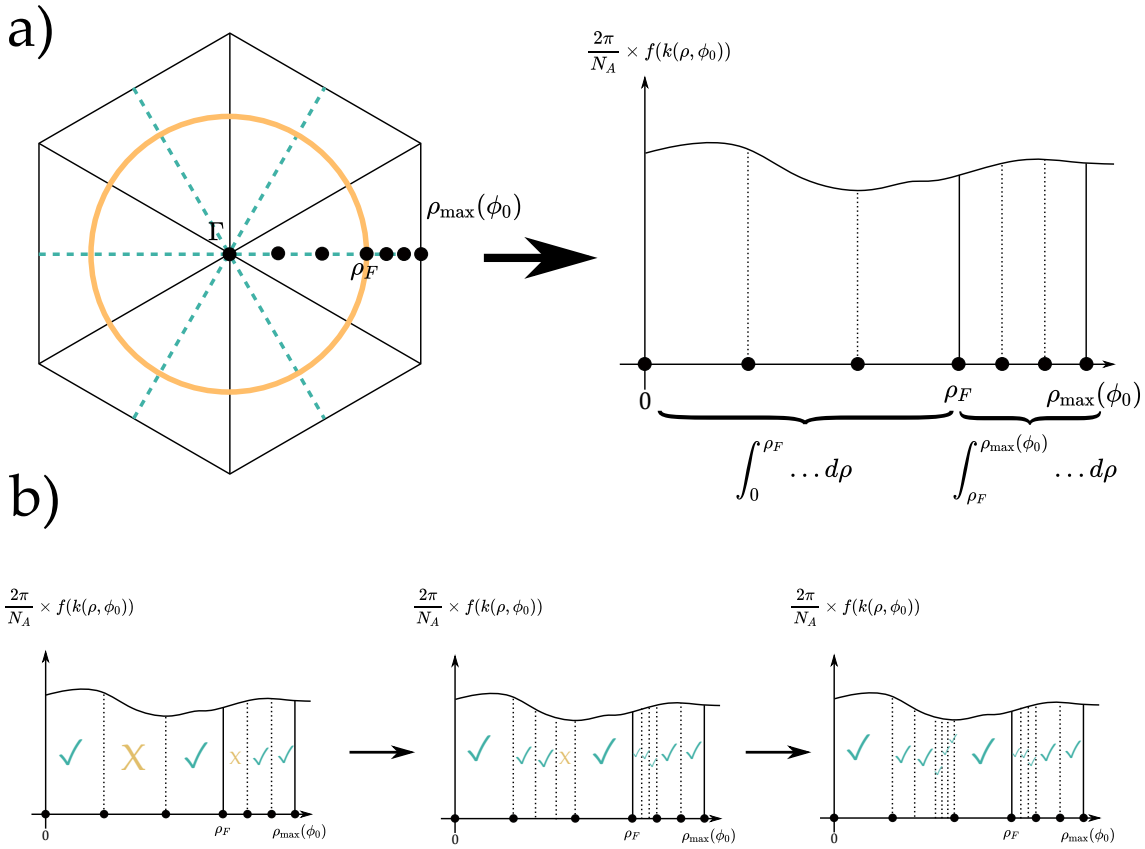

Figure 2.8: **Adaptive integration routine for an underdoped system:** a) One of the 1D integrations with $N_R = 4$. The interval from 0 to the edge of the Brillouin zone is divided into two sub-intervals, defined by the Fermi surface (yellow). b) For each 1D integration, the intervals are successively treated with a trapzoidal rule. If the desired precision is met, the interval is deemed as convergend (green tick). If this is not the case (yellow cross), the interval of interest is again divided into $N_R - 1$ intervals where the procedure is repeated until all sub-interval integrations are converged.

For this purpose we explicitly write the form factors of the bubbles as only one plane wave:

$$\begin{aligned}\dot{B}(\boldsymbol{q})^{+}_{l,l'} &= -\int_{\boldsymbol{p}} \frac{n'_F(\xi(\boldsymbol{q}+\boldsymbol{p})) - n'_F(\xi(\boldsymbol{p}))}{\xi(\boldsymbol{q}+\boldsymbol{p}) - \xi(\boldsymbol{p})} f_l(\boldsymbol{p}) f^*_{l'}(\boldsymbol{p}) \\ &= -\int_{\boldsymbol{p}} \frac{n'_F(\xi(\boldsymbol{q}+\boldsymbol{p})) - n'_F(\xi(\boldsymbol{p}))}{\xi(\boldsymbol{q}+\boldsymbol{p}) - \xi(\boldsymbol{p})} e^{i(\boldsymbol{R}_l - \boldsymbol{R}_{l'})\boldsymbol{p}}. \end{aligned} \tag{2.131}$$

Of course the following discussion also holds for the particle-particle bubble, but we will treat the particle-hole bubble only now for brevity. Since all terms besides the plane wave in Eq. (2.131) are real, it directly follows:

$$\left(\dot{B}(\boldsymbol{q})^{+}_{l,l'}\right)^* = \dot{B}(\boldsymbol{q})^{+}_{l',l}, \tag{2.132}$$

which already roughly halves the amount of integrals to calculate. Moreover, we see that form factor dependent part, i.e. the plane wave:

$$e^{i(\boldsymbol{R}_l - \boldsymbol{R}_{l'})\boldsymbol{p}} = e^{i\boldsymbol{R}_{l-l'}\boldsymbol{p}} \tag{2.133}$$

can result into the same value for different sets of form factors l, l'. As a direct example, for all bubbles with $l = l'$ this composed plane wave will just return $e^0 = 1$ such that all these bubble integrals have the same value. By inspecting again our numeration of form factors Fig. 2.10, we can find a plethora

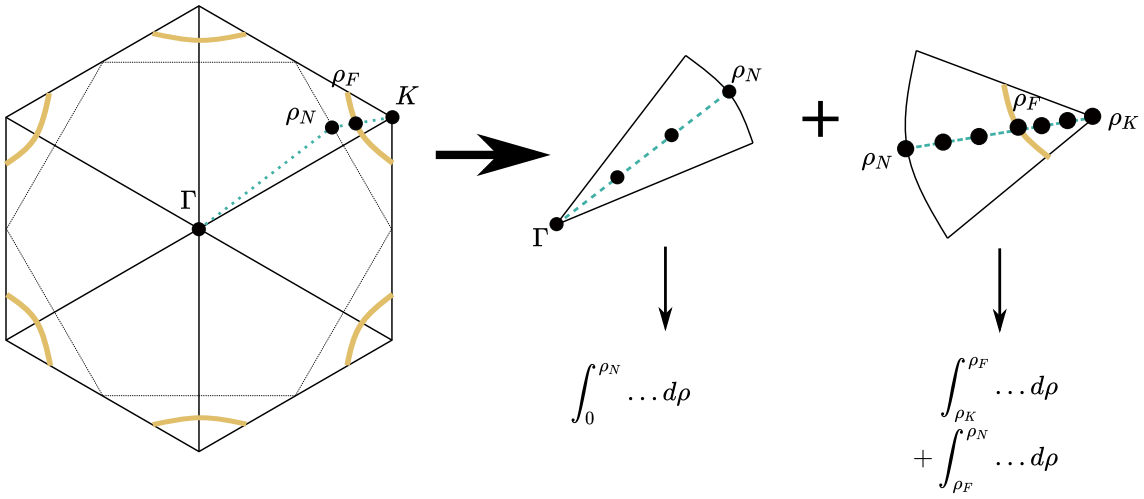

Figure 2.9: **Adaptive integration routine for an overdoped system with $N_R = 4$:** The beam defining the 1D integration (dashed green) will feature a kink at the nesting line at ρ_N. The complement part of this beam is then constructed by going from the Dirac point to the nesting line. In total, there will be three sub-intervals to integrate. The first one comes from the *inner* beam. The *outer* beam will be divided with respect to the Fermi surface at ρ_F, exactly as in the underdoped case.

of these cases. Another example of combinations resulting in the same plane wave would be:

$$\boldsymbol{R}_2 - \boldsymbol{R}_5 = \boldsymbol{R}_{12} - \boldsymbol{R}_6 = \boldsymbol{R}_{10}.$$

We will exploit this property to circumvent superfluous calculations which could have been related to integrations of other form factor combinations. At this point, we can now finally motivate the selection of the amount of form factors by *hexagons* and not distances alone. We will for example consider $N_s = 2$, namely the second hexagon which corresponds to form factors 1 to 19. We can conclude from Fig. 2.10 that all combinations of these 19 real space vectors will point to lattice vectors which belong at maximum to the fourth hexagon shell. Therefore, if we consider $N_s = 2$ without symmetries we would have to calculate $19 \times 19 = 361$ bubble integrals for each momentum $\boldsymbol{q}$. Using the presented property, all of these 361 integrals can actually be related to one of the form factors up to the fourth hexagon shell which is 61 bubble integrations. This grants as a numerical speedup of factor 6. An additional factor of 2 can then also be concluded from Eq. (2.132), although this symmetry is useless for $l = l' = 1$, i.e. the on-site form factor.

By geometry, it can be easily concluded that for a selected hexagon shell N_s the resulting combinations $\boldsymbol{R}_{l-l'}$ are lying in the hexagon shell up to $2 \times N_s$. The strategy is then as follows:

1. We chose a form factor shell N_s which we want to include in our TUFRG calculations.
2. For a fixed $\boldsymbol{q}$, we calculate $\dot{B}(\boldsymbol{q})^{\pm}_{l,l'} = \dot{B}(\boldsymbol{q})^{\pm}_{l-l'}$ for all $\boldsymbol{R}_{l-l'}$ which are lying in the hexagon shell $2 \times N_s$ where we also use the symmetry Eq. (2.132) to restore roughly half of these integrations just by complex conjugation.
3. We repeat this for all desired $\boldsymbol{q}$.

The speedup for the first four shells using this strategy is then given by presented Table 2.1. It can not exaggerated how important these symmetries condition is for the actual implementation of the TUFRG. We will see that using higher shells N_s is not only useful for achieving convergence, but that there are still qualitative results which rely on taking a high amount of form factors into account. For the fourth shell, performing 3721 calculations for each momentum $\boldsymbol{q}$ would be absolutely unfeasible, but by reducing this number to 109, a calculation for this shell can be realistically carried out.

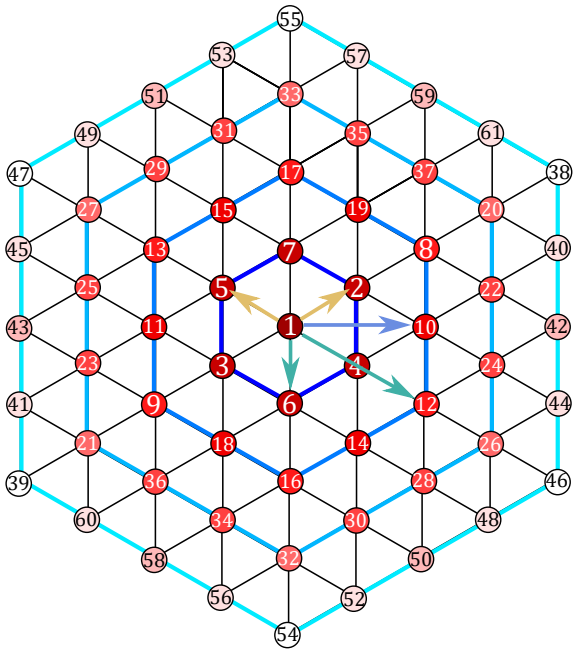

Figure 2.10: **Symmetry consideration of form factors:** The combinations $\boldsymbol{R}_2 - \boldsymbol{R}_5$ (yellow) and $\boldsymbol{R}_{12} - \boldsymbol{R}_6$ (green) do both result to $\boldsymbol{R}_{10}$ (blue) such that the bubble integral for $(l = 2, l' = 5)$ and $(l = 12, l' = 6)$ are equal.

N_s	N_l	Calculations without using symmetries	Calculations with using symmetries	Speedup
1	7	49	19	2.6
2	19	361	31	11.6
3	37	1369	64	21.4
4	61	3721	109	34.1

Table 2.1: Advantages of using symmetry properties of form factors for calculating $\dot{B}(\boldsymbol{q})^{\pm}_{l,l'}$ for a fixed momentum $\boldsymbol{q}$.

2.3.3 Use of symmetries and momentum discretization

We will now finally use the advantage of including the symmetries of the underlying lattice to our calculation. Effectively, the C_{6v} structure will impose symmetry relations for the momentum $\boldsymbol{q}$ such that the actual flow equations only have to be calculated for a smaller set of momenta, while the rest is restored by these symmetry relations. We will see that for the models in project A and B this will result into a speedup of factor 12. The philosophy of how to implement the point group symmetries in the TUFRG scheme is concisely laid out in [78]. We will adapt this method to the triangular lattice in detail now where we directly start from the action of the point group on the fermionic creation and annihilation operators. For this discussion, we will call an arbitrary element of the point group C_{6v} to be Q which can be either one of the rotations or reflections of said group. Given one of these symmetry operations Q, the fermionic operators in momentum space transform by a unitary transform U_Q[78]:

$$Q: \qquad U_Q c_\sigma(\boldsymbol{k})^{(\dagger)} U_Q^\dagger = c_\sigma^{(\dagger)}(Q^{-1}\boldsymbol{k})^{(\dagger)}. \tag{2.134}$$

The property $U_Q H U_Q^\dagger = H$ holds for symmetries of the Hamiltonian. Since this has to be true for all kinetic and interaction parts of the Hamiltonian Eq. (2.115), it also has to hold for the general interaction Eq. (2.48) during the whole flow, since we do not assume that the symmetries are broken at some point in flow. Therefore, the strategy is to derive constraints on the general interaction V^Λ by

applying the object Q to Eq. (2.48)[5]:

$$\begin{aligned}
Q : \Gamma_V^\Lambda \\
=&\frac{1}{2}\int\limits_{k_1,k_2,k_3,k_4} V^\Lambda(k_1,k_2,k_3,k_4)\delta(k_1+k_2-k_3-k_4)\sum_{\sigma,\sigma'} U_Q\bar{\psi}_\sigma(k_1)\bar{\psi}_{\sigma'}(k_2)\psi_{\sigma'}(k_4)\psi_\sigma(k_3)U_Q^\dagger \\
=&\frac{1}{2}\int\limits_{k_1,k_2,k_3,k_4} V^\Lambda(k_1,k_2,k_3,k_4)\delta(k_1+k_2-k_3-k_4)\times \\
&\sum_{\sigma,\sigma'} U_Q\bar{\psi}_\sigma(k_1)U_Q^\dagger U_Q\bar{\psi}_{\sigma'}(k_2)U_Q^\dagger U_Q\psi_{\sigma'}(k_4)U_Q^\dagger U_Q\psi_\sigma(k_3)U_Q^\dagger \\
=&\frac{1}{2}\int\limits_{k_1,k_2,k_3,k_4} V^\Lambda(k_1,k_2,k_3,k_4)\delta(k_1+k_2-k_3-k_4)\times \\
&\sum_{\sigma,\sigma'} \bar{\psi}_\sigma(Q^{-1}k_1)\psi_{\sigma'}(Q^{-1}k_2)\psi_{\sigma'}(Q^{-1}k_4)\psi_\sigma(Q^{-1}k_3). \qquad (2.135)
\end{aligned}$$

Since the Brillouin zone inherits the C_{6v} symmetry of the lattice, we can safely shift the integration variables $\boldsymbol{k}_i \to Q\boldsymbol{k}_i$ without changing the integral. Finally we arrive at:

$$Q : \Gamma_V^\Lambda = \frac{1}{2}\int\limits_{k_1,k_2,k_3,k_4} V^\Lambda(Qk_1,Qk_2,Qk_3,Qk_4)\delta(k_1+k_2-k_3-k_4)\sum_{\sigma,\sigma'}\bar{\psi}_\sigma(k_1)\bar{\psi}_{\sigma'}(k_2)\psi_{\sigma'}(k_4)\psi_\sigma(k_3) \qquad (2.136)$$

and by $\Gamma_V^\Lambda = U_Q\Gamma_V^\Lambda U_Q^\dagger$ the symmetry constraint is given by:

$$V^\Lambda(Q\boldsymbol{k}_1,Q\boldsymbol{k}_2,Q\boldsymbol{k}_3,Q\boldsymbol{k}_4) = V^\Lambda(\boldsymbol{k}_1,\boldsymbol{k}_2,\boldsymbol{k}_3,\boldsymbol{k}_4). \qquad (2.137)$$

To demonstrate the numerical advantage from this relation, we will as an example treat the P channel flow equation. The effect of Eq. (2.137) must be applied on the vertices $V^P_{l,l'}(\boldsymbol{q})$ connected by the bubble integration before deriving the cross-channel projections:

$$\begin{aligned}
V^P_{l,l'}(\boldsymbol{q}) &= \int\limits_{\boldsymbol{k},\boldsymbol{k}'} V^\Lambda(\boldsymbol{q}+\boldsymbol{k},-\boldsymbol{k},\boldsymbol{q}+\boldsymbol{k}')\times f_l(\boldsymbol{k})f^*_{l'}(\boldsymbol{k}') \\
&\overset{(2.137)}{=} \int\limits_{\boldsymbol{k},\boldsymbol{k}'} V^\Lambda(Q\boldsymbol{q}+Q\boldsymbol{k},-Q\boldsymbol{k},Q\boldsymbol{q}+Q\boldsymbol{k}')\times f_l(\boldsymbol{k})f^*_{l'}(\boldsymbol{k}') \qquad (2.138) \\
&\overset{\boldsymbol{k}^{(\prime)}\to Q^{-1}\boldsymbol{k}^{(\prime)}}{=} \int\limits_{\boldsymbol{k},\boldsymbol{k}'} V^\Lambda(Q\boldsymbol{q}+\boldsymbol{k},-\boldsymbol{k},Q\boldsymbol{q}+\boldsymbol{k}')\times f_l(Q^{-1}\boldsymbol{k})f^*_{l'}(Q^{-1}\boldsymbol{k}') \qquad (2.139) \\
&= \int\limits_{\boldsymbol{k},\boldsymbol{k}'} V^\Lambda(Q\boldsymbol{q}+\boldsymbol{k},-\boldsymbol{k},Q\boldsymbol{q}+\boldsymbol{k}')\times f_{Ql}(\boldsymbol{k})f^*_{Ql'}(\boldsymbol{k}') \\
&= V^P_{Ql,Ql'}(Q\boldsymbol{q}). \qquad (2.140)
\end{aligned}$$

Where in the last step we used the plane wave form of the form factors to shift Q to the real space lattice vectors $\boldsymbol{R}_l, \boldsymbol{R}_{l'}$. The same result can also be obtained for the other channels, i.e. $V^{C,D}_{l,l'}(\boldsymbol{q})$. In a similar fashion, it can be shown that just by a shift of integration variables and by using the symmetry of the dispersion $\xi(\boldsymbol{k})$, the bubble integrations inhabit a similar symmetry:

$$\dot{B}(\boldsymbol{q})^\pm_{l,l'} = \dot{B}(Q\boldsymbol{q})^\pm_{Ql,Ql'}. \qquad (2.141)$$

[5]The application of the operator Q on k, i.e. Qk is still meant as only acting on the momentum $\boldsymbol{k}$.

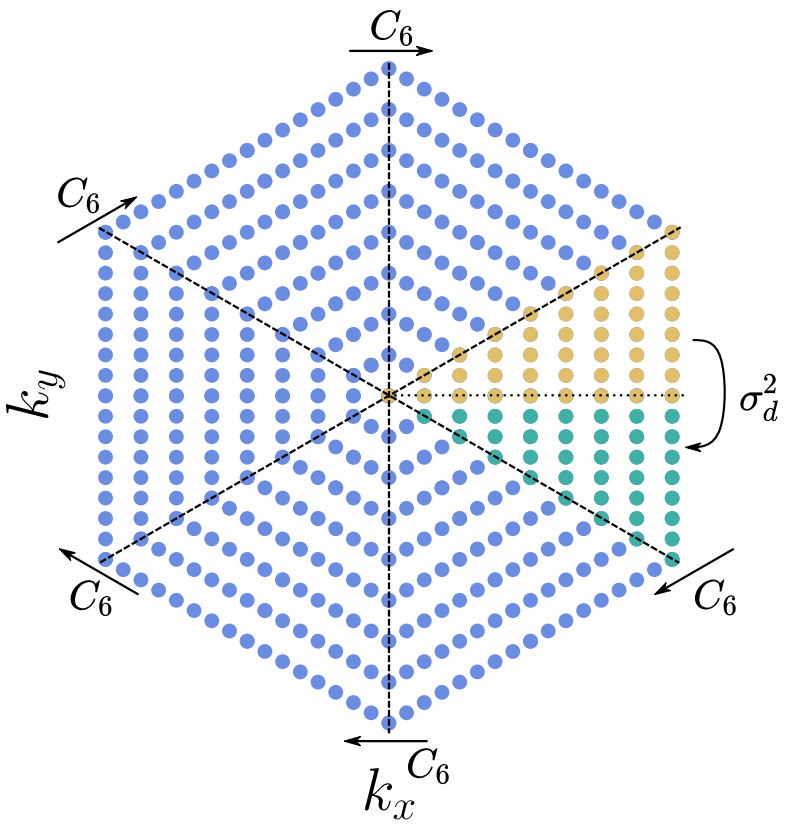

Figure 2.11: **Discretization of Brillouin zone and symmetry:** in this example, the Brillouin zone is sampled by 540 momentum points. At first, the flow step for $X^{l,l'}(\boldsymbol{q})$ is actually calculated by the flow equations for the momenta $\boldsymbol{q}$ in the yellow triangle. By using the reflection $Q = \sigma_d^2$, the symmetry relation delivers the values for the momenta in the green triangle area. Finally, by fivefold application of $Q = \mathrm{C}_6$, the remaining blue area is recovered.

Finally, we can derive the symmetry condition for the P-channel as follows:

$$\begin{aligned}\frac{d}{d\Lambda}P^{l,l'}(\boldsymbol{q}) &= \sum_{l_1,l_2} V^P_{l,l_1}(\boldsymbol{q}) \times \dot{B}^-_{l_1,l_2}(\boldsymbol{q}) \times V^P_{l',l_2}(\boldsymbol{q}) \\ &= \sum_{l_1,l_2} V^P_{Ql,Ql_1}(Q\boldsymbol{q}) \times \dot{B}^-_{Ql_1,Ql_2}(Q\boldsymbol{q}) \times V^P_{Ql',Ql_2}(Q\boldsymbol{q}) \\ &= \frac{d}{d\Lambda}P^{Ql,Ql'}(Q\boldsymbol{q}). \end{aligned} \tag{2.142}$$

This result does in the same way also hold for the C and D channel.

We directly see from the derived symmetry relation that it is not necessary to calculate the flow for all momenta $\boldsymbol{q}$ which are chosen to sample the Brillouin zone, but only for a subset of them. The majority of the entries of the vertices can be restored by symmetry relations. In practice, our method of discretizing the Brillouin zone will be as follows:

- We will place $N_{\boldsymbol{q}}$ discrete points in the Brillouin zone to evaluate the flow equations. These points will be placed in an equidistant manner and also in such a way that the different points can be mapped on each other by the symmetry relations of the point group.
- We will only perform the actual TUFRG flow equations for a small subset of momenta (the yellow triangle, see Fig. 2.11).

- In a first step, we will use the reflection across the x-axis (σ_d^2) to restore the values for the vertices of the second green triangle.
- Then we will recover the values of the remaining 5 blue triangles by using the rotation symmetry with angle $2\pi/6$ (C_6). For this purpose, each triangle is restored by the values of the triangle which is its left neighbour.
- Evidently, the only two operations we therefore need are $Q = \sigma_d^2$ and $Q = C_6$, while the latter is applied 5 times. In total, the amount of integrations is reduced by a factor of 12.

In consequence, this also means that the bubble integrations and cross-projections must not be performed for all $\boldsymbol{q}$, but only for the selected momenta in the yellow triangle area.

We exploited the symmetry of the lattice now in an optimal way. In addition to using the symmetries of the form factors in the previous section, all symmetry considerations of the application are now implemented. The final step for the implementation is now the integration of the actual differential equations for $X^{l,l'}(\boldsymbol{q})$.

2.3.4 Integration of differential equations

Until this section, we focused on how the right hand side (RHS) of the flow equations can be efficiently computed:

$$\frac{d}{dT}P^{l,l'}(\boldsymbol{q}) = \underbrace{\sum_{l_1,l_2} V^P_{l,l_1}(\boldsymbol{q}) \times \dot{B}^-_{l_1,l_2}(\boldsymbol{q}) \times V^P_{l',l_2}(\boldsymbol{q})}_{RHS},$$

whereas we want now to discuss how to solve this differential equation in the numerical implementation. In comparison to evaluating the right hand side, this is actually much less challenging and will be constructed in straight-forward way. Moreover, we alluded to a sign convention in section 2.1 with respect to the flow equations which we will also explain now.

The initial temperature will be set to the bandwidth $T_0 = W$, since all propagations above this value are frozen out by the regularization inherent in FRG methods such that the bandwidth will be a suitable starting point for the ultraviolet initial point. Basically, we will implement a forward Euler scheme for solving our flow equations starting from W and going *downwards* to 0. If i marks the discretized RG steps and considering that $T_i > T_{i+1}$, this is constructed for some test function $g(T)$ as:

$$\begin{aligned}
&\frac{dg(T)}{dT} = RHS,\\
\rightarrow&\frac{g(T_i) - g(T_{i+1})}{T_i - T_{i+1}} = RHS,\\
\rightarrow&g(T_{i+1}) = g(T_i) - RHS \cdot (T_i - T_{i+1}).
\end{aligned}$$

Since $T_i > T_{i+1}$, the difference of temperature $\Delta T = (T_i - T_{i+1})$ is positive. Conventionally, the Euler method *adds* an increment to the former value of the function such that we absorb the sign in RHS:

$$g(T_{i+1}) = g(T_i) + (-RHS)\Delta T. \tag{2.143}$$

Therefore, if we use this Euler scheme, we have to add a global sign to the RHS, namely the flow equations. In the end, we will absorb this global sign just in the definition of the bubble integrals $\dot{B}(\boldsymbol{q})^{\pm}_{l,l'}$ which is exactly the way it is done in the applications later.[6] Since we are looking for the onset of an instability in the channels P, C and D, we must consider the case that these instabilities are expressed

[6] We will highlight this aspect later when summarising the method before application in chapter 3.

by divergent behaviour and therefore a steep increase of the respective component of the channel. For that reason, it is not wise to use the Euler scheme Eq. (2.143) in terms of a linear discretization. Instead, we propose the following method.

We apply Eq. (2.143) on the channels with a variable step-size ΔT_i:

$$\begin{aligned}
\Delta T_i =& \min\left(\frac{1}{20}T_i, \frac{1}{20}\max|P^{l,l'}(\boldsymbol{q})|, \frac{1}{20}\max|D^{l,l'}(\boldsymbol{q})|, \frac{1}{20}\max|C^{l,l'}(\boldsymbol{q})|\right),\\
T_{i+1} =& T_i - \Delta T_i,\\
P^{l,l'}_{i+1}(\boldsymbol{q}) =& P^{l,l'}_i(\boldsymbol{q}) + \left(-\frac{d}{dT}P^{l,l'}(\boldsymbol{q})\right)\Delta T_i,\\
D^{l,l'}_{i+1}(\boldsymbol{q}) =& D^{l,l'}_i(\boldsymbol{q}) + \left(-\frac{d}{dT}D^{l,l'}(\boldsymbol{q})\right)\Delta T_i,\\
C^{l,l'}_{i+1}(\boldsymbol{q}) =& C^{l,l'}_i(\boldsymbol{q}) + \left(-\frac{d}{dT}C^{l,l'}(\boldsymbol{q})\right)\Delta T_i.
\end{aligned}$$

Where $\left(-\frac{d}{dT}P^{l,l'}(\boldsymbol{q})\right)$ is recovered from the RHS of the flow equation. This procedure takes two considerations into account. At first, the scaling of the steps with $\frac{1}{20}T_i$ leads to a differential equation solver which (in absolute numbers) takes larger steps in the beginning and smaller steps for lower temperatures. Since we expect that the instabilities happen to occur at smaller scales, this step-size ensures that the solver carefully approaches the temperature region of interest while also not wasting computational power on irrelevant scale regimes. At some point, one component of the P, C or D channel will diverge if the formation of an instability sets on. At this point, the second criterion $\max|X^{l,l'}(\boldsymbol{q})|$ kicks in which reduces the step-size even more if this instability becomes overwhelmingly steep. While this Euler scheme looks at first glance quite simple, we will see later that it is a sufficient way of solving the flow equations and find the respective instabilities. A recent study comparing an adaptive Euler integrator with various other schemes for the square lattice Hubbard model revealed that no qualitative changes are to be expected by using more sophisticated integrators and no dramatic changes in quantitative results were reported [8]. Since we are already confronted with the challenging bubble integrals in the TUFRG implementation, we will allow us to refrain from more complex differential integrator schemes to keep computation times low.

The value of $\frac{1}{20}$ in the adaptive Euler is purely empirical and maybe other values can be used to improve the effectiveness of the scheme. Since the numerical bottleneck lies in the calculation the bubble integrations, the small computational speedups which could be generated here are deemed as negligible.

As a final remark on solving the differential equations, it should not only be mentioned how to start the flow, but also how to end it. We will stop the solver if the absolute value of any component of the P, C or D channel becomes larger than $3W$. If no instability occurs, we will also implement a fixed threshold T_{Stop}, at which we stop solving the flow equations. This threshold depends on the model we investigate, but in general it will be something between 10^{-6} and 10^{-4}.

2.3.5 Solving the gap equation

For a last minor aspect we want to focus once again on the calculation of the superconducting gap function before summing up the whole procedure. We remind ourselves that the gap can be derived from solving the eigenvalue equation of the pairing interaction $V_{\boldsymbol{k},\boldsymbol{k}'}$:

$$\Delta_{\boldsymbol{k}} = -\sum_{\boldsymbol{k}'} V_{\boldsymbol{k},\boldsymbol{k}'}\frac{\Delta_{\boldsymbol{k}'}}{2\xi_{\boldsymbol{k}'}}\tanh\left(\frac{\xi_{\boldsymbol{k}'}}{2T_c}\right) = -\sum_{\boldsymbol{k}'}\tilde{V}_{\boldsymbol{k},\boldsymbol{k}'}\Delta_{\boldsymbol{k}'}. \tag{2.144}$$

here we absorbed everything besides the gap itself on the right hand side by introducing $\tilde{V}_{\boldsymbol{k},\boldsymbol{k}'}$. From the construction of the superconducting channel Φ^P in the TUFRG section 1.2, it becomes clear that the pairing interaction is precisely given by (compare Eq. (2.49)):

$$V_{\boldsymbol{k},\boldsymbol{k}'} = \Phi^P(\boldsymbol{q}=0,\boldsymbol{k},\boldsymbol{k}'). \tag{2.145}$$

Therefore, if we find a diverging P channel in our TUFRG calculations, we have to reconstruct the initial superconducting channel eventually by the definition of the form factor expansion using the final P channel:

$$\Phi^P(\boldsymbol{q}=0,\boldsymbol{k},\boldsymbol{k}') = \sum_{l,l'} P^{l,l'}(\boldsymbol{q}=0) \times f_l^*(\boldsymbol{k}) f_{l'}(\boldsymbol{k}'), \tag{2.146}$$

which can be done directly without dealing with any further challenges. Then, by inserting Eq. (2.145) into Eq. (2.144) we get:

$$\Delta_{\boldsymbol{k}} = -\sum_{\boldsymbol{k}'} \Phi^P(\boldsymbol{q}=0,\boldsymbol{k},\boldsymbol{k}') \frac{\Delta_{\boldsymbol{k}'}}{2\xi_{\boldsymbol{k}'}} \tanh\left(\frac{\xi_{\boldsymbol{k}'}}{2T_c}\right), \tag{2.147}$$

where T_c is the temperature T we stopped our flow at. If this happens to be very small, we can also approximate the eigenvalue equation as:

$$\Delta_{\boldsymbol{k}} = -\sum_{\boldsymbol{k}'} \Phi^P(\boldsymbol{q}=0,\boldsymbol{k},\boldsymbol{k}') \Delta_{\boldsymbol{k}'}. \tag{2.148}$$

The diagonalization of the superconducting channels will then deliver the leading gap functions as discussed in section 1.2. This final aspect closes the discussion of the implementation of the flow equation. After a short précis and description of the workflow, we will proceed to the application of the numerical machinery as it was laid out here.

2.3.6 Summary and workflow

In this last section, the TUFRG method and implementation is summarized such that the reader is well equipped to proceed to the applications of the method to the triangular lattice systems in chapter 3. We will furthermore describe how the *workflow* of this method in practice usually looks like. This workflow is not hypothetical, but we will pick these notions up again in the first application as a hands-on example of how to apply this framework.

The TUFRG is a method to treat a given Hamiltonian. In our case we developed this method towards the application on a SU(2)-invariant Hubbard model on a triangular lattice with different - possibly long-range - hoppings and interactions:

$$\begin{aligned} H = &-\sum_n \sum_{\langle ij\rangle_n} \sum_\sigma t_n \left(c_{i\sigma}^\dagger c_{j\sigma} + \text{h.c.}\right) - \mu \sum_{i\sigma} n_{i\sigma} \\ &+ U \sum_i n_{i\uparrow} n_{i\downarrow} + \sum_n \sum_{\langle ij\rangle_n} \sum_{\sigma\sigma'} V_n n_{i\sigma} n_{j\sigma'}. \end{aligned} \tag{2.149}$$

The selection of the kinetic parameters t_n and μ will define the energy dispersion $\xi(\boldsymbol{k})$ and will therefore affect the bubble integrations. The choice of interaction parameters U, V_n affects the vertices of the right hand side of the TUFRG flow equations, since they will be projected onto the channels as initial conditions. By entertaining an overly simplified statement, the application of the TUFRG to this

Hamiltonian is *just solving three differential equations*:

$$\begin{aligned}
\frac{d}{dT}P^{l,l'}(\boldsymbol{q}) =& \sum_{l_1,l_2} V^P_{l,l_1}(\boldsymbol{q}) \times \dot{B}^-_{l_1,l_2}(\boldsymbol{q}) \times V^P_{l',l_2}(\boldsymbol{q}) \\
\frac{d}{dT}D^{l,l'}(\boldsymbol{q}) =& \sum_{l_1,l_2} \Big[V^C_{l,l_1}(\boldsymbol{q}) \times \dot{B}^+_{l_1,l_2}(\boldsymbol{q}) \times V^D_{l',l_2}(\boldsymbol{q}) \\
&+ V^D_{l,l_1}(\boldsymbol{q}) \times \dot{B}^+_{l_1,l_2}(\boldsymbol{q}) \times V^C_{l',l_2}(\boldsymbol{q}) - 2V^D_{l,l_1}(\boldsymbol{q}) \times \dot{B}^+_{l_1,l_2}(\boldsymbol{q}) \times V^D_{l',l_2}(\boldsymbol{q}) \Big], \\
\frac{d}{dT}C^{l,l'}(\boldsymbol{q}) =& \sum_{l_1,l_2} V^C_{l,l_1}(\boldsymbol{q}) \times \dot{B}^+_{l_1,l_2}(\boldsymbol{q}) \times V^C_{l',l_2}(\boldsymbol{q}).
\end{aligned}$$

For a selected amount of $N_{\boldsymbol{q}}$ momenta and N_l form factors, this results into $3 \times N_{\boldsymbol{q}} \times N_l^2$ equations to solve for each RG step (where we saw in the previous sections that a lot of these entries can be gathered for free by symmetry relations). We will use between 180 and 1092 momentum points and between 19 and 61 form factors in our calculations, see Fig. 2.12. These differential equations are solved by applying the Euler scheme as presented in the previous section. The right hand side of these equations consists of the contraction of three objects: two vertices $V^X_{l,l'}(\boldsymbol{q})$ and one bubble integration $\dot{B}^{\pm}_{l,l'}(\boldsymbol{q})$. We showed in section 2.2.3 that the vertices will decompose into four parts: the projection of the initial conditions, the channel itself and the cross-channel projections of the other two channels onto the selected channel:

$$\begin{aligned}
V^P_{l,l'}(\boldsymbol{q}) =& V^{0,P}_{l,l'}(\boldsymbol{q}) + P^{l,l}(\boldsymbol{q}) + V^{D\to P}_{l,l'}(\boldsymbol{q}) + V^{C\to P}_{l,l'}(\boldsymbol{q}), \\
V^D_{l,l'}(\boldsymbol{q}) =& V^{0,D}_{l,l'}(\boldsymbol{q}) + D^{l,l}(\boldsymbol{q}) + V^{P\to D}_{l,l'}(\boldsymbol{q}) + V^{C\to D}_{l,l'}(\boldsymbol{q}), \\
V^C_{l,l'}(\boldsymbol{q}) =& V^{0,C}_{l,l'}(\boldsymbol{q}) + C^{l,l}(\boldsymbol{q}) + V^{P\to C}_{l,l'}(\boldsymbol{q}) + V^{D\to C}_{l,l'}(\boldsymbol{q}),
\end{aligned}$$

where also in section 2.2.3 the explicit form of the cross-channel projections were derived. These objects are in a simple form due to the usage of the properties of the form factors. The concept of projecting the initial conditions of a given interacting Hamiltonian into the channels was presented in section 2.3.1. None of these tasks is either numerically or analytically difficult. In fact, both of these objects can be implemented in a code in a straight-forward fashion without further challenges.

A more demanding numerical difficulty is presented by the bubble integration $\dot{B}^{\pm}_{l,l'}(\boldsymbol{q})$ which connects the vertices. We showed in section 2.3.2 how for a fixed momentum $\boldsymbol{q}$ not all combinations of l, l' actually have to be calculated, but can be restored by the symmetry properties of the plane wave form factors. Still, for lower and lower scales, the integrand of this object will develop sharper features and is therefore harder to integrate. We presented an adaptive scheme to treat these problematic functions, but nevertheless the bubble integrations will be the computational bottleneck.

Once the bubble integrations are performed, the right hand side of the flow equations can be evaluated and the Euler scheme is applied. As described before, we will solve this equations starting at the bandwidth $T_0 = W$ going downwards to 0. We will stop the flow if one of the channel components exceeds $3W$ which we install as a criterion for an instability. If no instability occurs, a hard threshold at small temperatures will stop the flow eventually.

If an instability occurs, we will basically be confronted with two options:

1. A divergence in C or D channel was found. In this case, we will have found a magnetic (C) or charge-density (D) instability. Typically, for plain SDWs or CDWs the instability will only express itselfs by peaks in the on-site component, i.e. $C^{1,1}(\boldsymbol{q})$ or $D^{1,1}(\boldsymbol{q})$. We will then investigate the momentum-resolved vertex for the on-site component to extract the position of the peak in momentum space which is the modulation vector of the instability. Nevertheless, it is

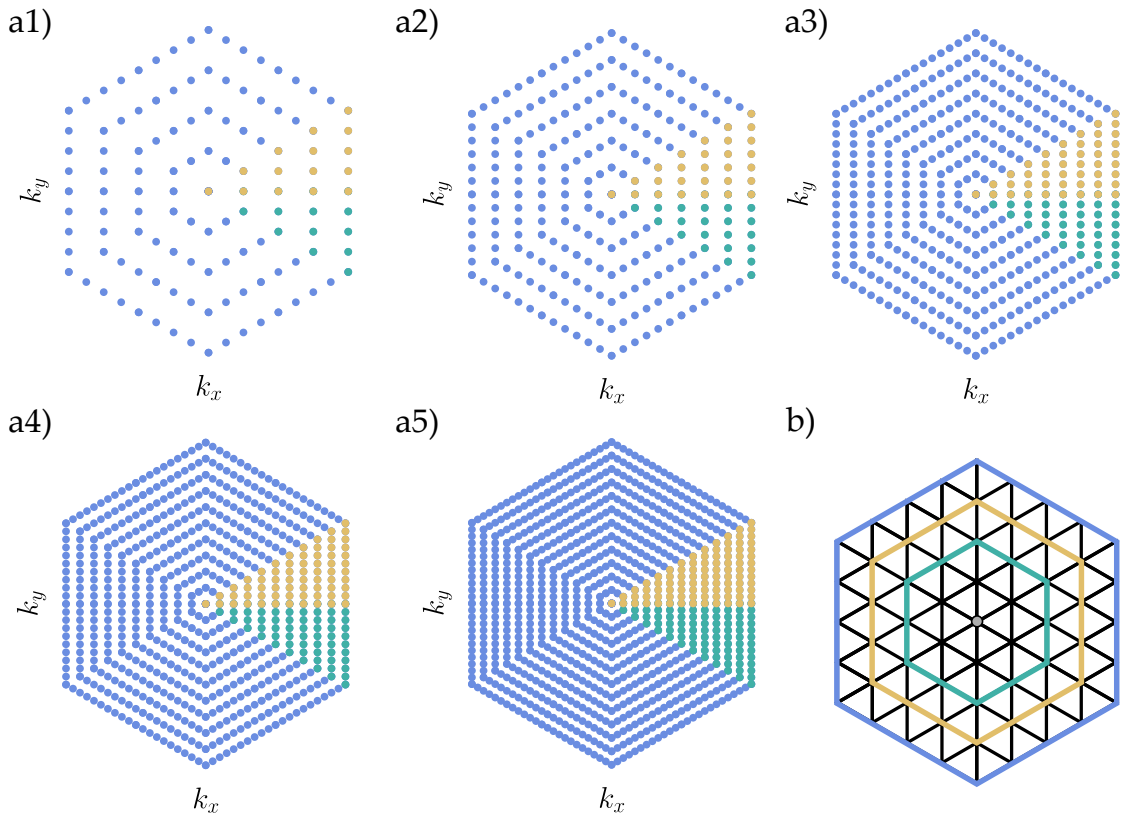

Figure 2.12: **Possible resolutions for momenta and form factors:** a1)-a5) Resolutions for discretization of the Brillouin zone with momenta $\boldsymbol{q}$. In this work we will use with five different resolutions, $N_{\boldsymbol{q}} = 180, 336, 540, 792$ and 1092. The shaded area indicates for which momenta the flow equation is actually calculated (yellow) and for which momenta the flow equations are derived by mirror symmetry (green) and rotation symmetry (blue). b) Different choices for the selection of form factors N_l. In this work, we will use three different hexagonal form factor shells: $N_s = 2$ (19 form factors,green), $N_s = 3$ (37 form factors, yellow) and $N_s = 4$ (61 form factors, blue).

also possible that other form-factor components grow which is typically connected to quantum spin hall states [81]. However, in this work these phenomena will only be of interest for a minor aspect in the application for spinless models.

2. A divergence in the P channel was found. This indicates the onset of a superconducting instability. In this case, the peak is almost exclusively at zero momentum $P^{l,l'}(\boldsymbol{q} = 0)$, but a lot of different combinations of l, l' are diverging simultaneously. The combination of all these form factor combinations is indicative of the emerging symmetry of the gap function. We furthermore derive the pairing interaction from the P channel as described in section 2.3.5 and extract the leading gap function $\Delta(\boldsymbol{k})$ to investigate the symmetry of the gap. This gap will then be one of the basis functions of the C_{6v} irreps as described in Figure 1.7.

In each case, it is always advised to inspect the behaviour of the bubble integrations while the flow is calculated. For that reason, we will also save and return the bubbles at specific symmetry points for $\boldsymbol{q}$ to ensure ourselves that the adaptive integration routine worked without failure. We can compare the behaviour of these bubble integrations with analytical results in some cases which we will be presented in the next chapter when applying the method.

As a final remark it should be mentioned that the code which implements the TUFRG method, is written in the **Julia** programming language. We implemented a simple parallelization scheme by using the inbuilt *distributed* package for shared memory parallelization. Here, we used the parallel map

(**pmap**) approach which is beneficial if the chunks of code we want to parallelize have relatively long execution times. This is the case for the bubble integrations. The optimal way to parallelize the bubble integrations is therefore to implement $\boldsymbol{q}/12$ worker, each worker performing one of the integrations $\dot{B}^{\pm}_{l,l'}(\boldsymbol{q})$ for all l, l'. After the application of the pmap, the code is executed serially.

CHAPTER 3

Application: Instabilities in Triangular Lattice Hubbard Models

In this chapter, we will finally apply the developed numerical machinery to investigate the possibility of competing instabilities in three different triangular lattice Hubbard models in the vicinity of Van Hove singularities.

In application A, we will treat an extended $\mathrm{SU}(2)$-invariant Hubbard model which we used as main example in section 2 to develop and motivate the aspects of the numerical implementation. In more detail, we will treat two variations of this model. At first, the model is reduced to only a small set of interacting parameters, acting as a *paradigmatic model*. Here, it will become apparent that already in this simple scenario an extensive amount of various instabilities towards superconductivity featuring different gap symmetries are detectable. We will use this paradigmatic model to demonstrate the TUFRG workflow as presented in section 2.3.6 and then proceed to calculate a phase diagram. Then, in a second variation of the model, we will add longer-ranged hoppings and electron-electron interactions to describe a tTMD heterobilayer system as described in section 1.3. Interestingly, a lot of qualitative results of this *realistic* model are already present in the paradigmatic case. The results of this application were published in [29]. Original figures of this publication used in this section are marked as such. For visibility, we will not adapt the color scheme of this thesis to those figures to highlight their origin.

In application B, the model of interest is given by a spinless Hubbard model with nearest-neighbour interaction V_1 and nearest-neighbour hopping t. Here, we will investigate the effects of the nearest-neighbour interaction V_1 for an attractive and a repulsive case, revealing instabilities towards superconductivity inhabiting various gap symmetries. Moreover, besides an *ordinary* charge density wave stemming from the perfect nesting, also a charge instability with $\boldsymbol{q} = 0$ emerges, whose origin is grounded in a different mechanism. These results haven been published in paper [30]. In this publication, we used the proposed model to investigate qualitative differences of the results coming from the TUFRG in comparison to the patching scheme. The results of the patching scheme are out of the scope of this chapter and we will focus exclusively on the TUFRG data in this section.

In application C, we will treat a spinful model without $\mathrm{SU}(2)$-invariance leading to two non-degenerate bands regarding the spin degrees of freedom. Effectively, this model will describe a tTMD homobilayer system where we also include the possibility of applying a displacement field as described in section 1.3. With the loss of the spin symmetry, this model will be more complex than the model in application A. We will show which tweaks and adjustments have to be made in contrast to the implementation in section 2.3 to render this application feasible again. At first, we will investigate how the vertices of magnetic instabilities at Van Hove filling will change by increasing the displacement field. Following this, we will select some special values of the field and examine the effect of altering the filling of the system such that we will again find instabilities of unconventional superconductivity. These results are preliminary and more in a sense of being *proof-of-concept* and have not been published yet.

3.1 Application A: Spinful triangular models with SU(2)-invariance

The triangular lattice Hubbard model is a suitable description for correlated electrons exposed to geometrical frustration. The model happens to feature a rich variety of exotic phases, including various form of magnetism, unconventional superconductivity, spin-liquid phases and charge density phenomena (e.g. see reviews [4],[87]). As prepared in this work, we will investigate this model at Van Hove filling to study the possibility of competing instabilities. For our case, a foundational work treating this model is presented by the application of the patching FRG scheme [41]. Furthermore, competing instabilities at Van Hove filling were also already investigated in terms of Quantum Monte Carlo [18], Parquet RG [75] and density-matrix RG [105] studies. Also, several (F)RG studies have been conducted in addition to complementary many-body methods which reveal the onset of unconventional and topological superconductivity in triangular lattice Hubbard models [88, 56, 110, 111, 13, 33, 97].

Naturally, some of the basic equations and objects shown in the following subsection were already presented in this thesis at earlier sections. Nevertheless, we decided to recapitulate all basic objects here again to deliver a practical summary of the desired application.

3.1.1 Model and implementation

The general Hamiltonian is given by:

$$\begin{aligned} H = &- \sum_n \sum_{\langle ij\rangle_n} \sum_\sigma t_n \left(c^\dagger_{i\sigma} c_{j\sigma} + \text{h.c.} \right) - \mu \sum_{i\sigma} n_{i\sigma} \\ &+ U \sum_i n_{i\uparrow} n_{i\downarrow} + \sum_n \sum_{\langle ij\rangle_n} \sum_{\sigma\sigma'} V_n n_{i\sigma} n_{j\sigma'}. \end{aligned} \tag{3.1}$$

where $c^{(\dagger)}_{i\sigma}$ annihilates(creates) an electron on site i with spin σ. For the kinetic part, we allow for nth-nearest neighbour hopping, indicated by the hopping t_n and the sum over nth-nearest neighbours $\langle ij\rangle_n$. Moreover, the chemical potential μ coupling to the density operator $n_{i\sigma}$ is included allowing for varying the filling of the system. For the interactions we introduce a Hubbard interaction U representing the on-site Coulomb interaction and nth-nearest neighbour density-density interactions V_n. For the kinetic and the interacting part, we will maximally allow for $n = 3$ regarding hoppings and interactions. By defining this model on a triangular lattice, (see Fig. 3.1) the dispersion of this model is given by:

$$\begin{aligned} \xi(\boldsymbol{k}) = \epsilon(\boldsymbol{k}) - \mu \\ &- 2t_1[\cos(k_y) + 2\cos(k_y/2)\cos(\sqrt{3}k_x/2)] \\ &- 2t_2[2\cos(3k_y/2)\cos(\sqrt{3}k_x/2) + \cos(\sqrt{3}k_x)] \\ &- 2t_3[\cos(2k_y) + 2\cos(k_y)\cos(\sqrt{3}k_x)] - \mu, \end{aligned} \tag{3.2}$$

derived by a Fourier transform of the kinetic part in Eq. (3.1). The dispersion will feature a Van Hove singularity at the $\boldsymbol{M}_i$ points of the Brillouin zone where the density of states will feature a logarithmic divergence:

$$\epsilon(\boldsymbol{M}_i) = 2(t_1 + t_2 - 3t_3) = \epsilon_{\text{VH}}, \tag{3.3}$$

$$\rho(\epsilon) \propto \log \frac{W}{|\epsilon - \epsilon_{\text{VH}}|}, \tag{3.4}$$

where W is the bandwidth of the model. If only nearest-neighbour hoppings t_1 are included, then the Fermi surface at Van Hove filling is nested with nesting vector $\boldsymbol{Q}$. This vector is equivalent to one of the $\boldsymbol{M}_i$ vectors by backfolding. We want to implement the TUFRG as described in chapter 2. Starting

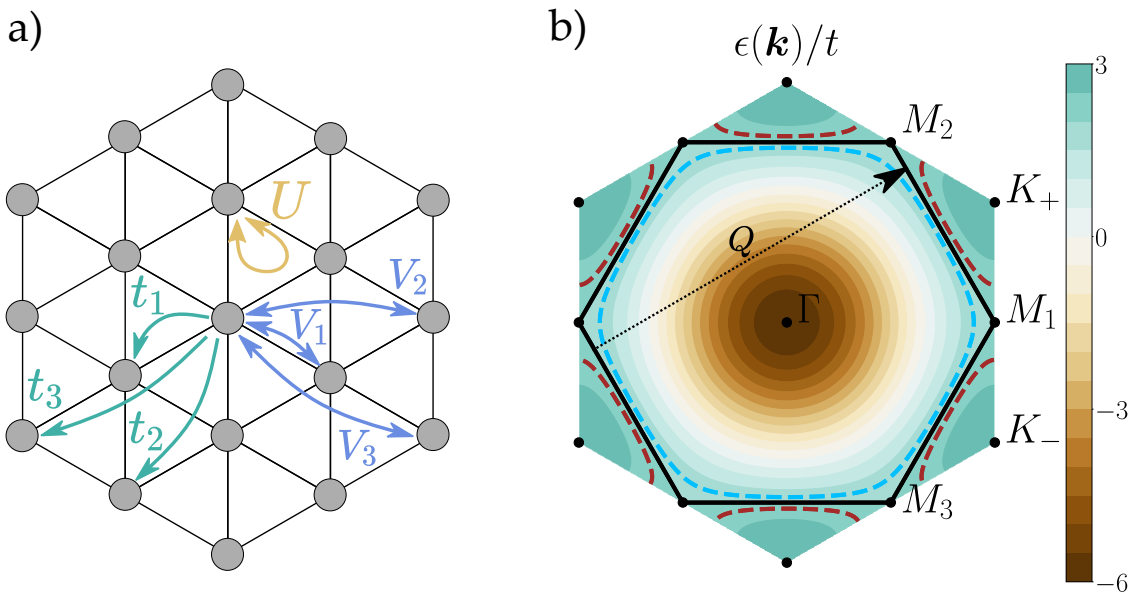

Figure 3.1: SU(2)**-invariant Hubbard model on a triangular lattice:** a) Real space lattice with hoppings $t_{1,2,3}$, Hubbard interaction U and density-density interactions $V_{1,2,3}$. b) Dispersion for $t_1 = 1.0$ and $t_2 = t_3 = 0.0$. The Fermi surfaces correspond to $\mu = 1.9t_1$ (blue), $\mu = 2t_1$ (black) and $\mu = 2.1t_1$ (red). The $\boldsymbol{M}_{1,2,3}$ points are Van Hove singularities inhabiting a logarithmic divergence regarding the density of states. At $\mu = 2.0t_1$ and t_1 only, the model features perfect nesting with nesting vector $\boldsymbol{Q}$.

from the SU(2)-invariant flow equations Eqs. (2.45)-(2.47), we gain the TUFRG flow equations:

$$\frac{d}{d\Lambda}P^{l,l'}(\boldsymbol{q}) = \sum_{l_1,l_2} V^P_{l,l_1}(\boldsymbol{q}) \times \dot{B}^-_{l_1,l_2}(\boldsymbol{q}) \times V^P_{l',l_2}(\boldsymbol{q}), \tag{3.5}$$

$$\begin{aligned}\frac{d}{d\Lambda}D^{l,l'}(\boldsymbol{q}) = \sum_{l_1,l_2} \Big[& V^C_{l,l_1}(\boldsymbol{q}) \times \dot{B}^+_{l_1,l_2}(\boldsymbol{q}) \times V^D_{l',l_2}(\boldsymbol{q}) + V^D_{l,l_1}(\boldsymbol{q}) \times \dot{B}^+_{l_1,l_2}(\boldsymbol{q}) \times V^C_{l',l_2}(\boldsymbol{q}) \\ & - 2V^D_{l,l_1}(\boldsymbol{q}) \times \dot{B}^+_{l_1,l_2}(\boldsymbol{q}) \times V^D_{l',l_2}(\boldsymbol{q}) \Big],\end{aligned} \tag{3.6}$$

$$\frac{d}{d\Lambda}C^{l,l'}(\boldsymbol{q}) = \sum_{l_1,l_2} V^C_{l,l_1}(\boldsymbol{q}) \times \dot{B}^+_{l_1,l_2}(\boldsymbol{q}) \times V^C_{l',l_2}(\boldsymbol{q}). \tag{3.7}$$

Here, the kinetic information of the Hamiltonian Eq. (3.1) is encoded in the bubble integrations[1]:

$$\dot{B}(\boldsymbol{q})^+_{l,l'} = +\int_{\boldsymbol{p}} \frac{n'_F(\xi(\boldsymbol{q}+\boldsymbol{p})) - n'_F(\xi(\boldsymbol{p}))}{\xi(\boldsymbol{q}+\boldsymbol{p}) - \xi(\boldsymbol{p})} f_l(\boldsymbol{p}) f^*_{l'}(\boldsymbol{p}), \tag{3.8}$$

$$\dot{B}(\boldsymbol{q})^-_{l,l'} = -\int_{\boldsymbol{p}} \frac{n'_F(\xi(\boldsymbol{q}+\boldsymbol{p})) + n'_F(\xi(-\boldsymbol{p}))}{\xi(\boldsymbol{q}+\boldsymbol{p}) + \xi(-\boldsymbol{p})} f_l(\boldsymbol{p}) f^*_{l'}(\boldsymbol{p}), \tag{3.9}$$

where we used the temperature flow scheme as described in section 2.2.3 such that n'_F is the temperature derivative of the Fermi function. The cross-channel projections are given as described in section

[1] Caution: notice that in the definition here, a global sign was included in contrast to the bubbles in section 2 as explained in section 2.3.3.

2.2.3. For the P channel:

$$V^P_{l,l'}(\boldsymbol{q}) = V^{0,P}_{l,l'}(\boldsymbol{q}) + P^{l,l}(\boldsymbol{q}) + V^{D\to P}_{l,l'}(\boldsymbol{q}) + V^{C\to P}_{l,l'}(\boldsymbol{q}), \tag{3.10}$$

$$V^{D\to P}_{l,l'}(\boldsymbol{q}) = \sum_L \tilde{D}^{L,-L+l-l'}(-\boldsymbol{R}_{l'} - \boldsymbol{R}_L) \times e^{-i\boldsymbol{q}\boldsymbol{R}_L}, \tag{3.11}$$

$$V^{C\to P}_{l,l'}(\boldsymbol{q}) = \sum_L \tilde{C}^{L,-L+l+l'}(-\boldsymbol{R}_L + \boldsymbol{R}_{l'}) \times e^{-i\boldsymbol{q}(\boldsymbol{R}_L - \boldsymbol{R}_{l'})}. \tag{3.12}$$

For the D channel:

$$V^D_{l,l'}(\boldsymbol{q}) = V^{0,D}_{l,l'}(\boldsymbol{q}) + D^{l,l}(\boldsymbol{q}) + V^{P\to D}_{l,l'}(\boldsymbol{q}) + V^{C\to D}_{l,l'}(\boldsymbol{q}), \tag{3.13}$$

$$V^{P\to D}_{l,l'}(\boldsymbol{q}) = \sum_L \tilde{P}^{L,L-l-l'}(-\boldsymbol{R}_l) \times e^{-i\boldsymbol{q}(\boldsymbol{R}_L - \boldsymbol{R}_{l'})}, \tag{3.14}$$

$$V^{C\to D}_{l,l'}(\boldsymbol{q}) = \sum_L \tilde{C}^{L,L-l+l'}(-\boldsymbol{R}_l) \times e^{-i\boldsymbol{q}\boldsymbol{R}_L}. \tag{3.15}$$

And for the C channel:

$$V^C_{l,l'}(\boldsymbol{q}) = V^{0,C}_{l,l'}(\boldsymbol{q}) + C^{l,l}(\boldsymbol{q}) + V^{P\to C}_{l,l'}(\boldsymbol{q}) + V^{D\to C}_{l,l'}(\boldsymbol{q}), \tag{3.16}$$

$$V^{P\to C}_{l,l'}(\boldsymbol{q}) = \sum_L \tilde{P}^{L,-L+l+l'}(-\boldsymbol{R}_L + \boldsymbol{R}_{l'}) \times e^{-i\boldsymbol{q}(\boldsymbol{R}_L - \boldsymbol{R}'_l)}, \tag{3.17}$$

$$V^{D\to C}_{l,l'}(\boldsymbol{q}) = \sum_L \tilde{D}^{L,L-l+l'}(-\boldsymbol{R}_l) \times e^{-i\boldsymbol{q}\boldsymbol{R}_L}. \tag{3.18}$$

Finally, the interactions of the model Hamiltonian Eq. (3.1) are manifested in the initial conditions as derived in section 2.3.1:

$$V^{0,P}_{1,1}(\boldsymbol{q}) = V^{0,C}_{1,1}(\boldsymbol{q}) = U \tag{3.19}$$

$$V^{0,P}_{l,l}(\boldsymbol{q}) = V^{0,C}_{l,l}(\boldsymbol{q}) = V_1, \qquad \text{for} : l \in \{2,3,4,5,6,7\} \tag{3.20}$$

$$V^{0,P}_{l',l'}(\boldsymbol{q}) = V^{0,C}_{l',l'}(\boldsymbol{q}) = V_2, \qquad \text{for} : l' \in \{10,11,14,15,18,19\} \tag{3.21}$$

$$V^{0,P}_{l'',l''}(\boldsymbol{q}) = V^{0,C}_{l'',l''}(\boldsymbol{q}) = V_3, \qquad \text{for} : l'' \in \{8,9,12,13,16,17\} \tag{3.22}$$

$$V^{0,D}_{1,1}(\boldsymbol{q}) = U + V_1 \sum_l e^{i\boldsymbol{R}_l\boldsymbol{q}} + V_2 \sum_{l'} e^{i\boldsymbol{R}_{l'}\boldsymbol{q}} + V_3 \sum_{l''} e^{i\boldsymbol{R}_{l''}\boldsymbol{q}}. \tag{3.23}$$

We will implement the TUFRG for the given model with resolutions as proposed in section 2.3.6. The main results are calculated with $N_{\boldsymbol{q}} = 540$ and hexagon shell $N_s = 4$, i.e. 61 plane wave form factors.

3.1.2 Demonstration of workflow: competition of magnetism and superconductivity

We will now demonstrate the proposed workflow as presented in section 2.3.6 for application of the TUFRG. For that purpose, we restrain ourselves to a simple model which only includes nearest-neighbour hopping $t = t_1$, Hubbard interaction U and the chemical potential μ and investigate instabilities in the vicinity of Van Hove filling. We showed in section 1.1 that hints for instabilities are already extractable from the particle-particle and particle-hole bubble. These effects are rooted in the logarithmic divergence of those objects. We recall the three possible sources of these divergencies:

1. A generic logarithmic divergence exists always for the particle-particle bubble $B^{\text{PP}}(0)$ as long as the dispersion inhabits inversion symmetry which is evidently true here.

2. The presence of the Van Hove singularity leads to a logarithmic divergence of the density of states which therefore also induces a logarithmic divergence in both bubbles.

3. If nesting is present, i.e. $\epsilon(\boldsymbol{k}) = -\epsilon(\boldsymbol{k}+\boldsymbol{Q})$ for some vector $\boldsymbol{Q}$, then the particle-hole bubble also gains a logarithmic divergence for $B^{\text{ph}}(\boldsymbol{Q})$.

At Van Hove filling and in the case of the two symmetry points $\boldsymbol{\Gamma}$, $\boldsymbol{M}$ this leads to:

$$B^{\text{pp}}(\boldsymbol{\Gamma}) \propto +\log^2\left(\frac{W}{T}\right) \qquad (\textit{Generic + Van Hove}), \tag{3.24}$$

$$B^{\text{ph}}(\boldsymbol{\Gamma}) \propto -\log\left(\frac{W}{T}\right) \qquad (\textit{Van Hove}), \tag{3.25}$$

$$B^{\text{pp}}(\boldsymbol{M}) \propto +\log\left(\frac{W}{T}\right) \qquad (\textit{Van Hove}), \tag{3.26}$$

$$B^{\text{ph}}(\boldsymbol{M}) \propto -\log^2\left(\frac{W}{T}\right) \qquad (\textit{Nesting + Van Hove}). \tag{3.27}$$

Therefore, the strongest tendencies towards instabilities are stemming from the particle-hole bubble with transfer momentum $\boldsymbol{M}$ and from the particle-particle bubble with transfer momentum $\boldsymbol{\Gamma} = \boldsymbol{0}$. As discussed in section 1.1, the first tendency describes the possibility of a SDW or CDW instability with modulation vector $\boldsymbol{M}$, while the latter tendency describes the possibility of an instability towards superconductivity with zero transfer momentum. We also discussed in section 1.1 that just from the initial interactions the onset of the superconductive instability is not possible if this initial interaction happens to be repulsive. Therefore, the superconductivity can only emerge, if the strong fluctuations of the particle-hole channels induce an attractive interaction component in the particle-particle channel under the renormalization procedure. So, magnetism and superconductivity are in competition in the present scenario. We will now study this competition in our TUFRG approach. At first, we will run a calculation exactly at Van Hove filling. In detail, these parameters are:

$$\begin{aligned} t &= 1.0, \\ U &= 4t, \\ \mu &= 2.0t. \end{aligned}$$

Here, we approximated $U = 4t$ to be a reasonable value for an intermediate interaction regime. We track the evolution of the maximal value of the P,C and D channel. As described in the implementation section, we will stop the flow if one of these components exceeds a value larger than $3W$ (the bandwidth is given as $W = 9t$ here). The result of the calculation can be seen in Fig. 3.2 a. We detect a flow to strong coupling which is mainly exerted in the C channel at a critical temperature of $T_c \approx \mathcal{O}(10^{-2}t)$. So, the first result of the TUFRG calculation indicates an instability towards magnetism. In a next step, we will investigate which component of the C channel inhabits the divergent peak. An examination reveals that the singular behaviour is only present in the on-site component regarding the form factors, i.e. $C^{1,1}(\boldsymbol{q})$. Therefore we display the momentum dependence of this object, as seen in Fig. 3.2 b. We acknowledge that the peaks are indeed near the different $\boldsymbol{M}$ points, signaling a SDW instability where the modulation is given by one of the vectors $\boldsymbol{q} = \boldsymbol{M}_{1,2,3}$. The actual realized SDW imposed by these vectors has to be calculated by methods beyond our implementation. Other studies point to the formation of an uniaxial or chiral SDW state [74, 70].

Conclusively, the emerging instability at Van Hove filling is no surprise and was already telegraphed by the strong double logarithmic divergence of the particle-hole channel. Nevertheless, we want to support ourselves with a sanity check. As discussed in chapter 2, the bubble integrations remain the most challenging part of the TUFRG for which we carefully implemented an adaptive integration routine. At first, we identify that the on-site bubble integrations and the bubbles are connected by:

$$\dot{B}(\boldsymbol{q})^{+}_{1,1} = \frac{d}{dT} B^{\text{ph}}(\boldsymbol{q}) \tag{3.28}$$

$$\dot{B}(\boldsymbol{q})^{-}_{1,1} = \frac{d}{dT} B^{\text{pp}}(\boldsymbol{q}) \tag{3.29}$$

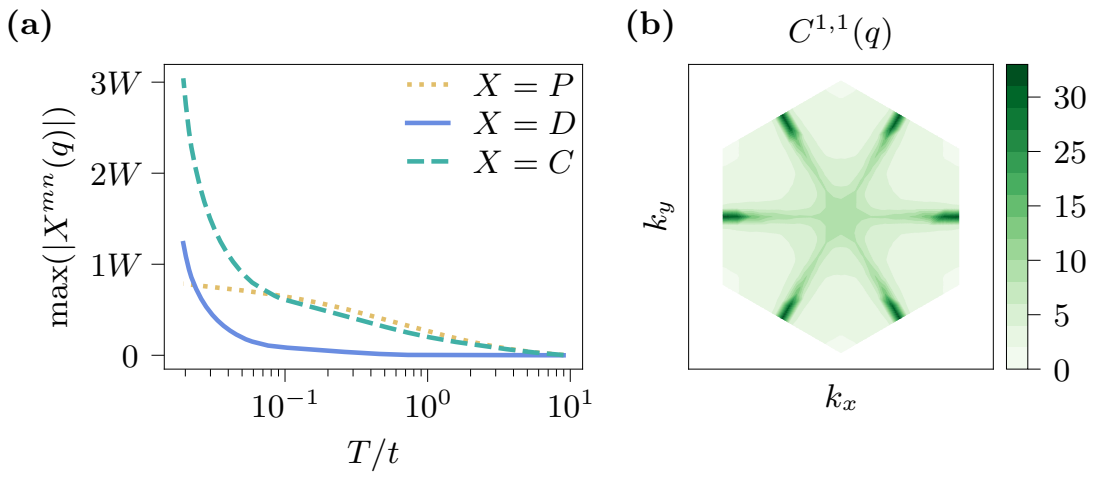

Figure 3.2: **TUFRG flow and singular vertex at Van Hove filling $\mu = 2t$:** The TUFRG calculation was done with $N_{\boldsymbol{q}} = 540$ momenta and on the hexagon shell $N_s = 4$. The Hubbard interaction was chosen as $U = 4t$. a) Evolution of the maximum absolute value of the respective channels P,C and D. We observe that the C channel will develop the strongest divergence for the chosen parameters. b) Momentum resolved on-site component of the magnetic channel $C^{1,1}(\boldsymbol{q})$ at the end of the flow. We register pronounced peaks at the $\boldsymbol{M}_i$ points.

Therefore, a comparison with the dependencies of the bubbles Eqs. (3.24)-(3.27) yields:

$$\dot{B}(\mathbf{\Gamma})^{-}_{1,1} \propto -\log\left(\frac{W}{T}\right)\frac{1}{T} \quad \Longleftrightarrow \quad T \times \dot{B}(\mathbf{\Gamma})^{-}_{1,1} \propto -\log\left(\frac{W}{T}\right), \tag{3.30}$$

$$\dot{B}(\mathbf{\Gamma})^{+}_{1,1} \propto +\frac{1}{T} \quad \Longleftrightarrow \quad T \times \dot{B}(\mathbf{\Gamma})^{+}_{1,1} \propto +1, \tag{3.31}$$

$$\dot{B}(\boldsymbol{M})^{-}_{1,1} \propto -\frac{1}{T} \quad \Longleftrightarrow \quad T \times \dot{B}(\boldsymbol{M})^{-}_{1,1} \propto -1, \tag{3.32}$$

$$\dot{B}(\boldsymbol{M})^{+}_{1,1} \propto +\log\left(\frac{W}{T}\right)\frac{1}{T} \quad \Longleftrightarrow \quad T \times \dot{B}(\boldsymbol{M})^{+}_{1,1} \propto +\log\left(\frac{W}{T}\right). \tag{3.33}$$

So, we reach at a set of benchmark values which ensure the correctness of our bubble integrations. We will save these quantities while performing the flow calculations such that we can check the fulfillment of these conditions after successfully detecting an instability. The results of these checks are displayed in Fig. 3.3. Indeed, the behaviour of the bubble integrations is reproduced and we are confident in the correctness of our application.

In the next step, we want to investigate the model by changing the electronic filling. We will treat both cases here: underdoping $\mu < \mu_{\mathrm{VH}}$ and overdoping $\mu > \mu_{\mathrm{VH}}$. We will start with the underdoping case. In either filling situation, the Fermi surface is not directly at the Van Hove point anymore (cf. Fig. 3.1 b) such that the the analysis for Eqs. (3.24)-(3.27) is not completely valid. Still, we expect that remnants of the logarithmic divergence $\rho(\epsilon) \propto \log(W/|\epsilon - \epsilon_{\mathrm{VH}}|)$ are still present since we will tune the Fermi surface only slightly away from the this scenario. In terms of competing instabilities, we are now interested if the weakening of the divergence leads to a different hierarchy of the singular behaviour, i.e. if under the RG flow an attractive interaction for the particle-particle channel emerges. For that purpose, we change the chemical potential to $\mu = 1.96t$ and perform the TUFRG calculation.

The results of these calculations are displayed in Fig. 3.4. Here, we detect an instability towards superconductivity at $T_c \approx \mathcal{O}(10^{-5}t)$. Components of the particle-hole related channels C and D still gain substantial increments in the beginning of the flow until a turning point at $T_c \approx \mathcal{O}(10^{-2}t)$ is

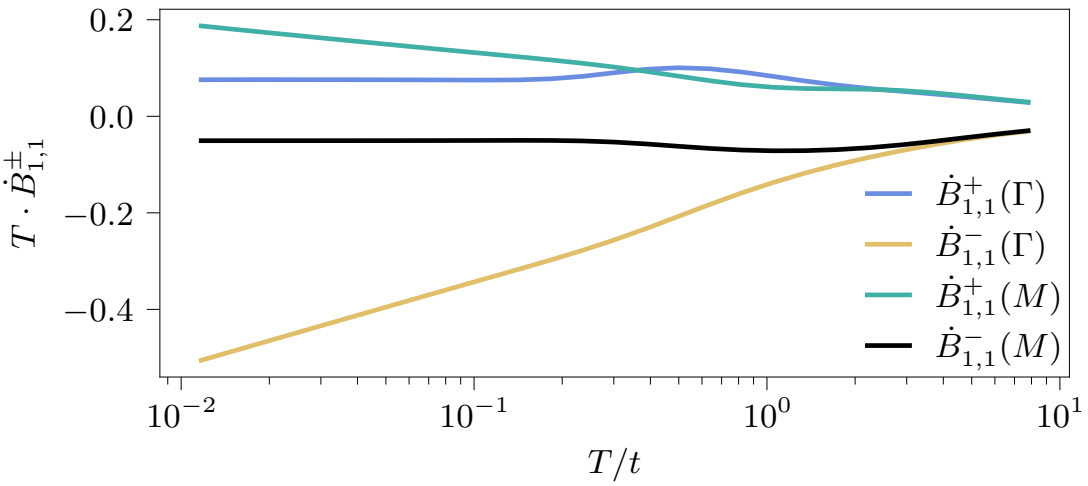

Figure 3.3: **Consistency check at Van Hove filling by tracking bubble integrations while performing the TUFRG calculation:** We chose an angular resolution of $N_A = 120$ in our calculations as described in section 2.3.2. The bubble integrations multiplied with T fulfill the checks Eqs. (3.30)-(3.33). The bubbles featuring a double logarithmic divergence develop a linear slope at low T while the bubbles with the single logarithmic divergence become constant.

reached, after which these channels saturate. The extremely sharp behaviour of the P channel does look peculiar at first glance, but can be reasonable explained. For the majority of the flow, some component of the P channel will be the largest absolute value. While the flow continues, the growth of the components of the C and D channel generate new momentum structures by the renormalization procedure which eventually lead to contributions to some other P channel components. At some point, this component will overtake the former largest component, such that the tracking of the absolute value in Fig. 3.4 a will feature the apparent sharp kink.
In the Van Hove case, the singular C channel component was only given by the on-site vertex, i.e. $(l, l') = (1, 1)$. In the present case of an instability towards superconductivity, the P channel does actually inhabit divergent momentum peaks in several combinations of (l, l') (and interestingly, not in the on-site component). For example, we displayed the $(l, l') = (61, 61)$ component in Fig. 3.4 b, where a sharp momentum peak sits at $\mathbf{\Gamma}$, i.e. transfer momentum $\boldsymbol{q} = 0$.

For a more concise overview about the diverging components of $P^{l,l'}(\boldsymbol{q})$ we advise to Fig. 3.5 a. The peaks in this channel do always only occur at the $\mathbf{\Gamma}$-point, and only differ in being either a positive or negative valued peak. We see that all significant peaks are actually located in combinations of form factors (l, l') which lie in the outmost hexagon shell. By reminding ourselves how we constructed the different lattice harmonics in section 1.2, it is safe to assume that the symmetry of the corresponding leading gap function of channel P on hand will be of higher order. Therefore, we proceed and calculate the leading gap function as described in the implementation section, namely we reconstruct the pairing interaction Φ^P from the P channel and diagonalize the eigenvalue equation of the BCS theory Eq. (1.49). The eigenvector corresponding to the highest eigenvalue is the leading gap function, depicted in Fig. 3.5 b. A comparison with the lattice harmonics in section 1.3 (Fig. 1.7) reveals that the symmetry of this gap corresponds to the A_2 irrep of 7th order. From Fig. 3.5 a it is obvious that the inclusion of long ranged form factors is absolutely crucial for resolving this gap symmetry. By the amount of zero crossings of the Fermi surface in Fig. 3.5 b we will call this instability an i-wave superconductor. The findings of our study here are consistent with previous patching scheme studies [41, 97]. Again, we want to check the correctness of these results by checking how the bubble integrations behaved while executing the TUFRG flow equations. Since we are still close - but not directly at - the Van Hove point, we expect some remnant effects of the logarithmic divergence before these

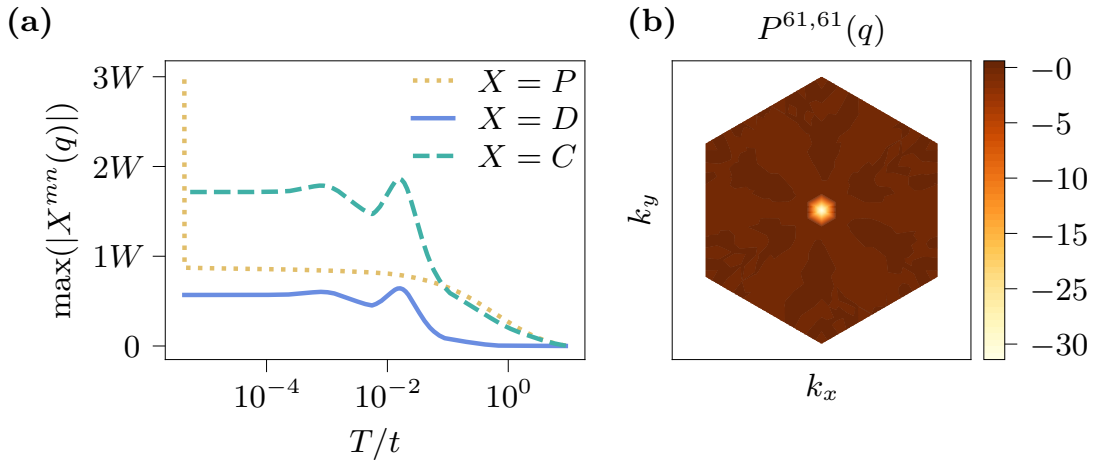

Figure 3.4: **TUFRG flow and singular vertex below Van Hove filling $\mu = 1.96t$:** The TUFRG calculation was done with $N_{\boldsymbol{q}} = 540$ momenta and with hexagon shell $N_s = 4$. The Hubbard U is chosen as $U = 4t$. a) Evolution of the maximum absolute value of the respective channels P,C and D. We observe that the P channel will develop the strongest divergence for the chosen parameters. b) Momentum resolved $(l, l') = (61, 61)$ component of the pairing channel $P^{61,61}(\boldsymbol{q})$ at the end of the flow. A sharp peak at $\boldsymbol{\Gamma}$ emerges.

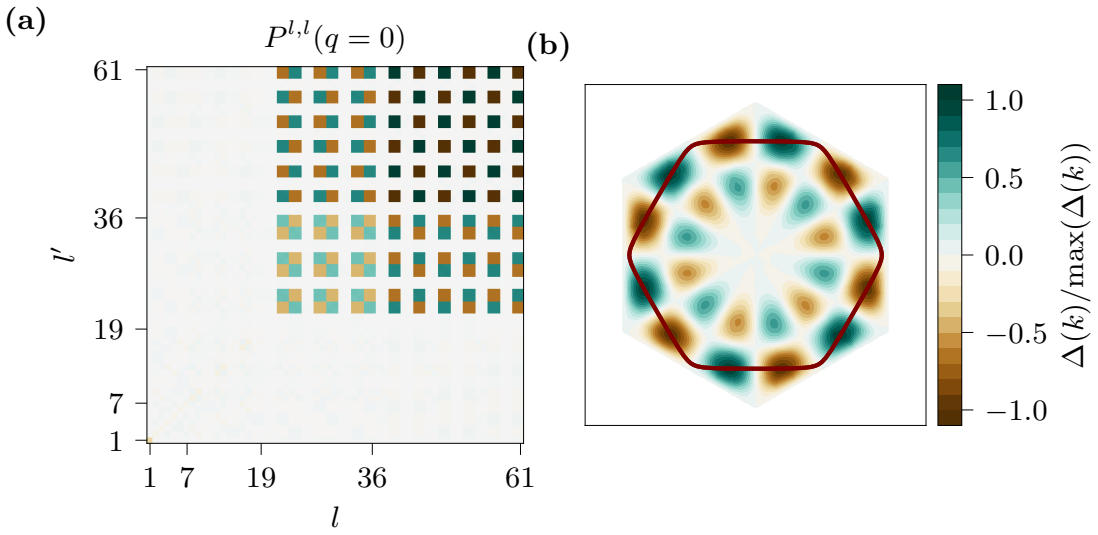

Figure 3.5: **Examination of the singular channel P at underdoping $\mu = 1.96t$:** a) All form factor components (l, l') for which the P channel features a peak, whereas positive (negative) peaks are green (brown). The intensity of the color indicates the strength of the peak, whereas darker shades imply larger values. The numbering of the axes intends to show that all strong dependencies are of combinations with $l, l' \in [37 : 61]$, i.e. from form factors lying on the 4th hexagon shell. b) The leading gap function reconstructed from the P channel. The symmetry of this gap can be classified to be a 7th order lattice harmonic of the A_2 irrep. If we draw the Fermi surface (red) on top of the gap function, we will register 12 zero-crossings with the gap function.

contributions extinct. This holds also true for the logarithmic divergence contributed by the nesting of the Fermi surface since the perfect nesting is only approximately present for the underdoped Fermi surface. Conclusively, only the generic logarithmic divergence in the particle-particle channel for zero transfer momentum should survive. For low temperatures we expect that - after the rem-

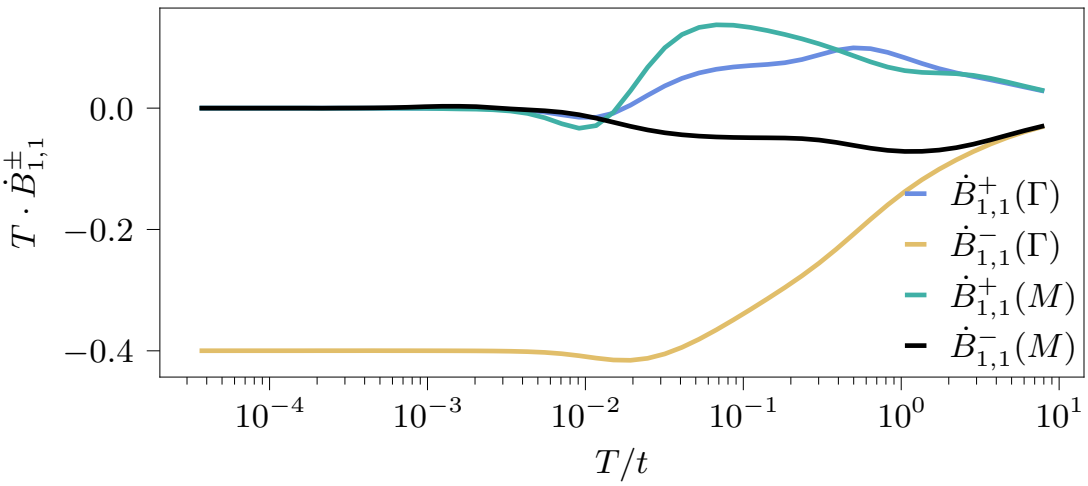

Figure 3.6: **Consistency check by tracking bubble integrations while performing TUFRG calculation for $\mu = 1.96t$:** Again, we chose an angular resolution of $N_A = 120$ as described before. Further checks of increasing this value reveal that this resolution is already sufficient for reaching convergence. Only the particle-particle channel at zero transfer momentum will have significant increments for low temperatures, while the other temperature-scaled bubble integrations are approaching zero due to the absence of perfect nesting and distance to the Van Hove point.

nants of the divergencies stemming from Van Hove filling and nesting are extinguished - the analysis in Eqs. (3.24)-(3.27) can be reduced to:

$$\dot{B}(\mathbf{\Gamma})^{-}_{1,1} \propto -\frac{1}{T} \iff \qquad T \times \dot{B}(\mathbf{\Gamma})^{-}_{1,1} \propto (-1)$$

while the other three temperature-scaled bubble integrations are going to zero. The numerical results are displayed in Fig. 3.6 and confirm these considerations. We want to apply the TUFRG to a system of overdoping now, i.e. $\mu > \mu_{\mathrm{VH}}$. This will be the final case for illustrating the methodological workflow. For that purpose we select $\mu = 2.04t$ and apply the TUFRG again. From the phenomenological understanding established before, we expect a similar behaviour of the P,C and D channel also here: the remnants of perfect nesting and the vicinity to the Van Hove point still induce fluctuations in the particle-hole channels which eventually may trigger the possibility of an attractive interaction under the renormalization procedure, leading to an instability towards superconductivity since the contributions from the generic logarithmic divergence will always contribute to the particle-particle channel at zero transfer momentum. The results of the application are presented in Fig. 3.7.
Indeed, the behaviour of the system is qualitatively similar to the underdoping case. We detect again a superconducting instability at $T_c \approx \mathcal{O}(10^{-5}t)$ (see Fig. 3.7 a). The P channel does again happen to form several peaks in various combinations of (l, l'). Analogous to the underdoping case, we present the diverging components of the channel in Fig. 3.8 a. Interestingly, all divergent components are now in the zeroth ($l = 1$) or first ($l \in [1, 7]$) hexagon shell. Consequently, we speculate that the leading gap is of first order. As a matter of fact, by calculating again the leading gap function as before, we can classify the leading gap as representing the first order lattice harmonic of the B_1 irrep. This superconductivity instability is usually called f-wave superconductivity and has been found in this regime also by previous RG studies [110]. Actually, we are not dependent on using the fourth hexagon shell $N_s = 4$ here since the main contributions to the pairing function stem from components of small distance. We will see in convergence checks later that the selection of different shells does not change the qualitative result of this calculation, in contrast to the underdoping case with the emergent i-wave which strongly depends on the inclusion of form factors of long range.

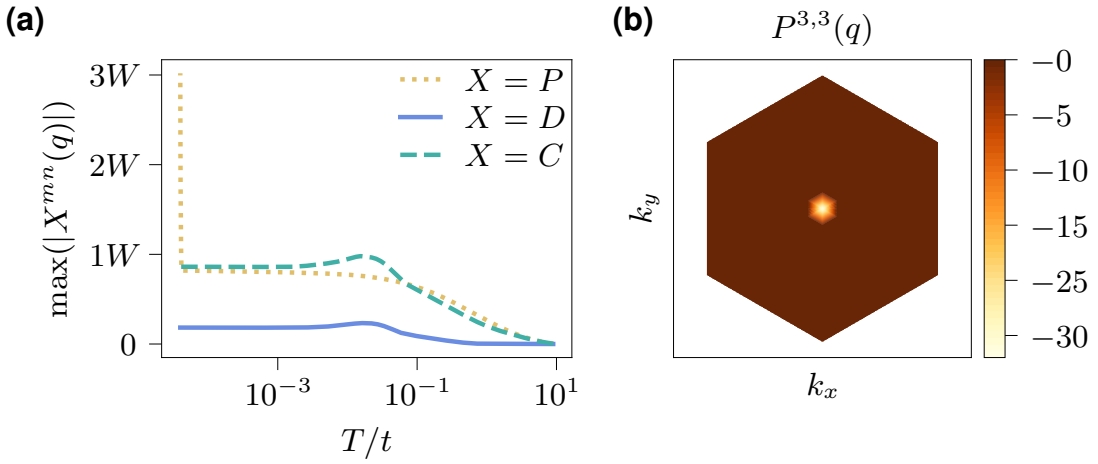

Figure 3.7: **TUFRG flow and singular vertex above Van Hove filling $\mu = 2.04t$:** The TUFRG calculation was done with $N_{\boldsymbol{q}} = 540$ momenta and on the hexagon shell $N_s = 4$. The Hubbard U is chosen as $U = 4t$. a) Evolution of the maximum absolute value of the respective channels P,C and D. The P channel will develop the strongest divergence for the chosen set of parameters. b) Momentum resolved $(l, l') = (3, 3)$ component of the superconducting channel $P^{3,3}(\boldsymbol{q})$ at the end of the flow, again featuring a sharp peak at the Γ-point.

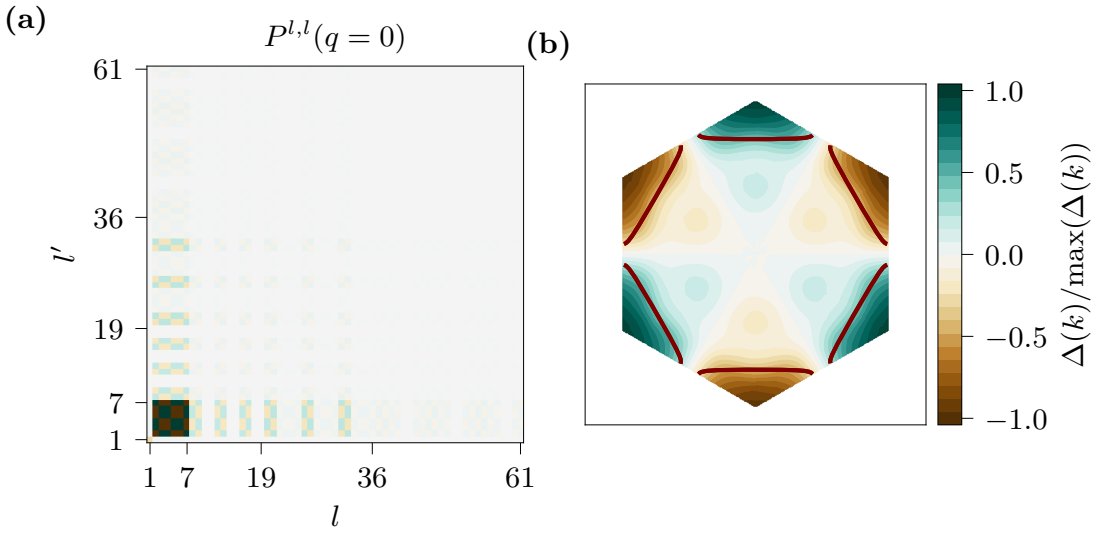

Figure 3.8: **Examination of the singular channel P at overdoping $\mu = 2.04t$:** a) All form factor components (l, l') for which the P channels features a peak, whereas positive (negative) peaks are green (brown) and darker shades indicate stronger peaks. The numbering of the axes intends to show that all strong dependencies are in the in combinations with $l, l' \in [1 : 7]$, i.e. from form factors lying on the 0th or 1st hexagon shell. b) The leading gap function reconstructed from the P channel. The symmetry of this gap can be classified to be an 1st order lattice harmonic of the B_1 irrep. If we draw the Fermi surface (red) on top of the gap function, we will register no zero-crossings with the gap function. Interestingly, the leading gap therefore fulfills the heuristic argument made in section 1.2 which implies that the leading gap tends to be completely gapped.

For the presence of logarithmic divergencies, we safely assume a similar qualitative picture as in the underdoping case. Although we already alluded in section 2.3.2 that the *pockets*, which are typically a feature for overdoped Fermi surfaces, pose a numerical challenge. While checks for the Van Hove sce-

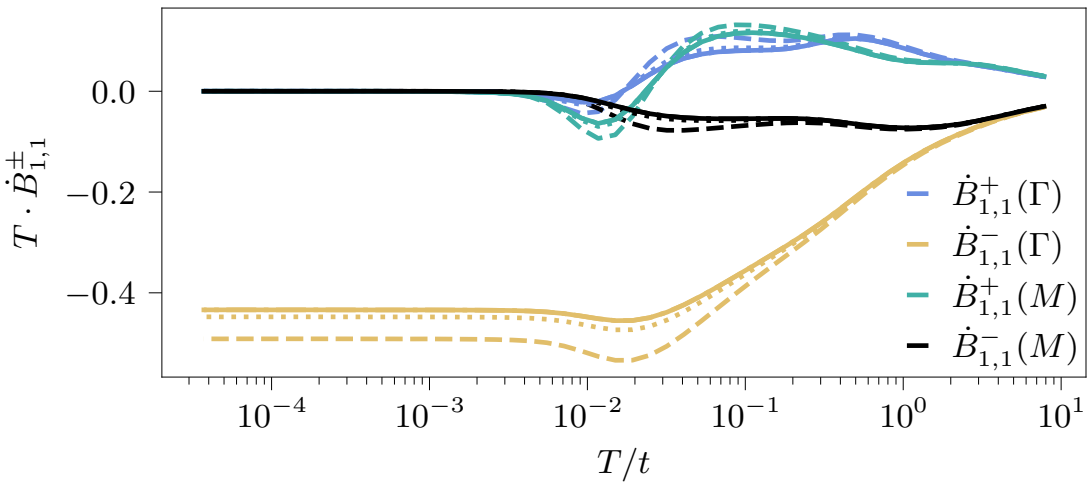

Figure 3.9: **Consistency check by tracking bubble integrations while performing TUFRG calculation for $\mu = 2.04t$:** For the angular resolutions we chose $N_A = 120$ (dashed), $N_A = 240$ (dotted), $N_A = 360$ (dashdotted) and $N_A = 480$ (solid). The behaviour of the temperature-scaled bubble integrations is qualitatively similar to the underdoping case as expected. However, it becomes apparent that a higher angular resolution of the integration routine is necessary to reach convergence for the overdoped case, especially for the particle-particle bubble at zero momentum. Here, the dashed-dotted and the solid line lie upon on each other such that we assume reasonable convergence for $N_A = 360$.

nario and the underdoping scenario did not appear to be particularly challenging, this changes now for the overdoping case. The results of the bubble integration checks are presented in Fig 3.9. From these results we conclude that for an application to overdoped systems (i.e. the presence of pockets in the Fermi surface), a higher angular resolution should be chosen for the adaptive integration routine. We find that a reasonable convergence is reached for $N_A = 360$, in contrast to using a resolution of only $N_A = 120$ in the underdoping case.

With the discussion of the three presented cases, the instruction of the TUFRG application is finalized. We will state a brief summary to cover the key elements which were provided here.

- In the paradigm of competing instabilities discussed in section 1.1, we expected strong particle-hole fluctuations at Van Hove filling. Indeed, our numerical implementation confirms this assumption and signals the occurrence of a SDW with modulating vector $\boldsymbol{M}$ in this scenario. Since our bubble integrations can be related to the particle-hole and particle-particle bubble, we could also recover the correct behaviour of these objects at low temperatures and frame the considerations about the onset of instabilities valid.

- From the bubble analysis, the particle-hole and particle-particle fluctuations at Van Hove filling do both possess a double logarithmic divergence. Still, as we discussed also in section 1.1 and 1.2, the possibility of a superconductive instability is only possible for an attractive interaction. We observe that away from Van Hove filling, the particle-hole fluctuations induce this attractive interaction under renormalization. The particle-hole fluctuations themselves extinct for low temperatures away from Van Hove filling and - with the presence of the generic logarithmic divergence in the particle-particle channel - the emergence of superconductivity is finally possible.

- In the TUFRG, we find these superconductive instabilities in the underdoping ($\mu < \mu_{\mathrm{VH}}$) and the overdoping ($\mu > \mu_{\mathrm{VH}}$) case. The singular channel $P^{l,l'}(\boldsymbol{q})$ features a plethora of peaks

at different combinations of (l, l') at $\boldsymbol{q} = 0$. By reconstructing the pairing interaction from this channel, we successfully calculated the leading gap function $\Delta(\boldsymbol{k})$ for the aforementioned cases. As discussed in section 1.2, the symmetry of the gap functions are dictated by the underlying C_{6v} point group. We find a gap function of 7th order of the irrep A_2 (underdoping) and a gap function of 1st order of the B_2 irrep (overdoping). The former gap function highlights the importance of taking long-ranged form factors into account since the strong divergencies in components of high form factor indices l, l' are crucial for deducing this gap function from the singular vertex.

- As a final remark it should be mentioned that the examination of the values of the bubble integrations represents a helpful sanity check of the numerical implementation. The expected behaviour of the bubbles at and in vicinity of the Van Hove singularity was well reproduced and a reasonable convergence can be assumed. In addition, we extract from these checks that for the overdoping case a higher angular resolution N_A should be used for the integration routine.

We will now proceed and map out a complete phase diagram for the model, including also longer range interactions.

3.1.3 Instabilities of the paradigmatic Hubbard model

To pave the way to more realistic models we will now start to take interactions besides the local Hubbard interaction into account. For that purpose, we include a non-zero nearest-neighbour density-density interaction V_1. Before presenting the whole phase diagram, we want to keep the focus on the effect of these new interactions to a single superconductive instability. Therefore, we consider the previously discussed case at overdoping ($\mu = 2.04t$) and add an interaction of $V_1 = 1t$.

The application of the TUFRG to a model of these parameters finds indeed instabilities which were not detected previously. The emerging instability is still a superconductor (cf. Fig. 3.10 a) at $T_c \approx \mathcal{O}(10^{-4}t)$, but the symmetry of the leading gap changes. In fact, we will find two degenerate leading gaps with the same eigenvalue. This signals a symmetry which belongs to either the E_1 or E_2 irrep since these are the two-dimensional irreps of the underlying point group C_{6v}. A comparison with the lattice harmonics derived in section 1.2. allows for the identification of these gaps as being second order E_2 gap functions. Typically, gaps which can be described by the first order lattice harmonics of E_2 are called a d-wave superconductors. By the doubling of zero-crossing of the Fermi surface in the second order lattice harmonic (namely eight crossings), we will therefore call this emergent instability a g-wave superconductor. Interestingly, by comparing the evolution of the channels in Fig. 3.10 a with the the counterpart plot Fig. 3.7 a, it becomes apparent that the evolution of the C channel is barely altered, while the D channel is strongly affected. The inclusion of a non-zero V_1 leads to a strong enhancement of the D channel at the beginning of the flow before it eventually saturates. While continuing the flow, the C channel overtakes the D channel at $T_c \approx \mathcal{O}(10^{-1})$. We conclude from this that the alteration of the gap function by including V_1 is mainly mediated by the feedback of the D channel to the P channel. It should be highlighted that the emerging gap symmetry opens up the possibility of topological superconductivity as discussed in section 1.2. The two degenerate leading gaps can be combined by a complex superposition, leading to a fully gapped function. In the present case, this would be called a $g+ig$ superconductor, featuring a Chern number of $|\mathcal{N}| = 4$ [97].

Consequently, we calculate the phase diagram around Van Hove filling by employing a range between $\mu = 1.9t$ and $\mu = 2.1t$ for the chemical potential and between $V_1 = 0$ and $V_1 = 1.6t$ for the nearest-neighbour interaction. Our applications with larger interaction strengths for V_1 showed that the initial growth in the D channel is drastically enhanced, such that we directly find a CDW after very short flows. Therefore, we keep the interaction V_1 smaller than $1.6t$, such that we are still treating the model in the paradigm of a competition between magnetism and superconductivity. The

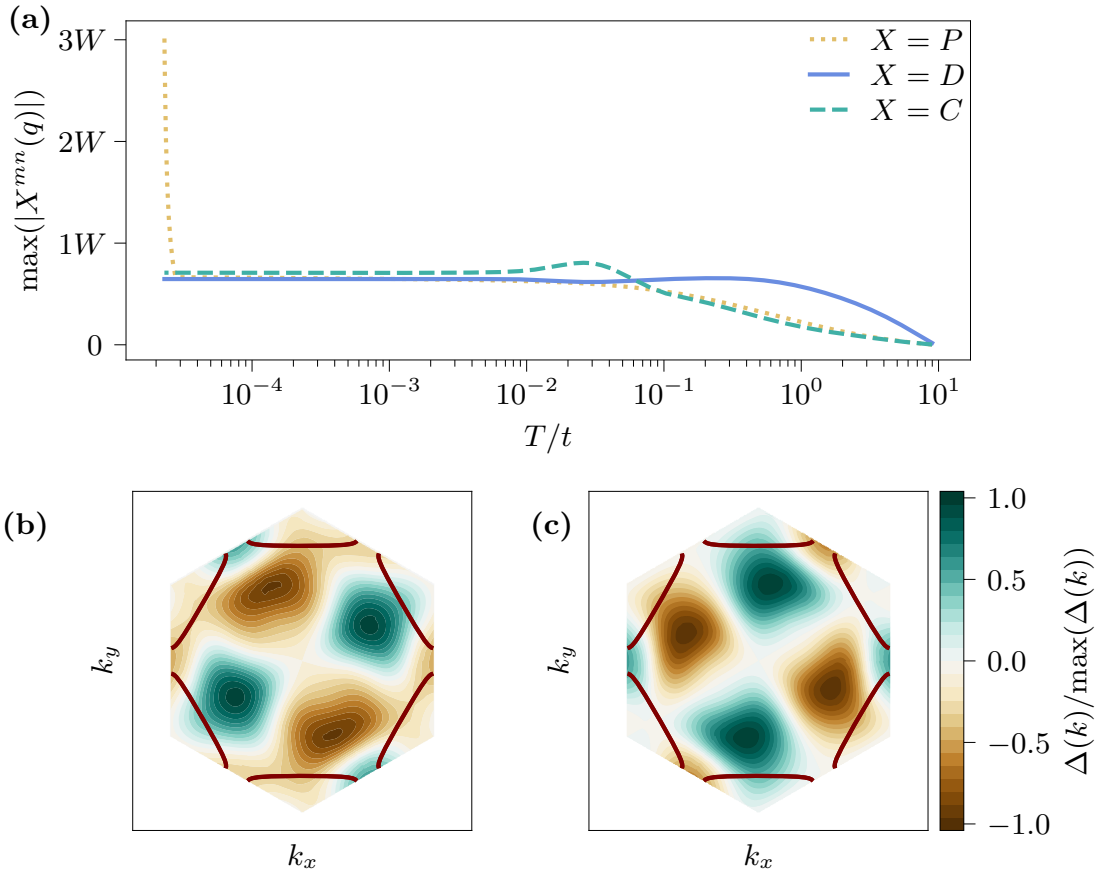

Figure 3.10: **TUFRG flow at $\mu = 2.06t$ with $U = 4t$ and interaction $V_1 = 1t$:** The TUFRG calculation was done with $N_{\boldsymbol{q}} = 540$ momenta and on the hexagon shell $N_s = 4$ a) Evolution of the maximum values of the P,C and D channel. Eventually the P channel will develop singular behaviour, signaling the instability. In contrast to the calculations without a non-zero V_1, the D channel has significant initial growth but is eventually overtaken by the C channel. b) Leading gap functions reconstructed from the singular vertex. The two degenerate leading gaps represent second order lattice harmonics of the two-dimensional irrep E_2. The red line indicates the Fermi surface which features 8 zero crossings with the single gap functions.

results are compiled in the phase diagram Fig. 3.11. From examining this phase diagram, we divide the occurring instabilities in three areas regarding the chemical potential. At first, there is a region at and in close vicinity to the Van Hove filling $\mu = 2t$. We know from the explanatory analysis that a SDW is to be expected here for $V_1 = 0$. In fact, this instability occupies a small range of the chemical potential in regards of under- and overdoping before the respective superconductivity takes over. The SDW instability is stable against effects of increasing the interaction V_1 and the occupied region in the phase diagram even broadens in size for higher interaction strength. For the overdoping case, eventually the f-wave superconductivity emerges when μ is tuned considerably enough away from Van Hove filling as described in the previous section. The f-wave superconductivity occupies the whole bottom right region of the phase diagram regarding chemical potential and interaction strength V_1. Then, by increasing V_1, we can change the emerging superconductivity to have a g-wave symmetry, as presented before. There exist transition lines by tuning V_1 featuring a typical fan, such that the critical temperature for the f-wave steadily decreases until the transition point is met towards a g-wave instability. From that point on, the critical temperature of the g-wave constantly increases again for higher values of V_1 for the rest of this region of the phase diagram. The third region at underdoping ($\mu < 2.0t$) behaves similarly to the overdoping region. Again for zero or low values of V_1, we will find

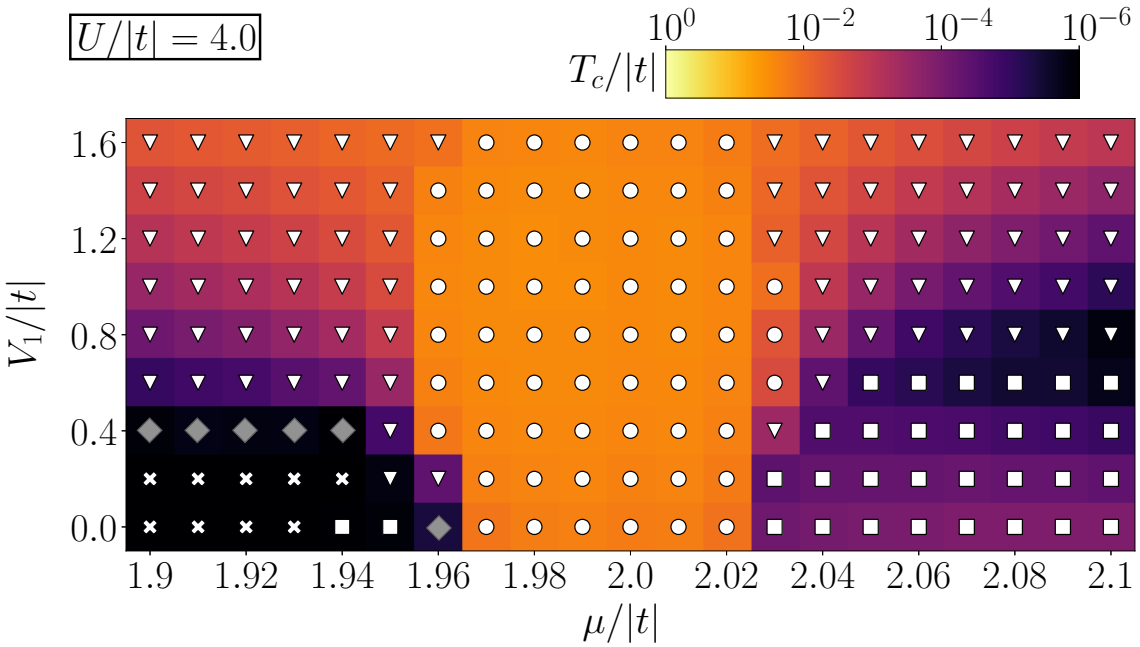

Figure 3.11: **Phase diagram of the paradigmatic $t-U-V_1$ model:** Original plot taken from [29]. For $U = 4t$ and around Van Hove filling, various instabilities occur. Around Van Hove filling the SDW ($\circ$) dominates regardless of V_1. At overdoping, we will find g-wave superconductivity ($\triangledown$) and f-wave superconductivity ($\square$). At underdoping, the i-wave superconductivity ($\diamond$) can be found. If no instability occurs for $T/t \geq 10^{-6}$, then the area is marked as metallic ($\times$). For the i-wave superconductivity we use grey shades to highlight the fragility with respect to the inclusion of form factor shells.

the i-wave superconductivity as described in the section before. This instability has the lowest critical temperature and indeed we do not find another instability of this kind at zero interaction strength when a cutoff of $T_{\text{stop}} = 10^{-6}$ is employed. For chemical potentials below $\mu = 1.96t$, the instability will change to a f-wave superconductor, before no instability forms at all above the cutoff. For higher interaction strengths, the i-wave appears again. Similar to the overdoping case, a transition towards the g-wave is formed along the axis defined by V_1. In the phase diagram, we displayed the markers of the i-waves as grey to highlight their fragility with respect to the employed form factor shells. As discussed before, this instability can only be correctly resolved by taking at least $N_s = 4$ form factor shells into account. For a value below $N_s = 4$, we will find a f-wave instability instead.

3.1.4 Instabilities of the realistic tTMD model

In section 1.3, we discussed the possibility of describing Moiré materials effectively by Hubbard models. It has been shown for small twist angles that the AA-stacked WSe_2/MoS_2 can be effectively described by an extended triangular lattice model where the spin index σ and valley index ξ play the same role due to the strong spin-valley locking [112]. For that purpose we extract from [112] the following parameters to describe the WSe_2/MoS_2 tTMD:

$$\begin{aligned} t_1 &\approx -2.5\text{meV}, \\ t_2 &\approx \ \ 0.5\text{meV}, \\ t_3 &\approx \ \ 0.25\text{meV}. \end{aligned}$$

The inclusion of t_2 and t_3 leads to a small curvature of the Fermi surface at Van Hove filling, such that the nesting is not perfect anymore, but still approximately present. The interactions $V_{1,2,3}$ are

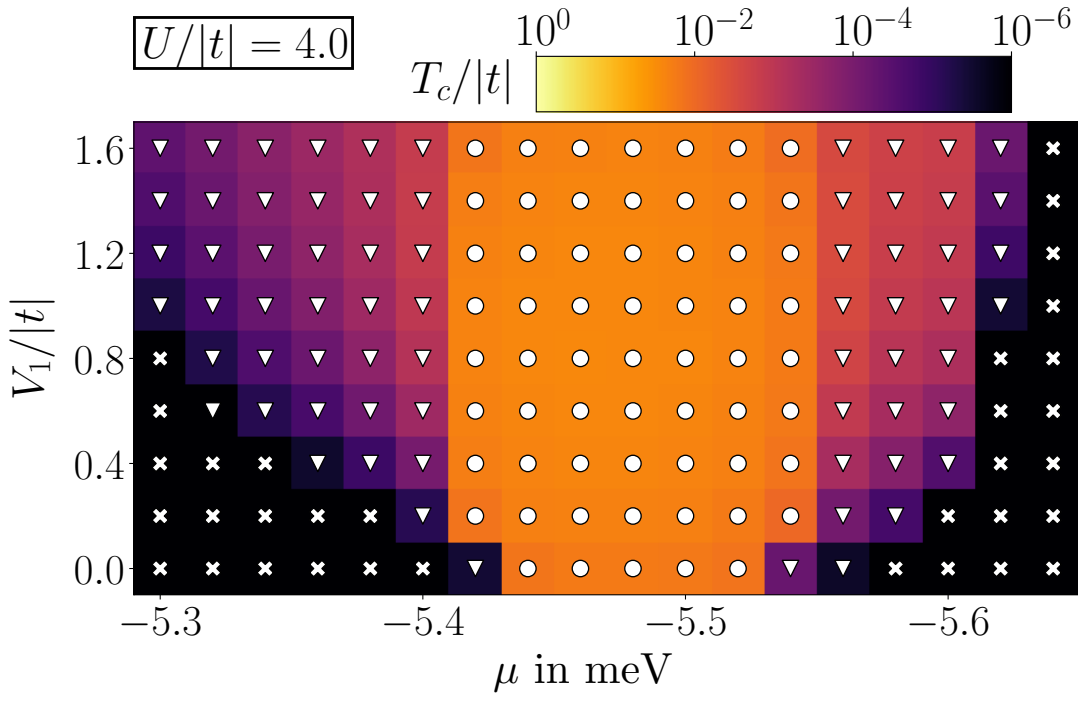

Figure 3.12: **Phase diagram of the realistic tTMD model:** Original plot taken from [29]. Around Van Hove point we find SDW/VDW instabilities (○). The remaning areas of superconductivity are exclusively of the type of g-waves (▽). An absence of an instability for $T/t \geq 10^{-6}$, is marked as metallic (×).

experimentally accessible and can tuned by the dielectric environment. We also extract here [121]:

$$V_2/V_1 \approx 0.357\text{meV},$$
$$V_3/V_1 \approx 0.26\text{meV}.$$

We will again set $U = 4t$ and vary V_1 and μ to map out a phase diagram. For $V_1/|t_1|$, we again chose the range between 0 and $1.6t$ such that the diagram is comparable to the paradigmatic case. For the chemical potential it should be noticed that for the given parameters the Van Hove filling is now located at $\mu_{\text{VH}} \approx -5.5\text{meV}$. We therefore select μ to be in the range between -5.3meV and -5.7meV. The phase diagram can be seen in Fig. 3.12.

Both phase diagrams are qualitatively similar to each other, such that the majority of the effects are already captured by the simple paradigmatic model. Again, we find around Van Hove filling an extended region indicating the onset of a SDW (which can also be understood as a Valley density wave (VDW) due to the double role of the spin/valley index in the model). For both cases -underdoping and overdoping- the areas which formerly inhabited superconductivity at low values of V_1 do not feature any instability at all now. A possible explanation of this absence is given by the fact that the effect of the parameters t_2, t_3 weaken the nesting quality of the Fermi surface so much that the necessary fluctuations in the particle-hole channels are not significant enough to induce an attractive interaction for the onset of superconductivity under renormalization. This effect basically erases most of the occurring superconductivities for low values of V_1. For higher values of V_1, we still find an extensive region of g-wave superconductivity for underdoping and overdoping. This does again reinforce the hypothesis made in the paradigmatic case, namely that mainly the interaction V_1 enhancing the density channel D is necessary for the emergence of the g-wave superconductivity. If this claim turns out to be true, then it would be of no surprise that the superconductivity at the lower part of the phase diagram (i.e. smaller V_1) disappears due to the weakening of the nesting, while the superconductivity in the upper part (larger V_1), mainly caused by interaction effects, remains stable.

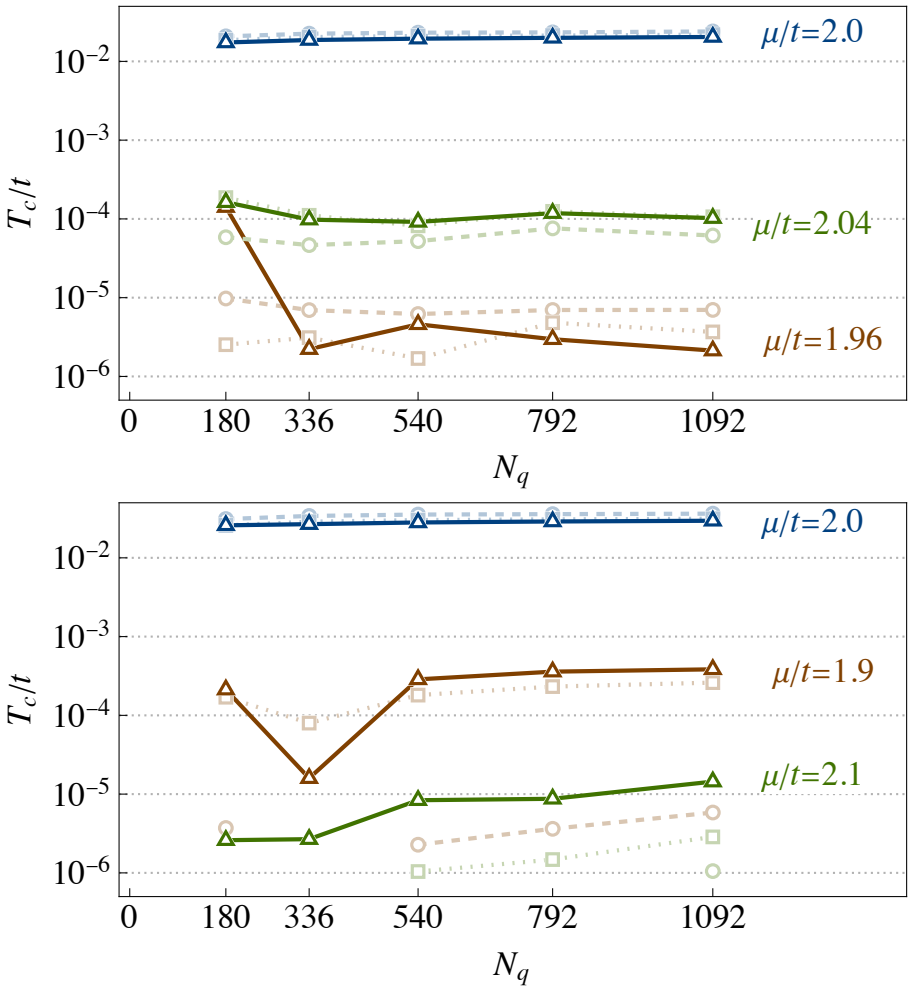

Figure 3.13: **Convergence checks for critical temperature T_c:** Original plot from [29]. Top: $U = 4t$ and $V_1 = 0$. Bottom: $U = 4t$ and $V_1 = 1t$. We portray the dependence of the critical temperature on the momentum resolution. Legend for form factor shells: $N_s = 2$ (dashed), $N_s = 3$ (dotted), $N_s = 4$ (solid).

3.1.5 Convergence tests

Before summarizing the presented results, we briefly want to dive into a technical excursion and discuss the convergence of the calculations. As stated before, we calculated the phase diagrams with $N_{\boldsymbol{q}} = 540$ momenta in the Brillouin zone and using the fourth form factor shell $N_s = 4$, corresponding to 61 form factors. These parameters were naturally not chosen randomly, but turned out to be a good trade-off of convergence and performance. At first, we ran convergence checks for $N_{\boldsymbol{q}} \in [180, 336, 540, 792, 1092]$ and $N_s \in [2, 3, 4]$. We did these tests for the selection of parameters presented in section 3.1.1 and also for a different set of parameters with $V_1 = 1t$ and $\mu = 1.9, 2.0, 2.1$, see Fig. 3.13. From these checks we conclude that $N_{\boldsymbol{q}} = 540$ is a good value for running the calculations since the corrections to the critical temperatures beyond are small but numerically expensive. For the form factor shells we always select $N_s = 4$ such that we do not overly bias the system which is for example the case when we try to resolve the i-wave superconductivity with less than four form factor shells. We employ a second convergence test to account for the effects of the form factor shells on the critical temperature. We calculate two slices of the presented phase diagram at $V_1 = 0$ and $V_1 = 1t$ for $N_s = 2, 3, 4$ at a high momentum resolution of $N_{\boldsymbol{q}} = 1092$, see Fig. 3.14. From these plots we are generally satisfied with the quantitative convergence.

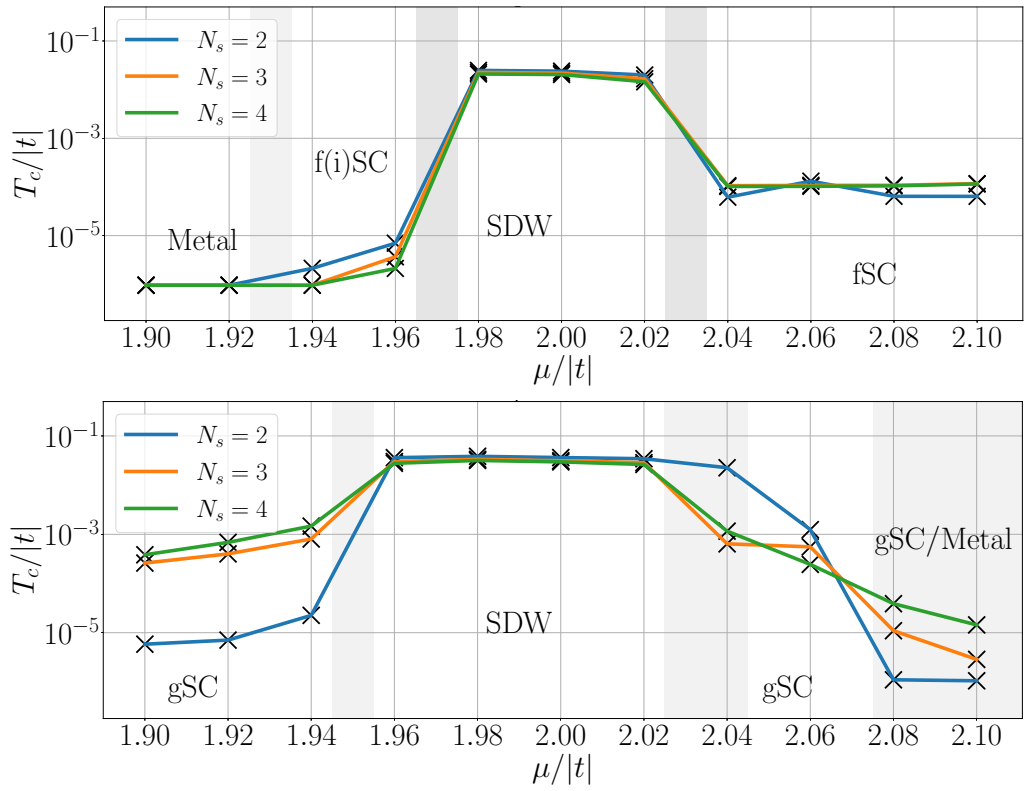

Figure 3.14: **Convergence checks for phase diagram at $N_q = 1092$:** Original plot from [**PubA**]. Top: $U = 4t$ and $V_1 = 0$. Bottom: $U = 4t$ and $V_1 = 1t$. Areas of instabilities are labeled as such, with the grey bars representing phase boundaries. For the case with $V_1 = 0$, the results of different form factor shells do align very consistently, where a qualitative difference can be seen in the regime of the i-wave superconductivity. For the case with $V_1 = 1t$, desired convergence is harder to reach. Phase boundaries may vary depending which form factors are included as seen in the bottom plot at $\mu = 2.04t$ or $\mu = 2.08t$. In both cases, the convergence of the SDW is extraordinary fast secured.

3.1.6 Summary

In this section, we successfully applied the derived TUFRG implementation to the SU(2)-invariant triangular Hubbard model. The results of this application serve us in two different ways. At first, we examined the paradigmatic model with $t = 1$ and $U = 4t$ as fixed parameters at Van Hove filling ($\mu = 2t$) and slightly tuned away from it ($\mu = 1.96t, 2.04t$). The results agree with the notions of competing instabilities as presented in section 1.1 and by the connection of the bubble integrations to the particle-particle and particle-hole bubble, we retrieved a practical criterion for the soundness of the performed calculations. Following this, we mapped out a phase diagram for an extended range of nearest-neighbour interactions V_1 and chemical potentials μ. This phase diagram precisely reflects the paradigm of competing instabilities where around Van Hove filling an extended range of magnetism (SDWs) appears which eventually translates to superconductivity for filling situations away from Van Hove filling. By reconstruction of the pairing interaction from the TUFRG, we successfully identified the emergent symmetries of the leading gap functions and recognize f-wave, g-wave and i-wave superconductivity. All of these symmetries were possible to expect by our analysis of the C_{6v} point group in section 1.2. For the realistic description of the tTMD material WSe_2/MoS_2, we performed another set of TUFRG calculations, including also longer ranged hoppings t_2, t_3 and interactions V_2, V_3. The established phase diagram in this case is qualitatively similar to the paradigmatic case, highlighting that the mechanism which leads to superconductivity in this tTMD is already present in the paradigmatic model. Noticeably, the variety of superconductive instabilities shrinks down to the presence of the g-wave superconductivity only. The absence of the f-wave and i-wave

may be explainable by the distortion of the nesting by additional hoppings t_2, t_3 while the g-wave remains stable since it may be mainly caused by the interaction V_1. Besides from these results, we want to emphasize the technical advancement of this study. The features of the TUFRG method in general lead to an advantageous FRG approach for strongly correlated systems, allowing for high momentum resolution. The numerical challenge is posed by performing stable flow calculations down to very low temperatures T and still maintaining reasonable computation times. By using the integration routine and fully exploiting the geometrical structure of the plane wave form factors shown in section 2.3.2 we did not only overcome this challenge, but also made it possible to include 61 form factors. This is an unprecedented value for this parameter comparing to previous works and also enables the possibility to correctly resolving the i-wave superconductivity.

3.2 Application B: Spinless triangular models

In this section, we will study competing orders of spinless fermions on a triangular lattice with nearest-neighbour interaction V_1. We already discussed in section 1.3 before that a single TMD system may inhabit strong spin-orbit coupling leading to spin-splitting of the valence bands [65, 91]. Effective models of tTMD systems formed by these split bands will inherit parts of this structure, leading also to a description including spin-split bands [79, 112]. The model of an isolated band may be achieved if we consider a strong spin polarization by external manipulation, e.g. applied fields. In this case, we would then treat a single polarized band where all electrons carry the same spin (which is effectively equivalent to excluding the spin quantum number). The main idea behind this analysis is driven by the question if the emerging orders of the full model are also already encrypted in the behaviour of electrons in a single band. Moreover, we used the spinless model for a technical case study. The results of this subsection were published in [30] where we compared the results of the TUFRG with the patching scheme. Nevertheless, this section will purely focus on the TUFRG calculations.

Two distinct cases will be presented here. At first, we will set $V_1 < 0$ to start with an attractive interaction. By this choice, we will directly have an attractive component in the particle-particle channel without the necessity to generate it by the RG flow such that particle-hole and particle-particle fluctuations are directly in competition from the start. In a second case, we will set $V_1 > 0$, employing a repulsive interaction. In this scenario, we are closer to the situation already treated in application A where it will become apparent in which way the instabilities change when the spin degree of freedom is absent. We will map out a correlated phase diagram for various values of V_1 for a range of the chemical potential μ for both of these cases. In this section, we will only treat underdoped cases i.e. $\mu < \mu_{\mathrm{VH}}$. This originated from the comparison with the patching code which was written for underdoped cases only.

3.2.1 Model and implementation

We consider a minimal model for spinless fermions on a triangular lattice. The most simple interaction term is a nearest-neighbour interaction term V_1, because no Hubbard interaction U can be included since double occupation of a single site is not possible for spinless fermions. We also consider nearest-neighbour hoppings only for the kinetic part and include the coupling to the density operator $n_i = c_i^\dagger c_i$ by the chemical potential:

$$H = -t \sum_{\langle i,j \rangle} \left(c_i^\dagger c_j + \text{h.c.} \right) + \mu \sum_i n_i + V_1 \sum_{\langle i,j \rangle} n_i n_j, \tag{3.34}$$

where $c_i^{(\dagger)}$ annihilates(creates) a fermion on lattice site i. The dispersion of the band can be retrieved by Fourier transform:

$$\begin{aligned} \xi(\boldsymbol{k}) &= \epsilon(\boldsymbol{k}) - \mu \\ &= -2t[\cos(k_y) + 2\cos(k_y/2)\cos(\sqrt{3}k_x/2)] - \mu \end{aligned} \tag{3.35}$$

which is of course the same dispersion already used in the previous application. Therefore, the Van Hove singularity at the $\boldsymbol{M}$ points of the Brillouin zone is also present here, for which the chemical potential has to be tuned to $\mu_{\mathrm{VH}} = 2t$. As stated before, we will only investigate underdoped cases here and cover the whole range between $\mu = 0$ and $\mu = 2t$ for our calculations.

For the application of the TUFRG to the spinless model, we are obligated to employ the TUFRG equa-

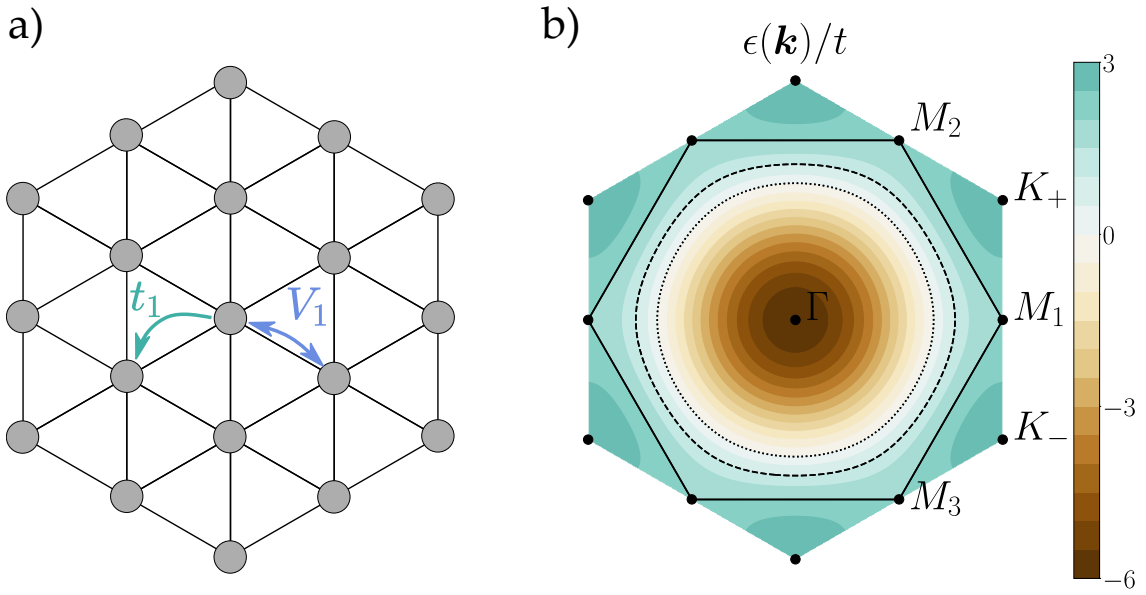

Figure 3.15: **Spinless model on a triangular lattice:** a) Real space lattice with hopping t and density-density interactions V_1. b) Dispersion for $t = 1.0$. The Fermi surfaces correspond to $\mu = 2.0t$ (solid), $\mu = 1t$ (dashed) and $\mu = 0$ (dotted). The $\boldsymbol{M}_{1,2,3}$ points are Van Hove points with a logarithmic divergences regarding the density of states. At $\mu = 2.0t$.

tions stemming from the spinless FRG flow equations Eqs[2]. (2.40)-(2.42):

$$\frac{d}{d\Lambda}P^{l,l'}(\boldsymbol{q}) = \frac{1}{2}\sum_{l_1,l_2} V^P_{l,l_1}(\boldsymbol{q}) \times \dot{B}^-_{l_1,l_2}(\boldsymbol{q}) \times V^P_{l',l_2}(\boldsymbol{q}), \tag{3.36}$$

$$\frac{d}{d\Lambda}D^{l,l'}(\boldsymbol{q}) = \sum_{l_1,l_2} V^D_{l,l_1}(\boldsymbol{q}) \times \dot{B}^+_{l_1,l_2}(\boldsymbol{q}) \times V^D_{l',l_2}(\boldsymbol{q}), \tag{3.37}$$

$$\frac{d}{d\Lambda}C^{l,l'}(\boldsymbol{q}) = \sum_{l_1,l_2} V^C_{l,l_1}(\boldsymbol{q}) \times \dot{B}^+_{l_1,l_2}(\boldsymbol{q}) \times V^C_{l',l_2}(\boldsymbol{q}). \tag{3.38}$$

Since the dispersion of this model is equal to the dispersion of the model in application A, the bubble integrations $\dot{B}^{\pm}$ are also exactly the same objects as in the former application, see Eq. (3.8) and Eq. (3.9). This also applies to the cross-projection operators V^X which are identical to Eqs. (3.10)-(3.23). A substantial difference in the application to spinless fermions (besides the structure of the Flow equations (3.36)-(3.38)) is given by the implementation of the initial conditions. For the nearest-neighbour interaction V_1, these conditions are given by:

$$V^{0,C}_{1,1}(\boldsymbol{q}) = -V^{0,D}_{1,1}(\boldsymbol{q}) = -V_1 \sum_l e^{i\boldsymbol{q}\boldsymbol{R}_l}, \tag{3.39}$$

$$V^{0,P}_{l,l}(\boldsymbol{q}) = V^{0,C}_{l,l}(\boldsymbol{q}) = -V^{0,D}_{l,l}(\boldsymbol{q}) = V_1, \tag{3.40}$$

$$V^{0,P}_{-l,l}(\boldsymbol{q}) = -V_1 e^{-i\boldsymbol{q}\boldsymbol{R}_l}. \tag{3.41}$$

Where l are the form factors in the first form factor shell, $l \in \{2,3,4,5,6,7\}$. The notation $-l$ indicates the real space vector in the oppposite direction of $\boldsymbol{R}_l$, e.g. $-l = -2 \rightarrow \boldsymbol{R}_{-2} = \boldsymbol{R}_3 \rightarrow l = 3$.

For the numerical implementation, we follow the steps outlined in the second chapter. Since the bubble integrations were already successfully tested for convergence and stability in application A

[2]We we again used the convention leading to global sign.

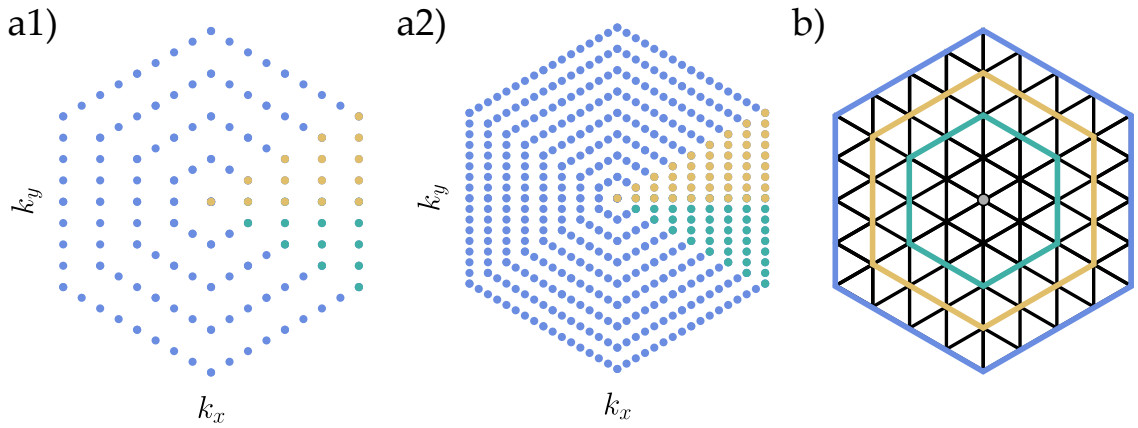

Figure 3.16: **Momentum and form factor resolution used for the spinless model:** a1) 180 and a2) 540 momentum points. The first resolution is used to compare the TUFRG results to patching results. The latter resolution is used to examine selected phases in more detail. The color of the discretization points indicates the use of symmetries as described in section 2.3.3. b) For the main results, form factors up to the second shell (green) $N_s = 2$ are used. Convergence checks including shells up to $N_s = 3$ (yellow) and $N_s = 4$ (blue) are contributed at the end of this section.

before, we do not expect any technical difficulties in the flows calculated here.
We will use two different resolutions to treat the spinless model. For laying out the phase diagrams, we will use a rather small momentum resolution of $N_{\boldsymbol{q}} = 180$. This choice was initially made to compare it to patching calculation which are often implemented with a rather small choice of momentum patches. In publication [30] the complementary patching code used 192 patches, so we chose $N_{\boldsymbol{q}} = 180$ for a better comparison. For further analysis of selected instabilities in the phase diagram, we then switch to $N_{\boldsymbol{q}} = 540$ as it already turned out to be a good trade-off between numerical cost and convergence as demonstrated in the convergence checks in application A. For the resolution regarding form factors, we chose to include form factors up to the second hexagon shell, i.e. $N_s = 2$ what translates to 19 form factors. From the calculations of the patching scheme, we do not expect to be confronted with gap symmetries which need more than the second shell to be properly resolved such that $N_s = 2$ can be safely selected to maintain computational speed. Nevertheless, we will complete this section with a convergence check to investigate the effects of taking higher form factor shells into account.

Before presenting the results, we want to briefly discuss the physical interpretation of the C channel. In the former application, this channel faithfully represented spin interactions like SDWs. Since a spinless system cannot exhibit these types of interactions anymore, the question of a suitable interpretation of the C channel is posed. At first it should be noted that the two particle-hole channels are connected for a system without SU(2)-invariance. This can easily been seen by investigating the diagram types in the FRG formalism Eq. (2.41) and Eq. (2.42). By using Grassmann anti-symmetry we find:

$$\tau^{\mathrm{ph,d}}(\boldsymbol{k}_1, \boldsymbol{k}_2, \boldsymbol{k}_3, \boldsymbol{k}_4) = -\tau^{\mathrm{ph,cr}}(\boldsymbol{k}_1, \boldsymbol{k}_2, \boldsymbol{k}_4, \boldsymbol{k}_3). \tag{3.42}$$

This translates to the TUFRG as:

$$D^{l,l'}(\boldsymbol{q}) = -C^{l,l'}(\boldsymbol{q}). \tag{3.43}$$

From which we conclude that the C channel is actually redundant and is just another density channel. This becomes also apparent when we compare the proposed model actions S_C Eq. (2.59) and S_D Eq. (2.53) where we motivated the channel decomposition. If we liberate both actions from their spin degrees of freedom, then two identical actions will remain which only differ by a global sign. Conclusively, we expect that the emerging instabilities are a result of the competition of superconductivity

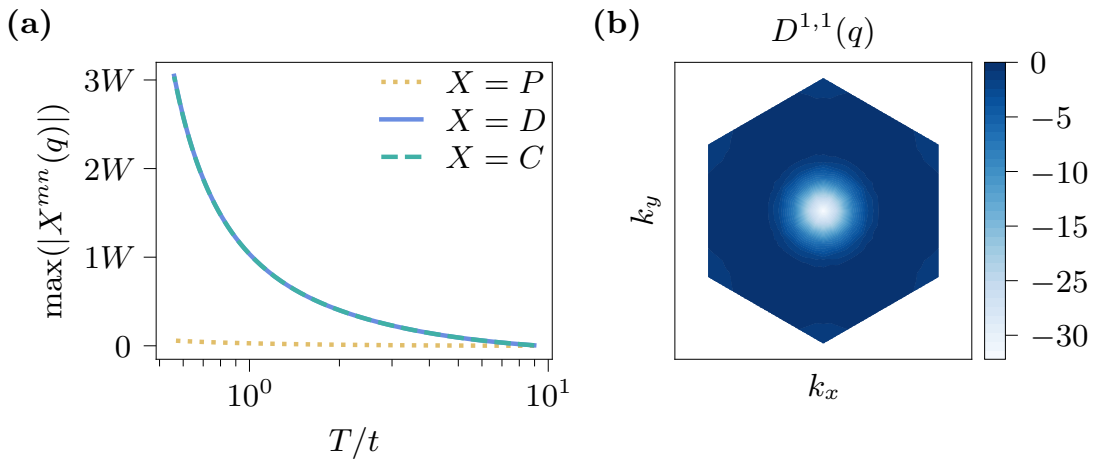

Figure 3.17: **TUFRG results at Van Hove filling $\mu = 2t$ for $V_1 = -1t$, with $N_{\boldsymbol{q}} = 540$ and $N_s = 2$ (19 form factors):** a) The tracking the evolution of the maximum absolute value of the three channels while performing the TUFRG calculations reveals a divergence in the D/C channel. The matching behaviour of these channels was not externally imposed and confirms the symmetry consideration Eq. (3.43). b) Momentum resolved on-site component of the density channel $D^{1,1}(\boldsymbol{q})$ at the end of the flow at T_c. The peak at the $\boldsymbol{\Gamma}$ point indicates a Pomeranchuk instability.

and charge density phenomena instead of superconductivity and magnetism in the present spinless model. Although a TUFRG approach with P and D channels only certainly can be constructed for the spinless model, we still keep the C channel as a sanity check to ensure the consistency of our implementation. This also provides us with a sanity check for the application A retrospectively since the projections and bubble integrations which have to work in a numerical flawless manner to fulfill the symmetry relation Eq. (3.43) are also used in the former application. As before, we will use $T_0 = 3W$ as starting scale and impose a hard cutoff at $T_{\text{stop}} = 10^{-5}t$ where the flow stops.

3.2.2 Instabilities at attractive interaction

We will start with an attractive nearest-neighbour interaction $V_1 < 0$. From the analysis of the bubble integrations in the SU(2) case before, we expect the following scenario: at Van Hove filling $\mu = 2t$, the particle-hole fluctuations are enhanced by perfect nesting and the Van Hove singularity. The particle-particle fluctuations are also enhanced by the Van Hove singularity, in addition to the generic logarithmic divergence at $\boldsymbol{q} = 0$. Interestingly, the attractive interaction $V_1 < 0$ allows directly for Cooper pairing. So, although we are expecting a competition between charge density instabilities (triggered by particle-hole fluctuations) and instabilities towards superconductivity (induced by particle-particle fluctuations), it is not directly clear which of these effects will remain stronger at Van Hove filling. We will therefore start at $\mu = 2t$ and systematically reduce the chemical potential to investigate the effect on the emerging instabilities.

At Van Hove filling

By tracking down the evolution of the channels while integrating the TUFRG flow equations, we eventually find a divergence of the D/C channel at $T_c \approx \mathcal{O}(10^{-1}t)$ indicating a charge density instability. Inspecting the momentum structure of the $D^{1,1}(\boldsymbol{q})$ component, a pronounced peak at $\boldsymbol{q} = 0$ is revealed (see Fig. 3.17 b). This instability is called a **Pomeranchuk** instability (for studies regarding this instability in the square lattice Hubbard model, the reader is advised to [17, 118]) and can be understood as the density channel counterpart to a ferromagnet since both phases are defined as the special case of a SDW/CDW with zero momentum transfer.

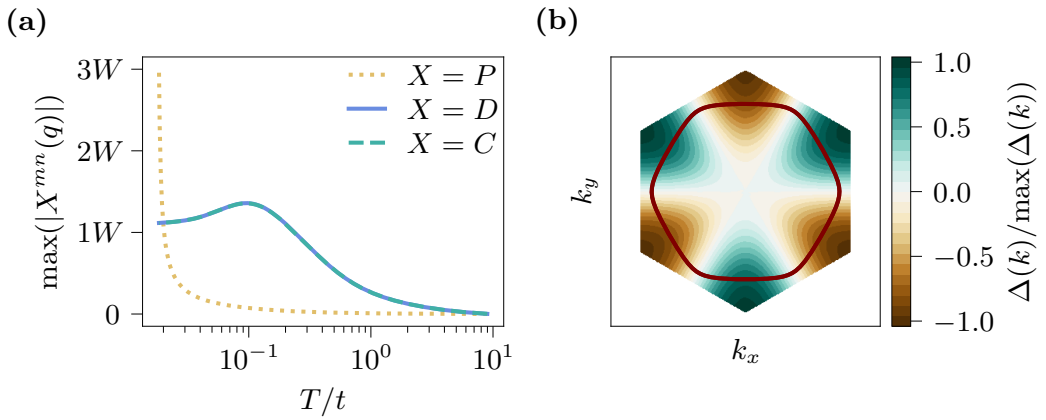

Figure 3.18: **TUFRG results for $\mu = 1.8$ and $V_1 = -0.6$, with $N_{\boldsymbol{q}} = 540$, $N_s = 2$ (19 form factors) :** a) By tracking the maximum value of the channels, eventually a P divergence appears. The C/D symmetry relation holds as expected. b) f-wave leading gap represented by a first order B_1 lattice harmonic. The red line represents the Fermi surface of the system.

The nature of this Pomeranchuck instability remains peculiar and cannot be explained completely in the framework of our former bubble analysis. From the bubble integrations alone, there should be no strong tendency for particle-hole instabilities at zero momentum transfer. Therefore, this mechanism has to be explained by some other effects which are not provided by the bubbles. Also, a complete description of the Pomeranchuck instability can not be made in our truncation since the order parameter which considerably grows for a Pomeranchuck instability (i.e. a CDW with zero momentum transfer) is just the standard density operator. Therefore we are objected to a renormalization of the chemical potential which should lead to changes of the Fermi surface while the flow integration is performed. Since we discard self-energy corrections completely in our approach, there is no way to faithfully incorporate the feedback of this effect to the Fermi surface.
In addition, we will find minor contributions in other components of $D^{l,l'}(\boldsymbol{q} = \boldsymbol{0})$ for various l, l'. At this point, we could construct a decoupling of the density-density interaction similar to the BCS theory to determine the symmetry of the order parameter. In fact, this analysis is a bit overeagerous since the strong on-site component of the singular vertex $D^{1,1}(\boldsymbol{q})$ can only ever describe a A_1 symmetry in any way. Indeed, we performed this construction in [30] and confirm this intuitive expectation.

Below Van Hove filling

For values of μ below Van Hove filling, we can for find two different areas of superconductivity. Both of these phases are again characterized by a singular P channel where the singular vertex again diverges at $\boldsymbol{q} = 0$ in various combinations of l, l'. We reconstruct the leading gap $\Delta(\boldsymbol{k})$ from these singular vertices and find the following two phases of superconductivity:

- Adjacent to the area of the Pomeranchuck instability, we will find a phase of f-wave superconductivity. The size of this phase shrinks with larger absolute values of the interaction $|V_1|$. This symmetry is described by a first order B_1 lattice harmonic.

- By lowering μ even further, the symmetry of the superconductivity changes to p-wave. The degenerated leading gaps are described by first order E_1 lattice harmonics. For lower values of $|V_1|$, this phase occurs also at lower temperatures, until it eventually drops under the imposed cut-off of $T = 10^{-5}$. This instability is a candidate for a topological superconductor since the two-dimensional irrep E_1 allows for a complex superposition of the leading lattice harmonics. This phase is called a $p + ip$ superconductor. The corresponding Chern number is $\mathcal{C} = -1$.

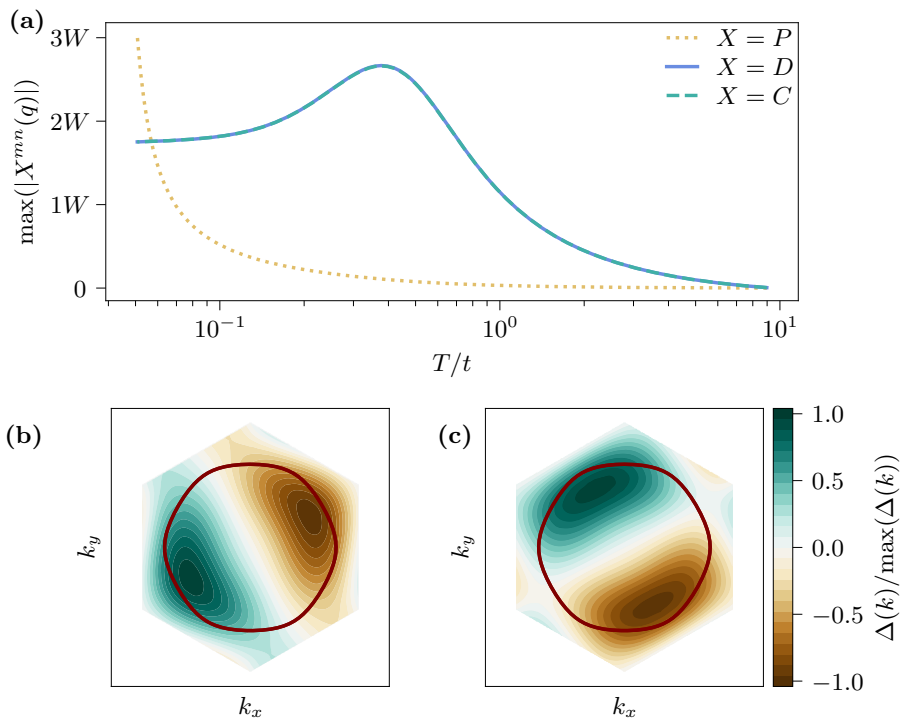

Figure 3.19: **TUFRG results for $\mu = 1.2$ and $V_1 = -1t$, with $N(\boldsymbol{q}) = 540$, $N_s = 2$ (19 form factors) :** a) Tracking the maximum value of the channels, eventually a P divergence appears. The C/D symmetry relation holds as expected. b) p-wave leading gap represented by a two-dimensional first order E_1 lattice harmonic. The red line represents the Fermi surface of the system.

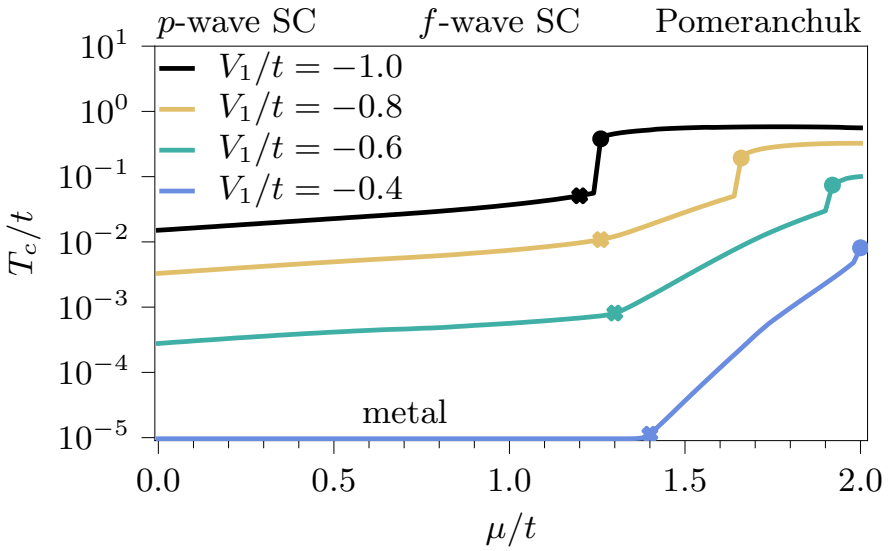

Figure 3.20: **Phase diagram for an attractive interaction V_1:** At and around Van Hove filling $\mu = 2t$, the Pomeranchuk instability consistently emerges for various interaction strengths V_1. By lowering μ, this phase is eventually replaced by a region of f-wave superconductivity (dot). For even lower chemical potential, the symmetry of the superconductivity changes to a p-wave superconductor (cross). For a weak interaction strength, i.e. $V_1 = -0.4t$, this phase does not occur above the cut-off temperature $T = 10^{-5}t$.

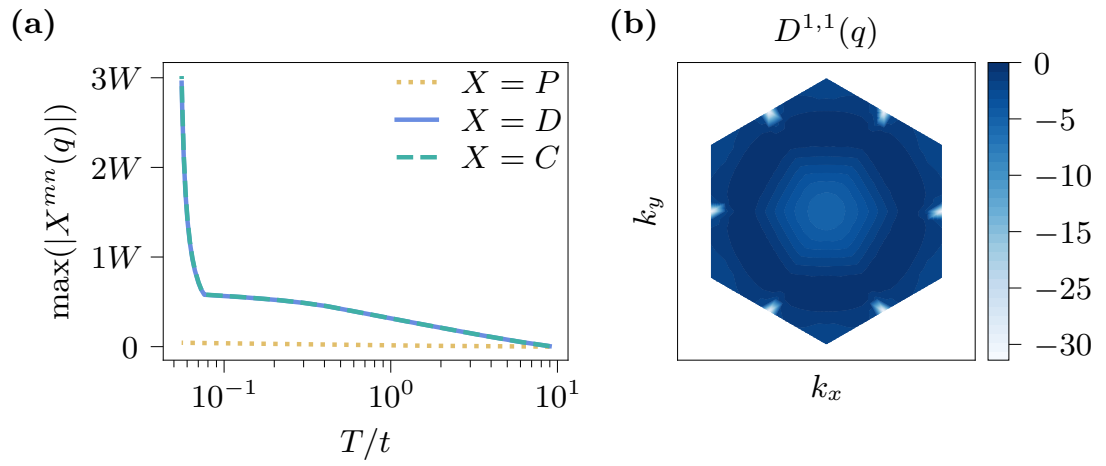

Figure 3.21: **TUFRG results at Van Hove filling $\mu = 2t$ for $V_1 = 1t$, with $N_{\boldsymbol{q}} = 540$ and $N_s = 2$ (19 form factors):** a) The D/C channel will develop a divergence while tracking the maximum absolute value in the TUFRG calculation. As before, these channels still align as predicted by the symmetry condition. b) Momentum resolved on-site component of the density channel $D^{1,1}(\boldsymbol{q})$ at the end of the flow at T_c. The peaks of the singular vertex are located at the $\boldsymbol{M}$ points, indicating a CDW instability.

The phase diagram for a selection of interaction strengths V_1 is depicted in Fig. 3.20. In addition, we display an example of the f-wave and p-wave superconductivity in Fig. 3.18 and Fig. 3.19 respectively. Both of these superconducting phases were also found in mean-field studies before [19]. Interestingly, the symmetries of the gaps in our studies do not deviate from the symmetries found in this mean-field study. From that we conclude that the onset of the superconductivity is mainly an effect of the presence of the bare attractive interaction V_1 alone and that no additional momentum structures, which could be formed under renormalization, are necessary to resolve the correct type of superconductivity of the system. A leading question for further studies is posed by the suppression of this superconductivity by the Pomeranchuck instability in close vicinity of the Van Hove singularity, for which we have to go beyond our truncation scheme.

3.2.3 Instabilities at repulsive interaction

In a second variation, we will now change the interaction to be repulsive, $V_1 > 0$. This case is much more akin to the application A where also all initial interactions are repulsive. From the studies performed for the spinful SU(2) model, we expect a very similar phase diagram here by tuning the chemical potential. At Van Hove filling, the particle-hole fluctuations should enhance the D/C channel at the $\boldsymbol{M}$ points. Away from Van Hove filling, it may be possible to generate an attractive component in the P channel, such that by the divergent behaviour of the particle-particle bubble (stemming from the generic logarithmic divergence at zero momentum), a region of superconductivity can appear in the phase diagram.

At Van Hove filling

Directly at Van Hove filling ($\mu = 2t$) we will find again a divergence in the D/C channel, similar to the attractive case (see Fig. 3.21). In contrast to the former case, the peaks of the singular vertex are now located at finite transfer momenta, namely the $\boldsymbol{M}$ points, and they strictly appear in the on-site component. Therefore, the TUFRG indicates the onset of a CDW as expected from the bubble analysis.

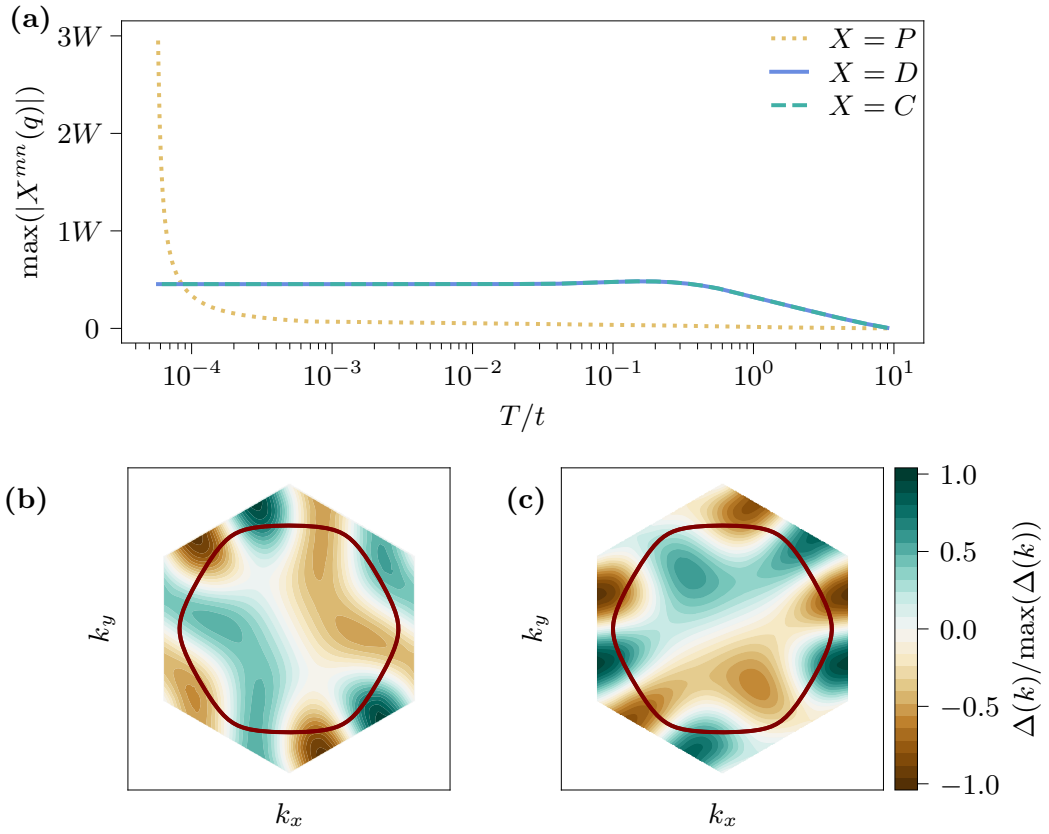

Figure 3.22: **TUFRG results for $\mu = 1.7$ and $V_1 = 1t$, with $N(\boldsymbol{q}) = 540$, $N_s = 2$ (19 form factors) :** a) By tracking the evolution of the channels, we recognize strong growth in the C/D channel initially, before a phase of saturation begins. At low temperatures however, the P channel starts developing singular behaviour. The C/D symmetry relation holds as expected. b) extended p-wave leading gap represented by a two-dimensional second order E_1 lattice harmonic. The red line represents the Fermi surface of the system.

Below Van Hove filling

Lowering the chemical potential leads to weakening the perfect nesting of the system such that the system may undergo a transition to superconductivity. Interestingly, we will only find one type of superconductivity regarding the gap function, instead of two symmetries like in the attractive case. Here, the TUFRG detects two degenerate leading gaps which represent second order E_1 lattice harmonics. Since the first order variation of this symmetry is usually called p-wave, we will call this phase an *extended* p-wave, or $\tilde{p}$-wave for brevity (see Fig. 3.22 b).

By checking the evolution of the channels (see Fig. 3.22 a), there are noticeable differences to the attractive case which reveal hints of the fundamental mechanisms of superconductivity in both instances. In the repulsive case discussed here, the D/C channel grows initially before a saturation eventually governs the evolution of these channels. In contrast, the P channel stays at a low value for the majority of the time, until significant increments are gained at low temperatures. This fits the paradigm established in application A where an attractive interaction has to be generated under renormalization to eventually trigger the onset of an instability towards superconductivity. In the attractive case however, the P channel grows already strongly in the beginning of the flow, induced by an already present attractive interaction, such that the emerging superconductivity in this case does not depend strongly on the feedback of the particle-hole channels to the particle-particle channels. This claim is also supported by the single-channel treatment of this model in reference to [19] which

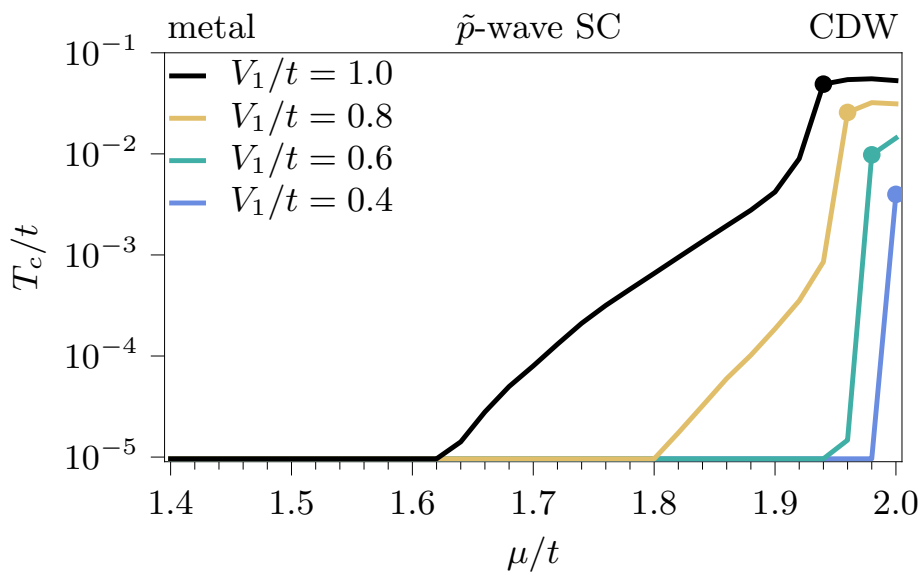

Figure 3.23: **Phase diagram for an repulsive interaction V_1:** Around Van Hove filling $\mu = 2t$ the CDW instability consistently emerges for all values of V_1. By lowering μ, the regime is replaced by a phase of extended p-wave superconductivity. The transition is marked by a dot. The area occupied by the CDW instability continuously shrinks with decreasing interaction strength V_1. The areas of μ where no instability forms above the cutoff $T = 10^{-5}t$ are be labeled as *metal*.

already finds the same superconductive gap symmetries completely without feedback. Therefore we conclude that in the repulsive case $V_1 > 0$, we are actually in the situation of competing instabilities which are heavily influenced by each other, whereas in the attractive case it is more a *race* of which of the single-channel summations *wins* at different filling situations.

We finally present the phase diagram for various repulsive interaction strengths V_1 and an extended range of fillings in Fig. 3.23.

3.2.4 Convergence tests

As a supplementary study, we will investigate the convergence in this section. We know that the stability and correctness of the implementation mainly depends on the bubble integration which was already shown to work as intended in the previous application. Still, we will perform a quick test for both, the attractive and repulsive case, to ensure that our choice of momenta and form factors are converged and do not bias the system in any way.

The results are shown in Fig. 3.24 and Fig. 3.25 respectively. For the attractive case, we demonstrate that the effects of increasing the momentum resolution $N_{\boldsymbol{q}}$ or taking higher form factor shells N_s into account are minor. For the repulsive case, the effects are still small, but more noticeably. We can find a reasonable convergence in momenta and form factors. The choice of resolution does mainly affect the quantitative value of the critical temperatures, while the general properties of the phase diagram are qualitatively unchanged. The shift of the phase boundary is also noticeable, but not of a dramatic quality. Most importantly, we find that for both cases the inclusion of higher form factor shells N_s does not lead to different types of superconductivity. This is in contrast to application A, where $N_s = 4$ is a necessary parameter to resolve the i-wave instability. Therefore, we can safely use $N_s = 2$ in this application here to gain a numerical advantage.

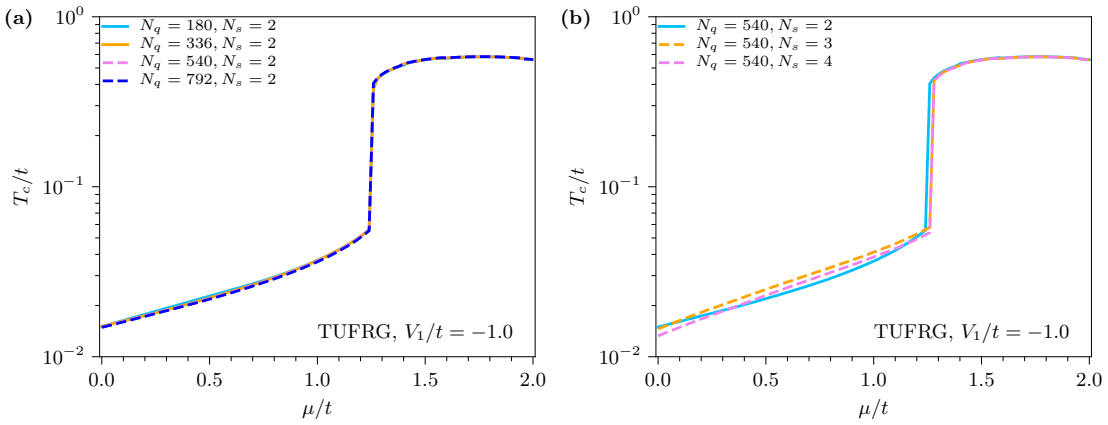

Figure 3.24: **Convergence check of the TUFRG calculations for attractive interaction:** Original plot taken from [30]. a) Dependence of critical temperatures on increasing momentum resolution $N_{\boldsymbol{q}}$. Overwhelming convergence is reached quickly for this model regarding the momentum resolution. b) Dependence of critical temperatures on taking higher form factor shells N_s into account. While the phase diagram is qualitatively unchanged, minor deviations in the superconducting branch are induced by increasing N_s.

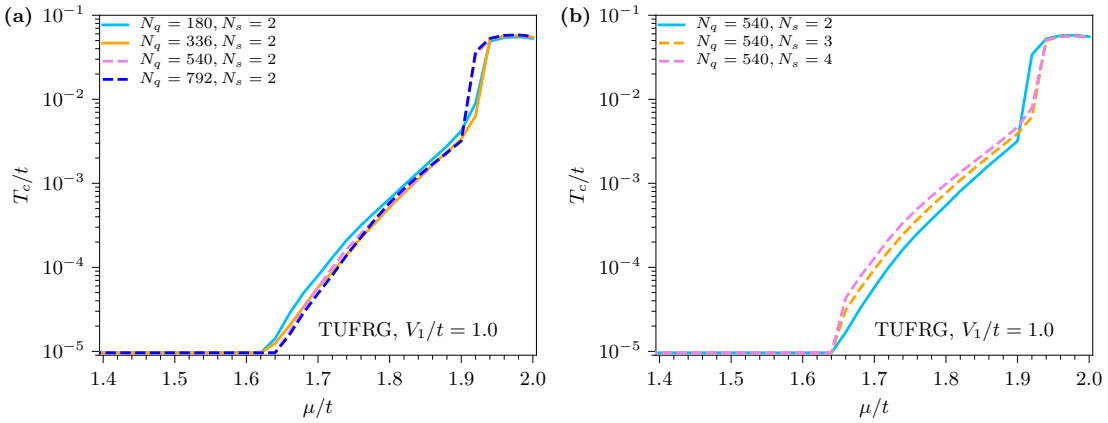

Figure 3.25: **Convergence check of the TUFRG calculations for repulsive interaction:** Original plot taken from [30]. a) The dependence of the critical temperatures on increasing momentum resolution $N_{\boldsymbol{q}}$. We detect no qualitative changes due to increasing the momentum resolution. The value of the phase boundary does slightly change. b) Dependence of critical temperatures on taking higher form factor shells N_s into account. Again, the changes are only quantitative, where higher N_s typically lead to slightly higher critical temperatures for the instabilities towards superconductivity.

3.2.5 Summary

In this section, we applied the TUFRG method to a minimal model of spinless fermions on a triangular lattice, including nearest-neighbour hopping t and nearest-neighbour interaction V_1 around Van Hove filling. For an attractive interaction $V_1 < 0$, the TUFRG detects a Pomeranchuck instability in close vicinity of the Van Hove filling. The exact nature of this instability remains peculiar since none of the strong divergencies mediated by the particle-hole bubble does directly support an intuitive understanding of this phase. Since the Pomeranchuk instability is directly linked to a change of the chemical potential μ, we are advised at this point to study this phase with self-energy corrections to fully account for the feedback caused by the formation of this instability. Away from Van Hove filling, we will find f- and p-wave superconductivity. By examining the evolution of the flow, it appears that

the mechanism for these regions of superconductivity is not sophisticated at all, and the instability is directly induced by the presence of an attractive initial interaction. This claim is supported by the fact that these superconductors are already found in single-channel studies [19] which omit the feedback of the C/D channel. For the repulsive case $V_1 > 0$, we find ourselves in a situation which resembles the scenario in application A. The main difference is represented by the absence of spins such that the competition is now between superconductivity and a charge-density effects instead of magnetism. Indeed, we detect a CDW around Van Hove filling with pronounced peaks at the M points as expected from the bubble analysis. Tuning μ away from this point leads to the formation of an extended p-wave superconductor. By investigating the evolution of the flows, the mechanism seems to be similar to the application A, whereas the particle-hole fluctuations eventually induce an attractive interaction in the particle-particle channel, allowing the P channel to diverge. These results withstand convergence tests for increasing momentum resolution and form factor shells and we are confident that no qualitative changes to the phase diagrams of both cases may appear by increasing these parameters even further.

3.3 Application C: Spinful triangular models without SU(2)-invariance

In this last section, we are going to apply the TUFRG to a more complex model with additional quantum numbers: a spinful model *without* SU(2)-invariance. As foreshadowed in section 1.3, the model treated here is an effective description of a tTMD homobilayer system. More precisely, the presented Hamiltonian may describe twisted tungsten diselenide ($tWSe_2$) and allows for the application of an out-of-plane electric field which is used to change the geometry of the Fermi surface [79]. As a consequence of this field application, the degeneracy of the spin-up and spin-down bands is lifted such that the model does not longer possess a C_{6v} but features now a C_{3v} symmetry. Since the two bands will maintain an inversion symmetry, i.e. $\epsilon_\sigma(\boldsymbol{k}) = \epsilon_{-\sigma}(-\boldsymbol{k})$, we will still be in the position to exploit some symmetry considerations in the application of the TUFRG.

The results of this application are *preliminary* and are part of a larger study which still has to be conducted. Therefore, the following results are not published anywhere yet and serve as a *proof-of-concept* of the TUFRG application for models with additional quantum numbers where several adjustments for the implementation as presented in section 2.3 have to be made. We will eventually treat scenarios regarding specific displacement fields which help us to inspect the correctness of our implementation. At first, we will treat systems at Van Hove filling only and investigate which effects to the nature of emerging magnetic instabilities by variation of the displacement field. By the notions established in section 1.1, we are able to understand these instabilities in terms of different nesting situations which can be successfully reproduced by the TUFRG. In a second study, we will generate some slices of a correlated phase diagram for different values of the displacement field by changing the filling around the Van Hove situation. Especially, we will investigate the situation with a zero displacement field such that the results are relatable to application A of this thesis. Other studies for this model haven been conducted, including (F)RG studies [57, 113] and Hartree-Fock applications [116]. We will compare results of these works with our calculations.

3.3.1 Model

The model of choice is given by:

$$H = -\sum_{\langle i,j\rangle}\sum_{\sigma}\left(t_{ij}^{\sigma}c_{i\sigma}^{\dagger}c_{j\sigma} + \text{h.c.}\right) - \mu\sum_{i,\sigma} n_i + U\sum_{i,\sigma} n_{i\uparrow}n_{i\downarrow} \tag{3.44}$$

where $c_{i\sigma}^{(\dagger)}$ annihilates(creates) an electron on site i with spin σ. The hopping t_{ij}^{σ} is complex and incorporates the effect of the external field, modeled by the parameter ϕ, as follows:

$$t_{ij}^{\sigma} = \begin{cases} te^{i\phi\sigma} & , \boldsymbol{R}_i - \boldsymbol{R}_j \in [\boldsymbol{\delta}_1, \boldsymbol{\delta}_2, \boldsymbol{\delta}_3] \\ te^{-i\phi\sigma} & , \boldsymbol{R}_i - \boldsymbol{R}_j \in [-\boldsymbol{\delta}_1, -\boldsymbol{\delta}_2, -\boldsymbol{\delta}_3] \\ 0 & , \text{else} \end{cases}$$

where $\boldsymbol{\delta}_i$ are the three real space lattice vectors defined in Fig. 3.44 a. By Fourier transformation, the dispersion for both bands ($\sigma = \uparrow$ and $\sigma = \downarrow$) can be derived as:

$$\begin{aligned} \xi_\sigma(\boldsymbol{k}) &= \epsilon_\sigma(\boldsymbol{k}) - \mu \\ &= -2t\sum_{i=1,2,3}\cos\left(\boldsymbol{k}\cdot\boldsymbol{\delta}_i + \phi\sigma\right) - \mu. \end{aligned} \tag{3.45}$$

From the expression of the dispersion, it is directly obvious that the bands of both spins are connected by an inversion symmetry:

$$\xi_\sigma(\boldsymbol{k}) = \xi_{-\sigma}(-\boldsymbol{k}). \tag{3.46}$$

As usual, the chemical potential μ determines the filling of the system and for a minimal interaction the Hubbard interaction U is added in Eq. (3.44). We displayed some of the dispersions for $\sigma = \uparrow$

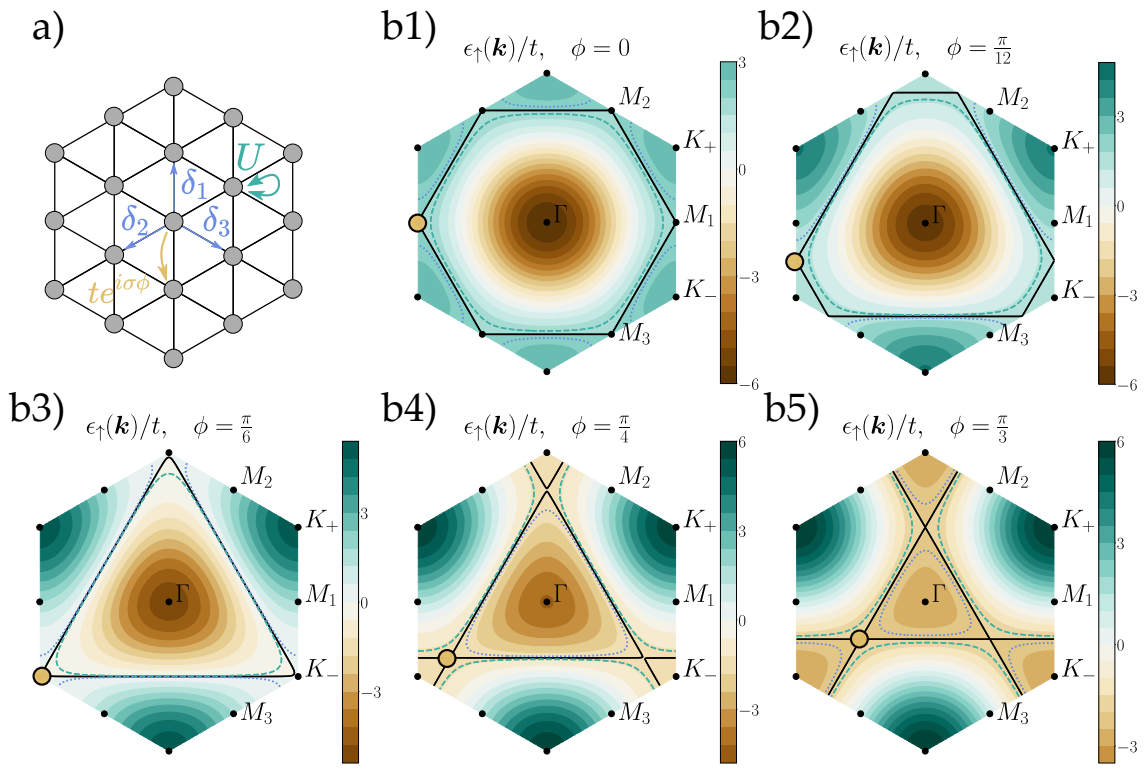

Figure 3.26: **Model and dispersion of the spin-up band:** a) Real space lattice with complex hoppings and Hubbard interaction. b1-5) Dispersion fr $t = 1.0$ and $\sigma =\uparrow$ for several choices of the paramter ϕ. The black line indicates the Fermi surface at Van Hove filling. The Van Hove point (yellow) wanders in the Brillouin zone depending on ϕ. Two example cases for overdoping (blue) and underdoping (green) are also displayed for each ϕ.

in Fig. 3.26 b1-5. The band for $\sigma =\downarrow$ will be of the same form, with the sole difference that by the inversion symmetry Eq. (3.46) the whole dispersion is rotated by an angle of π. For $\phi = 0$, we actually recover the dispersion used in application A. This is the only scenario where both bands are degenerated. Interestingly, the location of the Van Hove points change with the application of the displacement field. By alternating ϕ starting from 0, the Van Hove points will wander from the $\boldsymbol{M}$ points to the $\boldsymbol{K}_-$ points ($\boldsymbol{K}_+$ for $\sigma =\downarrow$) which are eventually reached for $\phi = \frac{\pi}{6}$. This value is of ϕ is special, because the Van Hove point will transform to a *higher order Van Hove point*, where the density of states will not feature a logarithmic divergence, but a divergence obeying a power law behaviour [48, 21]. By increasing the parameter beyond $\frac{\pi}{6}$, the point will start moving towards the $\boldsymbol{\Gamma}$ point. The highest value we want to investigate here is $\phi = \frac{\pi}{3}$ which will feature exotic behaviour regarding the pairing vertex as we will see later. For the application of the TUFRG to this spinful model, we are now obligated to employ the TUFRG to the spinful FRG equations without SU(2)-invariance Eqs. (2.40)-(2.42). These translate to the TUFRG equations as follows:

$$\frac{d}{d\Lambda} P^{l,l'}_{\sigma_1,\sigma_2,\sigma_3,\sigma_4}(\boldsymbol{q}) = \frac{1}{2} \sum_{l_1,l_2} \sum_{\substack{\nu_1,\nu_2,\\ \nu_3,\nu_4}} V^{P,(l,l_1)}_{\sigma_1,\sigma_2,\nu_1,\nu_2}(\boldsymbol{q}) \times \dot{B}^{-,(l_1,l_2)}_{\nu_1,\nu_2,\nu_3,\nu_4}(\boldsymbol{q}) \times V^{P,(l_2,l')}_{\nu_3,\nu_4,\sigma_3,\sigma_4}(\boldsymbol{q}), \tag{3.47}$$

$$\frac{d}{d\Lambda} D^{l,l'}_{\sigma_1,\sigma_2,\sigma_3,\sigma_4}(\boldsymbol{q}) = \sum_{l_1,l_2} \sum_{\substack{\nu_1,\nu_2,\\ \nu_3,\nu_4}} V^{D,(l,l_1)}_{\sigma_1,\sigma_2,\nu_1,\nu_2}(\boldsymbol{q}) \times \dot{B}^{+,(l_1,l_2)}_{\nu_1,\nu_2,\nu_3,\nu_4}(\boldsymbol{q}) \times V^{D,(l_2,l')}_{\nu_3,\nu_4,\sigma_3,\sigma_4}(\boldsymbol{q}), \tag{3.48}$$

$$\frac{d}{d\Lambda} C^{l,l'}_{\sigma_1,\sigma_2,\sigma_3,\sigma_4}(\boldsymbol{q}) = \sum_{l_1,l_2} \sum_{\substack{\nu_1,\nu_2,\\ \nu_3,\nu_4}} V^{C,(l,l_1)}_{\sigma_1,\sigma_2,\nu_1,\nu_2}(\boldsymbol{q}) \times \dot{B}^{+,(l_1,l_2)}_{\nu_1,\nu_2,\nu_3,\nu_4}(\boldsymbol{q}) \times V^{C,(l_2,l')}_{\nu_3,\nu_4,\sigma_3,\sigma_4}(\boldsymbol{q}). \tag{3.49}$$

Here, all objects are also equipped with four spin indices. We will inspect the effect of these additional degrees of freedom to our TUFRG method. By deriving the bubble integrations as laid out in section 2.2, the spin-dependent objects are defined as[3]:

$$\dot{B}^{-,(l,l')}_{\nu_1,\nu_2,\nu_3,\nu_4}(\boldsymbol{q}) = -\int_p \frac{d}{dT}\left[G^{0,T}_{\nu_1,\nu_3}(i\omega_p,\boldsymbol{p}+\boldsymbol{q})G^{0,T}_{\nu_2,\nu_4}(-i\omega_p,-\boldsymbol{p})\right] f_l(\boldsymbol{p})f^*_{l'}(\boldsymbol{p}), \tag{3.50}$$

$$\dot{B}^{+,(l,l')}_{\nu_1,\nu_2,\nu_3,\nu_4}(\boldsymbol{q}) = -\int_p \frac{d}{dT}\left[G^{0,T}_{\nu_1,\nu_3}(i\omega_p,\boldsymbol{p}+\boldsymbol{q})G^{0,T}_{\nu_4,\nu_2}(+i\omega_p,+\boldsymbol{p})\right] f_l(\boldsymbol{p})f^*_{l'}(\boldsymbol{p}). \tag{3.51}$$

In general, the TUFRG equations can be defined for an arbitrary additional quantum number o which can be for example an orbital, sublattice or spin degree of freedom. Here, we have the choice of deriving the TUFRG in two different ways. The first possibility is given by describing the channels with four **band indices** b which reflect the band structure after diagonalizing the Hamiltonian with respect to the new quantum number o. This description comes with the disadvantage of choosing an *orbital makeup* which is given by the non-unique unitary transformation which diagonalizes the Hamiltonian. It has been shown that the choice of this transformation indeed effects the quantitative results of the TUFRG [81, 66]. Instead, we will choose the description in the **orbital indices** o (i.e. the spins in our case, as already employed in Eqs. (3.47)-(3.49)) which do not feature this problem. For a general index o, the bare propagator has the form [78]:

$$G^{0,T}_{o_1,o_2}(i\omega_p,\boldsymbol{p}) = \sum_b U_{o_1 b}(\boldsymbol{k})U^*_{o_2 b}(\boldsymbol{k})\frac{1}{i\omega_{\boldsymbol{p}}-\xi_b(\boldsymbol{k})}, \tag{3.52}$$

where U is the unitary transform which diagonalizes the Hamiltonian. Fortunately, the Hamiltonian is already diagonal in spin space in our case by the given dispersion Eq. (3.45). Therefore, the transformation matrix is given by $U_{\nu_1 b}(\boldsymbol{k}) = \delta_{\nu_1 b}$. The spin-dependent propagtor is therefore given by:

$$G^{0,T}_{\nu_1,\nu_2}(i\omega_p,\boldsymbol{p}) = \delta_{\nu_1,\nu_2}\frac{1}{i\omega_{\boldsymbol{p}}-\xi_{\nu_1}(\boldsymbol{k})}. \tag{3.53}$$

Finally, the spin-dependent bubble integrations are cast into the following form after executing the Matsubara sum:

$$\dot{B}^{-,(l,l')}_{\nu_1,\nu_2,\nu_3,\nu_4}(\boldsymbol{q}) = -\delta_{\nu_1,\nu_3}\delta_{\nu_2,\nu_4}\int_{\boldsymbol{p}} \frac{n'_F(\xi_{\nu_1}(\boldsymbol{q}+\boldsymbol{p}))+n'_F(\xi_{\nu_2}(-\boldsymbol{p}))}{\xi_{\nu_1}(\boldsymbol{q}+\boldsymbol{p})+\xi_{\nu_2}(-\boldsymbol{p})} f_l(\boldsymbol{p})f^*_{l'}(\boldsymbol{p}), \tag{3.54}$$

$$\dot{B}^{+,(l,l')}_{\nu_1,\nu_2,\nu_3,\nu_4}(\boldsymbol{q}) = +\delta_{\nu_1,\nu_3}\delta_{\nu_2,\nu_4}\int_{\boldsymbol{p}} \frac{n'_F(\xi_{\nu_1}(\boldsymbol{q}+\boldsymbol{p}))-n'_F(\xi_{\nu_2}(\boldsymbol{p}))}{\xi_{\nu_1}(\boldsymbol{q}+\boldsymbol{p})-\xi_{\nu_2}(\boldsymbol{p})} f_l(\boldsymbol{p})f^*_{l'}(\boldsymbol{p}). \tag{3.55}$$

We will see in the next section how the form of the bubble integrations Eqs. (3.54),(3.55) allows for further symmetry considerations. The vertices in the flow equations (3.47)-(3.49)), including their respective cross-projections, are also equipped with additional spin indices[4] and are by the derivation defined as follows. For the P channel:

$$V^{P,(l,l')}_{\sigma_1,\sigma_2,\sigma_3,\sigma_4}(\boldsymbol{q}) = V^{0,P,(l,l')}_{\sigma_1,\sigma_2,\sigma_3,\sigma_4}(\boldsymbol{q}) + P^{l,l'}_{\sigma_1,\sigma_2,\sigma_3,\sigma_4}(\boldsymbol{q}) + V^{D\to P,(l,l')}_{\sigma_1,\sigma_2,\sigma_3,\sigma_4}(\boldsymbol{q}) + V^{C\to P,(l,l')}_{\sigma_1,\sigma_2,\sigma_3,\sigma_4}(\boldsymbol{q}), \tag{3.56}$$

$$V^{D\to P,(l,l')}_{\sigma_1,\sigma_2,\sigma_3,\sigma_4}(\boldsymbol{q}) = \sum_L \tilde{D}^{L,-L+l-l'}_{\sigma_1,\sigma_3,\sigma_4,\sigma_2}(-\boldsymbol{R}_{l'}-\boldsymbol{R}_L)\times e^{-i\boldsymbol{q}\boldsymbol{R}_L}, \tag{3.57}$$

$$V^{C\to P,(l,l')}_{\sigma_1,\sigma_2,\sigma_3,\sigma_4}(\boldsymbol{q}) = \sum_L \tilde{C}^{L,-L+l+l'}_{\sigma_1,\sigma_4,\sigma_3,\sigma_2}(-\boldsymbol{R}_L+\boldsymbol{R}_{l'})\times e^{-i\boldsymbol{q}(\boldsymbol{R}_L-\boldsymbol{R}_{l'})}. \tag{3.58}$$

[3] Again, using the convention of an additional sign

[4] For a detailed definition of the three channels regarding the spin indices, see App. A.4.

For the D channel:

$$V^{D,(l,l')}_{\sigma_1,\sigma_2,\sigma_3,\sigma_4}(\boldsymbol{q}) = V^{0,D,(l,l')}_{\sigma_1,\sigma_2,\sigma_3,\sigma_4}(\boldsymbol{q}) + D^{l,l'}_{\sigma_1,\sigma_2,\sigma_3,\sigma_4}(\boldsymbol{q}) + V^{P\to D,(l,l')}_{\sigma_1,\sigma_2,\sigma_3,\sigma_4}(\boldsymbol{q}) + V^{C\to D,(l,l')}_{\sigma_1,\sigma_2,\sigma_3,\sigma_4}(\boldsymbol{q}), \tag{3.59}$$

$$V^{P\to D,(l,l')}_{\sigma_1,\sigma_2,\sigma_3,\sigma_4}(\boldsymbol{q}) = \sum_L \tilde{P}^{L,L-l-l'}_{\sigma_1,\sigma_4,\sigma_2,\sigma_3}(-\boldsymbol{R}_l) \times e^{-i\boldsymbol{q}(\boldsymbol{R}_L-\boldsymbol{R}_{l'})}, \tag{3.60}$$

$$V^{C\to D,(l,l')}_{\sigma_1,\sigma_2,\sigma_3,\sigma_4}(\boldsymbol{q}) = \sum_L \tilde{C}^{L,L-l+l'}_{\sigma_1,\sigma_3,\sigma_2,\sigma_4}(-\boldsymbol{R}_l) \times e^{-i\boldsymbol{q}\boldsymbol{R}_L}. \tag{3.61}$$

And for the C channel:

$$V^{C,(l,l')}_{\sigma_1,\sigma_2,\sigma_3,\sigma_4}(\boldsymbol{q}) = V^{0,C,(l,l')}_{\sigma_1,\sigma_2,\sigma_3,\sigma_4}(\boldsymbol{q}) + C^{l,l'}_{\sigma_1,\sigma_2,\sigma_3,\sigma_4}(\boldsymbol{q}) + V^{P\to C,(l,l')}_{\sigma_1,\sigma_2,\sigma_3,\sigma_4}(\boldsymbol{q}) + V^{D\to C,(l,l')}_{\sigma_1,\sigma_2,\sigma_3,\sigma_4}(\boldsymbol{q}), \tag{3.62}$$

$$V^{P\to C,(l,l')}_{\sigma_1,\sigma_2,\sigma_3,\sigma_4}(\boldsymbol{q}) = \sum_L \tilde{P}^{L,-L+l+l'}_{\sigma_1,\sigma_4,\sigma_3,\sigma_2}(-\boldsymbol{R}_L+\boldsymbol{R}_{l'}) \times e^{-i\boldsymbol{q}(\boldsymbol{R}_L-\boldsymbol{R}'_l)}, \tag{3.63}$$

$$V^{D\to C,(l,l')}_{\sigma_1,\sigma_2,\sigma_3,\sigma_4}(\boldsymbol{q}) = \sum_L \tilde{D}^{L,L-l+l'}_{\sigma_1,\sigma_3,\sigma_2,\sigma_4}(-\boldsymbol{R}_l) \times e^{-i\boldsymbol{q}\boldsymbol{R}_L}. \tag{3.64}$$

And the projections for the initial conditions read:

$$V^{0,P,(l,l')}_{\sigma_1,\sigma_2,\sigma_3,\sigma_4}(\boldsymbol{q}) = \int_{\boldsymbol{k},\boldsymbol{k}'} V^0_{\sigma_1,\sigma_2,\sigma_3,\sigma_4}(\boldsymbol{q}+\boldsymbol{k},-\boldsymbol{k},\boldsymbol{q}+\boldsymbol{k}') \times f_l(\boldsymbol{k}) f^*_{l'}(\boldsymbol{k}'), \tag{3.65}$$

$$V^{0,D,(l,l')}_{\sigma_1,\sigma_2,\sigma_3,\sigma_4}(\boldsymbol{q}) = \int_{\boldsymbol{k},\boldsymbol{k}'} V^0_{\sigma_1,\sigma_4,\sigma_2,\sigma_3}(\boldsymbol{q}+\boldsymbol{k},\boldsymbol{k}',\boldsymbol{k}) \times f_l(\boldsymbol{k}) f^*_{l'}(\boldsymbol{k}'), \tag{3.66}$$

$$V^{0,C,(l,l')}_{\sigma_1,\sigma_2,\sigma_3,\sigma_4}(\boldsymbol{q}) = \int_{\boldsymbol{k},\boldsymbol{k}'} V^0_{\sigma_1,\sigma_4,\sigma_3,\sigma_2}(\boldsymbol{q}+\boldsymbol{k},\boldsymbol{k}',\boldsymbol{q}+\boldsymbol{k}') \times f_l(\boldsymbol{k}) f^*_{l'}(\boldsymbol{k}'). \tag{3.67}$$

Where the initial interaction has to be cast into the form stemming from the vertex expansion with including spin degrees of freedom as follows:

$$H_{\text{Int}} \to \frac{1}{4} \int_{\boldsymbol{k}_1,\boldsymbol{k}_2,\boldsymbol{k}_3,\boldsymbol{k}_4} V^0_{\sigma_1,\sigma_2,\sigma_3,\sigma_4}(\boldsymbol{k}_1,\boldsymbol{k}_2,\boldsymbol{k}_3,\boldsymbol{k}_4)\delta(\boldsymbol{k}_1+\boldsymbol{k}_2-\boldsymbol{k}_3-\boldsymbol{k}_4) \sum_{\substack{\sigma_1,\sigma_2,\\ \sigma_3,\sigma_4}} \times$$
$$c^\dagger_{\sigma_1}(\boldsymbol{k}_1) c^\dagger_{\sigma_2}(\boldsymbol{k}_2) c_{\sigma_4}(\boldsymbol{k}_4) c_{\sigma_3}(\boldsymbol{k}_3). \tag{3.68}$$

From this, we can derive the (properly anti-symmetrized) initial conditions induced by the initial Hubbard interaction U, exactly as in the other applications (see App. A.5):

$$V^{0,P,(1,1)}_{\uparrow\downarrow\uparrow\downarrow}(\boldsymbol{q}) = \quad V^{0,P,(1,1)}_{\downarrow\uparrow\downarrow\uparrow}(\boldsymbol{q}) = \quad -V^{0,P,(1,1)}_{\uparrow\downarrow\downarrow\uparrow}(\boldsymbol{q}) = \quad -V^{0,P,(1,1)}_{\downarrow\uparrow\uparrow\downarrow}(\boldsymbol{q}) = \quad U \tag{3.69}$$

$$V^{0,D,(1,1)}_{\uparrow\uparrow\downarrow\downarrow}(\boldsymbol{q}) = \quad V^{0,D,(1,1)}_{\downarrow\downarrow\uparrow\uparrow}(\boldsymbol{q}) = \quad -V^{0,D,(1,1)}_{\uparrow\downarrow\uparrow\downarrow}(\boldsymbol{q}) = \quad -V^{0,D,(1,1)}_{\downarrow\uparrow\downarrow\uparrow}(\boldsymbol{q}) = \quad U \tag{3.70}$$

$$V^{0,C,(1,1)}_{\uparrow\downarrow\uparrow\downarrow}(\boldsymbol{q}) = \quad V^{0,C,(1,1)}_{\downarrow\uparrow\downarrow\uparrow}(\boldsymbol{q}) = \quad -V^{0,C,(1,1)}_{\uparrow\uparrow\downarrow\downarrow}(\boldsymbol{q}) = \quad -V^{0,C,(1,1)}_{\downarrow\downarrow\uparrow\uparrow}(\boldsymbol{q}) = \quad U \tag{3.71}$$

It should be noticed with great caution that the order of the spin indices on the right hand side do in general *appear in a different order compared to the left hand side* for the majority of the objects presented here. These definitions were chosen (see App. A.4) such that all three flow equations (3.47)-(3.49) have the same simple structure which is a tensor contraction of the two vertices and a bubble integration from the left to right. Although the complexity of the TUFRG equations is now significantly increased in contrast to the previous applications, the general workflow does not change at all. Eventually, we will solve the differential equations for the three channels P, C, D and find instabilities by detecting diverging components of these objects which received four additional spin indices now. Nevertheless, the introduced model Eq. (3.44) provides additional numerical challenges, for which we have to adapt our implementation as presented in the next section.

3.3.2 Alterations of implementation

Three aspects impede a straight forward application of the derived TUFRG method as described in the previous sections:

1. Most obvious, the flow equations possess an additional scaling due to the spin degree of freedom, namely N_σ^4, with $N_\sigma = 2$ accounting for spin-up and spin-down. Consequently, the computational complexity increases instantaneously with a factor of 16. This is especially problematic for the bubble integrations which pose the numerical bottleneck of the method. Without any use of symmetries, we are now deemed to solve $2 \times N_{\boldsymbol{q}} \times N_l^2 \times N_\sigma^4$ bubble integrations per renormalization step.

2. In application A and B, the underlying model Hamiltonians provided a C_{6v} symmetry from which we could deduce a numerical speedup of factor 12. Now, our model does only inhabit a C_{3v} symmetry (excluding the case for $\phi = 0$ which is still C_{6v} symmetric) such that we get a lower speedup factor of only 6 instead 12. Therefore the new (lower) symmetry of the model costs us a factor of 2 in comparison to the previous applications.

3. Most importantly, we have to be very careful with the bubble integrations regarding the form of the dispersions. As it becomes apparent from Fig. 3.26 b1-5, we are confronted with complicated forms for the Fermi surface depending on filling and displacement field ϕ. To ensure a correct integration, we will have to include these complex features stemming from the dispersion accordingly to the integration routine.

With the addition of the spin indices and the reduction to C_{3v} symmetry, our method is already affected by being a factor of 16×2 slower than before. On top of this slowdown, the used integration routine which has to account to the various features of the complex Fermi surfaces, will also be slower. We will guide through these three aspects and demonstrate how meaningful advantages can be exploited to mitigate these effects.

Symmetries of bubble symmetries and the C_{3v} symmetry.

As a first obvious measure to improve the implementation, we register that the bubble integrations Eqs. (3.54),(3.55) only allow for 4 non-zero components regarding the spin indices by the structure of the Kronecker deltas. We will name these components:

$$\begin{aligned}(\nu_1,\nu_2,\nu_3,\nu_4) &\to (\uparrow,\uparrow,\uparrow,\uparrow),(\downarrow,\downarrow,\downarrow,\downarrow), \quad \text{Intra}-\text{spin}\\ (\nu_1,\nu_2,\nu_3,\nu_4) &\to (\uparrow,\downarrow,\uparrow,\downarrow),(\downarrow,\uparrow,\downarrow,\uparrow), \quad \text{Inter}-\text{spin}\end{aligned}$$

Since all other combinations of the bubble integrations are directly 0, the slowdown factor is not given by 16, but actually by just 4. This slowdown factor can even be further reduced by using the inversion symmetry of the dispersion, $\xi_\sigma(\boldsymbol{k}) = \xi_{-\sigma}(-\boldsymbol{k})$. By a change of integration variables,the following symmetry of the bubble integrations is directly derived:

$$\begin{aligned}\dot{B}^{\pm,(l,l')}_{\nu_1,\nu_2,\nu_3,\nu_4}(\boldsymbol{q}) &= \dot{B}^{\pm,(l',l)}_{-\nu_1,-\nu_2,-\nu_3,-\nu_4}(-\boldsymbol{q}),\\ \to \dot{B}^{\pm,(l,l')}_{\uparrow\uparrow\uparrow\uparrow}(\boldsymbol{q}) &= \dot{B}^{\pm,(l',l)}_{\downarrow\downarrow\downarrow\downarrow}(-\boldsymbol{q}),\\ \to \dot{B}^{\pm,(l,l')}_{\uparrow\downarrow\uparrow\downarrow}(\boldsymbol{q}) &= \dot{B}^{\pm,(l',l)}_{\downarrow\uparrow\downarrow\uparrow}(-\boldsymbol{q}).\end{aligned} \tag{3.72}$$

Thus, we only need one intra-spin bubble integration and one inter-spin bubble integration and restore the complement bubble integration by symmetry. Admittely, we have to be careful which initial momenta $\boldsymbol{q}$ we select in our resolution to exploit this symmetry relation accordingly. To motivate this, we will switch the focus on the use of the C_{3v} symmetry.

The point group C_{3v} includes the identiy operation E, two rotations around the angles $\pm\frac{2\pi}{3}$ ($2C_3$)

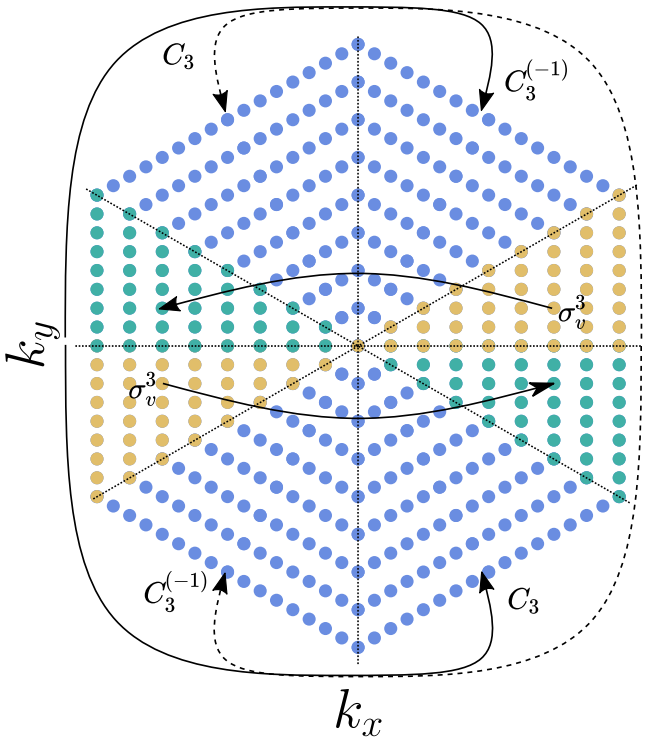

Figure 3.27: **Optimal exploitation of symmetries:** Before the flow is calculated, the bubble integrations for yellow momenta for spin combinations ↑↑↑↑ and ↑↓↑↓ are calculated. Their respective counterpart with flipped spins is then obtained by symmetry. Then, the flow equations can be calculated for the complete yellow patch. By mirror symmetry, we can obtain the vertex values for the green patch. Then, with the C_3 rotations, the remaining patches are restored (blue).

and the three reflections according to the conjugacy class $3\sigma_v$ identically defined as in the case of C_{6v} symmetry. We only need the rotations and one of the three reflection planes in our application, namely the reflection plane defined by the y-axis. From section 2.3.3, the point group still affects the differential equations in the same way since the aforementioned selection of symmetry relations (which are represented as Q) leave the spin indices untouched. We therefore use analogously:

$$X^{l,l'}_{\sigma_1,\sigma_2,\sigma_3,\sigma_4}(\boldsymbol{q}) = X^{Ql,Ql'}_{\sigma_1,\sigma_2,\sigma_3,\sigma_4}(Q\boldsymbol{q}), \tag{3.73}$$

with $X = P, C, D$. The optimal use of symmetries of both, bubbles and vertices, is then employed as follows:

1. We will select a momentum patch in the momentum discretization which includes for each momentum $\boldsymbol{q}$ also its inverted momentum $-\boldsymbol{q}$ (see yellow points Fig. 3.27). When the bubble integrations are performed, we will only explicitly calculate those integrations for the spin combinations ↑↑↑↑ and ↑↓↑↓. Their respective intra-spin and inter-spin counterpart can then be restored by symmetry relation Eq. (3.72), such that we half the numerical effort.

2. When the flow equations are calculated, we will proceed using the mirror and rotation symmetry as displayed in Eq. (3.73) (see green and blue points in Fig. 3.27), such that only $1/6$ of the flow equations are explicitly calculated, while the rest is restored by symmetry.

Conclusively, we want to compare the numerical advantage gained here with the speedup obtained in the SU(2)-invariant case. We will discard the effects of the form factor symmetry here since this speedup is achieved for both implementations equally. In the case including spin-rotation symmetry, the bubbles are not equipped with spin indices and are exposed to a C_{6v} point group symmetry.

Therefore for each type of bubble integration, there are in total $N_{\boldsymbol{q}} \times N_l^2$ integrations to perform. By the C_{6v} point group, this can be reduced by a factor of 12 since only for $1/12$ of the momenta these integrations have to be calculated:

$$\#\,\text{bubble integrations including SU}(2)-\text{invariance} = \frac{N_{\boldsymbol{q}}}{12} \times N_l^2.$$

In the case without SU(2)-invariance, we do have explicit spin indices for the bubble integrations and the underlying symmetry of the Hamiltonian is C_{3v}. Therfore, the total amount of integrations $N_{\boldsymbol{q}} \times N_l^2 \times N_\sigma^4$ can be reduced by a factor of 6 due to the momentum symmetry and by a factor of 4 since only a selection of four spin index combinations is non-zero for the bubble integrations. Furthermore, always two of these spin combinations are symmetrically connected, also delivering a speedup of factor 2 such that in total:

$$\#\,\text{bubble integrations without SU}(2)-\text{invariance} = \frac{N_{\boldsymbol{q}}}{6} \times N_l^2 \times \frac{N_\sigma^4}{2 \cdot 4}.$$

The quotient which indicating the overall slowdown in this application is then given by:

$$\rightarrow \frac{12}{6 \cdot 2 \cdot 4} N_\sigma^4 = 4,$$

where obviously $N_\sigma = 2$ since we include spin-up and spin-down. Therefore, we expect *at least* a factor of 4 compared to application A when it comes to computational runtime of comparable parameters. This slowdown can also be considerably higher, when in addition the adaptive integration routine takes more time to calculate the integrals correctly.

Adjusting integration routine

While the Fermi surface for different fillings was rather simple in application A and B, this radically changes now, as already recognizable by the Fermi surfaces in Fig. 3.26 for different values of ϕ. In addition, the spin-dependent bubble integrations Eqs. (3.54),(3.55) will depend on both bands for the inter-spin component. Therefore the integrand will develop sharp features for both Fermi surfaces belonging to both of the two non-degenerated bands.

To treat these new structures accordingly, we have to adjust the proposed adaptive integration routine. The general procedure will still remain unchanged: we will perform 1D integrations of beams in the Brillouin zone multiplied with the angular weight. The changes are as follows:

- We will integrate the objects $\dot{B}^{\pm,(l,l')}_{\uparrow\uparrow\uparrow\uparrow}(\boldsymbol{q})$ (intra-spin) and $\dot{B}^{\pm,(l,l')}_{\uparrow\downarrow\uparrow\downarrow}(\boldsymbol{q})$ (inter-spin) for the momenta in the yellow patch in Fig. 3.27. The respective counterparts regarding the spin indices of these objects are obtainable by symmetry.

- For a chosen μ and regardless of under- or overdoping, we will decompose the integration into two parts: an *interior* and an *exterior* integration.

- The interior integration consists of beams starting at the $\boldsymbol{\Gamma}$ point of the Brillouin zone and going radially until the Fermi surface of the Van Hove doped scenario μ_{VH} is met. Any crossings with the Fermi surface of the system with μ is chosen as an explicit discretization point similar to the routine in the former application. In addition, the inter-spin integration will also include cuts with the Fermi surfaces of both bands as discretization points. These points define the intervals where the adaptive routine is applied to.

- The exterior integration uses beams starting at the $\mathbf{K}^{\pm}$ points going radially to the Fermi surface of the system at Van Hove filling μ_{VH}. Again, all cuts with Fermi surfaces are used as explicit discretization points, where again for the inter-spin bubble integration both bands are considered for these points.

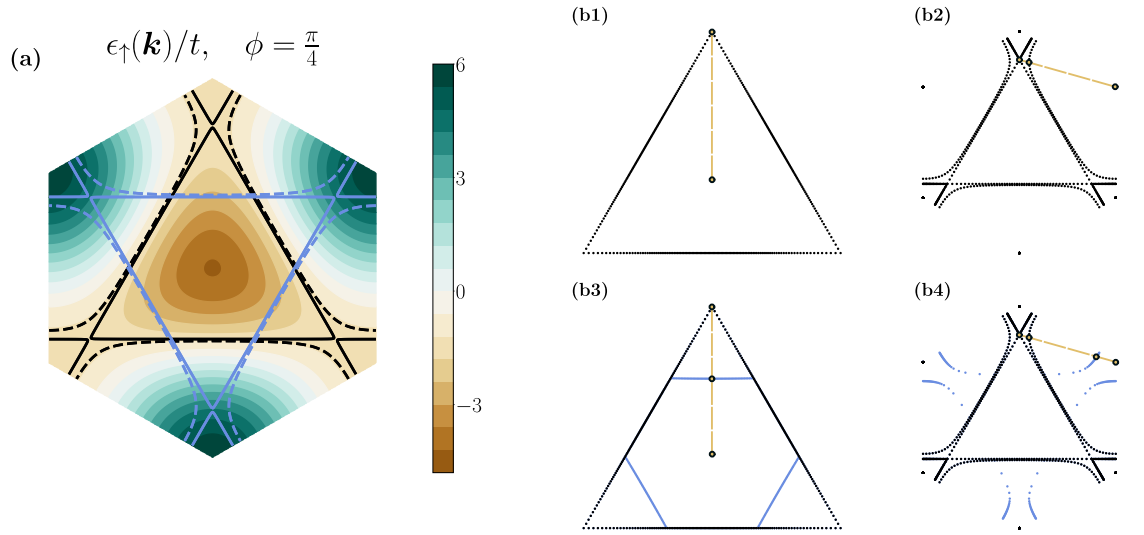

Figure 3.28: **Example of integration beams for $\mu = 0.9\mu_{\mathrm{VH}}$, $\phi = \frac{\pi}{4}$:** a) Dispersion of the system. The black solid line indicates the Fermi surface at Van Hove filling, while the dashed line is the actual Fermi surface of the given μ. The blue lines are displayed for visibility and represent the Fermi surface counterparts of the spin-down band drawn into the dispersion of the spin-up band. b1) Interior integration for the intra-spin bubble integration. One example beam (yellow), defining the integration intervals, includes the $\mathbf{\Gamma}$ point and the Fermi surface at Van Hove filling as explicit discretization points. b2) Exterior integration for the intra-spin bubble integration. The example beam (yellow) goes radially from the $\mathbf{K}^+$ point to the Fermi surface at Van Hove filling. On this line, there is one cut with the actual Fermi surface at μ, such that 3 explicit discretization points are included, forming 2 intervals for the adaptive integration. b3),b4) Interior and exterior integration for the inter-spin bubble. The construction is in general analogous to the intra-spin case, with the addition that also cuts with the Fermi surface of the spin-down band at μ (blue) are included as explicit discretization points.

- The angular resolution is always to be chosen as $N_A = 360$, regardless of the choice for μ. This results in 360 beams for the interior integration and for the 6 pockets of the exterior integration this results onto 60 beams for each $\mathrm{K}^\pm$ point.
- The case of $\phi = \frac{\pi}{6}$ is special since the Fermi surface has a triangular shape here. In consequence, the exterior integration will be distributed to 3 pockets instead of 6 with 120 beams.

To illustrate these changes we added Fig. 3.28. To save computational time, all the cuts with Fermi surfaces resulting into discretization points are pre-calculated before starting the TUFRG flow calculation. These points are then repeatedly used throughout the application since the position of these points do not change.

This finalises the changes of the implementation with respect to the bubble integrations. We will now move forward to two case studies conducted with this method which proof the general correctness of our implementation.

3.3.3 Model at Van Hove filling: effects of displacement field on magnetism

In this first study, we will focus only on systems at Van Hove filling for various values of the parameter ϕ controlling the external displacement field. The values of the Van Hove filling for $\phi \in [0, \frac{\pi}{3}]$ were obtained numerically and can be seen in Fig. 3.29. Similarly to another study [57], we will choose $t = 1$ and $U = 6t$ for framing an intermediate coupling regime (this interaction value is still smaller than the bandwidth). From application A and B, we are confident to assume that also in this model

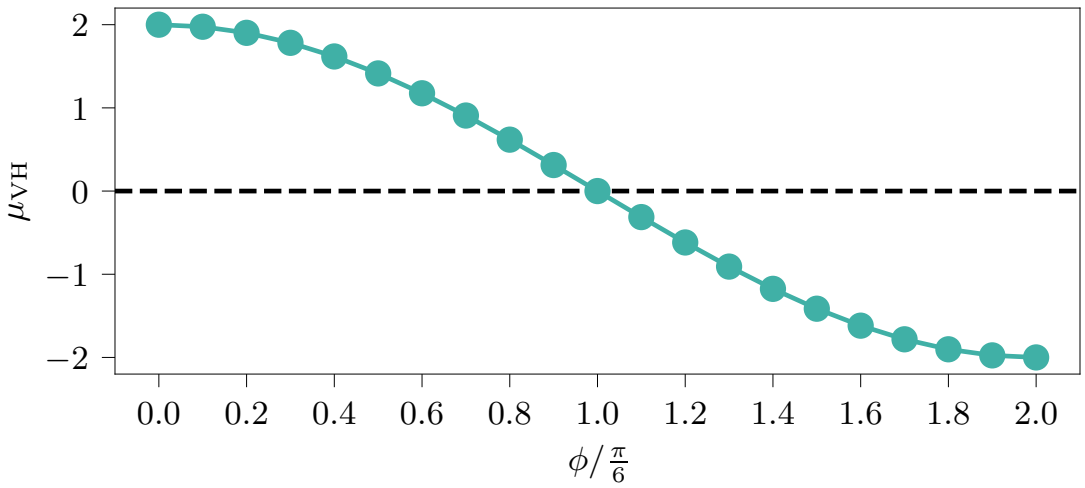

Figure 3.29: **Values for μ determining Van Hove filling for $t = 1$:** These values were obtained numerically. For $\phi = 0$ we recover the value $\mu_{\mathrm{VH}} = 2$ as in application A and B.

instabilities arise exactly at Van Hove filling and be in the form of magnetism. As the former results showed, these instabilities are driven by the strong fluctuations of the particle-hole channels which are induced by the presence of perfect nesting. Interestingly, the presence of two non-degenerate bands opens up an interesting scenario for the presence of perfect nesting which was already previously analysed in [116]. For this purpose, we want to examine the form of the intra-spin and inter-spin particle-hole bubble to predict the occurring magnetic instabilities.

In terms of the formalism, the effects of nesting affect the denominator of the particle-hole bubble. Since we deal with two non-degenerate bands for the different spins now, the bubble will also depend on these spin degrees of freedom. From Eq. (3.55) the nesting condition is now:

$$\xi_{\nu_2}(\boldsymbol{p}) = -\xi_{\nu_1}(\boldsymbol{q} + \boldsymbol{p}). \tag{3.74}$$

Therefore, particle-hole instabilities are now also possible by finding a nesting vector $\boldsymbol{q} = \boldsymbol{Q}$ which connects the Fermi surfaces of two different bands $\nu_1 \neq \nu_2$. Indeed, these inter-spin nesting vectors do exist for different values of ϕ, see Fig. 3.30. Admittedly, we find that we can perfectly nest the complete Fermi surface(s) only with vectors connecting two different bands for $\phi \neq 0$. We want to investigate the effect of this Fermi surface structure to the emergence of instabilities. Consequently, we will keep the the system strictly at Van Hove filling and change the parameter ϕ. For each value a TUFRG calculation is employed to analyse the emerging instability. From the view point of competing instabilities, these situations are equivalent to the studies of application A and B at Van Hove filling. We expect large enhancements of particle-hole fluctuations due to the perfect nesting and the presence of a Van Hove singularity which should directly lead to the manifestation of a magnetic instability.

We performed TUFRG calculations with a momentum resolution $N_{\boldsymbol{q}} = 540$ and $N_s = 2$ (19 form factors). We chose this small amount of form factors since we expect ordinary SDW instabilities which are only strongly pronounced in the on-site component $(l, l') = (1, 1)$. Therefore there is no danger of biasing the system by not including enough form factors. The calculations do directly confirm the aforementioned presumptions made about the onset of magnetic instabilities. For every ϕ, we find the C channel to diverge at high scales $T_c \approx 0.1t$ at the nesting vectors $\boldsymbol{Q}$ in the on-site form factor components. For the spin components, two specific spin components inhabit the divergences, such

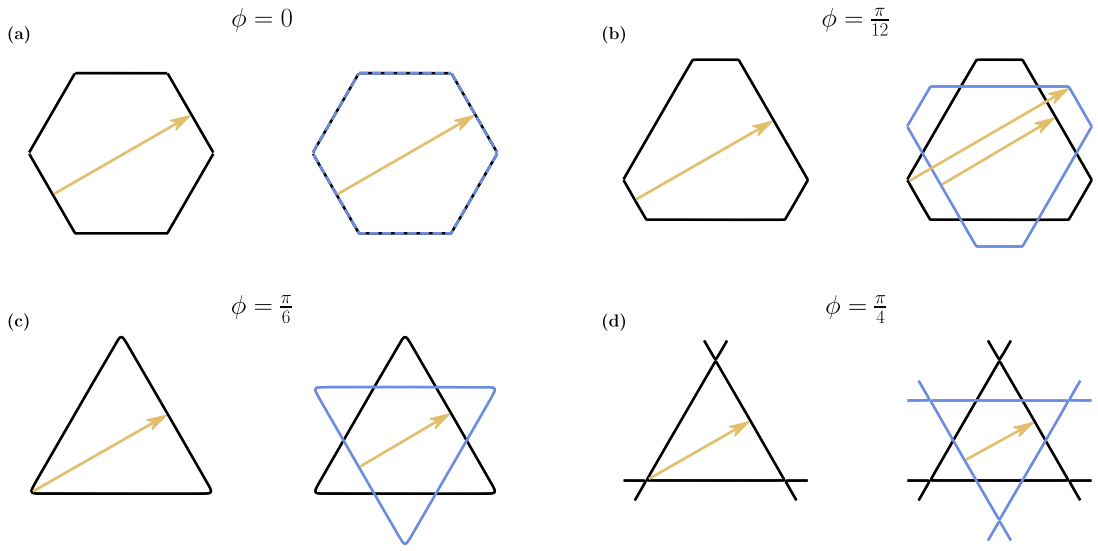

Figure 3.30: **Intra- and inter-spin nesting vectors (yellow):** a) For $\phi = 0$ the bands are degenerated and both types of nesting feature the same nesting vector $\boldsymbol{Q} = \boldsymbol{M}_{1,2,3}$ (this can be seen by back-folding the nesting vector into the first Brillouin zone). b) For $0 < \phi < \pi/6$, only the small edges are nested, leaving a fraction of the long edges of the Fermi surface un-nested (left). For the nesting between two different bands, we can find a two nesting vectors connecting the long edges and short edges each (right). c) The special case $\phi = \pi/6$ leading to a perfectly triangular Fermi surface. In the intra-spin case, only the three corners of the Fermi surface are nested to the opposite edge (left). In the inter-spin case (right), the complete edges are nested. The nesting vectors happens to be the vectors pointing to the $\boldsymbol{K}^{\pm}$ points. d) For $\pi/6 < \phi \leq \pi/4$, the nesting behaviour is equal to the special case of $\phi = \pi/6$ with a decreasing length of the nesting vector $\boldsymbol{Q}$.

that we can reconstruct the effective interaction(s) as:

$$\begin{aligned} C^{1,1}_{\uparrow\downarrow\uparrow\downarrow}(\boldsymbol{Q}) &\to \int_{\boldsymbol{k},\boldsymbol{k}'} C^{1,1}_{\uparrow\downarrow\uparrow\downarrow}(\boldsymbol{Q})\, \bar{\psi}_{\uparrow}(\boldsymbol{Q}+\boldsymbol{k})\bar{\psi}_{\downarrow}(\boldsymbol{k}')\psi_{\downarrow}(\boldsymbol{k})\psi_{\uparrow}(\boldsymbol{Q}+\boldsymbol{k}'), \\ C^{1,1}_{\downarrow\uparrow\downarrow\uparrow}(\boldsymbol{Q}) &\to \int_{\boldsymbol{k},\boldsymbol{k}'} C^{1,1}_{\downarrow\uparrow\downarrow\uparrow}(\boldsymbol{Q})\, \bar{\psi}_{\downarrow}(\boldsymbol{Q}+\boldsymbol{k})\bar{\psi}_{\uparrow}(\boldsymbol{k}')\psi_{\uparrow}(\boldsymbol{k})\psi_{\downarrow}(\boldsymbol{Q}+\boldsymbol{k}'). \end{aligned} \tag{3.75}$$

Which are antiferromagnetic spin density waves with modulation vector $\boldsymbol{Q}$. We displayed one of these singular vertices for a selection of values of ϕ between 0 and $\frac{\pi}{3}$, see Fig. 3.31. There are two sanity checks which are fulfilled by these results. At first, for $\phi = 0$ we should recover the result from application A which is a SDW with peaks at the $\boldsymbol{M}$ points. As a qualitative change, the region near the $\boldsymbol{\Gamma}$ point does also grow significantly which we attribute to the larger initial Hubbard interaction $U = 6t$ as in contrast to $U = 4t$ used in the first application. Moreover, the nesting vector for $\phi = \pi/6$ happens to be the $\boldsymbol{K}^{\pm}$ points which we also successfully reproduce in our approach. The course of the vertices in Fig. 3.31 is also identical found in the aforementioned FRG study [57]. Regarding the critical temperature of these instabilities, we notice a peak at $\phi = \frac{\pi}{6}$ and deviations from this value lead to a lowering of the critical temperature, see Fig. 3.32. The maximal difference of the critical temperature, as seen by comparing the values at $\phi = 0$ and $\phi = \frac{\pi}{6}$, is posed by one order of magnitude. We will offer an explanation for this peak in the next section. This first study ensures the correctness of our implementation for the spinful model without SU(2)-invariance in the vicinity of Van Hove filling. In a next step, we will chose some values of ϕ and examine the competing instabilities regarding the filling as a preliminary study.

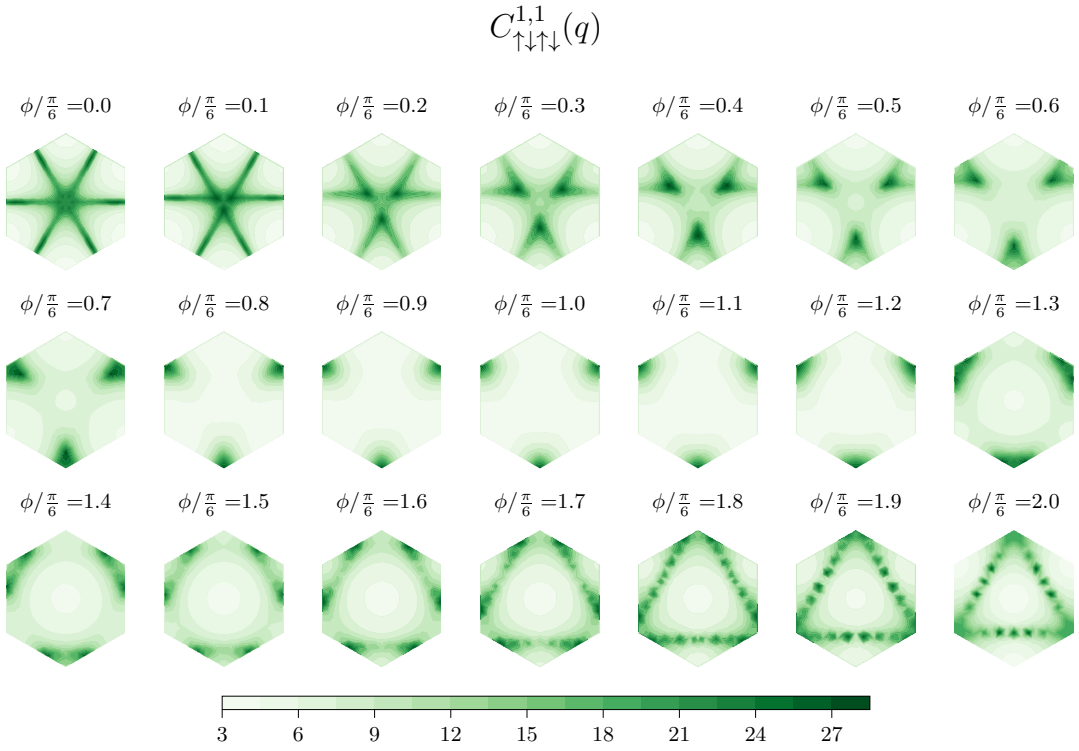

Figure 3.31: **Singular magnetic vertex for selection of ϕ, for $t = 1$ and $U/t = 6$ at Van Hove filling:** The effect of the wandering nesting vector by changing ϕ is reflected by the wandering of the peak in the singular vertex. For the corresponding counterpart vertex with spin combination $\downarrow\uparrow\downarrow\uparrow$, the emerging vertices are inverted.

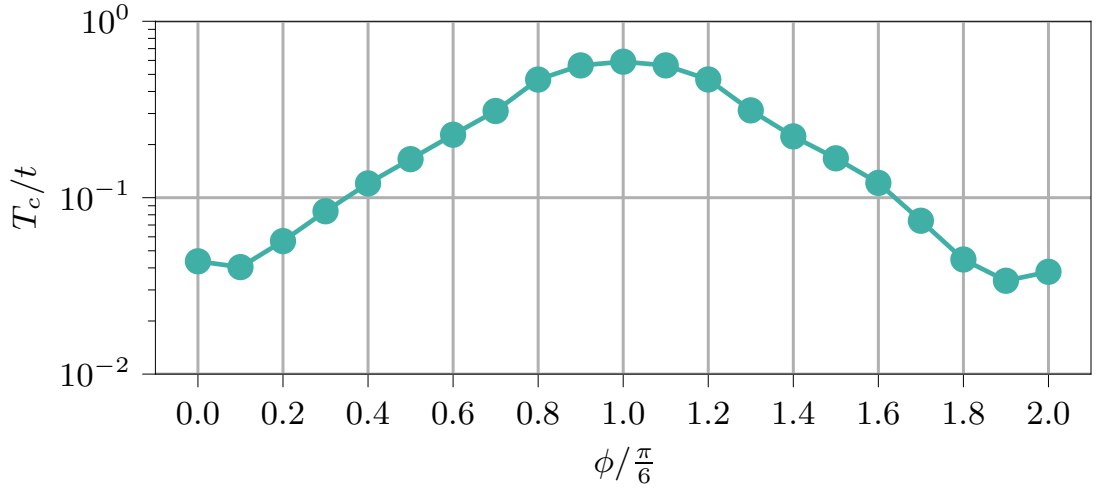

Figure 3.32: **Critical temperature for the selection of ϕ, for $t = 1$ and $U/t = 6$ at Van Hove filling:** The critical temperature has its highest value at $\phi = \pi/6$ where the value is separated from the value at $\phi = 0$ by one order of magnitude.

3.3.4 Competing orders at fixed displacement fields

In this section we will treat competing instabilities for three cases:

1. $\phi = 0$. This case is equivalent to the model treated in application A and will therefore serve as a benchmarking case.
2. $\phi = \pi/6$. Here, the Van Hove singularity will actually be of *higher order*. We will check the behaviour of this new quality.
3. $\phi = \pi/3$. A very exotic instability will occur here, namely a pair density wave. This is described by a pairing vertex which does diverge, but *not* at the $\mathbf{\Gamma}$ point.

At this stage of the project we are still confronted with numerical limitations of our implementation which affect the progress of this study in two ways. At first, there is the issue of computational time. As discussed before, we have a non-negotiable slowdown factor of 4 in contrast to the implementation where SU(2)-invariance is employed. In addition to this, carrying out the bubble integrations is also affected by the changes to the integration routine to handle the new Fermi surface geometries properly. For this reason, these preliminary studies are carried out with a low momentum resolution $N_{\boldsymbol{q}} = 180$. However, we still employ a high resolution of form factors, i.e. $N_s = 4$ (61 form factors) to avoid a bias affecting the instabilities towards superconductivity. The second issue is numerical stability. We found that our integration routine seems starting to be unstable far away from Van Hove filling approximately somewhere between $T \approx 10^{-3}t$ and $T \approx 10^{-4}t$. Therefore, we set the cutoff of the temperature to be $T_{\text{Stop}} = 10^{-4}t$ and only display results where the bubble integrations remain stable.

A short final remark should be made regarding the analysis of superconductivity. In section 1.2, we analyzed the resulting gap functions with respect to SU(2)-invariance or without spins with an underlying C_{6v} point group symmetry. While this discussion still holds for the $\phi = 0$ case (and we will apply the foundations made here in this case), it is not valid anymore for $\phi \neq 0$. Since this project is still in its early phases, we will refrain of further analysing the gaps belonging to the instabilities of superconductivity.

$\phi = 0$, a benchmarking case

By setting $\phi = 0$, we restoring the model from application A with the difference that we do not use the SU(2)-invariance to reframe the model in a simpler form. Also we use $U = 6t$ for all studies in application C - in contrast to $U = 4t$ in application A - such that we expect some quantitative differences in the results here. Since the only included interaction here is the Hubbard U interaction, the emerging phases should resemble those discussed in the demonstration of the workflow of the SU(2)-invariant model, section 3.1.2. These results are displayed section 3.1. in Fig. 3.11 as the $V_1/t = 0$ cut of the phase diagram.

The TUFRG results are shown in Fig. 3.33. As a matter of fact, the results are qualitatively agreeing with those of application A. The main difference is given by the fact that the critical temperatures of the emerging instabilities are in general higher. We address this feature to the higher value of U. Moreover, the i-wave which occupied in application A only a small portion of the phase diagram, is now extensively stable along the underdoped regime of the phase diagram. Interestingly, this is in conflict with the other FRG study [57] which does find other forms of superconductivity here. Although, another weak coupling RG study [113] does also locate an i-wave in this regime.

$\phi = \pi/6$, effects of higher order Van Hove singularity

For $\phi = \pi/6$, the Fermi surface is triangular. At first we want to highlight a property which is also shared by systems for $0 < \phi \leq \pi/6$ regarding the onset of instabilities towards superconductivity. As

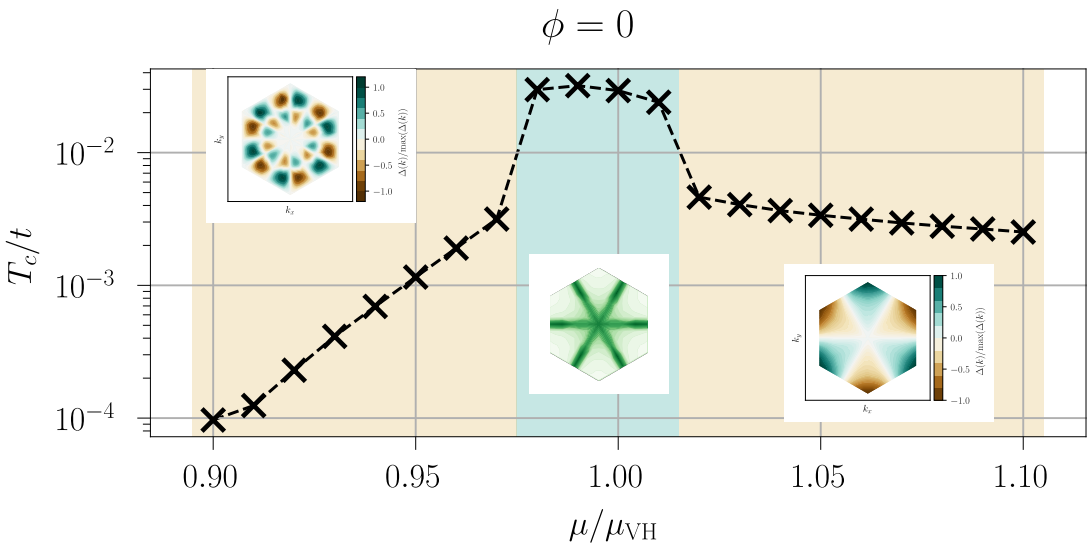

Figure 3.33: **Phase diagram around Van Hove filling $\mu_{\mathrm{VH}} = 2t$, at $U = 6t$:** Around Van Hove filling we find magnetic instabilities with peaks at the $\boldsymbol{M}$ points. Away from Van Hove filling we find for both cases - underdoping and overdoping- superconductive instabilities (yellow). The reconstruction of the gap functions results into an i-wave (underdoping) and f-wave (overdoping) gap symmetry. The magnetic singular vertex and the gap functions are displayed as insets.

shown in section 1.1, the generic divergence of the particle-particle bubble is ensured by the inversion symmetry of the dispersion[5]. This inversion symmetry is no longer present for a single band in our model for the intra-spin bubble integrations. Consequently, the inversion symmetry Eq. (3.46) shifts the generic divergence of the particle-particle bubble to the inter-spin bubble since this identity allows to combine the terms in the denominator of Eq. (3.54) at zero momentum:

$$\xi_{\nu_1}(\boldsymbol{p}) + \xi_{\nu_2}(-\boldsymbol{p}) = 2\xi_{\nu_1}(\boldsymbol{p}).$$

Combined with the insight of the previous section that the nesting condition is also only fulfilled by the inter-spin particle-hole bubble, the competition of instabilities in these scenarios happens to be between inter-spin properties only. A special feature of the model at $\phi = \pi/6$ is the occurrence of a higher order Van Hove singularity. These kinds of singularities were already treated in the context of competing instabilities recently [48, 21]. A higher order Van Hove singularity does not diverge logarithmically, but in terms of a power law:

$$\rho(\xi) \propto |\xi|^{-\alpha} \tag{3.76}$$

with some exponent α. Besides this new scaling for the density of states, we expect qualitatively no substantial changes in the narrative regarding the competition of instabilities. The particle-hole bubble will inhabit strong fluctuations at the nesting vectors $\boldsymbol{q} = \boldsymbol{K}^{\pm}$ which may extinct by tuning away from Van Hove filling. The generic divergence of the particle-particle bubble at zero momentum will be preserved for other fillings and the particle-hole fluctuations may induce an attractive interaction, ultimately triggering a superconductive instability. By following the calculation laid out in the appendices and replacing the density of states by the power-law, we find for the bubbles at Van Hove filling:

$$B(\boldsymbol{0})^{\mathrm{pp}}_{\uparrow\downarrow\uparrow\downarrow} \propto |T|^{-\alpha}, \tag{3.77}$$

$$B(\boldsymbol{K}^{+})^{\mathrm{ph}}_{\uparrow\downarrow\uparrow\downarrow} \propto |T|^{-\alpha}. \tag{3.78}$$

[5]Otherwise, we refer to App. A.1.

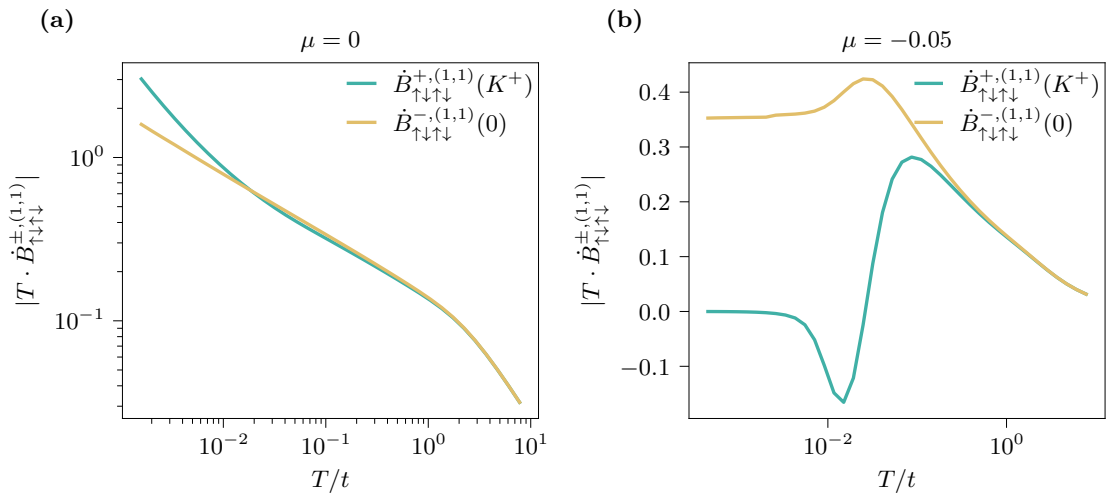

Figure 3.34: **Divergence of bubble integrations:** a) At Van Hove filling $\mu_{\text{VH}} = 0$, the double-log plot confirms the power law behaviour of the respective inter-spin bubbles at the 0 (particle-particle) and $\boldsymbol{K}^{\pm}$ (particle-hole) at low temperatures. b) Away from Van Hove filling, the generic logarithmic divergence in the particle-particle bubble persists, while - due to the lack of perfect nesting - the divergent behaviour of the particle-hole bubble will vanish such that it eventually drops to zero at low temperatures.

Which translates to our bubble integrations (as done similarly in application A):

$$T \times \dot{B}(\mathbf{0})^{-}_{\uparrow\downarrow\uparrow\downarrow} \propto |T|^{-\alpha}, \tag{3.79}$$

$$T \times \dot{B}(\boldsymbol{K}^{+})^{+}_{\uparrow\downarrow\uparrow\downarrow} \propto |T|^{-\alpha}. \tag{3.80}$$

This delivers a sanity check for our application by the usage of a log-log plot to validate the power-law of the bubble integrations. Away from Van Hove filling, the particle-particle bubble will remain at a simple logarithmic divergence from the generic behaviour, while the singular behaviour of the particle-hole bubble should extinct at low temperatures. We verified these characteristics in Fig. 3.34.

The TUFRG calculations for this model for small range of μ around Van Hove filling are displayed in Fig. 3.35. As expected, we find a SDW at Van Hove filling with pronounced peaks at the $\boldsymbol{K}^{\pm}$ points as already shown in the previous section. At some point, the SDW will be replaced by a region of superconductivity. Both instabilities appear in inter-spin components of the C and P channel only.

Coming back to the course of the critical temperature of magnetic instabilities in previous section, we can now understand the peak in Fig. 3.32 in terms of the higher order Van Hove singularity. Since the underlying mechanism for the onset of a magnetic instability does not change, the only substantial difference in the system at $\phi = \frac{\pi}{6}$ is given by the power-law divergence of the particle-hole bubble. This feature enhances the fluctuations by a larger amount in contrast to the logarithmically divergent particle-hole bubbles, eventually leading to a higher critical temperature.

$\phi = \pi/3$, the exotic case of pairing density waves

As a last selection of the preliminary TUFRG results, we want to examine the model at $\phi = \pi/3$ where we will detect a pairing density wave, i.e. an instability in the P channel at a transfer momentum different from 0. As a preparation, we once again investigate the behaviour of the bubbles since they already encode the origin of this peculiar instability type.

As the in previous cases, the particle-particle bubble will only develop a generic divergence for the

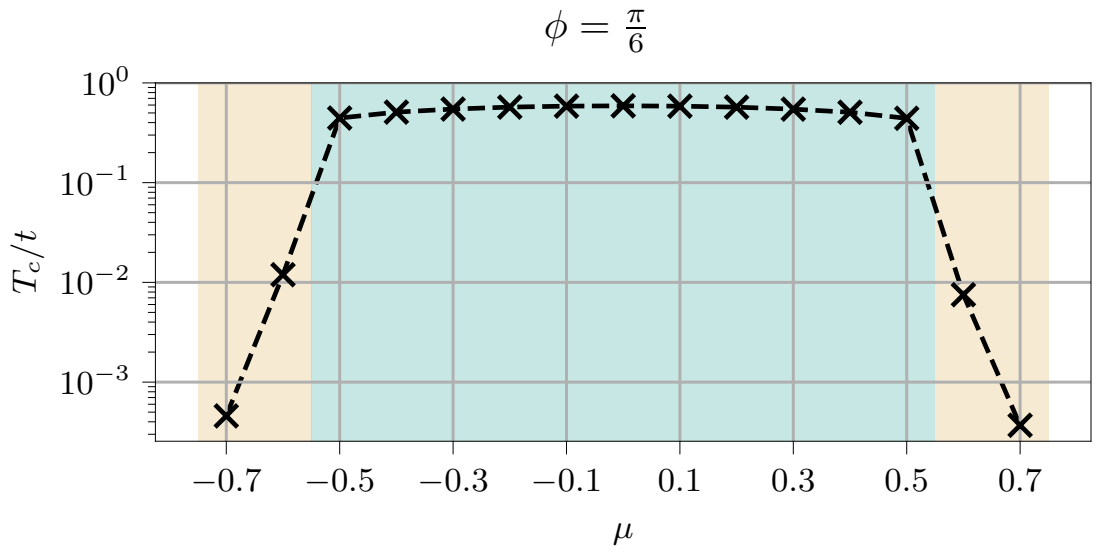

Figure 3.35: **Phase diagram around Van Hove filling $\mu_{\mathrm{VH}} = 0$, at $U = 6t$:** Widely around Van Hove filling we find magnetic instabilities featuring peaks at the $\boldsymbol{K}^{\pm}$ point (green). Away from Van Hove filling, we find superconductive instabilities (yellow).

inter-spin component since no inversion symmetry is present for the intra-spin bubble. Regarding the dispersion, the point $\phi = \pi/3$ is special since a new symmetry emerges:

$$\xi_{\uparrow(\downarrow)}(\boldsymbol{p} + \boldsymbol{K}^{\mp}) = \xi_{\downarrow(\uparrow)}(\boldsymbol{p}). \tag{3.81}$$

This symmetry is valid for all momenta $\boldsymbol{p}$ and importantly persists at and away from Van Hove filling. Regarding the intra-spin bubble directly at Van Hove filling, we can find therefore the following relation:

$$\begin{aligned} B(\boldsymbol{K}^{-})^{\mathrm{PP}}_{\uparrow\uparrow\uparrow\uparrow} &= \int_{\boldsymbol{p}} \frac{1 - n_F\left[\xi_\uparrow(-\boldsymbol{p})\right] - n_F\left[\xi_\uparrow(\boldsymbol{p} + \boldsymbol{K}^{-})\right]}{\xi_\uparrow(-\boldsymbol{p}) + \xi_\uparrow(\boldsymbol{p} + \boldsymbol{K}^{-})} \\ &\overset{(3.81)}{=} \int_{\boldsymbol{p}} \frac{1 - n_F\left[\xi_\uparrow(-\boldsymbol{p})\right] - n_F\left[\xi_\downarrow(\boldsymbol{p})\right]}{\xi_\uparrow(-\boldsymbol{p}) + \xi_\downarrow(\boldsymbol{p})} \\ &\overset{(3.46)}{=} \int_{\boldsymbol{p}} \frac{1 - n_F\left[\xi_\uparrow(-\boldsymbol{p})\right] - n_F\left[\xi_\uparrow(-\boldsymbol{p})\right]}{\xi_\uparrow(-\boldsymbol{p}) + \xi_\uparrow(-\boldsymbol{p})} \\ &= \int_{\boldsymbol{p}} \frac{1 - 2n_F\left[\xi_\uparrow(-\boldsymbol{p})\right]}{2\xi_\uparrow(-\boldsymbol{p})} \\ &\propto \frac{1}{2}\log^2\left(\frac{W}{T}\right). \end{aligned} \tag{3.82}$$

Since the symmetry Eq. (3.81) holds for all fillings, the intra-spin particle-particle bubbles inhabits a generic logarithmic divergence at $\boldsymbol{K}^{\pm}$ which becomes double-logarithmic at Van Hove filling. Therefore, this model features two divergent particle-particle bubbles at different momenta, depending on spin component. For the bubble integrations this translates to:

$$\mu = \mu_{\mathrm{VH}}:$$

$$T \times \dot{B}(\boldsymbol{0})^{-,(1,1)}_{\uparrow\downarrow\uparrow\downarrow} \propto -\log\left(\frac{W}{T}\right), \tag{3.83}$$

$$T \times \dot{B}(\boldsymbol{K}^{-})^{-,(1,1)}_{\uparrow\uparrow\uparrow\uparrow} \propto -\log\left(\frac{W}{T}\right). \tag{3.84}$$

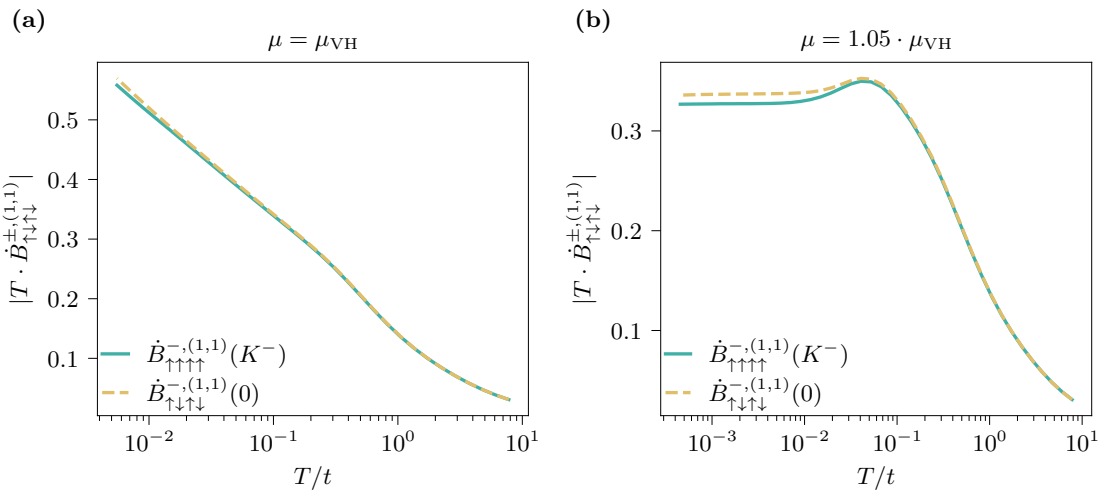

Figure 3.36: **Check of divergent behaviour of particle-particle bubble integrations at respective momenta:** a) At Van Hove filling, the bubble integrations feature the double logarithmic divergence at low temperatures. b) Away from Van Hove filling, the double logarithmic divergence is lost and only a single log divergence preserves at low temperatures. In both cases, the results deviate from each other slightly which is interpreted as an artifact of the integration routine.

And:

$$\mu \neq \mu_{\mathrm{VH}}:$$
$$T \times \dot{B}(\mathbf{0})^{-,(1,1)}_{\uparrow\downarrow\uparrow\downarrow} \propto (-1), \tag{3.85}$$
$$T \times \dot{B}(\boldsymbol{K}^-)^{-,(1,1)}_{\uparrow\uparrow\uparrow\uparrow} \propto (-1). \tag{3.86}$$

The fulfillment of these relations was successfully tested and is displayed in Fig. 3.36. While the behaviour of the bubble integrations are qualitatively correct, they feature a small quantitative deviation from each other which indicates that the adapted integration routine still is not optimally implemented. For these preliminary results, we are satisfied with the bubble integration and proceed with the TUFRG calculations.

Consequentially, we can expect the possibility of a superconductivity instability which features divergent peaks at the $\boldsymbol{K}^{\pm}$ points. We will call this kind of superconductivity a *pair density wave* (PDW), as an analogous phenomenon to the SDW and CDW instabilities. Furthermore, we cannot deduce from this analysis which of the superconductive instabilities will eventually emerge since the *ordinary* superconductivity tendency deviated by the inter-spin bubble and the PDW tendency deviated by the intra-spin bubble exhibit the same scaling behaviour. For this purpose, we exercise again a preliminary TUFRG calculation of the system around Van Hove filling. The corresponding results are shown in Fig. 3.37. Indeed, we find that the emerging instability succeeding in this scenario away from Van Hove filling of is the PDW, see Fig. 3.38.

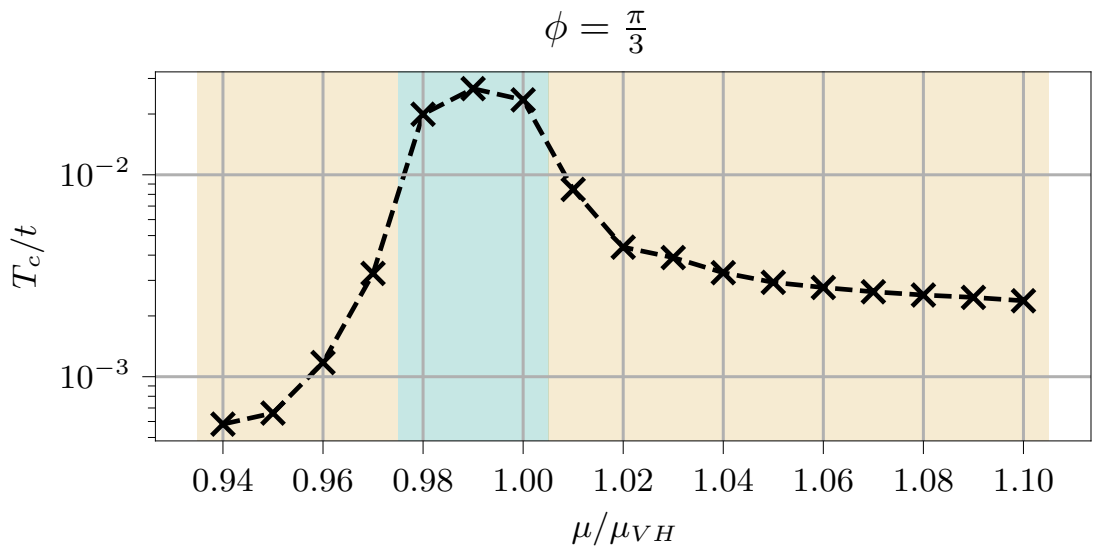

Figure 3.37: **Phase diagram around Van Hove filling $\mu_{\mathrm{VH}} = -2t$, at $U = 6t$:** In a short region around Van Hove filling we find the magnetic instabilities already described in the former section (green). Away from Van Hove filling, we find PDW instabilities (yellow).

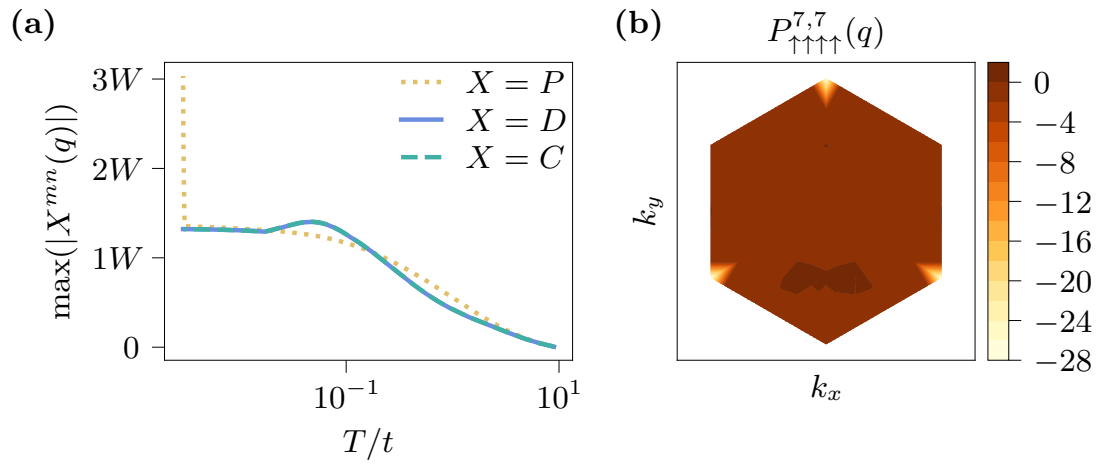

Figure 3.38: **TUFRG flow and singular vertex above Van Hove filling $\mu/\mu_{\mathrm{VH}} = 1.05$:** The Hubbard interaction is chosen as $U = 6t$. a) Evolution of the maximum absolute value of the respective channels P,C and D. The P channel will develop the strongest divergence for the chosen set of parameters. b) Momentum resolved $(l, l') = (7, 7)$ component of the superconducting channel $P^{7,7}_{\uparrow\uparrow\uparrow\uparrow}(\boldsymbol{q})$ at the end of the flow. The resulting instability is a PDW which features peaks at the $\boldsymbol{K}^-$ points of the Brillouin zone for the inter-spin component. The peaks for the respective spin-down counterpart of this vertex are placed at the $\boldsymbol{K}^+$ points.

3.3.5 Summary

We want to finalize this section with a brief summary of the presented insights and results. In this application, we explored first preliminary results of a non-SU(2) symmetric triangular Hubbard model. This model offers the opportunity to present the potential of TUFRG towards application with additional quantum numbers. This non-trivial extension of the method is accompanied with a set of numerical challenges:

1. The addition of spin quantum numbers σ directly increases the amount of numerical calculations per RG step by a substantial amount. We showed how in this special case, we were able to exploit the symmetries of the given model to successfully reduce this additional computational workload.

2. Moreover, the complicated structures of the non-degenerated band dispersion calls for a careful adaption of the bubble integration routine to the model. We implemented tentative alterations to our proposed routine to tackle this problem. Careful checks of the divergent behaviour of the bubbles at different values of ϕ deliver valuable sanity checks and benchmarks for the qualitative behaviour of the integrations at low temperatures. We were able to successfully reproduce these checks. In contrast, the routine behaves problematic for values too far away from Van Hove filling at very low temperatures. Moreover, the bubble integration is still the bottleneck regarding computation time while applying the TUFRG. We are advised at this point to invest additional work to improve the stability and speed of this routine which is already close to the necessary quality to investigate the model in a scope beyond what the results presented here.

The preliminary results displayed here confirm that we are still in a good position to understand the emerging behaviour of the system at various fillings and field parameters ϕ in terms of a competition of magnetic instabilities and superconductivity. The detected magnetic instabilities can be completely understood by the presence of perfect nesting which in this scenario has to be examined also in various geometries due to the shape of the two degenerated bands. Tuning the chemical potential around Van Hove filling reveals superconductive instabilities eventually. Two special features of this model can already be anticipated by the analysis of the bubble integrations:

1. At $\phi = \pi/6$, the Van Hove singularity will be of higher order, inducing a power-law divergence of the density of states. We saw that this enhancement of the scaling has a direct effect on the critical temperature of the emerging instabilities.

2. At $\phi = \pi/3$, a special symmetry enables the onset of a PDW for the intra-spin P channel. This instability should be in competition with the *ordinary* superconductivity regarding the inter-spin component. The exact mechanism of this competition still has to be thoroughly investigated.

Due to combination of analytic benchmarks derived from the bubbles which are successfully met by the TUFRG code, we value our results as satisfying first preliminary results confirming the correctness of our implementation. Starting from this, there is a clear road for further studies for this model after the aforementioned numerical details are added. In a first step, the three presented cases for ϕ can be completed by adding TUFRG calculations for the whole range between 0 and $\pi/3$, leading to a comprehensive phase diagram. Regarding the superconductive phases, we still have to stringently work out how to properly derive the gap functions which should be describable by lattice harmonics stemming from the C_{3v} point group irreps. Following this, we want to add a set of nearest-neighbour interactions V_n such that our model resembles the description of a realistic tTMD homobilayer system. This agenda would be similar to application A, where we also examined how the results of a paradigmatic model change by adding realistic parameters.

CHAPTER 4

Concluding remarks

Précis

In this thesis, we tried to paint a complete picture of competing electronic instabilities in triangular lattice Hubbard models and how the development and application of the TUFRG serve as a promising tool to capture them.

We showed that the tendencies of magnetic and superconductive instabilities are already encoded in the kinetic part of the underlying Hamiltonian of a system. The selection of the actual manifested instability however is highly dependent on the interacting part of the Hamiltonian and the electronic filling. Although the scaling of the particle-hole and particle-particle bubbles, which enhance magnetic or superconductive instabilities respectively, are equally strong at Van Hove filling, the initial repulsive interactions are not sufficient for the formation of superconductivity at bare level as we showed in terms of a ladder summation. Moreover, we presented that an attractive interaction is needed for the onset of superconductivity. This interaction can actually be generated as demonstrated by renormalization [67, 93] which points in the direction of developing and implementing a renormalization group method to treat the competing orders around Van Hove filling correctly.

As a centrepiece of this thesis, we then derived the TUFRG method [64, 40, 98]. FRG methods already proofed themselves as suitable methods for resolving competing instabilities in condensed matter systems in the past, especially also for Hubbard models defined on various lattice geometries [42, 39, 115, 32, 41, 55, 54]. The TUFRG advances these methods in two ways. At first, the channel decomposition transforms the flow equations in a more ordered structure, where the careful analysis of diagrams in the 2-level truncation FRG scheme revealed that different physical phenomena can actually be traced to substantial contributions of specific diagram types. The FRG flow equations could therefore be subdivided in a superconductive, magnetic and density channel, indicating the onset of a respective instability. In a second step, the analysis of the diagrams also unveils that only one of the parameterizing momenta of each diagram is important for the formation of singular contributions, namely the transfer momentum of the bubble. This fact could already be anticipated by the arguments made by the summations in section 1.1. By expanding the unimportant momenta into plane wave form factors, the TUFRG achieves a linear scaling in momenta, greatly advancing the numerical performance in contrast to previous FRG schemes. Nevertheless, the application of the TUFRG to a given model is highly non-general such that we also included a detailed implementation section, discussing the several numerical challenges arising by treating triangular lattice Hubbard models and how to overcome them. Triangular models typically involve effects of geometric frustration such that the correct and performant calculation of bubble integrations down to low temperature scales imposes the most challenging obstacle in this application. By constructing an adaptive integration routine which was explicitly tailored to the models of interest we were able to successfully tackle this problem.

After setting the physical context in section 1.2 and developing the method in section 2, we then pro-

ceeded to treat three different triangular lattice Hubbard models. In each of these models, we could successfully identify the situation of competing instabilities around Van Hove filling and generated comprehensive phase diagrams in application A and B by the usage of the TUFRG. From the emerging instabilities towards superconductivity, we subsequently constructed the according superconductive gap functions. By the brief investigation of the unconventional superconductivity in section 1, we are able to classify the gap symmetries according to the irreps belonging to the C_{6v} point group. We also showed here that the inclusion of longer ranged form factors is crucial to resolve the correct gap functions and avoid bias in our implementation. These results were checked for correctness in two ways. As an important first check, we could relate the behaviour of the bubble integrations to the particle-hole and particle-particle divergences at low temperatures. Here, we recovered all scaling laws stemming from the Van Hove singularity and the perfect nesting of the Fermi surface. As a second check, we performed several convergence tests regarding the momentum resolution and the amount of included form factors.
In application C, we considered a spinful model without spin-rotational invariance. Although this part was presented as a *work-in-progress* section, already the first preliminary results are promising and confirm the correctness of the non-trivial extension of our method to spin degrees of freedom. The presence of a higher order Van Hove singularity and the occurrence of a pair density wave as an exotic form of superconductivity are already foreshadowing the rich physical phenomena which are to be found in this model. Again, the soundness of these results could be checked by reproducing the complex behaviour of the particle-particle and particle-hole bubbles.

While the studies performed in this work are mostly done in the context of paradigmatic models, we still want to highlight their importance of describing novel Moiré materials. The effective description of these bilayer systems can be cast into the form of triangular lattice Hubbard models such that our results may contribute to the explanation and understanding of strongly correlated electron physics in these exiting novel materials.

Hic sunt dracones

The results presented in this thesis guide to several paths of research studies which may be performed in the future.

Most obviously, the spinful Hubbard model presented in application C should be thoroughly examined after the necessary final improvements of the bubble integrations are worked out. From the already presented results we expect that this approach could unveil a good amount of interesting physics. The inclusion of additional interactions to this model is then almost trivial, delivering results for a model describing a realistic tTMD homobilayer system. Candidate values for longer-ranged hoppings and interactions were already proposed in [79]. This study can potentially act as a convincing showcase of the TUFRG method, accentuating it as a powerful numerical technique to investigate multi-band models of correlated fermions at a level of performance beyond recent FRG applications [57].

A qualitative change of the TUFRG equations can be employed by including self-energy corrections, which haven been neglected in our studies. In the same vein, one could also include the novel multiloop scheme [61, 62] to the method to inspect the effect of truncations and how to control them. Recent studies on the square lattice Hubbard model were already conducted [36, 35, 102], demonstrating the general integration of these schemes. Nonetheless, the critical scales in the square lattice Hubbard model are much higher compared to the model defined on a triangular lattice geometry due to the absence of frustration. Also, fewer form factors are needed for the square lattice to resolve the expected superconductive instabilities since it lacks exotic gap symmetries like the i-wave superconductor. Considering that the inclusion of self-energy strongly affects the structure of the bubble inte-

grations, the task of including self-energy effects is possible, but will pose a huge numerical challenge.

A third direction is given by the treatment of honeycomb models. Triangular and honeycomb lattice structures share several geometric properties since the honeycomb model is a triangular lattice model with a two-atomic unit cell. A large amount of the structures and objects presented here are therefore in general transferable to the description of honeycomb models. The sublattice degree of freedom will then be incorporated as an additional quantum number, similar to the spin in application C. Several works already implemented TUFRG schemes for honeycomb lattices at half filling [82, 81, 78] and Van Hove filling [77, 34], demonstrating the general possibility of the application of the method. Although it should be remarked that some technical difficulties arise by using triangular lattice plane wave form factors since they artificially break the point group of the underlying graphene Hamiltonian pointed out by [77, 34] independently.
A working honeycomb implementation opens up the possibility to perform studies of various interesting models. In particular, the tight-binding model derived by Koshino et al.[60] describing twisted bilayer graphene represents an interesting and challenging case for the TUFRG. On the other hand, several works point to the importance of higher order Van Hove singularities for describing the behaviour of Moiré materials [114, 31]. Here, it could be proposed to fit tight-binding parameters of a graphene model to the band structure which then also poses a direct and promising case for a TUFRG honeycomb implementation.

Conclusion

Naturally, the vast majority of studies in physics are minor, with the hope of being incremental. We presented the basics, derivation and implementation of the novel TUFRG method here and demonstrated its usefulness in a selection of effective triangular lattice Hubbard models linked to the current research of Moiré materials. The examination of these results in combination with the analysis of the underlying bubbles deliver a promising soundness of the presented methodology. We illustrated the numerical and practical advantages of the TUFRG and the established results indicate that a wide range of interesting physical models relevant to current research are waiting to be investigated. To impose a callback to the overture of this thesis, we hoped to not only arrive at novel results, but also to deliver a starting point of future investigations using the TUFRG. The author regards this agenda as fulfilled.

APPENDIX A

Appendix

A.1 Divergence of particle-particle bubble

Here, we investigate the divergent behaviour of the particle-particle bubble for $T \to 0$ in more detail. We will discuss both cases, a regular density of states and the presence of a Van Hove singularity.

The particle-particle bubble is (after carrying out the Matsubara sum) given by:

$$B^{\text{pp}}(q) = \int_{\boldsymbol{p}} \frac{1 - n_F\left[\xi(-\boldsymbol{p})\right] - n_F\left[\xi(\boldsymbol{p}+\boldsymbol{q})\right]}{i\omega_q + \xi(-\boldsymbol{p}) + \xi(\boldsymbol{p}+\boldsymbol{q})}, \tag{A.1}$$

with $\int_{\boldsymbol{p}} = A_{\text{BZ}}^{-}1 \int_{\text{BZ}} d\boldsymbol{p}$, the normalized integral over the Brillouin zone. In the most cases, (and especially true for our ordinary triangular lattice Hubbard model) the dispersion features inversion symmetry:

$$\xi(\boldsymbol{p}) = \xi(-\boldsymbol{p}). \tag{A.2}$$

We will see that at zero external frequency $i\omega_q = 0$ and zero external momentum $\boldsymbol{q} = 0$ this object will develop a *generic* logarithmic divergence. For this purpose, we set $i\omega_q = \boldsymbol{q} = 0$ and use the inversion symmetry:

$$B^{\text{pp}}(0) = \int_{\boldsymbol{p}} \frac{1 - 2n_F\left[\xi(\boldsymbol{p})\right]}{2\xi(\boldsymbol{p})}. \tag{A.3}$$

We will proceed by translating this object into an energy integral, covering the bandwidth W of the model:

$$B^{\text{pp}}(0) = \int_{-W}^{W} \frac{1 - 2n_F\left[\xi\right]}{2\xi}\rho(\xi)d\xi. \tag{A.4}$$

Where $\rho(\xi)$ is the density of states. We are interested in the behaviour of the bubble at low temperatures. Therefore we split the integral in two by imposing the following limit:

$$B^{\text{pp}}(0) = \lim_{T\to 0}\left(\int_{-W}^{-T} \frac{1 - 2n_F\left[\xi\right]}{2\xi}\rho(\xi)d\xi + \int_{T}^{W} \frac{1 - 2n_F\left[\xi\right]}{2\xi}\rho(\xi)d\xi\right). \tag{A.5}$$

Approximating that this form holds for all situations where T is close to zero:

$$B^{\text{pp}}(0) \approx \left(\int_{-W}^{-T} \frac{1 - 2n_F\left[\xi\right]}{2\xi}\rho(\xi)d\xi + \int_{T}^{W} \frac{1 - 2n_F\left[\xi\right]}{2\xi}\rho(\xi)d\xi\right), \tag{A.6}$$

we can now investigate the divergent behaviour of the bubble with respect to the density of states. For this purpose, we acknowledge that the Fermi function at zero temperatures behaves as:

$$n_F(x) = \begin{cases} 1, & x \leq 0, T = 0 \\ 0, & x \geq 0, T = 0 \end{cases}. \tag{A.7}$$

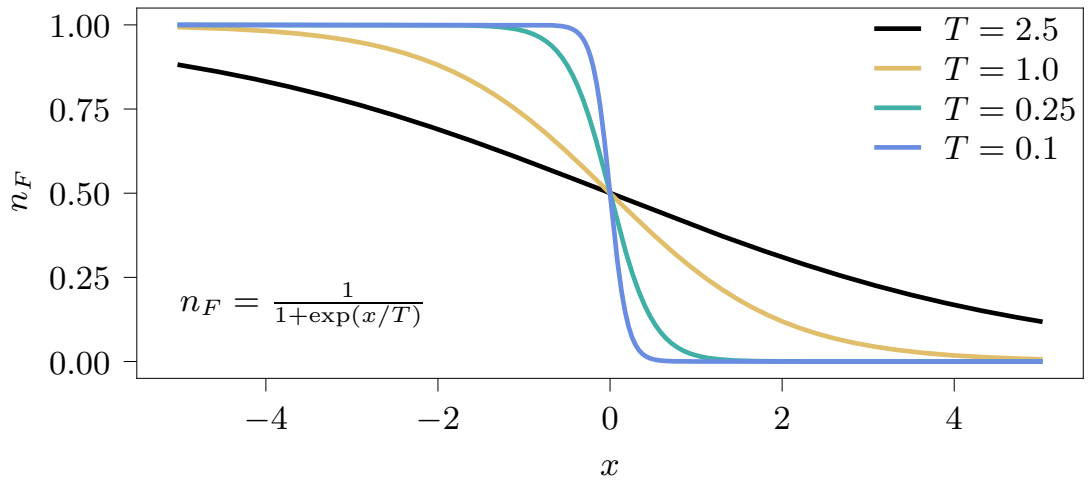

Figure A.1: **Behaviour of Fermi function at lower temperatures:**. For lower and lower temperatures T, the Fermi function resembles the step function defined by Eq. (A.7).

Which we approximate to be the case in the vicinity of zero, $T \approx 0$ (see Fig. A.2). In the first case, we assume a regular density of states with no singular contributions. We approximate the density of states to not vary much from the value at the Fermi surface, i.e. $\rho(\xi) \approx \rho(0)$. In this case, we can combine both integrals (by a substitution of variables in one of them) and carry it out explicitly:

$$B^{\text{pp}}(0) \approx \rho(0) \int_T^W \frac{1}{\xi}\, d\xi = \rho(0) \log\left(\frac{W}{T}\right) \tag{A.8}$$

The important feature of this logarithmic divergence is given by its *generic* quality. The particle-particle bubble will feature a logarithmic divergence at zero transfer momentum for every dispersion as long as an inversion symmetry is satisfied. Following the arguments in section 1.1 it becomes apparent that for every initial attractive strength - regardless of how weak this interaction is - eventually an instability of superconductivity will appear. This result is basically a re-iteration of the argument made by Cooper [22] in terms of perturbation theory, leading to the BCS theory.

As a second case, we will now consider the presence of a Van Hove singularity, i.e. a logarithmic divergence of the density of states at a specific point of the Brillouin zone. In the triangular lattice Hubbard model these points happen to be the M points. We will consider our system to be tuned to this point such that:

$$\rho(\xi) = \log\left(\frac{W}{|\xi|}\right). \tag{A.9}$$

Repeating the calculation done before we eventually reach at:

$$B^{\text{pp}}(0) \approx \int_T^W \frac{1}{\xi}\rho(\xi) d\xi = \int_T^W \frac{1}{\xi} \log\left(\frac{W}{|\xi|}\right) d\xi \tag{A.10}$$

$$= \frac{1}{2}\log^2\left(\frac{W}{T}\right). \tag{A.11}$$

Such that the divergent behaviour is enhanced to be double logarithmic.

A.2 Divergence of particle-hole bubble

Similarly to the particle-particle bubble, we will investigate the divergent behaviour of the particle-hole bubble. After carrying out the Matsubara sum, the particle-hole bubble is given by:

$$B^{\text{ph}}(q) = A_{\text{BZ}}^{-}1 \int_{\text{BZ}} d\boldsymbol{p} \quad \frac{n_F\left[\xi(\boldsymbol{p})\right] - n_F\left[\xi(\boldsymbol{p}+\boldsymbol{q})\right]}{i\omega_q + \xi(\boldsymbol{p}) - \xi(\boldsymbol{p}+\boldsymbol{q})}. \tag{A.12}$$

Again, we are will set the external frequency to be zero, $i\omega_q = 0$. From the former analysis of the particle-particle hole bubble, the expression can develop a logarithmic divergence if:

$$\xi(\boldsymbol{p}) = -\xi(\boldsymbol{p}+\boldsymbol{q}). \tag{A.13}$$

We can satisfy this condition to the whole Fermi surface ($\xi(\boldsymbol{p}) = 0$), by tuning the chemical potential such that the perfect nesting is achieved, so that both sides of Eq. (A.13) are fulfilled by being equally zero. We assume that the nesting condition holds for a small shell around the Fermi surface $[-\Delta\xi_{Nesting}, +\Delta\xi_{Nesting}]$ (see Fig. A.2).

We can rewrite then Eq. (A.12) again in terms of an energy integral, assuming that the major con-

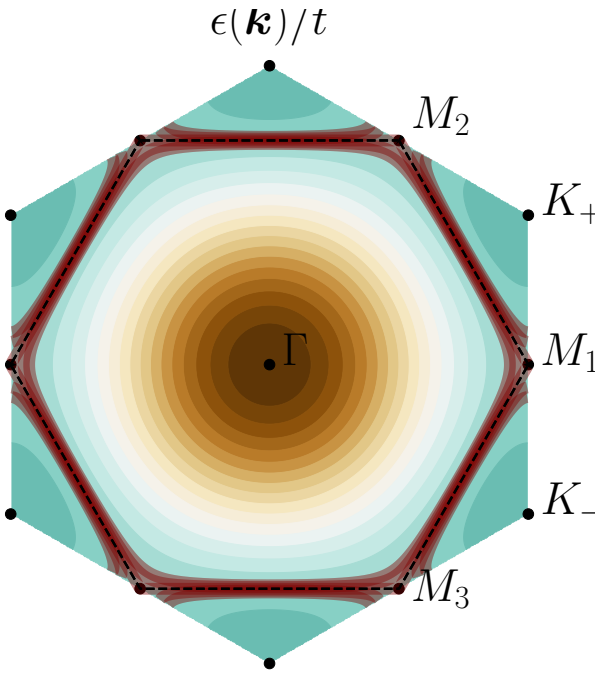

Figure A.2: **Dispersion and Fermi surface nesting:**. The Fermi surface is nested perfectly for the black dashed hexagon. For the red energy region, we assume that perfect nesting is approximately present.

tributions are coming from the aforementioned energy shell. We will again split this integral and assuming a low temperature limit.

$$B^{\text{ph}}(\boldsymbol{q}_{Nesting}) \approx \int_{-\Delta\xi_{Nesting}}^{+\Delta\xi_{Nesting}} \frac{2n_F\left[\xi\right] - 1}{2\xi}\rho(\xi)d\xi \tag{A.14}$$

$$\approx \int_{-\Delta\xi_{Nesting}}^{-T} \frac{2n_F\left[\xi\right] - 1}{2\xi}\rho(\xi)d\xi + \int_{T}^{+\Delta\xi_{Nesting}} \frac{2n_F\left[\xi\right] - 1}{2\xi}\rho(\xi)d\xi. \tag{A.15}$$

We can calculate the integral in this form completely analogous to the particle-particle bubble by combining the integrals when the function of the density of states is decided. We will again exploit

the form of the Fermi function for $T \to 0$. The results will differ with a global sign. For a regular density of states, approximated as being constant $\rho(\xi) \approx \rho(0)$, the bubble results to:

$$B^{\text{ph}}(\boldsymbol{q}_{Nesting}) \approx -\rho(0) \int_{T}^{+\Delta\xi_{Nesting}} \frac{1}{\xi} d\xi \propto -\log\left(\frac{\Delta\xi_{Nesting}}{T}\right) \tag{A.16}$$

The nominator of the logarithm reflects the energetic range for which perfect nesting can be assumed. In the case that the nested Fermi surface0 is at a Van Hove singularity (which is indeed the case in our model), the integral becomes:

$$B^{\text{ph}}(\boldsymbol{q}_{Nesting}) \approx -\int_{T}^{+\Delta\xi_{Nesting}} \frac{1}{\xi} \log\left(\frac{W}{|\xi|}\right) d\xi \propto -\log^2\left(\frac{W}{T}\right). \tag{A.17}$$

Conclusively: at Van Hove filling both, the particle-particle bubble (at $\boldsymbol{q} = 0$) and particle-hole bubble (at $\boldsymbol{q} = \boldsymbol{q}_{nesting}$) , will develop a double logarithmic divergence at low temperatures. It should be noted as a important difference that both sources of the particle-hole bubble divergence are *not generic*. They strictly exist as qualities caused by the dispersion and Fermi surface. Remnants of these effects can influence particle-hole bubbles which are slightly tuned away from Van Hove filling, but the logarithmic enhancement of the bubble will not persist at low temperatures. This is in strong contrast to the particle-particle bubble. While the contribution coming from the Van Hove singularity is also a quality reflecting the underlying system, there always exists one logarithmic divergence at low temperatures, regardless of the form and shape of the Fermi surface (as long as inversion symmetry is present).

A.3 Initial conditions for application B

For the initial conditions of the spinless model, we follow the same method as presented in section 2.3.1. We only do have to care for a proper anti-symmetrization of the initial conditions here. The initial condition projections for the three channels are given as:

$$V^{0,P}_{l,l'}(\boldsymbol{q}) = \int\limits_{\boldsymbol{k},\boldsymbol{k}'} V^0(\boldsymbol{q}+\boldsymbol{k},-\boldsymbol{k},\boldsymbol{q}+\boldsymbol{k}') \times f_l(\boldsymbol{k}) f^*_{l'}(\boldsymbol{k}'), \tag{A.18}$$

$$V^{0,D}_{l,l'}(\boldsymbol{q}) = \int\limits_{\boldsymbol{k},\boldsymbol{k}'} V^0(\boldsymbol{q}+\boldsymbol{k},\boldsymbol{k}',\boldsymbol{k}) \times f_l(\boldsymbol{k}) f^*_{l'}(\boldsymbol{k}'), \tag{A.19}$$

$$V^{0,C}_{l,l'}(\boldsymbol{q}) = \int\limits_{\boldsymbol{k},\boldsymbol{k}'} V^0(\boldsymbol{q}+\boldsymbol{k},\boldsymbol{k}',\boldsymbol{q}+\boldsymbol{k}') \times f_l(\boldsymbol{k}) f^*_{l'}(\boldsymbol{k}'). \tag{A.20}$$

The initial interaction V^0 is restored by casting the interacting Hamiltonian in the form of the four-legged vertex of the vertex expansion and Fourier transform it. For the spinless fermions this reads:

$$H_{\text{Int}} \to \frac{1}{4} \int\limits_{\boldsymbol{k}_1,\boldsymbol{k}_2,\boldsymbol{k}_3,\boldsymbol{k}_4} V^0(\boldsymbol{k}_1,\boldsymbol{k}_2,\boldsymbol{k}_3,\boldsymbol{k}_4)\delta(\boldsymbol{k}_1+\boldsymbol{k}_2-\boldsymbol{k}_3-\boldsymbol{k}_4) c^\dagger(\boldsymbol{k}_1)c^\dagger(\boldsymbol{k}_2)c(\boldsymbol{k}_4)c(\boldsymbol{k}_3). \tag{A.21}$$

The initial interaction Hamiltonian does exclusively contain the nearest-nearest neighbour interaction V_1. We rewrite this interaction as follows:

$$H_{\text{int}} = V_1 \sum_{\langle i,j\rangle} n_i n_j = V_1 \sum_{\langle i,j\rangle} c^\dagger_i c_i c^\dagger_j c_j = \frac{V_1}{4} \sum_{\langle i,j\rangle} \left(c^\dagger_i c^\dagger_j c_j c_i + c^\dagger_j c^\dagger_i c_i c_j - c^\dagger_i c^\dagger_j c_i c_j - c^\dagger_j c^\dagger_i c_j c_i \right) \tag{A.22}$$

The Fourier transform of this term reads:

$$H_{\text{int}} = \frac{1}{8} \int_{\boldsymbol{k}_1,\boldsymbol{k}_2,\boldsymbol{k}_3,\boldsymbol{k}_4} \delta(\boldsymbol{k}_1+\boldsymbol{k}_2-\boldsymbol{k}_3-\boldsymbol{k}_4) \times \sum_{\boldsymbol{\delta}} \left(e^{-i\boldsymbol{\delta}(\boldsymbol{k}_2-\boldsymbol{k}_4)} + e^{-i\boldsymbol{\delta}(\boldsymbol{k}_1-\boldsymbol{k}_3)} - e^{-i\boldsymbol{\delta}(\boldsymbol{k}_2-\boldsymbol{k}_3)} - e^{-i\boldsymbol{\delta}(\boldsymbol{k}_1-\boldsymbol{k}_4)} \right) c^\dagger(\boldsymbol{k}_1)c^\dagger(\boldsymbol{k}_2)c(\boldsymbol{k}_4)c(\boldsymbol{k}_3) \tag{A.23}$$

where a factor of $1/2$ emerges due compensation of over-counting lattice sites. $\boldsymbol{\delta}$ are the six displacement vectors connecting to nearest-neighbour lattice sites. From this we deduce the initial interaction:

$$V^0(\boldsymbol{k}_1,\boldsymbol{k}_2,\boldsymbol{k}_3,\boldsymbol{k}_4) = \frac{1}{2} \sum_{\boldsymbol{\delta}} \left(e^{-i\boldsymbol{\delta}(\boldsymbol{k}_2-\boldsymbol{k}_4)} + e^{-i\boldsymbol{\delta}(\boldsymbol{k}_1-\boldsymbol{k}_3)} - e^{-i\boldsymbol{\delta}(\boldsymbol{k}_2-\boldsymbol{k}_3)} - e^{-i\boldsymbol{\delta}(\boldsymbol{k}_1-\boldsymbol{k}_4)} \right). \tag{A.24}$$

This expression is now explictely anti-symmetric under switching $\boldsymbol{k}_1$ and $\boldsymbol{k}_2$ or $\boldsymbol{k}_3$ and $\boldsymbol{k}_4$ as it should be imposed by the Grassman properties of the fermionic fields. Plugging Eq. (A.24) finally into projections Eqs. (A.18)-(A.20) yields the initial conditions as presented in the application section:

$$V^{0,C}_{1,1}(\boldsymbol{q}) = -V^{0,D}_{1,1}(\boldsymbol{q}) = -V_1 \sum_l e^{i\boldsymbol{q}\boldsymbol{R}_l}, \tag{A.25}$$

$$V^{0,P}_{l,l}(\boldsymbol{q}) = V^{0,C}_{l,l}(\boldsymbol{q}) = -V^{0,D}_{l,l}(\boldsymbol{q}) = V_1, \tag{A.26}$$

$$V^{0,P}_{-l,l}(\boldsymbol{q}) = -V_1 e^{-i\boldsymbol{q}\boldsymbol{R}_l}\,. \tag{A.27}$$

For $l \in [2,3,4,5,6,7]$.

A.4 Channel decomposition with spin indices

In application C, we use vertices and channels dressed with spin indices. We derived the general flow equations including these spin indices (Eqs. (2.40)-(2.42)) already in section 2.1, from which we construct the TUFRG flow equations as described in section 2.2. This deriviation is carried out in a complete analogous way. The spin-dependent channel decomposition reads:

$$\begin{aligned} V^{\Lambda}_{\sigma_1,\sigma_2,\sigma_3,\sigma_4}(\boldsymbol{k}_1,\boldsymbol{k}_2,\boldsymbol{k}_3,\boldsymbol{k}_4) = V^{0}_{\sigma_1,\sigma_2,\sigma_3,\sigma_4}(\boldsymbol{k}_1,\boldsymbol{k}_2,\boldsymbol{k}_3,\boldsymbol{k}_4) \\ + \Phi^{P,\Lambda}_{\sigma_1,\sigma_2,\sigma_3,\sigma_4}(\boldsymbol{k}_1+\boldsymbol{k}_2;-\boldsymbol{k}_2,-\boldsymbol{k}_4) \\ + \Phi^{D,\Lambda}_{\sigma_1,\sigma_2,\sigma_3,\sigma_4}(\boldsymbol{k}_1-\boldsymbol{k}_3;\boldsymbol{k}_3,\boldsymbol{k}_2) \\ + \Phi^{C,\Lambda}_{\sigma_1,\sigma_2,\sigma_3,\sigma_4}(\boldsymbol{k}_1-\boldsymbol{k}_4;\boldsymbol{k}_4,\boldsymbol{k}_2). \end{aligned} \tag{A.28}$$

Now, we impose a specific order of the spin indices for the channels by imposing the form factor expansion:

$$\Phi^{P,\Lambda}_{\sigma_1,\sigma_2,\sigma_3,\sigma_4}(\boldsymbol{q};\boldsymbol{k},\boldsymbol{k'}) = \sum_{l,l'} P^{l,l'}_{\sigma_1,\sigma_2,\sigma_3,\sigma_4}(\boldsymbol{q}) \times f^*_l(\boldsymbol{k}) f_{l'}(\boldsymbol{k'}), \tag{A.29}$$

$$\Phi^{D,\Lambda}_{\sigma_1,\sigma_2,\sigma_3,\sigma_4}(\boldsymbol{q};\boldsymbol{k},\boldsymbol{k'}) = \sum_{l,l'} D^{l,l'}_{\sigma_1,\sigma_3,\sigma_4,\sigma_2}(\boldsymbol{q}) \times f^*_l(\boldsymbol{k}) f_{l'}(\boldsymbol{k'}), \tag{A.30}$$

$$\Phi^{C,\Lambda}_{\sigma_1,\sigma_2,\sigma_3,\sigma_4}(\boldsymbol{q};\boldsymbol{k},\boldsymbol{k'}) = \sum_{l,l'} C^{l,l'}_{\sigma_1,\sigma_4,\sigma_3,\sigma_2}(\boldsymbol{q}) \times f^*_l(\boldsymbol{k}) f_{l'}(\boldsymbol{k'}). \tag{A.31}$$

By this choice, the three final TUFRG flow equations Eqs. (3.47)-(3.49) have the same structure in terms of spin indices which is a simple matrix contraction with the external indices at the out-most left and right positions of the expression. The order of spin indices of the cross-projections and initial conditions follow directly from imposing this convention.

A.5 Initial conditions for application C

For the initial conditions of the spinful without SU(2), follow the method presented in section 2.3.1, where we now have to take additional care for the spin indices. The projections for the initial conditions read (including spin degrees of freedom):

$$V^{0,P,(l,l')}_{\sigma_1,\sigma_2,\sigma_3,\sigma_4}(\boldsymbol{q}) = \int\limits_{\boldsymbol{k},\boldsymbol{k}'} V^0_{\sigma_1,\sigma_2,\sigma_3,\sigma_4}(\boldsymbol{q}+\boldsymbol{k},-\boldsymbol{k},\boldsymbol{q}+\boldsymbol{k}') \times f_l(\boldsymbol{k}) f^*_{l'}(\boldsymbol{k}'), \tag{A.32}$$

$$V^{0,D,(l,l')}_{\sigma_1,\sigma_2,\sigma_3,\sigma_4}(\boldsymbol{q}) = \int\limits_{\boldsymbol{k},\boldsymbol{k}'} V^0_{\sigma_1,\sigma_4,\sigma_2,\sigma_3}(\boldsymbol{q}+\boldsymbol{k},\boldsymbol{k}',\boldsymbol{k}) \times f_l(\boldsymbol{k}) f^*_{l'}(\boldsymbol{k}'), \tag{A.33}$$

$$V^{0,C,(l,l')}_{\sigma_1,\sigma_2,\sigma_3,\sigma_4}(\boldsymbol{q}) = \int\limits_{\boldsymbol{k},\boldsymbol{k}'} V^0_{\sigma_1,\sigma_4,\sigma_3,\sigma_2}(\boldsymbol{q}+\boldsymbol{k},\boldsymbol{k}',\boldsymbol{q}+\boldsymbol{k}') \times f_l(\boldsymbol{k}) f^*_{l'}(\boldsymbol{k}'). \tag{A.34}$$

The initial interaction is derivable from casting the interaction Hamiltonian explicitly in the form of the four-legged contributions of the vertex expansion:

$$H_{\text{Int}} \to \frac{1}{4} \int\limits_{\boldsymbol{k}_1,\boldsymbol{k}_2,\boldsymbol{k}_3,\boldsymbol{k}_4} V^0_{\sigma_1,\sigma_2,\sigma_3,\sigma_4}(\boldsymbol{k}_1,\boldsymbol{k}_2,\boldsymbol{k}_3,\boldsymbol{k}_4)\delta(\boldsymbol{k}_1+\boldsymbol{k}_2-\boldsymbol{k}_3-\boldsymbol{k}_4) \sum_{\substack{\sigma_1,\sigma_2,\\ \sigma_3,\sigma_4}} \times$$
$$c^\dagger_{\sigma_1}(\boldsymbol{k}_1) c^\dagger_{\sigma_2}(\boldsymbol{k}_2) c_{\sigma_4}(\boldsymbol{k}_4) c_{\sigma_3}(\boldsymbol{k}_3). \tag{A.35}$$

In our application, the interaction Hamiltonian does only consist of the Hubbard interaction:

$$\begin{aligned} H_{\text{Int}} =& U \sum_i n_{i,\uparrow} n_{i,\downarrow} = U \sum_i c^\dagger_{i\uparrow} c_{i\uparrow} c^\dagger_{i\downarrow} c_{i\downarrow} \\ =& \frac{U}{4} \sum_i c^\dagger_{i\uparrow} c^\dagger_{i\downarrow} c_{i\downarrow} c_{i\uparrow} + c^\dagger_{i\downarrow} c^\dagger_{i\uparrow} c_{i\uparrow} c_{i\downarrow} - c^\dagger_{i\uparrow} c^\dagger_{i\downarrow} c_{i\uparrow} c_{i\downarrow} - c^\dagger_{i\downarrow} c^\dagger_{i\uparrow} c_{i\downarrow} c_{i\uparrow} \end{aligned} \tag{A.36}$$

Which we translate into the desired form by using a Fourier transform:

$$H_{\text{int}} = \frac{U}{4} \int_{\boldsymbol{k}_1,\boldsymbol{k}_2,\boldsymbol{k}_3,\boldsymbol{k}_4} \delta(\boldsymbol{k}_1+\boldsymbol{k}_2-\boldsymbol{k}_3-\boldsymbol{k}_4) \sum_{\substack{\sigma_1,\sigma_2,\\ \sigma_3,\sigma_4}} c^\dagger_{\sigma_1}(\boldsymbol{k}_1) c^\dagger_{\sigma_2}(\boldsymbol{k}_2) c_{\sigma_4}(\boldsymbol{k}_4) c_{\sigma_3}(\boldsymbol{k}_3) \times$$
$$\Big(\delta_{\sigma_1,\uparrow}\delta_{\sigma_2,\downarrow}\delta_{\sigma_3,\uparrow}\delta_{\sigma_4,\downarrow} + \delta_{\sigma_1,\downarrow}\delta_{\sigma_2,\uparrow}\delta_{\sigma_3,\downarrow}\delta_{\sigma_4,\uparrow} - \delta_{\sigma_1,\uparrow}\delta_{\sigma_2,\downarrow}\delta_{\sigma_3,\downarrow}\delta_{\sigma_4,\uparrow} - \delta_{\sigma_1,\downarrow}\delta_{\sigma_2,\uparrow}\delta_{\sigma_3,\uparrow}\delta_{\sigma_4,\downarrow} \Big). \tag{A.37}$$

Therefore, the initial interaction is given by:

$$\begin{aligned} &V^0_{\sigma_1,\sigma_2,\sigma_3,\sigma_4}(\boldsymbol{k}_1,\boldsymbol{k}_2,\boldsymbol{k}_3,\boldsymbol{k}_4) = \\ &U \left(\delta_{\sigma_1,\uparrow}\delta_{\sigma_2,\downarrow}\delta_{\sigma_3,\uparrow}\delta_{\sigma_4,\downarrow} + \delta_{\sigma_1,\downarrow}\delta_{\sigma_2,\uparrow}\delta_{\sigma_3,\downarrow}\delta_{\sigma_4,\uparrow} - \delta_{\sigma_1,\uparrow}\delta_{\sigma_2,\downarrow}\delta_{\sigma_3,\downarrow}\delta_{\sigma_4,\uparrow} - \delta_{\sigma_1,\downarrow}\delta_{\sigma_2,\uparrow}\delta_{\sigma_3,\uparrow}\delta_{\sigma_4,\downarrow} \right). \end{aligned} \tag{A.38}$$

The initial conditions for the TUFRG are then derived by employing the corresponding projections Eqs. (A.32)-(A.34). These are properly anti-symmetrized.

$$V^{0,P,(1,1)}_{\uparrow\downarrow\uparrow\downarrow}(\boldsymbol{q}) = \quad V^{0,P,(1,1)}_{\downarrow\uparrow\downarrow\uparrow}(\boldsymbol{q}) = \quad -V^{0,P,(1,1)}_{\uparrow\downarrow\downarrow\uparrow}(\boldsymbol{q}) = \quad -V^{0,P,(1,1)}_{\downarrow\uparrow\uparrow\downarrow}(\boldsymbol{q}) = \quad U \tag{A.39}$$

$$V^{0,D,(1,1)}_{\uparrow\uparrow\downarrow\downarrow}(\boldsymbol{q}) = \quad V^{0,D,(1,1)}_{\downarrow\downarrow\uparrow\uparrow}(\boldsymbol{q}) = \quad -V^{0,D,(1,1)}_{\uparrow\downarrow\uparrow\downarrow}(\boldsymbol{q}) = \quad -V^{0,D,(1,1)}_{\downarrow\uparrow\downarrow\uparrow}(\boldsymbol{q}) = \quad U \tag{A.40}$$

$$V^{0,C,(1,1)}_{\uparrow\downarrow\uparrow\downarrow}(\boldsymbol{q}) = \quad V^{0,C,(1,1)}_{\downarrow\uparrow\downarrow\uparrow}(\boldsymbol{q}) = \quad -V^{0,C,(1,1)}_{\uparrow\uparrow\downarrow\downarrow}(\boldsymbol{q}) = \quad -V^{0,C,(1,1)}_{\downarrow\downarrow\uparrow\uparrow}(\boldsymbol{q}) = \quad U \tag{A.41}$$

Bibliography

[1] P. W. Anderson. "More Is Different". In: *Science* 177.4047 (1972), pp. 393–396. DOI: 10.1126/science.177.4047.393.

[2] E. Y. Andrei and A. H. MacDonald. "Graphene bilayers with a twist". In: *Nature Materials* 19 (12 2020), pp. 1265–1275. DOI: https://doi.org/10.1038/s41563-020-00840-0.

[3] N. P. Armitage, P. Fournier, and R. L. Greene. "Progress and perspectives on electron-doped cuprates". In: *Rev. Mod. Phys.* 82 (3 Sept. 2010), pp. 2421–2487. DOI: 10.1103/RevModPhys.82.2421. URL: https://link.aps.org/doi/10.1103/RevModPhys.82.2421.

[4] Daniel P. Arovas et al. "The Hubbard Model". In: *Annual Review of Condensed Matter Physics* 13.1 (2022), pp. 239–274. DOI: 10.1146/annurev-conmatphys-031620-102024. eprint: https://doi.org/10.1146/annurev-conmatphys-031620-102024. URL: https://doi.org/10.1146/annurev-conmatphys-031620-102024.

[5] M. L. Baez and J. Reuther. "Numerical treatment of spin systems with unrestricted spin length S: A functional renormalization group study". In: *Phys. Rev. B* 96 (4 July 2017), p. 045144. DOI: 10.1103/PhysRevB.96.045144. URL: https://link.aps.org/doi/10.1103/PhysRevB.96.045144.

[6] C. Bagnuls and C. Bervillier. "Exact renormalization group equations. An Introductory review". In: *Physics Reports* 348 (2000), pp. 91–157.

[7] J. Bardeen, L. N. Cooper, and J. R. Schrieffer. "Theory of Superconductivity". In: *Phys. Rev.* 108 (5 Dec. 1957), pp. 1175–1204. DOI: 10.1103/PhysRev.108.1175. URL: https://link.aps.org/doi/10.1103/PhysRev.108.1175.

[8] Beyer, Jacob, Goth, Florian, and Müller, Tobias. "Better integrators for functional renormalization group calculations". In: *Eur. Phys. J. B* 95.7 (2022), p. 116. DOI: 10.1140/epjb/s10051-022-00378-x. URL: https://doi.org/10.1140/epjb/s10051-022-00378-x.

[9] R. Bistrizer and A.H. MacDonald. "Moire bands in twisted double-layer graphene." In: *Proceedings of the National Academy of Sciences of the United States of America* 108 (30 2011). DOI: doi:10.1073/pnas.1108174108.

[10] Annica M Black-Schaffer and Carsten Honerkamp. "Chiral d-wave superconductivity in doped graphene". In: *Journal of Physics: Condensed Matter* 26.42 (2014), p. 423201.

[11] Pietro M. Bonetti et al. "Single-boson exchange representation of the functional renormalization group for strongly interacting many-electron systems". In: *Phys. Rev. Research* 4 (1 Jan. 2022), p. 013034. DOI: 10.1103/PhysRevResearch.4.013034. URL: https://link.aps.org/doi/10.1103/PhysRevResearch.4.013034.

[12] Max Born and Werner Heisenberg. "Zur quantentheorie der molekeln". In: *Annalen der Physik* 379.9 (1924), pp. 1–31.

[13] Xiaodong Cao et al. "Chiral d-wave superconductivity in a triangular surface lattice mediated by long-range interaction". In: *Phys. Rev. B* 97 (15 Apr. 2018), p. 155145. DOI: 10.1103/PhysRevB.97.155145. URL: https://link.aps.org/doi/10.1103/PhysRevB.97.155145.

[14] Y. Cao et al. “Correlated insulator behaviour at half-filling in magic-angle graphene superlattices”. In: *Nature* 556 (7699 2018). DOI: https://doi.org/10.1038/nature26154.

[15] Y. Cao et al. “Unconventional superconductivity in magic-angle graphene superlattices”. In: *Nature* 556 (7699 2018). DOI: https://doi.org/10.1038/nature26160.

[16] A. H. Castro Neto et al. “The electronic properties of graphene”. In: *Rev. Mod. Phys.* 81 (1 Jan. 2009), pp. 109–162. DOI: 10.1103/RevModPhys.81.109. URL: https://link.aps.org/doi/10.1103/RevModPhys.81.109.

[17] Hui-Min Chen, Hui Zhao, and Chang-Qin Wu. “Pomeranchuk instability on a two-dimensional frustrated lattice”. In: *Phys. Rev. B* 82 (24 Dec. 2010), p. 245106. DOI: 10.1103/PhysRevB.82.245106. URL: https://link.aps.org/doi/10.1103/PhysRevB.82.245106.

[18] Kuang Shing Chen et al. “Unconventional superconductivity on the triangular lattice Hubbard model”. In: *Phys. Rev. B* 88 (4 July 2013), p. 041103. DOI: 10.1103/PhysRevB.88.041103. URL: https://link.aps.org/doi/10.1103/PhysRevB.88.041103.

[19] Meng Cheng et al. “Stable topological superconductivity in a family of two-dimensional fermion models”. In: *Phys. Rev. B* 81 (2 Jan. 2010), p. 024504. DOI: 10.1103/PhysRevB.81.024504. URL: https://link.aps.org/doi/10.1103/PhysRevB.81.024504.

[20] Laura Classen, Carsten Honerkamp, and Michael M. Scherer. “Competing phases of interacting electrons on triangular lattices in moiré heterostructures”. In: *Phys. Rev. B* 99 (19 May 2019), p. 195120. DOI: 10.1103/PhysRevB.99.195120. URL: https://link.aps.org/doi/10.1103/PhysRevB.99.195120.

[21] Laura Classen et al. “Competing orders at higher-order Van Hove points”. In: *Phys. Rev. B* 102 (12 Sept. 2020), p. 125141. DOI: 10.1103/PhysRevB.102.125141. URL: https://link.aps.org/doi/10.1103/PhysRevB.102.125141.

[22] Leon N. Cooper. “Bound Electron Pairs in a Degenerate Fermi Gas”. In: *Phys. Rev.* 104 (4 Nov. 1956), pp. 1189–1190. DOI: 10.1103/PhysRev.104.1189. URL: https://link.aps.org/doi/10.1103/PhysRev.104.1189.

[23] Andrea Damascelli, Zahid Hussain, and Zhi-Xun Shen. “Angle-resolved photoemission studies of the cuprate superconductors”. In: *Rev. Mod. Phys.* 75 (2 Apr. 2003), pp. 473–541. DOI: 10.1103/RevModPhys.75.473. URL: https://link.aps.org/doi/10.1103/RevModPhys.75.473.

[24] Bertrand Delamotte. “An Introduction to the Nonperturbative Renormalization Group”. In: *Lecture Notes in Physics* 852 (2007), pp. 49–132.

[25] C. J. Eckhardt et al. “Truncated-unity parquet equations: Application to the repulsive Hubbard model”. In: *Phys. Rev. B* 98 (7 Aug. 2018), p. 075143. DOI: 10.1103/PhysRevB.98.075143. URL: https://link.aps.org/doi/10.1103/PhysRevB.98.075143.

[26] U. Ellwanger and C. Wetterich. “Evolution equations for the quark-meson transition”. In: *Nuclear Physics B* 423.1 (1994), pp. 137–167. ISSN: 0550-3213. DOI: https://doi.org/10.1016/0550-3213(94)90568-1. URL: https://www.sciencedirect.com/science/article/pii/0550321394905681.

[27] H. Fröhlich. “Theory of the Superconducting State. I. The Ground State at the Absolute Zero of Temperature”. In: *Phys. Rev.* 79 (5 Sept. 1950), pp. 845–856. DOI: 10.1103/PhysRev.79.845. URL: https://link.aps.org/doi/10.1103/PhysRev.79.845.

[28] K.S. Geim et al. “Electric field effect in atomically thin carbon films”. In: *Science* 306 (1 2004), pp. 666–669. DOI: https://doi.org/10.1126/science.1102896.

[29] Nico Gneist, Laura Classen, and Michael M. Scherer. *Competing instabilities of the extended Hubbard model on the triangular lattice: Truncated-unity functional renormalization group and application to moiré materials*. 2022. DOI: 10.48550/ARXIV.2203.01226. URL: https://arxiv.org/abs/2203.01226.

[30] Nico Gneist et al. *Functional renormalization of spinless triangular-lattice fermions: N-patch vs. truncated-unity scheme*. 2022. DOI: 10.48550/ARXIV.2205.12547. URL: https://arxiv.org/abs/2205.12547.

[31] Daniele Guerci, Pascal Simon, and Christophe Mora. "Higher-order Van Hove singularity in magic-angle twisted trilayer graphene". In: *Phys. Rev. Research* 4 (1 Feb. 2022), p. L012013. DOI: 10.1103/PhysRevResearch.4.L012013. URL: https://link.aps.org/doi/10.1103/PhysRevResearch.4.L012013.

[32] Christoph J. Halboth and Walter Metzner. "Renormalization-group analysis of the two-dimensional Hubbard model". In: *Phys. Rev. B* 61 (11 Mar. 2000), pp. 7364–7377. DOI: 10.1103/PhysRevB.61.7364. URL: https://link.aps.org/doi/10.1103/PhysRevB.61.7364.

[33] P. Hansmann et al. "Long-Range Coulomb Interactions in Surface Systems: A First-Principles Description within Self-Consistently Combined GW and Dynamical Mean-Field Theory". In: *Phys. Rev. Lett.* 110 (16 Apr. 2013), p. 166401. DOI: 10.1103/PhysRevLett.110.166401. URL: https://link.aps.org/doi/10.1103/PhysRevLett.110.166401.

[34] Hauck, Jonas B. and Kennes, Dante M. "TU^{2}FRG: a scalable approach for truncated unity functional renormalization group in generic fermionic models". In: *Eur. Phys. J. B* 95.3 (2022), p. 60. DOI: 10.1140/epjb/s10051-022-00316-x. URL: https://doi.org/10.1140/epjb/s10051-022-00316-x.

[35] Cornelia Hille et al. "Pseudogap opening in the two-dimensional Hubbard model: A functional renormalization group analysis". In: *Phys. Rev. Research* 2 (3 July 2020), p. 033068. DOI: 10.1103/PhysRevResearch.2.033068. URL: https://link.aps.org/doi/10.1103/PhysRevResearch.2.033068.

[36] Cornelia Hille et al. "Quantitative functional renormalization group description of the two-dimensional Hubbard model". In: *Phys. Rev. Research* 2 (3 Sept. 2020), p. 033372. DOI: 10.1103/PhysRevResearch.2.033372. URL: https://link.aps.org/doi/10.1103/PhysRevResearch.2.033372.

[37] Motoaki Hirayama et al. "Ab initio effective Hamiltonians for cuprate superconductors". In: *Phys. Rev. B* 98 (13 Oct. 2018), p. 134501. DOI: 10.1103/PhysRevB.98.134501. URL: https://link.aps.org/doi/10.1103/PhysRevB.98.134501.

[38] Motoaki Hirayama et al. "Effective Hamiltonian for cuprate superconductors derived from multiscale ab initio scheme with level renormalization". In: *Phys. Rev. B* 99 (24 June 2019), p. 245155. DOI: 10.1103/PhysRevB.99.245155. URL: https://link.aps.org/doi/10.1103/PhysRevB.99.245155.

[39] C. Honerkamp et al. "Breakdown of the Landau-Fermi liquid in two dimensions due to umklapp scattering". In: *Phys. Rev. B* 63 (3 Jan. 2001), p. 035109. DOI: 10.1103/PhysRevB.63.035109. URL: https://link.aps.org/doi/10.1103/PhysRevB.63.035109.

[40] Carsten Honerkamp. "Efficient vertex parametrization for the constrained functional renormalization group for effective low-energy interactions in multiband systems". In: *Phys. Rev. B* 98 (15 Oct. 2018), p. 155132. DOI: 10.1103/PhysRevB.98.155132. URL: https://link.aps.org/doi/10.1103/PhysRevB.98.155132.

[41] Carsten Honerkamp. "Instabilities of interacting electrons on the triangular lattice". In: *Phys. Rev. B* 68 (10 Sept. 2003), p. 104510. DOI: 10.1103/PhysRevB.68.104510. URL: https://link.aps.org/doi/10.1103/PhysRevB.68.104510.

[42] Carsten Honerkamp and Manfred Salmhofer. "Magnetic and Superconducting Instabilities of the Hubbard Model at the Van Hove Filling". In: *Phys. Rev. Lett.* 87 (18 Oct. 2001), p. 187004. DOI: 10.1103/PhysRevLett.87.187004. URL: https://link.aps.org/doi/10.1103/PhysRevLett.87.187004.

[43] Carsten Honerkamp and Manfred Salmhofer. "Temperature-flow renormalization group and the competition between superconductivity and ferromagnetism". In: *Phys. Rev. B* 64 (18 Oct. 2001), p. 184516. DOI: 10.1103/PhysRevB.64.184516. URL: https://link.aps.org/doi/10.1103/PhysRevB.64.184516.

[44] Baruch Horovitz and Anatoly Golub. "Superconductors with broken time-reversal symmetry: Spontaneous magnetization and quantum Hall effects". In: *Phys. Rev. B* 68 (21 Dec. 2003), p. 214503. DOI: 10.1103/PhysRevB.68.214503. URL: https://link.aps.org/doi/10.1103/PhysRevB.68.214503.

[45] John Hubbard. "Electron correlations in narrow energy bands". In: *Proceedings of the Royal Society of London. Series A. Mathematical and Physical Sciences* 276.1365 (1963), pp. 238–257.

[46] C. Husemann and M. Salmhofer. "Efficient parametrization of the vertex function, Ω scheme, and the t, t' Hubbard model at van Hove filling". In: *Phys. Rev. B* 79 (19 May 2009), p. 195125. DOI: 10.1103/PhysRevB.79.195125. URL: https://link.aps.org/doi/10.1103/PhysRevB.79.195125.

[47] Mark S. Hybertsen, Michael Schlüter, and Niels E. Christensen. "Calculation of Coulomb-interaction parameters for La_2 CuO_4 using a constrained-density-functional approach". In: *Phys. Rev. B* 39 (13 May 1989), pp. 9028–9041. DOI: 10.1103/PhysRevB.39.9028. URL: https://link.aps.org/doi/10.1103/PhysRevB.39.9028.

[48] Hiroki Isobe and Liang Fu. "Supermetal". In: *Phys. Rev. Research* 1 (3 Dec. 2019), p. 033206. DOI: 10.1103/PhysRevResearch.1.033206. URL: https://link.aps.org/doi/10.1103/PhysRevResearch.1.033206.

[49] Jeil Jung et al. "Ab initio theory of moiré superlattice bands in layered two-dimensional materials". In: *Phys. Rev. B* 89 (20 May 2014), p. 205414. DOI: 10.1103/PhysRevB.89.205414. URL: https://link.aps.org/doi/10.1103/PhysRevB.89.205414.

[50] S.-O. Kaba and D. Sénéchal. "Group-theoretical classification of superconducting states of strontium ruthenate". In: *Phys. Rev. B* 100 (21 Dec. 2019), p. 214507. DOI: 10.1103/PhysRevB.100.214507. URL: https://link.aps.org/doi/10.1103/PhysRevB.100.214507.

[51] Leo P. Kadanoff. "Scaling laws for ising models near T_c". In: *Physics Physique Fizika* 2 (6 June 1966), pp. 263–272. DOI: 10.1103/PhysicsPhysiqueFizika.2.263. URL: https://link.aps.org/doi/10.1103/PhysicsPhysiqueFizika.2.263.

[52] Mikhail I. Katsnelson. *Graphene: Carbon in Two Dimensions*. Cambridge University Press, 2012. DOI: 10.1017/CBO9781139031080.

[53] Dominik Kiese et al. "Multiloop functional renormalization group approach to quantum spin systems". In: *Phys. Rev. Research* 4 (2 June 2022), p. 023185. DOI: 10.1103/PhysRevResearch.4.023185. URL: https://link.aps.org/doi/10.1103/PhysRevResearch.4.023185.

[54] Maximilian L. Kiesel, Christian Platt, and Ronny Thomale. "Unconventional Fermi Surface Instabilities in the Kagome Hubbard Model". In: *Phys. Rev. Lett.* 110 (12 Mar. 2013), p. 126405. DOI: 10.1103/PhysRevLett.110.126405. URL: https://link.aps.org/doi/10.1103/PhysRevLett.110.126405.

[55] Maximilian L. Kiesel et al. "Competing many-body instabilities and unconventional superconductivity in graphene". In: *Phys. Rev. B* 86 (2 July 2012), p. 020507. DOI: 10.1103/PhysRevB.86.020507. URL: https://link.aps.org/doi/10.1103/PhysRevB.86.020507.

[56] Maximilian L. Kiesel et al. "Model Evidence of an Anisotropic Chiral $d+id$-Wave Pairing State for the Water-Intercalated $Na_xCoO_2 \cdot y\mathbf{H_2O}$ Superconductor". In: *Phys. Rev. Lett.* 111 (9 Aug. 2013), p. 097001. DOI: 10.1103/PhysRevLett.111.097001. URL: https://link.aps.org/doi/10.1103/PhysRevLett.111.097001.

[57] Lennart Klebl et al. *Competition of Density Waves and Superconductivity in Twisted Tungsten Diselenide*. 2022. arXiv: 2204.00648 [cond-mat.str-el].

[58] Alexander V. Kolobov and Junji Tominaga. *Two-Dimensional Transition-Metal Dichalcogenides*. Springer Series in Materials Science. Springer Cham, 2016. DOI: https://doi.org/10.1007/978-3-319-31450-1.

[59] Mikito Koshino. "Interlayer interaction in general incommensurate atomic layers". In: *New Journal of Physics* 17 (Jan. 2015). DOI: 10.1088/1367-2630/17/1/015014.

[60] Mikito Koshino et al. "Maximally Localized Wannier Orbitals and the Extended Hubbard Model for Twisted Bilayer Graphene". In: *Phys. Rev. X* 8 (3 Sept. 2018), p. 031087. DOI: 10.1103/PhysRevX.8.031087. URL: https://link.aps.org/doi/10.1103/PhysRevX.8.031087.

[61] Fabian B. Kugler and Jan von Delft. "Multiloop functional renormalization group for general models". In: *Phys. Rev. B* 97 (3 Jan. 2018), p. 035162. DOI: 10.1103/PhysRevB.97.035162. URL: https://link.aps.org/doi/10.1103/PhysRevB.97.035162.

[62] Fabian B. Kugler and Jan von Delft. "Multiloop Functional Renormalization Group That Sums Up All Parquet Diagrams". In: *Phys. Rev. Lett.* 120 (5 Jan. 2018), p. 057403. DOI: 10.1103/PhysRevLett.120.057403. URL: https://link.aps.org/doi/10.1103/PhysRevLett.120.057403.

[63] Anthony J. Leggett. "A theoretical description of the new phases of liquid ^{3}He". In: *Rev. Mod. Phys.* 47 (2 Apr. 1975), pp. 331–414. DOI: 10.1103/RevModPhys.47.331. URL: https://link.aps.org/doi/10.1103/RevModPhys.47.331.

[64] J. Lichtenstein et al. "High-performance functional Renormalization Group calculations for interacting fermions". In: *Computer Physics Communications* 213 (2017), pp. 100–110. ISSN: 0010-4655. DOI: https://doi.org/10.1016/j.cpc.2016.12.013. URL: https://www.sciencedirect.com/science/article/pii/S0010465516303927.

[65] Gui-Bin Liu et al. "Three-band tight-binding model for monolayers of group-VIB transition metal dichalcogenides". In: *Phys. Rev. B* 88 (8 Aug. 2013), p. 085433. DOI: 10.1103/PhysRevB.88.085433. URL: https://link.aps.org/doi/10.1103/PhysRevB.88.085433.

[66] Stefan A. Maier, Carsten Honerkamp, and Qiang-Hua Wang. "Interplay between Point-Group Symmetries and the Choice of the Bloch Basis in Multiband Models". In: *Symmetry* 5.4 (2013), pp. 313–343. ISSN: 2073-8994. DOI: 10.3390/sym5040313. URL: https://www.mdpi.com/2073-8994/5/4/313.

[67] Saurabh Maiti and Andrey V. Chubukov. "Superconductivity from repulsive interaction". In: *AIP Conference Proceedings* 1550.1 (2013), pp. 3–73. DOI: 10.1063/1.4818400. eprint: https://aip.scitation.org/doi/pdf/10.1063/1.4818400. URL: https://aip.scitation.org/doi/abs/10.1063/1.4818400.

[68] S. Manzeli et al. "2D transition metal dichalcogenides". In: *Nat Rev Mater 2* 2 (17033 2017). DOI: https://doi.org/10.1038/natrevmats.2017.33.

[69] R. S. Markiewicz et al. "One-band tight-binding model parametrization of the high-T_c cuprates including the effect of k_z dispersion". In: *Phys. Rev. B* 72 (5 Aug. 2005), p. 054519. DOI: 10.1103/PhysRevB.72.054519. URL: https://link.aps.org/doi/10.1103/PhysRevB.72.054519.

[70] Ivar Martin and C. D. Batista. "Itinerant Electron-Driven Chiral Magnetic Ordering and Spontaneous Quantum Hall Effect in Triangular Lattice Models". In: *Phys. Rev. Lett.* 101 (15 Oct. 2008), p. 156402. DOI: 10.1103/PhysRevLett.101.156402. URL: https://link.aps.org/doi/10.1103/PhysRevLett.101.156402.

[71] W. Meissner and R. Ochsenfeld. "Ein neuer Effekt bei Eintritt der Supraleitfähigkeit". In: *Naturwissenschaften* 21.44 (1933), pp. 787–788. ISSN: 1432-1904. DOI: 10.1007/BF01504252. URL: https://doi.org/10.1007/BF01504252.

[72] Walter Metzner et al. "Functional renormalization group approach to correlated fermion systems". In: *Rev. Mod. Phys.* 84 (1 Mar. 2012), pp. 299–352. DOI: 10.1103/RevModPhys.84.299. URL: https://link.aps.org/doi/10.1103/RevModPhys.84.299.

[73] Pilkyung Moon and Mikito Koshino. "Optical absorption in twisted bilayer graphene". In: *Phys. Rev. B* 87 (20 May 2013), p. 205404. DOI: 10.1103/PhysRevB.87.205404. URL: https://link.aps.org/doi/10.1103/PhysRevB.87.205404.

[74] Rahul Nandkishore, Gia-Wei Chern, and Andrey V. Chubukov. "Itinerant Half-Metal Spin-Density-Wave State on the Hexagonal Lattice". In: *Phys. Rev. Lett.* 108 (22 May 2012), p. 227204. DOI: 10.1103/PhysRevLett.108.227204. URL: https://link.aps.org/doi/10.1103/PhysRevLett.108.227204.

[75] Rahul Nandkishore, Ronny Thomale, and Andrey V. Chubukov. "Superconductivity from weak repulsion in hexagonal lattice systems". In: *Phys. Rev. B* 89 (14 Apr. 2014), p. 144501. DOI: 10.1103/PhysRevB.89.144501. URL: https://link.aps.org/doi/10.1103/PhysRevB.89.144501.

[76] John W. Negele and Henri Orland. *Quantum Many-particle Systems*. Westview Press, Nov. 1998. ISBN: 0738200522. URL: http://www.worldcat.org/isbn/0738200522.

[77] Song-Jin O et al. "Competing electronic orders on a heavily doped honeycomb lattice with enhanced exchange coupling". In: *Phys. Rev. B* 103 (23 June 2021), p. 235150. DOI: 10.1103/PhysRevB.103.235150. URL: https://link.aps.org/doi/10.1103/PhysRevB.103.235150.

[78] Song-Jin O et al. "Effect of exchange interaction on electronic instabilities in the honeycomb lattice: A functional renormalization group study". In: *Phys. Rev. B* 99 (24 June 2019), p. 245140. DOI: 10.1103/PhysRevB.99.245140. URL: https://link.aps.org/doi/10.1103/PhysRevB.99.245140.

[79] Haining Pan, Fengcheng Wu, and Sankar Das Sarma. "Band topology, Hubbard model, Heisenberg model, and Dzyaloshinskii-Moriya interaction in twisted bilayer WSe_2". In: *Phys. Rev. Research* 2 (3 July 2020), p. 033087. DOI: 10.1103/PhysRevResearch.2.033087. URL: https://link.aps.org/doi/10.1103/PhysRevResearch.2.033087.

[80] Yi Pan et al. "Quantum-Confined Electronic States Arising from the Moiré Pattern of MoS2–WSe2 Heterobilayers". In: *Nano Letters* 18.3 (2018). PMID: 29415536, pp. 1849–1855. DOI: 10.1021/acs.nanolett.7b05125. eprint: https://doi.org/10.1021/acs.nanolett.7b05125. URL: https://doi.org/10.1021/acs.nanolett.7b05125.

[81] D. Sánchez de la Peña, J. Lichtenstein, and C. Honerkamp. "Competing electronic instabilities of extended Hubbard models on the honeycomb lattice: A functional renormalization group calculation with high-wave-vector resolution". In: *Phys. Rev. B* 95 (8 Feb. 2017), p. 085143. DOI: 10.1103/PhysRevB.95.085143. URL: https://link.aps.org/doi/10.1103/PhysRevB.95.085143.

[82] David Sánchez de la Peña et al. "Antiferromagnetism and competing charge instabilities of electrons in strained graphene from Coulomb interactions". In: *Phys. Rev. B* 96 (20 Nov. 2017), p. 205155. DOI: 10.1103/PhysRevB.96.205155. URL: https://link.aps.org/doi/10.1103/PhysRevB.96.205155.

[83] M. Platé et al. "Fermi Surface and Quasiparticle Excitations of Overdoped $Tl_2Ba_2CuO_{6+\delta}$". In: *Phys. Rev. Lett.* 95 (7 Aug. 2005), p. 077001. DOI: 10.1103/PhysRevLett.95.077001. URL: https://link.aps.org/doi/10.1103/PhysRevLett.95.077001.

[84] C. Platt, W. Hanke, and R. Thomale. "Functional renormalization group for multi-orbital Fermi surface instabilities". In: *Advances in Physics* 62.4-6 (2013), pp. 453–562. DOI: 10.1080/00018732.2013.862020. eprint: https://doi.org/10.1080/00018732.2013.862020. URL: https://doi.org/10.1080/00018732.2013.862020.

[85] Christian Platt. "A Common Thread in Unconventional Superconductivity: The Functional Renormalization Group in Multi-Band Systems". doctoralthesis. Universität Würzburg, 2012.

[86] Cyril Proust and Louis Taillefer. "The Remarkable Underlying Ground States of Cuprate Superconductors". In: *Annual Review of Condensed Matter Physics* 10.1 (2019), pp. 409–429. DOI: 10.1146/annurev-conmatphys-031218-013210. eprint: https://doi.org/10.1146/annurev-conmatphys-031218-013210. URL: https://doi.org/10.1146/annurev-conmatphys-031218-013210.

[87] Mingpu Qin et al. "The Hubbard Model: A Computational Perspective". In: *Annual Review of Condensed Matter Physics* 13.1 (2022), pp. 275–302. DOI: 10.1146/annurev-conmatphys-090921-033948. eprint: https://doi.org/10.1146/annurev-conmatphys-090921-033948. URL: https://doi.org/10.1146/annurev-conmatphys-090921-033948.

[88] S. Raghu, S. A. Kivelson, and D. J. Scalapino. "Superconductivity in the repulsive Hubbard model: An asymptotically exact weak-coupling solution". In: *Phys. Rev. B* 81 (22 June 2010), p. 224505. DOI: 10.1103/PhysRevB.81.224505. URL: https://link.aps.org/doi/10.1103/PhysRevB.81.224505.

[89] N. Read and Dmitry Green. "Paired states of fermions in two dimensions with breaking of parity and time-reversal symmetries and the fractional quantum Hall effect". In: *Phys. Rev. B* 61 (15 Apr. 2000), pp. 10267–10297. DOI: 10.1103/PhysRevB.61.10267. URL: https://link.aps.org/doi/10.1103/PhysRevB.61.10267.

[90] Johannes Reuther and Peter Wölfle. "J_1-J_2 frustrated two-dimensional Heisenberg model: Random phase approximation and functional renormalization group". In: *Phys. Rev. B* 81 (14 Apr. 2010), p. 144410. DOI: 10.1103/PhysRevB.81.144410. URL: https://link.aps.org/doi/10.1103/PhysRevB.81.144410.

[91] J. A. Reyes-Retana and F. Cervantes-Sodi. "Spin-orbital effects in metal-dichalcogenide semiconducting monolayers". In: *Scientific reports* 6 (24093). DOI: doi:10.1038/srep24093.

[92] Damian Rybicki et al. "Perspective on the phase diagram of cuprate high-temperature superconductors". In: *Nature Communications* 7.11413 (2016). DOI: 10.1038/ncomms11413. URL: https://doi.org/10.1038/ncomms11413.

[93] Manfred Salmhofer. "Renormalization in condensed matter: Fermionic systems – from mathematics to materials". In: *Nuclear Physics B* 941 (2019), pp. 868–899. ISSN: 0550-3213. DOI: https://doi.org/10.1016/j.nuclphysb.2018.07.004. URL: https://www.sciencedirect.com/science/article/pii/S0550321318301901.

[94] Manfred Salmhofer and Carsten Honerkamp. "Fermionic Renormalization Group Flows: Technique and Theory". In: *Progress of Theoretical Physics* 105.1 (Jan. 2001), pp. 1–35. ISSN: 0033-068X. DOI: 10.1143/PTP.105.1. eprint: https://academic.oup.com/ptp/article-pdf/105/1/1/5164880/105-1-1.pdf. URL: https://doi.org/10.1143/PTP.105.1.

[95] Manfred Salmhofer et al. "Renormalization Group Flows into Phases with Broken Symmetry". In: *Progress of Theoretical Physics* 112.6 (Dec. 2004), pp. 943–970. ISSN: 0033-068X. DOI: 10.1143/PTP.112.943. eprint: https://academic.oup.com/ptp/article-pdf/112/6/943/5394684/112-6-943.pdf. URL: https://doi.org/10.1143/PTP.112.943.

[96] D.J. Scalapino. "The case for dx2 − y2 pairing in the cuprate superconductors". In: *Physics Reports* 250.6 (1995), pp. 329–365. ISSN: 0370-1573. DOI: https://doi.org/10.1016/0370-1573(94)00086-I. URL: https://www.sciencedirect.com/science/article/pii/037015739400086I.

[97] Michael M. Scherer, Dante M. Kennes, and Laura Classen. $\mathcal{N} = 4$ *chiral superconductivity in moiré transition metal dichalcogenides*. 2021. DOI: 10.48550/ARXIV.2108.11406. URL: https://arxiv.org/abs/2108.11406.

[98] Giulio A. H. Schober et al. "Truncated-Unity Functional Renormalization Group for Multi-band Systems With Spin-Orbit Coupling". In: *Frontiers in Physics* 6 (2018). ISSN: 2296-424X. DOI: 10.3389/fphy.2018.00032. URL: https://www.frontiersin.org/articles/10.3389/fphy.2018.00032.

[99] T. Senthil, J. B. Marston, and Matthew P. A. Fisher. "Spin quantum Hall effect in unconventional superconductors". In: *Phys. Rev. B* 60 (6 Aug. 1999), pp. 4245–4254. DOI: 10.1103/PhysRevB.60.4245. URL: https://link.aps.org/doi/10.1103/PhysRevB.60.4245.

[100] Manfred Sigrist and Kazuo Ueda. "Phenomenological theory of unconventional superconductivity". In: *Rev. Mod. Phys.* 63 (2 Apr. 1991), pp. 239–311. DOI: 10.1103/RevModPhys.63.239. URL: https://link.aps.org/doi/10.1103/RevModPhys.63.239.

[101] J. C. Slater and G. F. Koster. "Simplified LCAO Method for the Periodic Potential Problem". In: *Phys. Rev.* 94 (6 June 1954), pp. 1498–1524. DOI: 10.1103/PhysRev.94.1498. URL: https://link.aps.org/doi/10.1103/PhysRev.94.1498.

[102] Agnese Tagliavini et al. "Multiloop functional renormalization group for the two-dimensional Hubbard model: Loop convergence of the response functions". In: *SciPost Phys.* 6 (1 2019), p. 9. DOI: 10.21468/SciPostPhys.6.1.009. URL: https://scipost.org/10.21468/SciPostPhys.6.1.009.

[103] "90 - THE THEORY OF A FERMI LIQUID". In: *Collected Papers of L.D. Landau*. Ed. by D. TER HAAR. Pergamon, 1965, pp. 723–730. ISBN: 978-0-08-010586-4. DOI: https://doi.org/10.1016/B978-0-08-010586-4.50095-X. URL: https://www.sciencedirect.com/science/article/pii/B978008010586450095X.

[104] C. C. Tsuei and J. R. Kirtley. "Pairing symmetry in cuprate superconductors". In: *Rev. Mod. Phys.* 72 (4 Oct. 2000), pp. 969–1016. DOI: 10.1103/RevModPhys.72.969. URL: https://link.aps.org/doi/10.1103/RevModPhys.72.969.

[105] Jordan Venderley and Eun-Ah Kim. "Density matrix renormalization group study of superconductivity in the triangular lattice Hubbard model". In: *Phys. Rev. B* 100 (6 Aug. 2019), p. 060506. DOI: 10.1103/PhysRevB.100.060506. URL: https://link.aps.org/doi/10.1103/PhysRevB.100.060506.

[106] Grigory E. Volovik. "On edge states in superconductors with time inversion symmetry breaking". In: *Journal of Experimental and Theoretical Physics Letters* 66 (1997), pp. 522–527.

[107] Christof Wetterich. "Exact evolution equation for the effective potential". In: *Physics Letters B* 301.1 (1993), pp. 90–94. ISSN: 0370-2693. DOI: https://doi.org/10.1016/0370-2693(93)90726-X. URL: https://www.sciencedirect.com/science/article/pii/037026939390726X.

[108] Kenneth G. Wilson. "Renormalization Group and Critical Phenomena. I. Renormalization Group and the Kadanoff Scaling Picture". In: *Phys. Rev. B* 4 (9 Nov. 1971), pp. 3174–3183. DOI: 10.1103/PhysRevB.4.3174. URL: https://link.aps.org/doi/10.1103/PhysRevB.4.3174.

[109] Kenneth G. Wilson. "Renormalization Group and Critical Phenomena. II. Phase-Space Cell Analysis of Critical Behavior". In: *Phys. Rev. B* 4 (9 Nov. 1971), pp. 3184–3205. DOI: 10.1103/PhysRevB.4.3184. URL: https://link.aps.org/doi/10.1103/PhysRevB.4.3184.

[110] Sebastian Wolf, Thomas L. Schmidt, and Stephan Rachel. "Unconventional superconductivity in the extended Hubbard model: Weak-coupling renormalization group". In: *Phys. Rev. B* 98 (17 Nov. 2018), p. 174515. DOI: 10.1103/PhysRevB.98.174515. URL: https://link.aps.org/doi/10.1103/PhysRevB.98.174515.

[111] Sebastian Wolf et al. "Triplet Superconductivity from Nonlocal Coulomb Repulsion in an Atomic Sn Layer Deposited onto a Si(111) Substrate". In: *Phys. Rev. Lett.* 128 (16 Apr. 2022), p. 167002. DOI: 10.1103/PhysRevLett.128.167002. URL: https://link.aps.org/doi/10.1103/PhysRevLett.128.167002.

[112] Fengcheng Wu et al. "Hubbard Model Physics in Transition Metal Dichalcogenide Moiré Bands". In: *Phys. Rev. Lett.* 121 (2 July 2018), p. 026402. DOI: 10.1103/PhysRevLett.121.026402. URL: https://link.aps.org/doi/10.1103/PhysRevLett.121.026402.

[113] Yi-Ming Wu, Zhengzhi Wu, and Hong Yao. *Pair-density-wave and chiral superconductivity in twisted bilayer transition-metal-dichalcogenides*. 2022. arXiv: 2203.05480 [cond-mat.supr-con].

[114] Noah F. Q. Yuan, Hiroki Isobe, and Liang Fu. "Magic of high-order van Hove singularity". In: *Nature Communications* 10, 5769 (2019). DOI: 10.1038/s41467-019-13670-9. URL: https://doi.org/10.1038/s41467-019-13670-9.

[115] D. Zanchi and H. J. Schulz. "Weakly correlated electrons on a square lattice: Renormalization-group theory". In: *Phys. Rev. B* 61 (20 May 2000), pp. 13609–13632. DOI: 10.1103/PhysRevB.61.13609. URL: https://link.aps.org/doi/10.1103/PhysRevB.61.13609.

[116] Jiawei Zang et al. "Hartree-Fock study of the moiré Hubbard model for twisted bilayer transition metal dichalcogenides". In: *Phys. Rev. B* 104 (7 Aug. 2021), p. 075150. DOI: 10.1103/PhysRevB.104.075150. URL: https://link.aps.org/doi/10.1103/PhysRevB.104.075150.

[117] A. Zee. *Group Theory in a Nutshell for Physicists*. USA: Princeton University Press, 2016. ISBN: 978-0-691-16269-0, 978-0-691-16269-0, 978-1-4008-8118-5.

[118] Hui Zhai, Fa Wang, and Dung-Hai Lee. "Antiferromagnetically driven electronic correlations in iron pnictides and cuprates". In: *Phys. Rev. B* 80 (6 Aug. 2009), p. 064517. DOI: 10.1103/PhysRevB.80.064517. URL: https://link.aps.org/doi/10.1103/PhysRevB.80.064517.

[119] Chendong Zhang et al. "Interlayer couplings, Moiré patterns, and 2D electronic superlattices in MoS_2/WSe_2 hetero-bilayers". In: *Science Advances* 3.1 (2017), e1601459. DOI: 10.1126/sciadv.1601459. eprint: https://www.science.org/doi/pdf/10.1126/sciadv.1601459. URL: https://www.science.org/doi/abs/10.1126/sciadv.1601459.

[120] F. C. Zhang and T. M. Rice. "Effective Hamiltonian for the superconducting Cu oxides". In: *Phys. Rev. B* 37 (7 Mar. 1988), pp. 3759–3761. DOI: 10.1103/PhysRevB.37.3759. URL: https://link.aps.org/doi/10.1103/PhysRevB.37.3759.

[121] Yiqing Zhou, D. N. Sheng, and Eun-Ah Kim. "Quantum Phases of Transition Metal Dichalcogenide Moiré Systems". In: *Phys. Rev. Lett.* 128 (15 Apr. 2022), p. 157602. DOI: 10.1103/PhysRevLett.128.157602. URL: https://link.aps.org/doi/10.1103/PhysRevLett.128.157602.

[122] Jean Zinn-Justin. *Quantum Field Theory and Critical Phenomena; 4th ed.* International series of monographs on physics. Oxford: Clarendon Press, 2002. DOI: 10.1093/acprof:oso/9780198509233.001.0001. URL: https://cds.cern.ch/record/572813.

Acknowledgements

A wise man once said:

-Konsequenz bedeutet auch Holzwege zu Ende zu gehen.
(*Consistency also means finishing wooden paths*)

Well, this proverb does not translate well to English. Anyhow, when I look back to the past years I often felt like being on an extraordinary long wooden path and It will remain unclear what one can win by finishing it and it is questionable if finishing the way makes even sense at all. Nevertheless, I have met many fantastic people along the way and I am confident that I would not have made it to the end without them. So, this section is dedicated to them.

At first, I want to thank you Michael for you supervision and guidance while conducting my PhD. Even when I was working at tremendously slow pace, you had patience with me and cast this work in the correct direction. Also, your ability of forming even in the pandemic an environment for your students which felt like there is still a lively and active working group was of immeasurable worth. This specific time was the hardest of my PhD and the Zoom-coffees back then helped a lot to cushion the pressing feeling of isolation we all felt back then.

I also want to thank Laura Classen for all the fruitful collaboration in the past and your significant input while I was working on my projects.

I must thank all permutations of the configurations of office 211, in order of appearance: Björn, Bernhard, Oriana, Paula and Passant. I had the feeling that we really had something very special inside this depressing PCB infested room made of ugly concrete and it is sad how the pandemic disrupted this environment. It was a pleasure being there with you in context of both, work and non-worked related activities.

A great thank you goes out for Bernhard, Björn, Dominik, Hannes, Ravn and Carl for proofreading parts of this thesis.

A special thanks goes to Dominik Kiese for all the help and support in regards of numerical and computational questions which arised in the past. Your expertise and joy of sharing all the knowledge you had about Julia without ever getting tired of it were of immeasurable value for me. If there is one person I met during my PhD who really deserve to thrive in academia, then it is you. I wish you the best of luck and success for your future physics career.

Moreover I express my gratitude to all people at institute in Cologne which made it a pleasant time there. There are too many to list, so please don't feel offended when I don't mention all of you now!

Of course I also want to thank my friends outside the physics cosmos. First of all, Felix and Tim. The conversations and your "outside" perspectives were absolutely crucial for me to not go crazy in the academic circus. Also my band mates Philipp, Leif and Laura. Making music with you was often the important "cooldown" I needed after some hard weeks in the last years.

But naturally the greatest thank you goes to you, Maike. I do not know how you managed to endure my presence in the last 4 years and the person I became while working on this thesis. For me it is a miracle that you never were tired of my down phases (and we know, there were plenty of them) and always under all circumstances granted me your unconditional love and support. I am to hundred percent sure that I would have not survived this time without you.

And last but not least, a very special thanks go to my parents, for which I will write the acknowledgement in German:
In Deutschland ist bis heute die Durchlässigkeit bezüglich des Bildungsniveaus defizitär. Kinder aus nicht-akademischen Haushalten werden seltener aufs Gymnasium empfohlen, nehmen noch seltener ein Studium auf und das Vollenden einer Doktorarbeit ist soziologisch gesehen eine wahre Anomalie. Ihr habt immer wenn es notwendig war alles gegeben damit ich ein Abitur machen konnte und ein Studium anfangen und beendeten durfte. Eure Unterstützung war immer ein immenses Privileg und ohne euch wäre ich nie dort wo ich heute bin.

Erklärung zur Dissertation

Hiermit versichere ich an Eides statt, dass ich die vorliegende Dissertation selbstständig und ohne die Benutzung anderer als der angegebenen Hilfsmittel und Literatur angefertigt habe. Alle Stellen, die wörtlich oder sinngemäß aus veröffentlichten und nicht veröffentlichten Werken dem Wortlaut oder dem Sinn nach entnommen wurden, sind als solche kenntlich gemacht. Ich versichere an Eides statt, dass diese Dissertation noch keiner anderen Fakultät oder Universität zur Prüfung vorgelegen hat; dass sie - abgesehen von unten angegebenen Teilpublikationen und eingebundenen Artikeln und Manuskripten - noch nicht veröffentlicht worden ist sowie, dass ich eine Veröffentlichung der Dissertation vor Abschluss der Promotion nicht ohne Genehmigung des Promotionsausschusses vornehmen werde. Die Bestimmungen dieser Ordnung sind mir bekannt. Darüber hinaus erkläre ich hiermit, dass ich die Ordnung zur Sicherung guter wissenschaftlicher Praxis und zum Umgang mit wissenschaftlichem Fehlverhalten der Universität zu Köln gelesen und sie bei der Durchführung der Dissertation zugrundeliegenden Arbeiten und der schriftlich verfassten Dissertation beachtet habe und verpflichte mich hiermit, die dort genannten Vorgaben bei allen wissenschaftlichen Tätigkeiten zu beachten und umzusetzen. Ich versichere, dass die eingereichte elektronische Fassung der eingereichten Druckfassung vollständig entspricht.

Teilpublikationen

Folgende Publikationen sind während der Promotionsphase entstanden. Die dritte Teilpublikation entstand im ersten Jahr der Promotion und ist nicht Gegenstand dieser Dissertation.

- **Nico Gneist**, Laura Classen, Michael M. Scherer,
  "Competing instabilities of the extended Hubbard model on the triangular lattice: Truncated-unity functional renormalization group and application to moiré materials".
- **Nico Gneist**, Dominik Kiese, Ravn Henkel, Ronny Thomale, Laura Classen, Michael M. Scherer,
  "Functional renormalization of spinless triangular-lattice fermions: N-patch vs. truncated-unity scheme".
- Dietrich Roscher, **Nico Gneist**, Michael M. Scherer, Simon Trebst, and Sebastian Diehl,
  "Cluster functional renormalization group and absence of a bilinear spin liquid in the J_1-J_2 Heisenberg model". In: Phys. Rev. B 100, 125130 (2019).

Nico Gneist,
Köln, den 19.08.2022